



**HAL**  
open science

# Creep Fatigue Interaction in Solder Joint Alloys of Electronic Packages

Stéphane Zanella

► **To cite this version:**

Stéphane Zanella. Creep Fatigue Interaction in Solder Joint Alloys of Electronic Packages. Mechanics [physics]. Université Paris Saclay (COMUE), 2018. English. NNT : 2018SACLX102 . tel-02131527

**HAL Id: tel-02131527**

**<https://theses.hal.science/tel-02131527v1>**

Submitted on 16 May 2019

**HAL** is a multi-disciplinary open access archive for the deposit and dissemination of scientific research documents, whether they are published or not. The documents may come from teaching and research institutions in France or abroad, or from public or private research centers.

L'archive ouverte pluridisciplinaire **HAL**, est destinée au dépôt et à la diffusion de documents scientifiques de niveau recherche, publiés ou non, émanant des établissements d'enseignement et de recherche français ou étrangers, des laboratoires publics ou privés.

# Creep Fatigue Interaction in Solder Joint Alloys of Electronic Packages

Thèse de doctorat de l'Université Paris-Saclay  
préparée à l'École Polytechnique

École doctorale n° 579 Sciences Mécaniques et Energétiques, Matériaux  
et Géosciences (SMEMAG)  
Spécialité de doctorat : Mécanique

Thèse présentée et soutenue à l'École Polytechnique, Palaiseau, le 13/12/2018, par

**Stéphane Zanella**

## Composition du Jury :

Aude Simar Professeure, UC Louvain, Belgique	Président
Hélène Frémont Professeure, IMS Bordeaux	Rapporteur
Jean-Yves Buffière Professeur, INSA Lyon	Rapporteur
Véronique Doquet Directrice de recherche CNRS, Ecole Polytechnique	Examineur
Andrei Constantinescu Directeur de recherche CNRS, Ecole Polytechnique	Directeur de thèse
Eric Charkaluk Directeur de recherche CNRS, Ecole Polytechnique	Co-Directeur de thèse
Aurélien Lecavelier des Etangs-Levallois Ingénieur Docteur, Industrie groupe Thales	Invité
Wilson Carlos Maia Filho Ingénieur Docteur, Industrie groupe Thales	Invité

*A ma famille et mes amis.*

## Remerciements

Cette thèse a été réalisée dans le cadre d'une Convention Industrielle de Formation par la Recherche (CIFRE) entre l'équipe Technologies et procédés de l'Industrie groupe Thales et le Laboratoire de Mécanique des Solides de l'École Polytechnique.

Je remercie dans un premier temps Andrei Constantinescu, Directeur de recherche à l'École Polytechnique et directeur de cette thèse, pour m'avoir donné l'opportunité de réaliser cette thèse dans les meilleures conditions. Sa disponibilité et ses précieux conseils ont été indispensables à la réalisation de ces travaux.

Je remercie également Éric Charkaluk, Directeur de recherche à l'École Polytechnique, et co-directeur de cette thèse, de m'avoir fait bénéficier de son attention, ses idées ainsi que de son entière disponibilité dans ces recherches. Je n'ai cessé d'apprendre à ses côtés.

Je souhaite remercier Wilson Carlos Maia Filho, responsable de l'équipe Technologies et Procédés Thales, pour m'avoir fait profiter de son expérience et de m'avoir accordé sa confiance dans l'exécution des études. J'ai bénéficié de nombreux conseils éclairés et du meilleur cadre de travail.

Je souhaite également remercier Aurélien Lecavelier-des-Etangs-Levallois, Ingénieur de l'équipe Technologies et Procédés Thales, pour m'avoir accompagné dans cette thèse et de m'avoir partagé l'ensemble de ses clairvoyantes et astucieuses remarques.

Je remercie Hélène Frémont, Professeur à l'IMS Bordeaux, ainsi que Jean-Yves Buffière, Professeur à l'INSA Lyon, d'avoir accepté de rapporter cette thèse. Je leur suis reconnaissant d'avoir accepté de lire et revoir ce manuscrit.

Je tiens à remercier l'ensemble de l'équipe Technologies et Procédés, et plus particulièrement Damien Baudet, Julien Vieilledent, Arnaud Grivon, Julien Baudet, Ngoc Quach, Victor Chastand, Yann Tricot ainsi que Sourasith Souvannasot. Je remercie également Julien Perraud du laboratoire LAT-PI Thales et Charlotte Belloc qui m'a accompagné à un moment décisif.

Je tiens également à remercier grandement l'ensemble du Laboratoire de Mécanique des Solides, et en particulier Simon Hallais, Alexandre Tanguy, Vincent De Greef, Erik Guimbretière, Jean-Christophe Eytard et Pascal Marie.

Enfin, je remercie ma famille et mes amis. Leur présence a été mon meilleur atout dans la réussite de cette thèse.



# Contents

Remerciements .....	3
Index.....	7
General introduction.....	8
Chapter I. Context and Objectives .....	10
1. Electronic boards.....	11
1.a. Aeronautic, space and defense critical markets.....	11
1.b. Electronic board structure .....	12
1.c. Electronic board assembly.....	14
2. Reliability of solder joints .....	15
2.a. Failure rate in time analysis.....	15
2.b. Stresses in solder joints during mission profile.....	16
2.c. Reliability challenges for critical applications .....	20
2.d. Prediction of solder joint failure with simulation.....	21
3. Mechanical properties of solder joints .....	22
3.a. Lead-Free solder joint microstructure .....	22
3.b. Elastic and plastic mechanical properties.....	23
3.c. Viscosity properties.....	31
3.d. Fatigue properties .....	35
4. Conclusions of the literature review and perspectives .....	41
5. Objectives.....	42
Chapter II. Experimental Setup .....	44
1. Innovative shear test bench .....	45
1.a. Shear test bench description.....	45
1.b. Samples of the shear test bench.....	46
1.c. Schematic representation of the shear test bench .....	47
1.d. Experimental results post-processing.....	48
1.e. Test in temperature.....	53
2. Accuracies of force and displacement measurements .....	55
2.a. Accuracy of the force sensor .....	55
2.b. Accuracy of the local displacement.....	57
2.c. Accuracy of tests in temperature .....	58
3. Monotonic tests .....	59
3.a. Results of the mechanical characterization .....	59
3.b. Comparison of the monotonic test results with the literature.....	60

3.c.	Residual stress for test in temperature.....	60
4.	Step-Stress Results .....	61
4.a.	Step-stress test .....	61
4.b.	Step-Stress Results .....	62
4.c.	Analysis of step-stress results.....	64
5.	Conclusions .....	66
Chapter III.	Failure Definition .....	67
1.	Mechanical and electrical failures .....	68
1.a.	Mechanical failure.....	68
1.b.	Electrical failure .....	69
1.c.	Specific configuration in this work .....	70
2.	Criterion and mechanism of failure.....	71
2.a.	Force and electrical resistance monitoring.....	71
2.b.	Initial inspection.....	74
2.c.	Failure mechanism during fatigue tests.....	75
2.d.	Homogeneity of the loading .....	78
3.	Mechanical parameters extraction.....	80
3.a.	Methodology .....	80
3.b.	Mechanical parameters for fatigue tests without dwell time.....	80
3.c.	Mechanical parameters for fatigue tests with dwell time .....	84
4.	Conclusions .....	87
Chapter IV.	Fatigue Results .....	88
1.	Fatigue tests.....	89
2.	Test controls .....	90
2.a.	Validation of experimental results based on selection criteria.....	90
2.b.	Disturbance detected during the test.....	90
2.c.	Disturbance detected after post-processing.....	91
2.d.	Test control synthesis .....	94
3.	Results and discussions .....	94
3.a.	Weibull distribution.....	94
3.b.	Mechanical response .....	100
3.c.	Damage indicators.....	103
3.d.	Discussions.....	105
4.	Conclusions .....	108
Chapter V.	Cyclic damage analysis .....	109
1.	Fatigue of solder joints .....	110

1.a.	Fatigue regimes .....	110
1.b.	Importance of creep-fatigue interaction for solder joint alloys .....	111
2.	Analysis of the results of the fatigue tests plan .....	112
2.a.	Shear stress and strain .....	112
2.b.	Inelastic strains .....	113
2.c.	Simulation of the sample mechanical response .....	121
3.	Creep-fatigue-interaction law for solder joint .....	122
3.a.	Damage indicators synthesis .....	122
3.b.	Damage law for solder joint material .....	123
3.c.	Duration of dwell time .....	129
4.	Conclusions .....	131
	General conclusion.....	132
	Bibliography.....	134
	Annex 1: Résumé en français.....	140
	Annex 2 : Microstructure evolutions with damage .....	142

# Index

ATC	Accelerated Thermal Cycling
BGA	Ball Grid Array
CM	Coffin-Manson's fatigue law
COST	Commercial Off-The-Shelf
CSP	Chip-Scale Package
CTE	Coefficient of Thermal Expansion
DIP	Dual Inline Package
DoE	Design of Experiment
EBSD	Electron BackScatter Diffraction
EDX	Energy Dispersive X-ray spectroscopy
FEA	Finite Element Analysis
IC	Integrate Circuit
I/O	Input/Output
IPC	Institute for Electronic Circuit Interconnects and Packaging
ITRS	International Technology Roadmap for Semiconductor
LF	Lead-Free
DW	Fatigue law based on dissipated energy per cycle
PCB	Printed Circuit Board
PCBA	Printed Circuit Board Assembly
QFN	Quad Flat No-lead
QFP	Quad Flat Package
RoHS	Restriction of Hazardous Substances
SoC	System-on-Chip
SiP	System-in-Package
SoP	System-on-Package
STD	Standard Deviation
T <sub>g</sub>	Glass transition Temperature
WLP	Wafer Level Package

# General introduction

Solder joint ensures the electrical, mechanical and thermal links between electronic packages and the printed circuit board. As a result of external loadings, including temperature variation and vibration, and structural effects, solder joints of electronic products are submitted to stresses. Thus, from a reliability point of view on electronic boards, this makes them one of the most critical parts. For the aerospace and defense industries, the complexity with regards to guaranteeing the solder joints' reliability in electronic products originates from a number of points including harsh environments, long mission profiles, as well as products' high reliability specificities that are designed for these critical applications.

Printed Circuit Board Assembly's evolution introduces new technology and materials that must be qualified for the aerospace and defense industries' constraints. Within the study of solder joint reliability, it appears that the use of Finite Element Analysis simulation is a promising solution; one whose outcome is to maintain the increasing costs of qualification tests. However, mechanical properties of alloys used for solder joints are required for such simulation. So far, there is no significant consensus in the literature regarding mechanical constitutive models, parameters or fatigue laws. The mechanical behavior of these alloys is complex due to their low melting temperature and the visible viscosity domain is reached even at room temperature. Moreover, the creep fatigue interaction cannot be neglected in the fatigue analysis of these alloys. Therefore, it becomes apparent that the solder joints' microstructure in the final application is nothing but complex.

The small size of solder joint, that being hundreds of micrometers, induces a small number of grains per solder joint. In addition, the assembly process induces intermetallic phases between the joint and the copper pads. Moreover, the shape of the solder joints is defined during the assembly process and therefore cannot be predicted. Subsequently, the assembly process of electronic packages introduces variabilities that change the mechanical properties of the alloy and the package in the final application. It is of course imperative to consider the final microstructure of the alloy when the mechanical properties of these alloys are studied through experimental tests.

When predicting lifetime, fatigue laws such as Coffin-Manson, based on the inelastic strain per cycle, as well as others based on the dissipated energy per cycle, are commonly used in the industry. Plastic and viscous strains are mingled in these laws and formulated as a total inelastic strain, thus supposing that damages from plastic and creep strains are comparable. Therefore, the relevance of these laws in the case of solder joint and the mission profiles of aerospace and defense industries are to be discussed. Important viscous strains are in fact developed due to not only a harsh environment within high temperatures, but also the mission profiles' long maintain phases. In order to address such critical applications, the creep-fatigue interaction must be taken into account with regards to the fatigue law for solder joint alloys.

The objective of this thesis is therefore to define a fatigue law for assembled solder joints of electronic package which takes into account the creep-fatigue interaction.

Chapter one provides the general context of the study and identifies that there exists a lack of clear and precise experimental data to calibrate a fatigue law for solder joint in in-service representation conditions. Chapter two explores the development of an innovative test bench whose objective is to perform fatigue shear tests of assembled packages. Chapter three deals with the failure criterion and the importance of electrical resistance monitoring, and this is demonstrated through a fatigue test plan being performed with the test bench. Its aim is to evaluate the influence of force, temperature and

dwell time parameters. Chapter four then provides the results of these tests and finally chapter five focuses on the calibration of a creep-fatigue law.

## Chapter I. Context and Objectives

*This chapter introduces the reliability of solder joints taking into account the constraints of aerospace and defense industries. The discussion starts with a description of electronic boards from a mechanical point of view. Specific role of solder joints is highlighted. Moreover, starting from the constraints of service loading and environment the mechanical stresses within the solder joints are reported.*

*The presentation of the subject continues with a literature review of mechanical properties of solder joints. The survey starts with the specific microstructure of solder joint and focuses then on their mechanical models. Elastic, plastic and viscous properties of solder materials are introduced for leaded and lead-free solder materials. The discussion emphasizes temperature and strain rate dependencies of the parameters and models as they play an important role under the prescribed service load conditions. Finally, fatigue results are presented both as the used criteria and applied lifetime predictions. The overview covers both classical fatigue criteria currently applied in industry as well as more complex models including damage evolution.*

*The literature review highlights that: (i) most material characterizations have been performed only on bulk samples, (ii) experimental setup rarely allows separated measurement of plastic and viscous strains and does not compare their relative impact on the mechanical and fatigue behavior of the solder joints and (iii) important scale effects are present in all physical phenomena under consideration analysis. The evolution of microstructure of the solder joints depends on several parameters and therefore the analysis of mechanical properties cannot be only performed by standard experiments on bulk samples. Moreover, this is accompanied by a shortage of precise experimental data which permit the definition and calibration of a fatigue law at the scale of the solder joint.*

# 1. Electronic boards

This section introduces the reliability of solder joints taking into account the constraints of aerospace and defense industries. Electronic boards are described in detail taking into account the global structure and its constitutive elements and materials. The Manufacturing process of electronic packages is recounted next and the implication for reliability are highlighted. Finally, the actual challenges for the reliability of solder joints for critical applications are introduced in a critical discussion.

## 1.a. Aeronautic, space and defense critical markets

Electronic boards are nowadays part of numerous daily used products: computer, mobile, car, home automation systems etc. and generate a large number of technological developments. Consumer electronics market, mainly driven by smartphone applications, requires strong and constant miniaturization effort associated to functional performance increase for high volume, low cost and mild environments applications. A large number of new technologies are therefore developed to reach higher interconnection density of electronic boards. Commercially available electronic packages are also mainly developed for this market. These new technologies and packages are interesting for critical applications. However, reliability is a critical aspect for applications such as commercial avionics, transportation, space and defense. Integration of such new packages and technologies requires to qualify their use with the constraints of critical markets: high reliability, harsh environment and long mission profiles. In addition, if required, the need must be highlighted to apply strengthening strategies or to restrict their use to applications in less severe environment.

Products developed for space, defense and avionics industries have low production volume (10-10,000 pieces/year). Due to the high cost of each electronic board and the efficiency requirement, packages also need to be able to be repaired after failure. Furthermore, products lifetime is longer for these applications than for consumer electronics. In this context, it is critical and meaningful to study end-of-life reliability and electronic board mechanical behavior. For example electronic equipment embedded in a satellite needs to resist more than thirty years with a failure acceptable level smaller than 0,001% (see table for illustration Figure 1). The markets classification is based on a proposition from the American industry association IPC (Institute for Electronic Circuit Interconnects and Packaging)-SM-785 standard [1].

Use Category	Typical years of Service	Accepted Cumulated Failure within Lifetime	Tmin [°C]	Tmax [°C]	Delta T [°C]	Mechanical Shock and High Vibration Level	Repair Needs	Typical Volume per Product Batch
Space (leo / geo)	5 to 30	0.001%	-55	95	3 / 100	Yes	Yes (rework)	3
Military Avionics (a / b / c)	10	0.01%	-55	95	40 / 60 / 80	Yes	Yes	10
Commercial Avionics	20	0.001%	-55	95	20	Yes	Yes	200
Military Ground & Ship	10	0.1%	-55	95	40 (+60)	Yes	Yes	50
Telecom	7 to 20	0.01%	-40	85	35	Yes	Yes (rework)	1000
Automotive under Hood	5	0.1%	-55	125	60 (+100;+140)	Yes	No	100 000
Industrial & Automotive Passenger Compartment	10	0.1%	-55	95	20 (+40;+60;+80)	Yes	No	100 000
Computers	5	0.1%	15	60	20	No	No	100 000
Consumer	1 to 3	1.0%	0	60	35	No	No	1 000 000

Long mission profile

Harsh environmental conditions

+ Power management

+ Signal integrity

Classification based on IPC-SM-785

High-Reliability Requirements	Harsh Thermo-mechanical Environment	Harsh Mechanical Environment	Repair-ability	Low Volume
-------------------------------	-------------------------------------	------------------------------	----------------	------------



Figure 1: Specific needs of space, defense and avionics industries [2]

### 1.b. Electronic board structure

Electronic boards are used to perform complex functions in larger systems. Electronic boards are basically composed of a Printed Circuit Board (PCB) on which electronic packages are assembled with solder joints (see Figure 2), and are connected to other systems with connectors. The assembled electronic board with its packages is called Printed Circuit Board Assembly (PCBA).

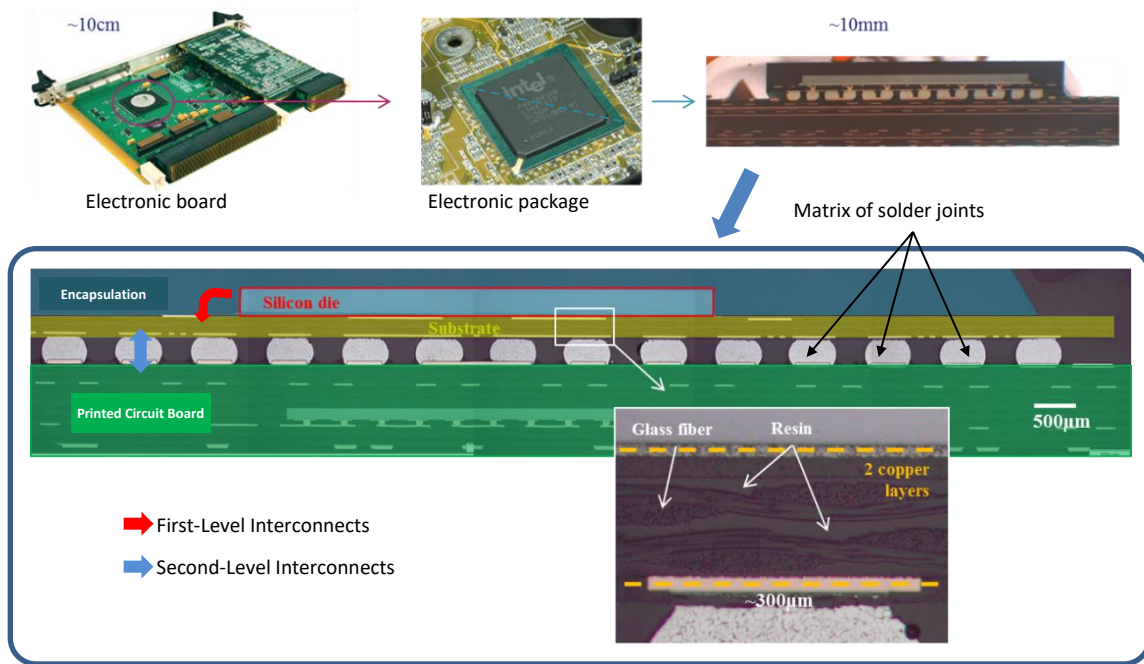


Figure 2: Electronic board assembled with a Ball Grid Array (BGA) Package

Electronic packages are composed of a silicon die, a substrate and the molding. The silicon die is programmed with algorithms to perform specific calculations and is connected to the package substrate. This connection is the First-Level Interconnects. The substrate, which can be assimilated to a PCB, connects outputs of the die to the solder joints. Substrate has a laminate structure with copper layers and laminates, which are composite material with resin and glass fibers. More details about laminates are given in the following paragraph dedicated to PCB materials.

Solder joint ensures the electrical link between electronic packages and the PCB (Second-Level Interconnects). Electronic packages are connected to perform complex functions. Solder joint maintains also mechanically electronic packages on the PCB. Silicon dies heat up during use. Solder joints are also used to dissipate this heat. Solder joint types are generally classified according to the form of their attachments on the board. In fact, these connections types have a direct impact on packages reliability because failure often occurs in interconnections. Figure 3 illustrates this classification. Understanding the packages structure is important to build relevant numerical models of board for simulation purpose.

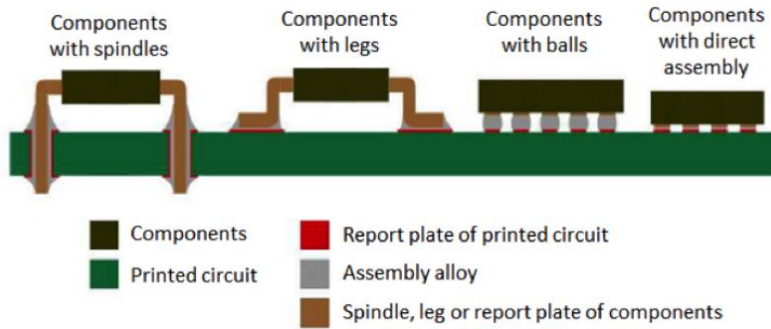


Figure 3: Classification for attachments of packages on PCB [3]

PCB main goal is to interconnect electronic packages together to create more complex functions. Historically, PCB where monolayer boards: only composed of a dielectric support with a single printed copper layer. PCB are nowadays composed of multiple copper and dielectric layers (laminates) alternatively stacked together. This multilayer structure of the PCB is required to due to the increasing interconnect density of nowadays electronic packages. Laminate layers are composite structure: matrix of resin is reinforced with fiber glasses. Resin content in the laminate is an important parameter to calculate laminate mechanical properties. Different natures of resins can be used as epoxy or polyimide resins. The resins, with Coefficient of Thermal Expansion (CTE) around 20 ppm/K, is reinforced with fiber glasses which gives to the laminate a CTE in the fiber direction around 13 ppm/K. This value must be considered as first order approximation. Calculation of PCB mechanical properties is complex and out of the scope of this thesis. Lot of parameters including PCB stack-up and resin content must be taken into account.

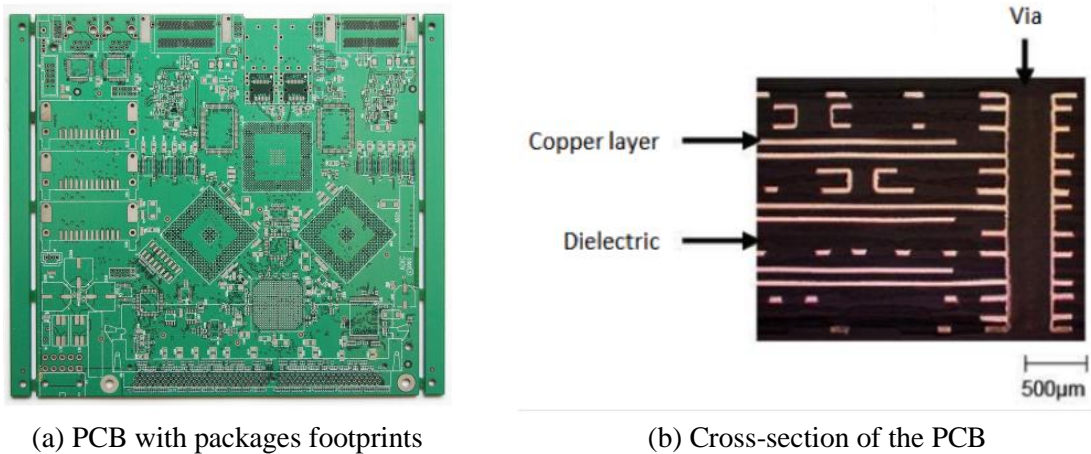


Figure 4: PCB multi-layers structure of electronic board

PCB manufacturing process can be decomposed in four main steps. First step is the etching of copper layers to form lines and planes to interconnect packages according to the electrical scheme. Packages footprints are added in the two external layers for the assembly of the packages. Second step is the manufacturing of the multilayer structure by laminating the different copper layers with dielectric in between for insulation. Third, after lamination, the different copper layers are linked together by mechanical or laser drilling and copper plating of vias. This process is repeated several times to obtain the desired PCB stack-up. Finally, finish plating and solder mask are deposited on the

outer layers to preserve exposed copper of footprints from oxidation and to help for packages assembly.

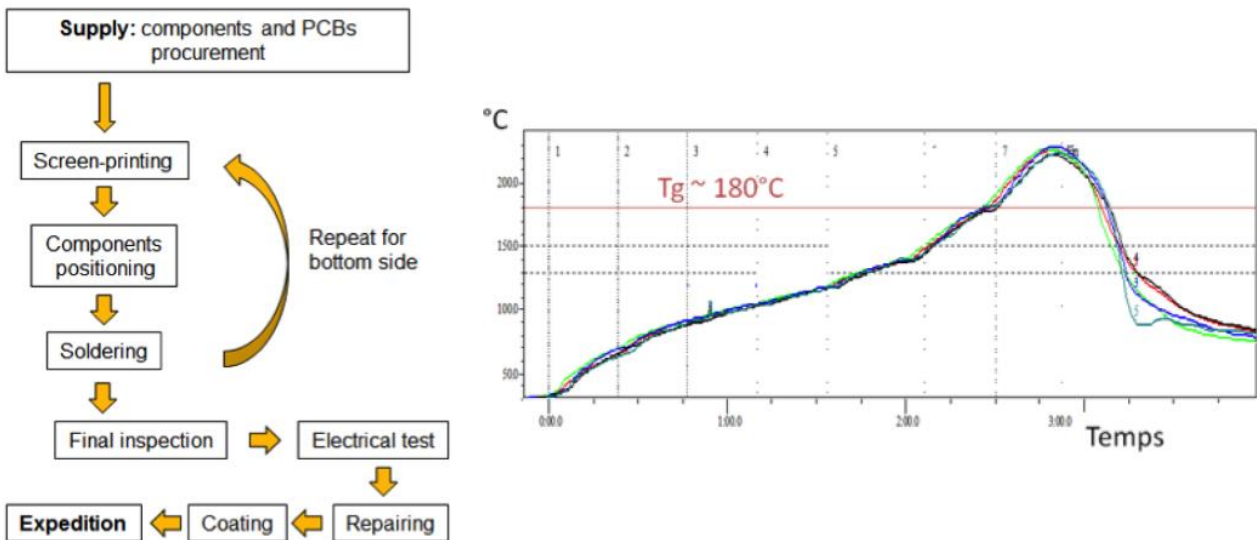
### 1.c. Electronic board assembly

Solder joints are formed during the assembly of the electronic board. A schema with the principal steps and the temperature profile of the PCB during the assembly is presented in Figure 5. More precisely the assembly process consists of the following steps:

- (i) Solder paste is deposited on PCB footprints by a screen-printing process,
- (ii) Package are deposited on top side with a pick and place loading arm.
- (iii) The board is heated up in a reflow oven following a dedicated thermal profile.

The thermal profile reaches a peak temperature above the melting point of the solder and presents specific heating and cooling ramps to minimize thermal residual stresses. For double-sided PCB architectures, the process is repeated in order to assembly an additional series of packages on the other side of the PCB. The process is ended by a series of inspections and electrical tests to verify the final package assembly. A protective layer can be applied by conformal coating on the complete board, without adding further temperature constraints on the packages.

Let us further remark that several process parameters have a direct impact on the reliability of the solder joints and consequently on the entire PCB assembly. Residual stresses are an outcome of the different coefficients of thermal expansion and the temperature changes during the assembly as they can facilitate the opening or closure of cracks if they have a tensile or compressive character. Moreover, cooling speeds will determine the precise crystallization process of solder joints and influence as such their joint microstructure.



(a) PCBA assembly process

(b) Thermal profil used for PCBA assembly process

Figure 5: Electronic package assembly: (a) PCBA process and (b) used thermal profile

Assemblies from two distinct processes will be studied in the following chapters, (a) SAC305 using a lead-free solder joint and (b) Backward SnPb+ using a lead-containing alloy SnPb. If lead-free joints are the standard norm in the consumer electronics, the use of lead is still tolerated in critical applications as aerospace and defense. In the lead-free SAC305 assembly process, solder balls and

solder paste are made out of the SAC305 alloy. The SAC305 alloy is chemically composed of 3 wt.% of silver, 0.5 wt.% of copper and 96.5 wt.% of tin. The backward SnPb+ process, uses a solder paste made out of a leaded Sn37Pb alloy (37 wt.% of lead and 63 wt.% of tin), whereas the balls of the electronic package are made out of SAC305. Let us further notice that the solder joints of the Wafer Level Package (WLP) which will be discussed in chapter 2 contains 7 wt.% of lead after backward SnPb+ process. This value has been computed from the deposited quantity of solder paste. Up to date, aerospace and defense applications are not in the scope of environmental directives restricting the use of Lead.

Heterogeneity of assembly processes is a difficult and complex task from an industrial point of view. A low volume of production increases the relative cost of development and manufacturing and can justify the mixing of assembly technologies, which drives in itself the increasing cost. An example of the complexity of the assembly is the size of the package pitch, defined as the distance between two solder joints. Current electronic boards have packages with pitches in the range of 0.4 to 1.27 mm. Have this variety on an assembly line requires the existence of stencils with different thicknesses in different areas during the assembly process. As a consequence, the qualification of such an assembly process becomes very difficult and expensive.

## 2. Reliability of solder joints

Failure is a state of inability to perform a normal function. Reliability is the ability of a product to perform a under given conditions and for a specified period of time with an acceptable failure risk. Miniaturization and densification of electronic boards increase the risk of solder joint failure due for example to the induced reduction of solder joint sizes. Electronic boards structure and solder joint have been described in the previous section. The definition of reliability of solder joints will be now introduced. Mission profiles and induced stresses for solder joints will be presented. Accelerated reliability tests performed by companies to guarantee the reliability of solder joints will be detailed. Finally, some details about the use of simulation to predict cycles to failure in the context of solder joint will be given. Simulation is in fact an interesting solution to help reliability tests, understand failure mechanism and increase results from experimental tests.

### 2.a. Failure rate in time analysis

Let us now consider at a fixed time instant the instantaneous failure rate of a device. The evolution of the later with increasing time has proven to be a “bathtub” curve as described in [4]. In this representation one can identify three distinct phases characterized as (i) infant mortality, (ii) useful life also denoted as the “random steady-state” and (iii) end of wear or wear out (see Figure 6 for schematic representation).

The “infant mortality” corresponds to early failure and is associated to weakness created during or due to the manufacturing process. The reduction of this initial failure rate is generally harnessed through improvements in the quality control of the manufacturing process manufacturing and is not within the purpose of this work.

The “random steady-state” period characterizes the useful lifetime. In this period experience shows that failure occurs mostly random due to exceptional accidental loadings and has a low rate. Moreover, no evidence exists that would incriminate solder joints for the failures in this region (see [1] for a detailed discussion of this topic).

The “wear-out” region corresponds to the end-of-lifetime of the device under standard service loadings. It is characterized by a high increase of the failure rate and is a direct consequence of accumulating damage on different components. The detailed understanding of the subsequent damage mechanism and the precise distribution lifetimes corresponding to each failure mode are important for several reasons. On the one hand side they define the reliable life-time of the components and define inspect periods and non-destructive failure detection techniques and on the other hand side they permit to improve the component design and the assembly process by eliminating failure mechanism or by increasing lifetime through optimal design. It is obvious that in order to guarantee lifetime of the products engineers has to understand both service and exceptional loadings, or what is denoted in aerospace and defense applications the mission profile.

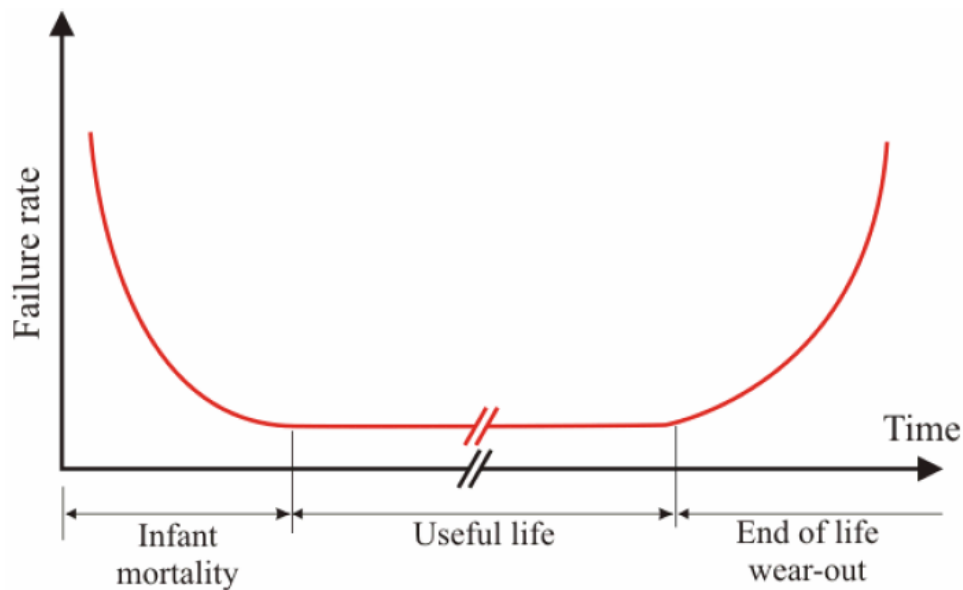


Figure 6: Failure rate bathtub curve [4]

## 2.b. Stresses in solder joints during mission profile

Electronic boards of space, defense and avionics products are used in harsh environment. Except manufacturing defects, corrosion and other chemical damage, there are three main sources of failure for solder joints of electronic boards: punctual mechanical shocks (during landing or operation for example), vibrations and large thermal variations [3]. Other environmental contributions, as corrosion or oxidation, induce damage mechanisms in solder joints but are not considered in the thesis. Manufacturers of critical markets need to guarantee long lifetime reliabilities in harsh environment for their products. If any failure occurs in the system, the consequences can be human casualties (for example in transport) or a huge financial losses (in satellite or space applications).

### 2.b.i. Mission profile analysis

Mission profile is the description of the product environment and the loadings submitted during the service. The environment loadings are described with physical quantities as temperature changes, vibration levels and relative humidity. An example of the daily temperature variations for two cities in different regions of the United States are represented in Figure 7 [5]. Possible mission profile definition for these two cities is highlighted by the two dotted lines. Red lines represent the maximum

and minimum temperatures and the blue line the most frequent cyclic stress. This analysis is presented as an example to illustrate how temperature variations from the environment can be evaluated. These temperature variations can describe for example the mission profile of a system which will be used in these cities. However, more investigations are required to evaluate the induced mission profile of the electronic boards of this hypothetical system.

Reliability of solder joint is qualified by manufacturers according to the product mission profile. However, it is not possible to perform 30 years of test before using technologies. Accelerated reliability tests are performed in order to evaluate the reliability of a product by subjecting it to conditions in excess of its normal service parameters. The equivalent lifetime in the field is predicted with accelerated test results and an acceleration factor (see Figure 8). These acceleration factors are estimated by engineers with the knowledges of fatigue properties of the considered component.

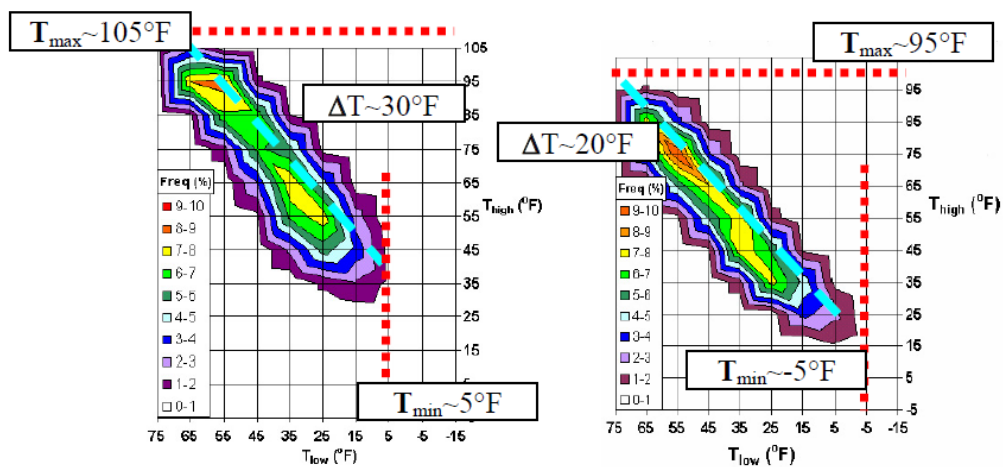


Figure 7: Temperature variation analyses for two US cities [5], red lines represent maximum and minimum temperatures and blues lines most frequently daily thermal changes

We recall the definition of failure mechanism as proposed in [6]:

*“Failure mechanisms are the physical, chemical, thermodynamic or other processes that result in failure. Failure mechanisms are categorized as either overstress or wear-out mechanisms. Overstress failure arises because of a single load (stress) condition, which exceeds a fundamental strength property. Wear-out failure arises as a result of cumulative damage related to loads (stresses) applied over an extended time”.*

Wear-out failure induced by cracks inside solder joint is the failure mechanism considered in this thesis. The failure mechanism during accelerated test needs to be the same as in the field. Prediction of reliability in the field is not possible if the failure mechanism during the accelerated test is not the same as in the field because the fatigue law may be different for another failure mechanism. Failure mechanism and fatigue law are important to compare test and operational environments and must be considered carefully.



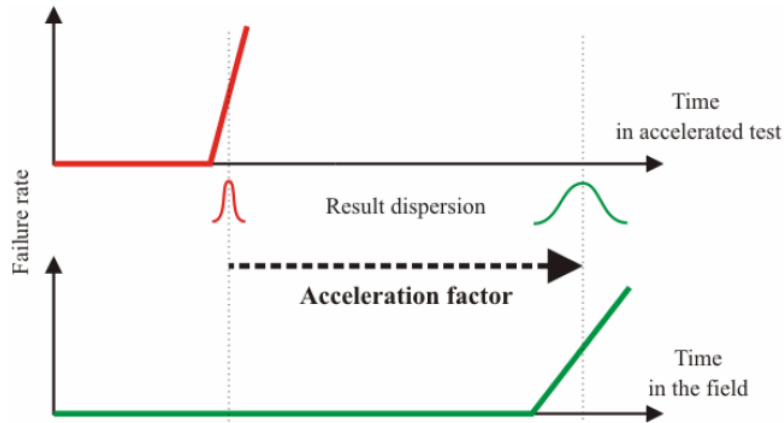


Figure 8: Simplified schematic representation of the acceleration factor [4]

### 2.b.ii. Thermo-mechanical stresses

As previously introduced, temperature variations represent one of the failure sources of solder joints. The difference of thermal expansion between the PCB and the package induces stresses in the solder joints as illustrated in Figure 9 for a BGA electronic package. Due to the Coefficient of Thermal Expansion (CTE) mismatch, the principal direction of loading is shear strain. Tensile stress can also be observed by structural effect in particular for large package. Shear strain evolution as a function of temperature variation can be estimated with a simple analytical model. Considering  $l$  the distance to the package center,  $h$  the height of solder joint, and  $\Delta\alpha$  the CTE mismatch between the PCB and the package, the shear strain  $\Delta\gamma$  can be evaluated in the case of a  $\Delta T$  temperature variation with the Eq. I-1. In this equation, the CTE of the PCB depends on the structure and the material used. The value given in Figure 9 (13 ppm/K) is approximative and is indicated for illustration. Equivalent CTE of the electronic package is lower than CTE of the PCB. One of the constituents of the package is the silicon die which has a CTE around 2.5 ppm/K [7].

$$\Delta\gamma = \frac{\Delta\alpha \cdot l \cdot \Delta T}{h} \quad \text{Eq. I-1}$$

Accelerated Thermal Cycling (ATC) are used by manufacturers in order to evaluate solder joint reliability. The electronic board is submitted to a temperature profile, including dwell times at extreme temperatures. The amplitude of thermal variation is adjusted depending on the application. Thermal shock tests can also be used. The difference between ATC and thermal shock is the velocity of temperature variation. The temperature in the electronic board must be maintained homogeneous during the temperature variation for ATC. In the case of thermal shock, temperature variation rate is high, which conducts to thermal gradients. The rate limit which allows to maintain an homogeneous temperature depends on the technologies used. Dual chamber can be used for thermal cycling if the maximum temperature variation rate is lower than 20°C/min.

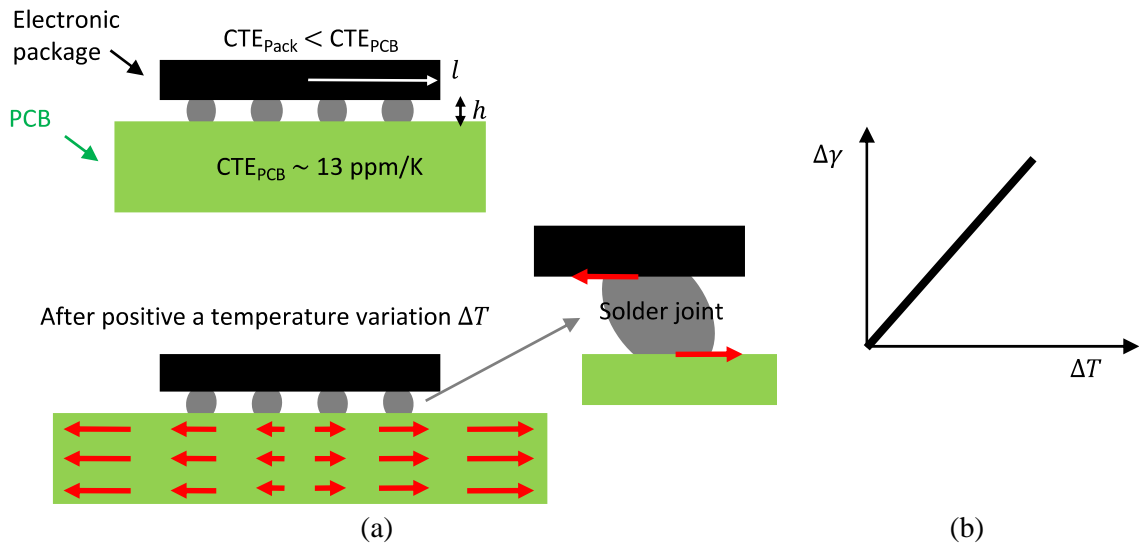


Figure 9: Loading state in the solder joints matrix of a BGA package induced by a temperature variation: (a) schematic view of the BGA package and loading of individual solder joint and (b) linear evolution of the shear strain with temperature as modeled in equation Eq. I-1 (b)

### 2.b.iii. Mechanical stresses

Electronic boards are also submitted to mechanical vibrations transmitted by the operating system (as helicopter rotor) and by the environment (as road not perfectly plane). Mechanical shocks induced for example by missile launch are not considered in this study. Mechanical stresses are transmitted by the system to the electronic board inducing the bending of the PCB, and especially for frequencies around the resonant frequency of the electronic board where the bending of the PCB is high. Mechanical shear stresses are also induced in the solder joints by this bending as depicted in Figure 10, conducting to the high cycle fatigue regime.

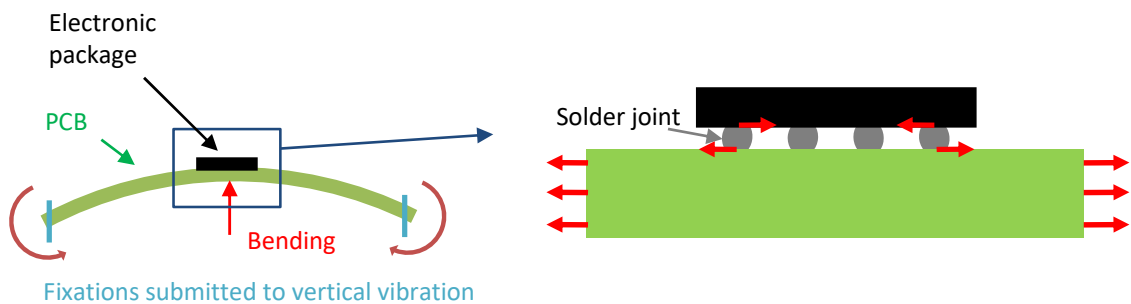


Figure 10: Mechanical shear stresses induced by the bending of the PCB due to vibration loading from the environment of a BGA package

Drop tests have been introduced with the development of mobiles in order to evaluate the reliability of solder joint under mechanical shock. Mission profile of mobile application contains potential mechanical shocks. Drop tests are used to identify weakness and simulate drop.



## 2.c. Reliability challenges for critical applications

Evolution of electronic packages, mostly driven by consumer civil applications, introduces new architectures [8] and materials and their reliability needs to be qualified for the aerospace and defense applications constraints. Reliability of new package architecture, fatigue properties of Lead-Free alloys and use of reliable Commercial Off-The-Shelf electronic boards are today challenges of the aerospace and defense industries.

### 2.c.i. Architecture evolutions

Electronic evolution can be measured by the increase of integration level. This integration is visible in electronic packages which are smaller and more complex, with increased number of I/O (inputs and outputs) as BGA (Ball Grid Array) for instance. Figure 11 illustrates the densification phenomenon in terms of package sizes. Evolution of electronic packages from 1960 until now and densification and miniaturization of them is presented.

Dual Inline Package (DIP) is an electronic package composed of two lines of solder joints. Quad Flat Package (QFP) have four lines of solder joints (at each side) which increases the I/O density. Ball Grid Array (BGA) and Wafer Level Package (WLP) have been developed with a matrix of solder joints in order to maximize the package I/O density. Integration of several functions in the same package, “System-in-Package” (SiP), or in the same chip, “System-on-a-Chip” (SoC), or on the same package, “System-on-Chip” (SoP), allows to increase even more the density and the functionality of electronic packages. The increased number of I/O is only possible with a general reduction of the solder joint size which increases reliability risk.

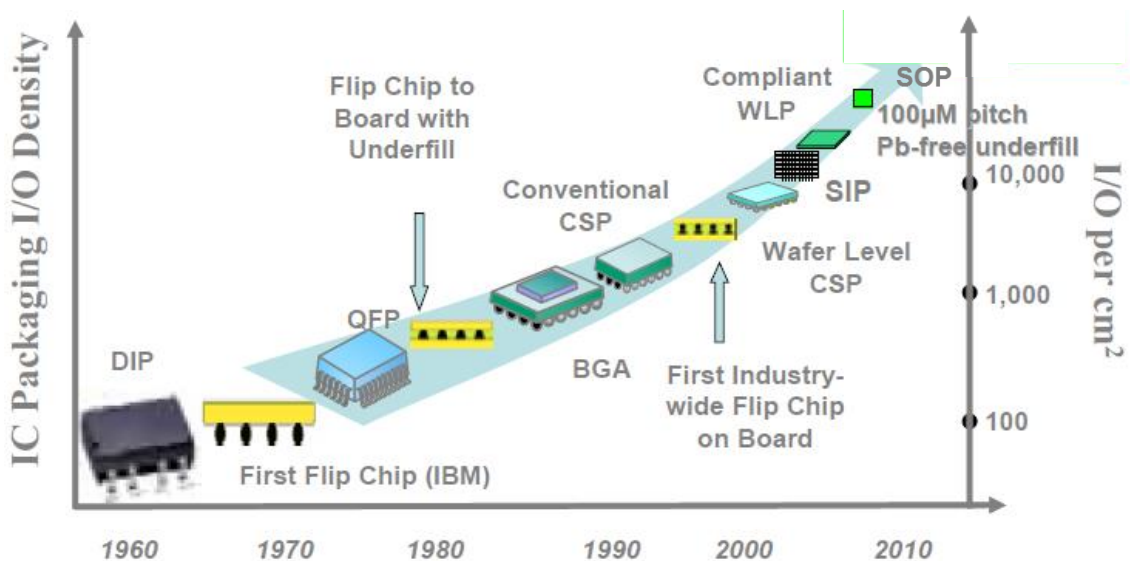


Figure 11: Evolution of technologies and sizes of packages: miniaturization and densification of electronic packages [9]

### 2.c.ii. Lead-Free solder

Since the ROHS registration in 2002 (in application since 2006), the use of lead in electronic devices of consumer applications is prohibited. Historically, tin-lead Sn37Pb alloy were used for solder joint due to its low melting point and a good thermo-mechanical behavior. Lead-free (LF) solders have been selected as candidates to remove lead from electronic devices. They are generally

alloys based on tin (Sn) with different weight percent of silver (Ag) and copper (Cu). Knowledge on fatigue properties of these new alloys is important to guarantee the reliability.

### 2.c.iii. COTS

Use of Commercial Off-The-Shelf (COTS) electronic boards is attracting to reduce development costs and time-to-market. COTS are electronic boards designed in order to accomplish a specific or adaptable function for various applications. For example, a COTS electronic board can be composed of general functions as processor and memory with connections in order to be assembled in a more complex system. The advantage is the procurement of a low cost part which can be adapted to accomplish a specific function. Reliability of COTS is a source of concern. In fact, COTS are mostly dedicated to consumer markets with requirements different than aerospace and defense industries. Manufacturing process as assembly and selected technologies must be analyzed before a potential use in those applications. COTS electronic boards are also developed for aerospace and defense applications. However, it is difficult to justify their reliability without knowing their technologies. COTS manufacturers sell their electronic boards without giving the complete design.

## 2.d. Prediction of solder joint failure with simulation

Introduction of new electronic packages, printed circuit boards (PCB) and assemblies increases the qualification cost. In this context, the use of Finite Element Analysis (FEA) and numerical modeling in addition to experimental tests is a promising solution. In fact, simulation could improve our physical understanding of observed phenomena and increase the amount of information extracted from a given experimental test. For example, simulation of experimentally untested configurations can increase qualification cost efficiency.

A short overview of simulation models of the literature is proposed in this section. Regarding the prediction of solder joints reliability, literature is large and only examples for illustration are presented. Works of the literature can be organized regarding the complexity of the simulation (see Figure 12). Three categories are defined with simulation levels: (i) analytical formulations, (ii) FEA combining as beam and shell and (iii) complete 3D FEA using beam, shell and volume elements. Examples from the literature for each category are given in the following paragraphs.

Simplest empirical analytical models have been developed by Engelmaier [10] in order to evaluate a cyclic fatigue damage indicator during thermal cycling. The cyclic fatigue damage is formulated as function of first-order parameters. This cyclic fatigue damage can be used to calibrate a fatigue law based on experimental thermal cycling results in order to predict the failure. The advantage of this simulation level is the reduced computational effort.

Other simulations use simple elements as beam and shell. For example, the elastic response of a complete electronic board have been studied with beam elements for solder balls and shell elements for the PCB and the BGA package by Wong *et al.* [11] for a vibration loading. This approach has also been used by Massiot *et al.* [12] to simulate the stress and strain in the solder joints of a package submitted to ATC. This global model is used with a refined model of one solder balls and a part of the PCB in order to evaluate the cyclic stress and inelastic strain in the solder joint. Lower calculation times are required with this method and the complete electronic board is considered.

Simulation of thermal cycling does not necessary imply the simulation of the complete electronic board. Package symmetries can be used to propose reduced models. This third simulation category can use 3D FEA elements without exceeding limits of computation time. For example, 3D elements have been used to simulate the effective assembly stiffness of flip-chip solder joints [7]. This effective

stiffness has been re-used after with a solder joint model to evaluate creep strain developed in the solder joints during temperature variation. Crack growth during temperature variation has also been studied with 3D elements [13]. In this case, the strain energy density per cycle is computed and is combined with a crack growth rate model to predict fatigue life from crack growth data. This methodology has for example been used more recently to predict fatigue life of BGA solder joints under thermal cycling [14].

$$\Delta D = \frac{F \cdot L_D \cdot \Delta\alpha \cdot \Delta T}{h}$$

with:

- $\Delta D$ : cyclic fatigue damage
- $F$ : deviation factor
- $L_D$ : solder to center distance
- $\Delta\alpha$ : thermal expansion mismatch
- $\Delta T$ : thermal range
- $h$ : solder joint height

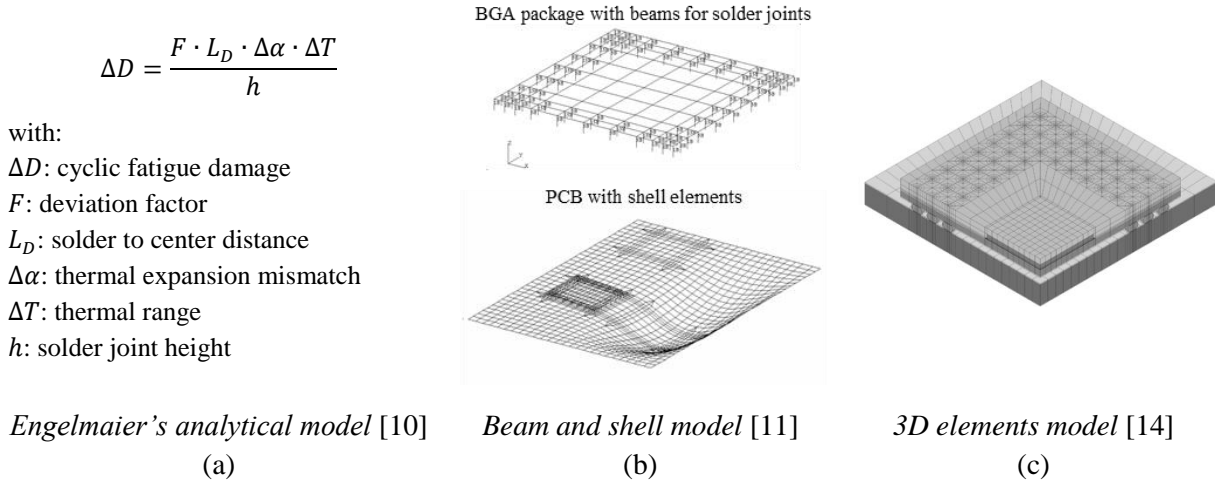


Figure 12: Different simulation levels found in the literature: from empirical analytical models (a) to beam and shell elements model (b) and 3D complex elements model (c)

The condition to use one of these methods is the knowledge of the mechanical behavior and fatigue properties of the solder joints material. Mechanical and fatigue properties of solder joints have been studied by numerous authors. The following section reviews the literature regarding elastic and plastic, viscous and fatigue properties of solder joint materials.

### 3. Mechanical properties of solder joints

The characterization of mechanical properties of solder joints is performed with experimental tests based on different types of specimen. The following sections describe the works from literature regarding different mechanical properties. First, LF solder joint microstructure is depicted. A review of mechanical properties is then proposed. Leaded and LF solders properties are compared. Time-independent mechanical properties are described. These properties are the Young's modulus, the yield stress and the ultimate tensile stress. Viscous properties are described after. Fatigue properties used for solder joints in the literature are finally detailed. The following annotation will be used. SACXYZ names a LF alloy which is composed of X.Y wt. % of Ag and 0.Z wt. % of Cu (the rest is Sn). For example, SAC305 is composed of 3.0 wt. % of Ag, 0.5 wt. % of Cu and 96.5 wt. % of Sn.

#### 3.a. Lead-Free solder joint microstructure

SAC solder joint materials matrix is composed of a matrix of Tin elements in the  $\beta$  crystallographic form. The allotropic form of tin depends on the temperature (as described in Figure 13). The dendritic structure of the matrix is constituted of  $Ag_3Sn$  and  $Cu_6Sn_5$  precipitates formed during the assembly process. Examples of LF SAC305 alloys microstructure are depicted in Figure 14.

Form	$\alpha$	$\beta$	$\gamma$
Temperature	$T < 13 \text{ }^\circ\text{C}$ [15]	$13 < T < 161 \text{ }^\circ\text{C}$ [16]	$161 < T < 232 \text{ }^\circ\text{C}$ [17]

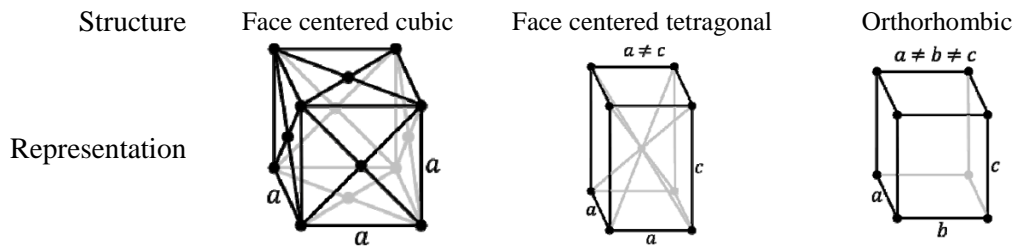


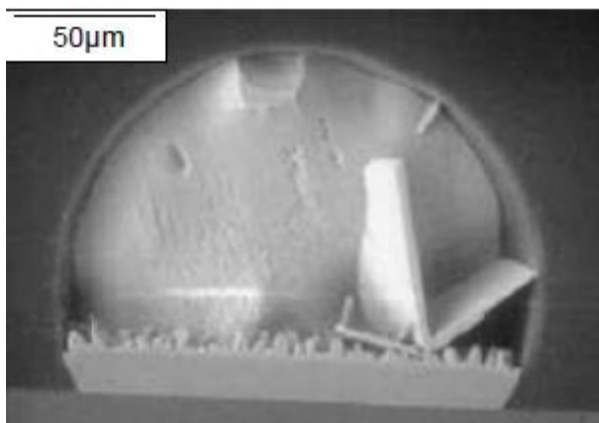
Figure 13: Description of cristallographic structure of tin as a function of temperature from literature [15] [16] [17]

Cooling rate of the reflow profile, solder volume and solder composition have an influence on solder joint microstructure [18]. These parameters are not independent from each other. Considering identical solder volume of samples, a coarsening of the dendritic structure has been observed for different SnAgCu alloys with the decrease of the cooling rate [19]. An Ag content above 3.5 wt.% causes the formation of large primary  $Ag_3Sn$  precipitates [18]. Similarly, a Cu content above 1 wt.% causes the formation of large primary  $Cu_6Sn_5$  precipitates.

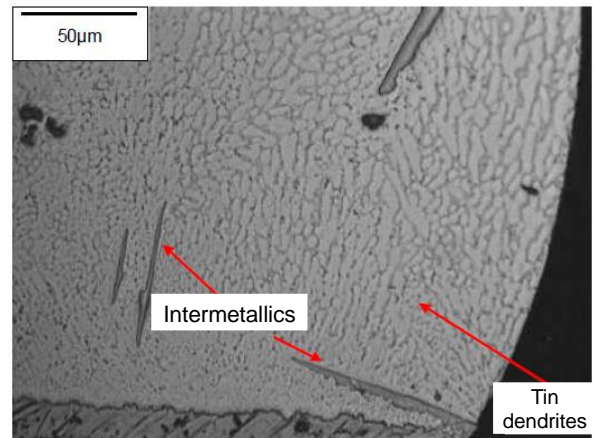
### 3.b. Elastic and plastic mechanical properties

Characterization of elastic and plastic properties is generally performed with monotonic experimental tests. These tests are commonly tensile or compression tests with bulk specimens. In the case of solder joint, because of the shear loading in the final application, shear tests have been performed in the literature. Elastic and plastic properties are represented in Figure 15. Young's modulus describes the linear evolution of stress with strain in the elastic region until a yield and inelastic strains. Ultimate tensile stress is the maximum stress amplitude reached before failure.

Mechanical general properties of LF alloys have been analyzed by different authors. Evolution of mechanical properties with aging of LF solders is also a recurrent topic. Analysis of mechanical properties in high strain rate is also developed in the literature to evaluate the lifetime under mechanical loadings as vibration. Experimental methods used are first described. Elastic and plastic mechanical properties found in the literature are then compared in the last section.



(a) Alloy with Sn and 3.5 wt.% Ag



(b) SAC387

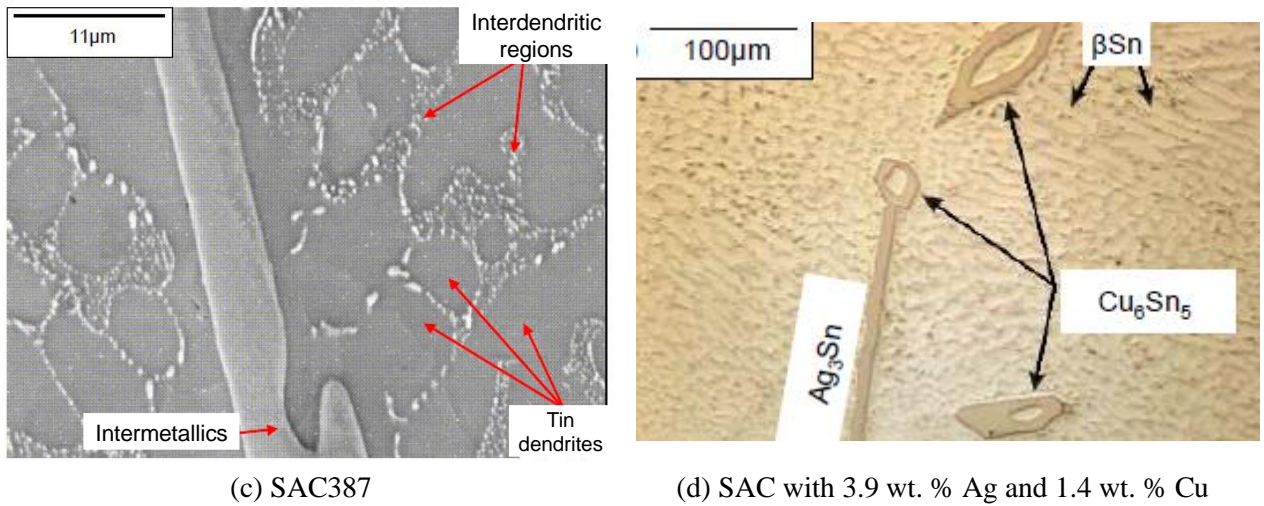


Figure 14: Lead-free solder joint microstructure [20]: (a) optical image after chemical attack in order to reveal  $Ag_3Sn$  intermetallic [21], (b) optical image of a BGA ball after cross-section [22], (c) SEM image of the dendritic structure [22] and (d) constituents of solder joint material [23]

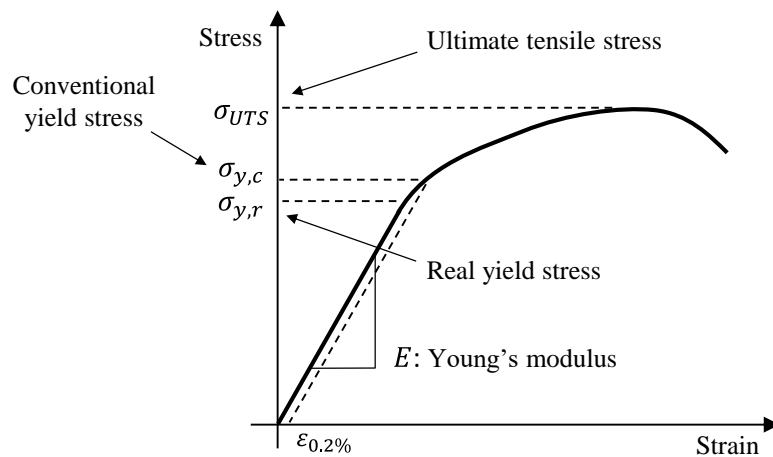


Figure 15: Elasto-plastic parameters measured defined with a schematic classic strain-stress response of material under tensile test

### 3.b.i. Elasto-plastic mechanical properties with different sample types

Most convenient specimens for tension or compression tests are bulk samples of the considered material. Figure 16 illustrates three types of bulk sample used in the literature. Vianco *et al.* [24] characterized the compression deformation response of SAC396 solder. Specimens are bulk samples machined in order to have cylindrical form with a height of 19 mm and a diameter of 10 mm. The strain/stress response of the samples is measured for a large temperature range from  $-25$  to  $160$  °C and at different strain rates. Pang *et al* [25] [26] [27] have also used bulk samples for the SAC387 alloy. Cylindrical bulk specimens of Pang are thinner with a length of 15 mm and a diameter of 3 mm. The apparent Young's modulus, the yield and the ultimate tensile stresses have been evaluated for different strain rates (from  $5.6 \times 10^{-4}$  to  $5.6 \times 10^{-2}$ ) and temperatures ( $25$ ,  $75$  and  $125$  °C) by Pang *et al.* Equations describing the evolution of these values are given as a function of these two parameters. Silver content impact has been analyzed by Che *et al* [28] with bulk of solders with different silver

content (SAC105, SAC205 and SAC305). The specimen is a rectangular shape of 30 mm length and 3 mm thickness dog-bone shape. The solder alloys were melted 100 °C above their respective melting point for 20 minutes. The bulk solder specimens were casted inside the designed aluminum mold and naturally air-cooled at ambient temperature. Tensile tests have been performed by Che *et al.* at different strain rates and for different temperatures (from -35 to 125 °C). The elastic modulus, yield stress and ultimate stress limit of SAC solders are highly strain rate and temperature dependent. These properties increase with increasing strain rate, but decrease with increasing temperature. Elastic and plastic properties found are compared in the last section.

In order to be representative to the microstructure of the final application, mechanical tests with specific design of specimen have been performed in the literature as depicted in Figure 17. Pang *et al.* [27] have performed shear test on an assembled solder ball between two FR4 substrate materials of 12x3x0.5 mm<sup>3</sup>. Von-Mises equivalent stress criterion (see Eq. I-3) is used to obtain the relationship between pure shear and pure tensile stress state in order to compare experimental results performed by Pang *et al.* with bulk and solder joint specimens. Interesting correlation between the yield stress and the ultimate tensile stress is found for the different temperatures and strain rates.

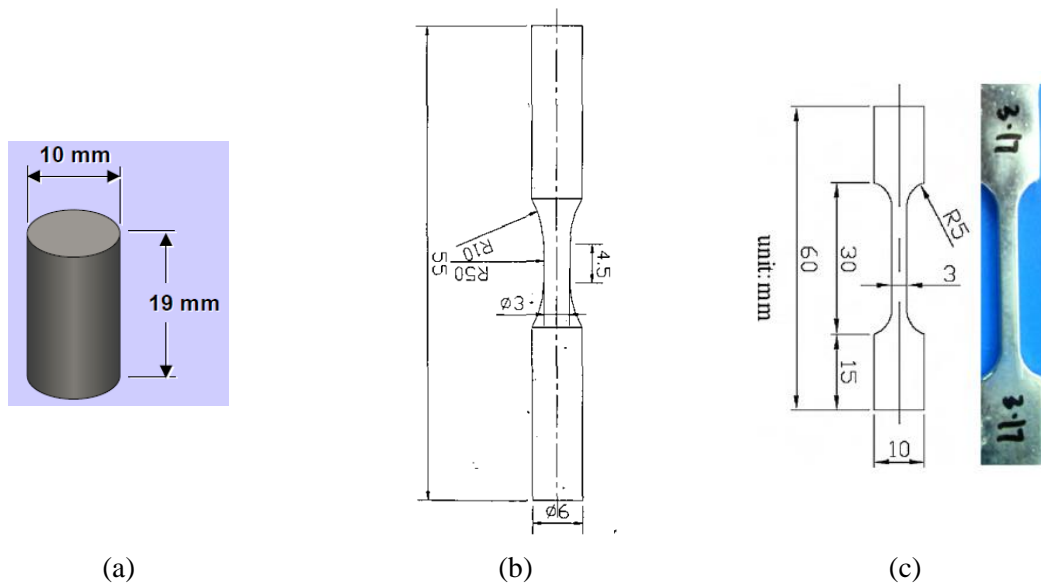


Figure 16: Bulk samples used by Vianco *et al.* [24] (a), Pang *et al.* [27] (b), and Che *et al.* [28] (c)



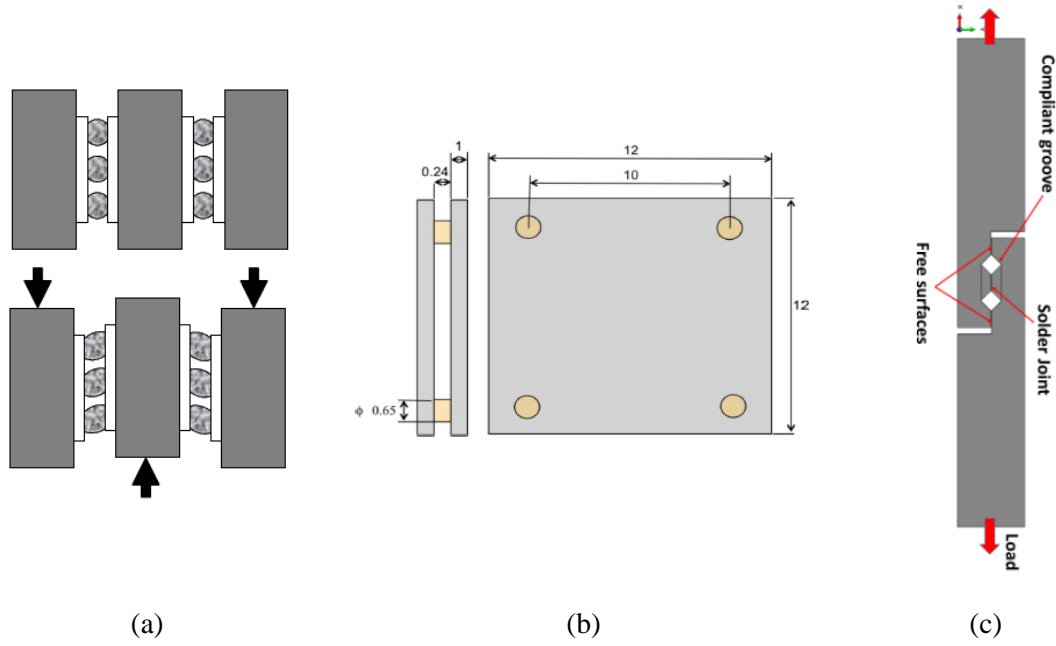


Figure 17: Specific samples used by Darveaux *et al.* [29] (a), Mysore *et al.* [30] (b), and Pin *et al.* [31] (c) in order to evaluate solder joint mechanical and fatigue properties

Von-Mises equivalent stress is used in order to express an equivalent stress scalar from a multi-axial stress state. The von-Mises equivalent stress  $\sigma_{eq}$  is expressed as following with the Cauchy stress tensor components ( $\sigma_{11}$ ,  $\sigma_{22}$ ,  $\sigma_{33}$  are the stresses in the tensile principal directions and  $\sigma_{12}$ ,  $\sigma_{23}$ ,  $\sigma_{31}$  are the stresses in the shear directions).

$$\sigma_{eq}^2 = \frac{1}{2} \left( (\sigma_{11} - \sigma_{22})^2 + (\sigma_{22} - \sigma_{33})^2 + (\sigma_{33} - \sigma_{11})^2 + 6(\sigma_{23}^2 + \sigma_{31}^2 + \sigma_{12}^2) \right) \quad Eq. I-2$$

The relation between pure tensile stress  $\sigma_{11}$  and pure shear stress states  $\sigma_{23}$  considering the von-Mises equivalent stress is then

$$\sigma_{11} = \sqrt{3} \sigma_{23} \quad Eq. I-3$$

Works of Bhate *et al.* [32] and Mysore *et al.* [30] are performed with dedicated specimens. The specimen consists in four solder interconnections located at the corners and “sandwiched” between two identical alumina substrates. The substrates are shear loaded at different temperatures (25, 75 and 125 °C) and for different strain rate (from  $4.02 \times 10^{-6}$  to  $4.02 \times 10^{-4} \text{ s}^{-1}$ ) in order to characterize the mechanical response of the four solder joints. The alloy studied by Bhate *et al.* is SAC387 and Mysore *et al.* SAC305.

Another specimen used in the literature is a thin layer of solder assembled between two rigid substrates. The microstructure and in particular the intermetallic layer with the copper pads can be respected with this type of specimen. The single lap shear of Pin *et al.* [31] is one example of this type of characterization. The mechanical response of the layer loaded in shear is measured and the shear modulus and the yield stress of the layer are defined at different temperatures.

### 3.b.ii. Mechanical properties evolution with aging

The evolution of the mechanical properties under specific conditions needs to be evaluated to guarantee the reliability of solder joint in some application domains. In this context, studies of the impact of aging at different temperatures have been performed for LF solders. Ma *et al.* [33] have observed that the material behavior evolution during thermal aging at room temperature and 125 °C is detrimental to the reliability with a reduction of stiffness, yield stress and ultimate strength and ductility. Specimens of Mustafa *et al.* have been manufactured with bulk samples of solders with a specific process in order to avoid residual stress and voids. Specimens have been prepared with a classic reflow profile to re-melt the solder in the tube using a vacuum suction process. The specimens used by Ma *et al.* are bulk rectangular specimens (80x3x0.5mm) of eutectic Sn37Pb or LF SAC405 solders. Mechanical properties evolutions with aging have been evaluated. Lead and lead-free solders show different behaviors with aging. Mustafa *et al.* [34] [35] [36] have used the same process than Ma *et al.* with SAC105 solder and specimen of the same dimension. Effect of aging at 125 °C in cyclic strain or stress control response has been studied. Hysteresis response has also been analyzed with thin layer sample shear loaded. Evolution of the hysteresis area is used to evaluate the effect of aging, which induces changes of the yield stress and the ultimate strength. Fatigue tests have also been performed with this method and results are detailed in the following section. Effect of aging on mechanical properties has also been studied by Dompierre [20]. Bulks of solder (SAC305) with flat dog-bone shapes have been used to perform uniaxial and cyclic tension/compression tests. Dimension of the rectangular bulk is 20x13x3 mm<sup>3</sup>. As for other studies, the increase of the strain rate increases the Young's modulus and the ultimate tensile stress.








### 3.b.iii. Solder joint mechanical properties at high strain rates

Because of the dependency of mechanical properties on the strain rate, it is important to evaluate these properties even for high strain rate. In fact, an electronic board can be loaded with vibration at frequencies higher than 100 Hz. In this context, Lall *et al.* [37] [38] have studied the Young's modulus and the ultimate tensile strength of lead-free SAC105 and SAC305 solders. The frequencies of the tests are sufficient to evaluate the solder at strain rates of 10, 35, 50 and 75 per second. Specimens are rectangular samples with a thickness of 0.5 mm. A dedicated experimental setup for the evaluation of the elastic deformation at high strain rates has been developed. As for Mustafa, the specimens have been submitted to an assembly reflow profile before testing in order to have a representative microstructure. The effect of aging on the properties has been characterized for different aging temperatures.

### 3.b.iv. Comparison of elastic and plastic properties from the literature

Elastic and plastic properties found in the literature are compared in this section. These properties are first compared regarding temperature. Then, evolution of properties with strain rate are compared at room temperature. Table 1 indicates color code used for the different solder joint materials found in the literature.

Table 1: Colors used to compare elastic and plastic properties of alloys from the literature

Color							
Alloy	SAC305	SAC405	SAC105	SAC205	SAC387	SAC396	Sn37Pb



Evolution of the apparent Young's modulus, yield stress and ultimate tensile stress with temperature are plotted in Figure 18, Figure 19, and Figure 20. Evolutions of these properties show a decrease of these properties with an increasing temperature, from room temperature to 200 °C. For temperature lower than 25 °C, no consensus exists on the variation of these properties.

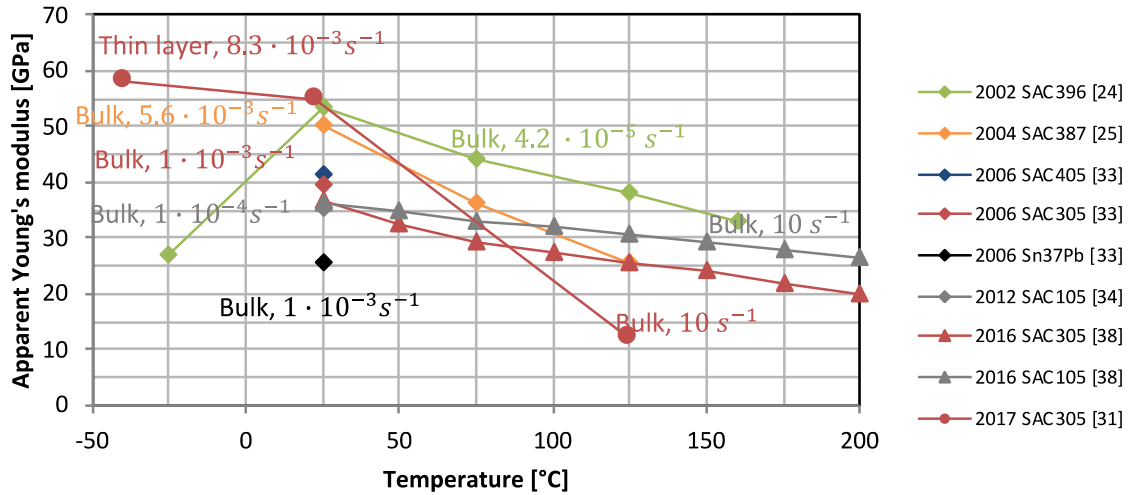


Figure 18: Evolution of apparent Young's modulus with temperature

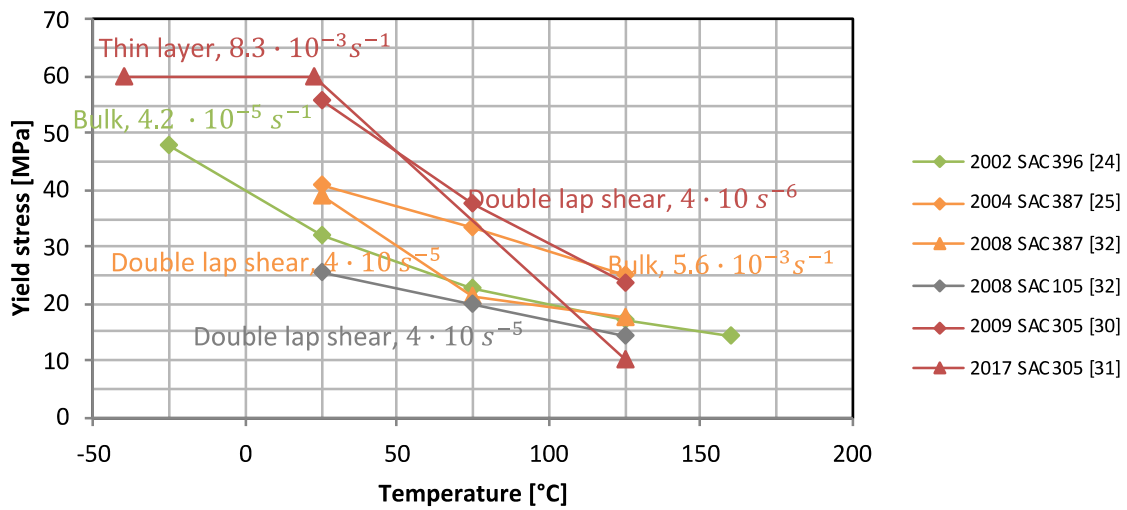


Figure 19: Evolution of plastic yield stress with temperature

The observed differences can be associate to the strain rate, the type of sample, the preparation and the test methods used. Different solders with different silver and copper content are also gathered in the same figure for LF solders. For the apparent Young's modulus, evolutions of SAC305 alloy with temperature are different and can be explained by the difference of sample used.

For ultimate tensile stress and SAC305 alloy, the difference obtained at 25 °C by the two authors can be explained by the strain rate used. More creep strains are developed at lower strain rate which explains the lower ultimate tensile stress found at  $10^{-3}$  than at  $10 s^{-1}$ . For all temperatures, ultimate tensile stress for SAC105 and SAC387 is always lower than for SAC305.

Evolution of the elastic and plastic properties with strain rate are depicted in Figure 21, Figure 22 and Figure 23. In order to compare the results, only experimental tests performed at room temperature are plotted. For all alloys, an increase of the strain rate induces an increase of the apparent Young's modulus, the yield stress and the ultimate tensile stress, which is due to the viscosity of the material.

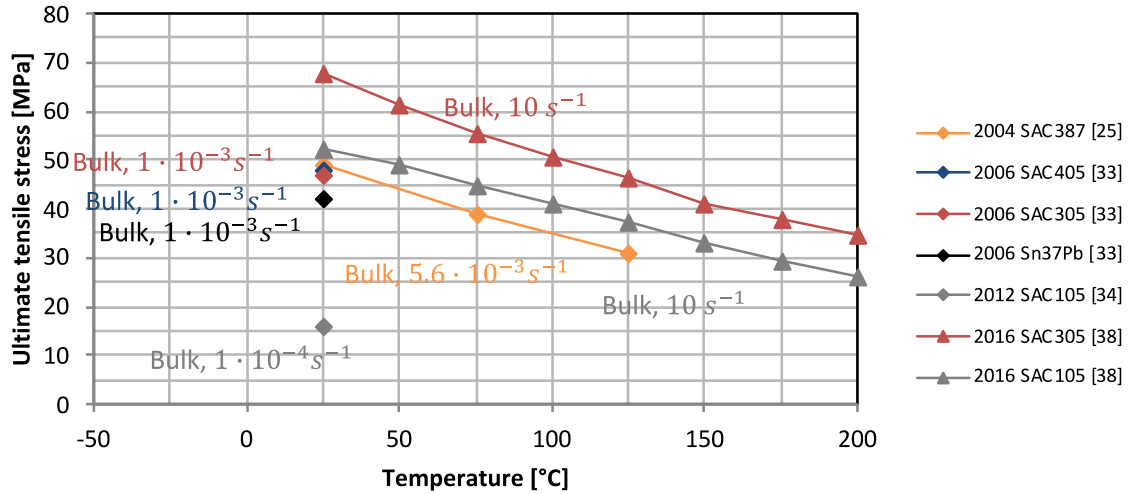


Figure 20: Evolution of ultimate tensile stress with temperature

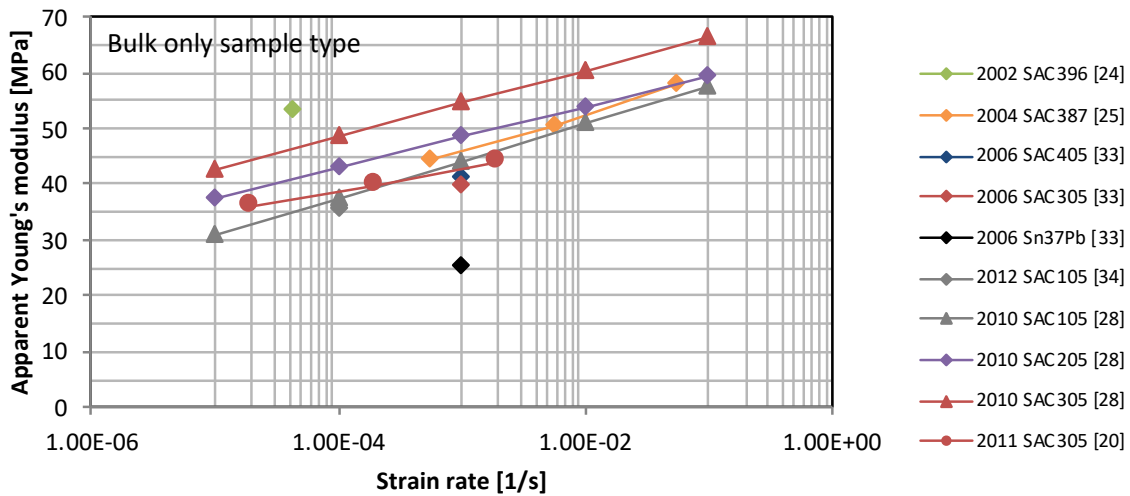


Figure 21: Evolution of apparent Young's modulus with strain rate at 25 °C

Scatterings are observed for SAC305 alloys even if temperature and sample type used are identical. In this context, it's difficult to compare the rigidity of SAC305 with other solder materials. Without viscosity, the Young's modulus is expected to be constant with strain rate. The "apparent" Young's modulus is measured based on experimental results without considering viscoelasticity.

Evolutions of Yield stress measured as function of strain rate are plotted in Figure 22. As for Young's modulus, yield stress is not expected to change with strain rate if the viscosity of the material is taken into account. Yield stress are measured by these authors directly from the result without considering the viscosity. Scattering between yield stress obtained with double lap shear and bulk

samples is more important for SAC305 than for SAC105 and SAC387. This difference is probably due to the methods used to calculate this parameter. Less scatterings are observed for experimental test performed with bulk samples. Experimental results show that viscosity for solder joint materials is important even at room temperature.

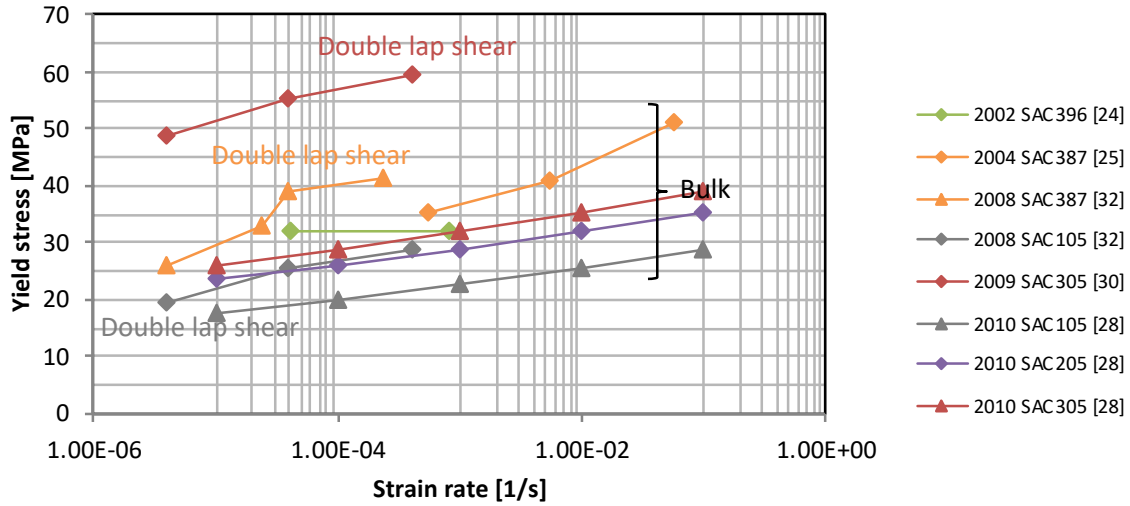


Figure 22: Evolution of plastic yield stress with strain rate at 25 °C

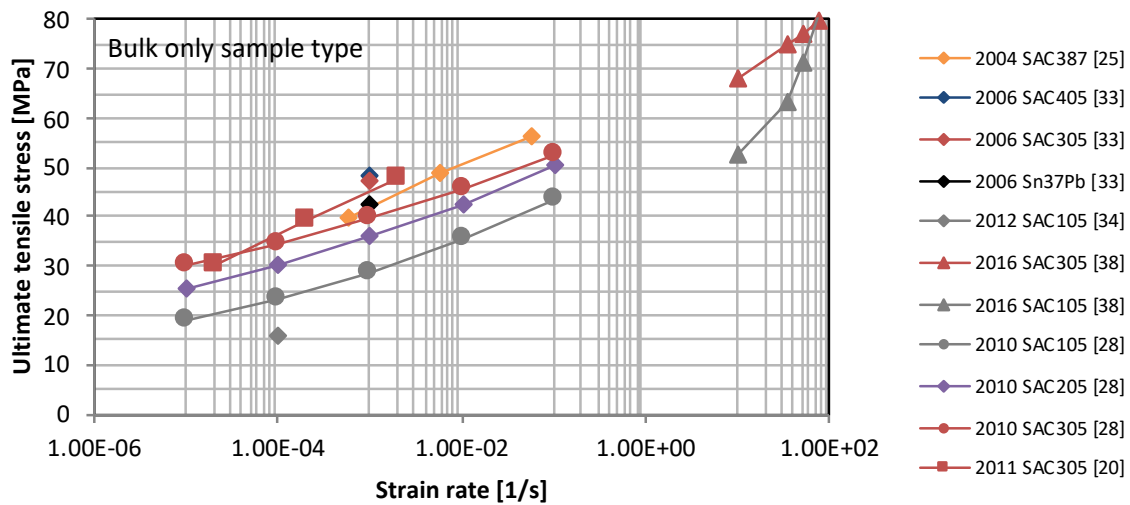


Figure 23: Evolution of ultimate tensile stress with strain rate at 25 °C

Evolution of Ultimate Tensile Stress as a function of strain rate for different solder joint materials is depicted in Figure 23. Two categories of experiments are depicted: at low and medium strain rates and at high strain rate ( $> 1 \text{ s}^{-1}$ ). Solder joint material characterization at high strain rate has been performed to evaluate properties for mechanical vibration loading.

Experimental tests performed at low and medium strain rates with high strain rate show an increase of ultimate tensile stress with strain rate for SAC305 and SAC105, values obtained for SAC105 being

lower than for SAC305. Evolution of ultimate tensile stress with strain rate is also due to the viscosity of the material. Viscous properties found in the literature are detailed in the following section.

### 3.c. Viscosity properties

Alloys used for solder joint are above half of their melting point at room temperature. In this context, creep processes are expected to dominate the deformation kinetics. Three regimes are described in the literature: primary transient creep (I), secondary steady-state creep (II) and tertiary creep (III). The different regimes are characterized by the creep strain rate. In the initial stage, the transient creep increases with a high strain rate but decreases with increasing time. Creep strain rate stabilizes to a constant value in the steady-state creep. Finally, the strain rate exponentially increases with time because of voids and cracks decreasing the loaded section of the specimen. The steady-state creep is the most studied regime in the literature with many proposed constitutive laws as the creep mechanism is function of the applied stress. Three main regions are described in the literature. The low stress regime (Nabarro-Heering creep) is the less developed. The intermediate (superplasticity) and high stress (climb controlled dislocation creep) regimes have been more studied. The literature regarding intermediate and high stress regimes is described in the following paragraphs.

#### 3.c.i. Viscous properties characterization from the literature

Mysore *et al.* [30] have studied steady-state creep with the four corner solder joints specimen previously described (see Figure 17). Steady-state creep strain data have been obtained at 25, 75 and 125 °C and for different stress levels from 19.5 to 45.6 MPa. The solders considered are SAC305, SAC387 and SAC105. Norton's law has been used with an additional factor to take into account the temperature effect (Arrhenius law) as formulated in Eq. I-4.

$$\frac{d\varepsilon_c}{dt} = A \left( \frac{\sigma}{\sigma_N} \right)^n \exp \left( -\frac{Q}{kT} \right) \quad \text{Eq. I-4}$$

$d\varepsilon_c/dt$  is the creep strain rate.  $\sigma$  is the applied stress in Pa.  $A$ , in 1/s, and  $\sigma_N$ , in Pa, are material constants.  $n$  is the stress exponent.  $Q$  is the activation energy in J and  $k$  is Boltzmann's constant in J/K.  $T$  is the temperature in K. The parameters are calibrated on the steady-state creep data.

Influence of the stress on the strain rate formulation is different depending on stress level. At intermediate stresses, the strain rate depends on stress with the power law exponent  $n$ . At high stresses, an exponential impact of stress on the strain rate has been observed. This regime change is called power law breakdown and an unified expression is generally used corresponding to Eq. I-5, where  $\sigma_N$  is a material constant representing the power law breakdown.

$$\frac{d\varepsilon_c}{dt} = A \left( \sinh \left( \frac{\sigma}{\sigma_N} \right) \right)^n \exp \left( -\frac{Q}{kT} \right) \quad \text{Eq. I-5}$$

This formulation has been used by numerous authors to calibrate experimental results performed with bulk samples of solder alloy. Wiese *et al.* [39] have used dog bone-shaped bulk specimens with

a rectangular cross section (about  $3 \times 3 \text{ mm}^2$ ) and a length of 60 mm (see Figure 24). Steady-state creep strain rate data from 2 to 20 MPa stress levels and with temperatures from 20 to 150 °C have been used. The considered solders are LF Sn-40Pb-1.0Ag, Sn-3.5Ag and Sn-3.8Ag-1.0Cu. Pang *et al.* [26] have also used this law for the cylindrical bulk specimen of SAC387 previously described. Creep tests have been performed at -40, 25, 75 and 125 °C for different stress levels from 2 to 70 MPa. Xiao *et al.* [40] performed creep tests with rectangular bulk specimens of  $12.7 \times 1.58 \text{ mm}^2$  and with gauge length of 25.4mm of leaded Sn-37Pb and lead-free SAC396 solders. Steady-state creep strain rate data at 80, 115 and 180 °C and for different stress levels from 6 to 20 MPa have been measured.

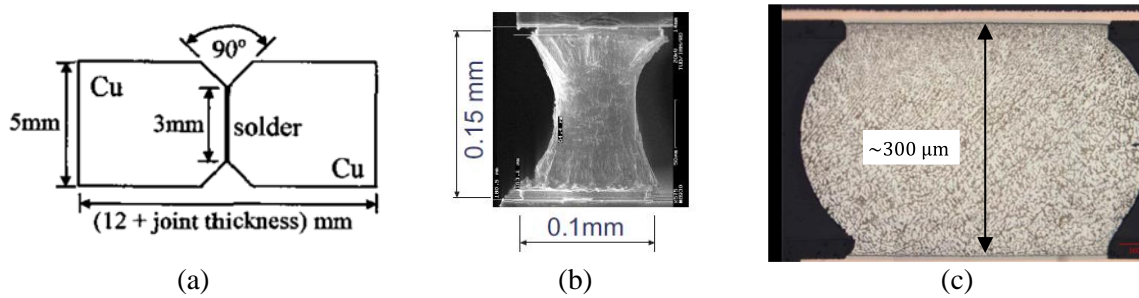


Figure 24: Different samples type used in order to evaluate viscous properties of solder joint materials : thin layer [31] (a), flip-chip sample [39] (b), and electronic package [41] (c)

In order to be more representative of the microstructure, Zhang *et al.* [42] have performed creep tests with thin layer samples with strain rate from  $10^{-11}$  to  $10^{-4} \text{ s}^{-1}$  and with temperature range from 20 to 180 °C. Viscoplastic constitutive properties of LF solder have been characterized with SAC396 solder and compared with eutectic Sn-37Pb. The specimen used by Zhang is a 3 mm length of thin layer of solder with a thickness of 0.18 mm between two shear substrates. Another specimen has been used by Röllig *et al.* [43]. This specimen is composed of four solder balls attached between two ceramic chips with adequate PCB pad metallization. Constant-load creep shear tests have been performed at different stress levels and temperatures (25, 75 and 125 °C) and parameters for the sinh-formulation have been defined for Sn-36Pb-2Ag, Sn-1.3Ag-0.2Cu-0.05Ni, Sn-1.3Ag-0.5Cu-0.05Ni and Sn-2.7Ag-0.4Cu-0.05Ni solders. The sample used by Darveaux [44] [45] [46] [29] is composed of two ceramic chips soldered with 98 solder joints (matrix of  $10 \times 10$  joints depopulated of 2 joints). Two specimens are loaded in shear simultaneously by the test bench. Numerous solder types and pad metallizations have been tested under shear loading for different temperatures from -55 to 125 °C and stress levels from 1 to 30 MPa. Coefficients for the sinh-formulation are given by Darveaux and compared with other authors in the following section.

### 3.c.ii. Comparison of viscous properties of the literature

Parameters for the sinh-formulation found in the literature for the leaded and lead-free solders are summarized in the following Figure 25, Figure 26, and Figure 27. The comparison shows an important high scatter for the material parameter  $A$  has a high scatter in the values found in the literature for leaded and lead-free solders. In the results presented for lead-free solders, the intermediate values obtained with bulk (Pang and Xiao) are surrounded by the lower value obtained by Zhang with thin layer sample and the matrix of solder balls used by Darveaux. The scatter of the results can be explained by the difference of test bench and used specimens.

The scatter found for the parameter  $A$  is also found for  $\sigma_N$ , as a lower value for  $\sigma_N$  can be balanced by a higher parameter  $A$ . For lead-free solders, the value measured by Pang with bulk specimen is close to the measured values of Darveaux for the different SAC solders. For leaded solders, the values of  $\sigma_N$  are significantly lower than those of lead-free solders.

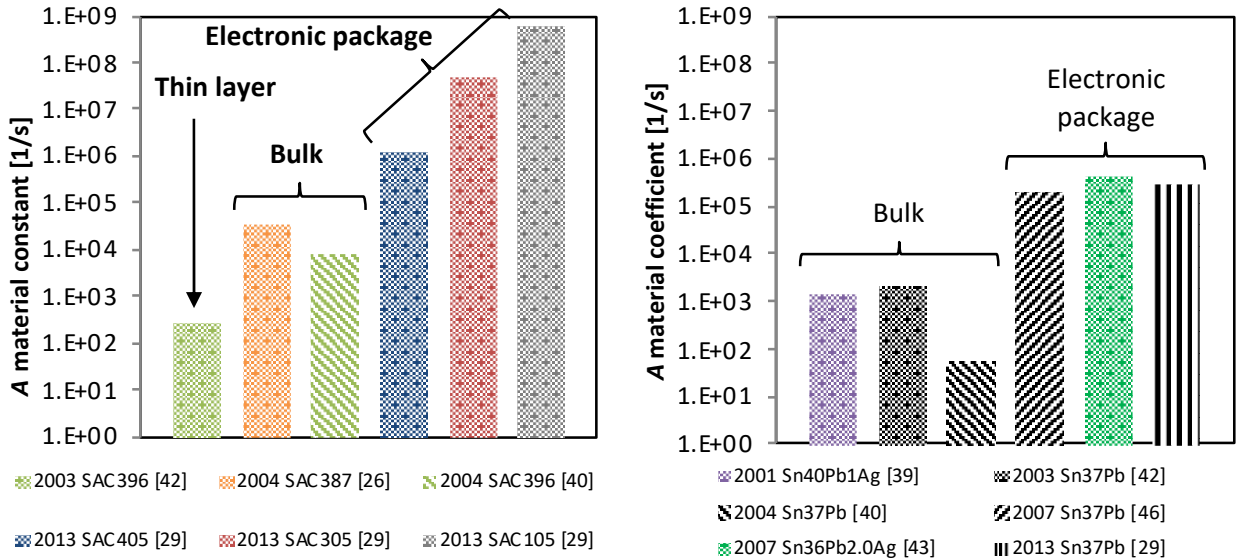


Figure 25: A material constant for sinh-formulation for lead-free (left) and leaded (right) solders

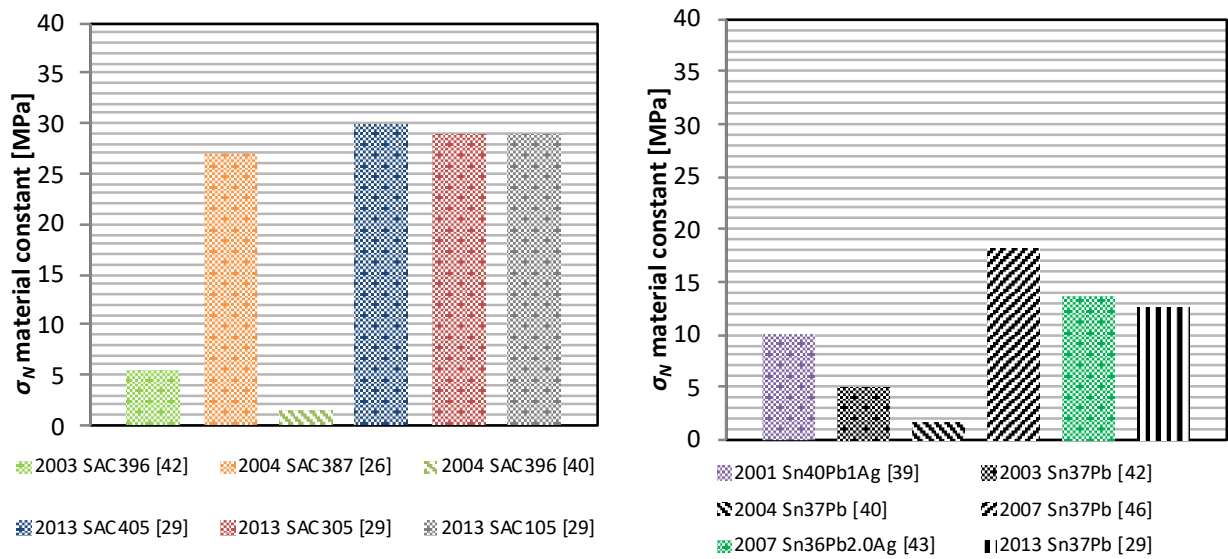


Figure 26:  $\sigma_N$  material constant for sinh-formulation for lead-free (left) and leaded (right) solders

Values measured for the stress exponent  $n$  have also a large scatter. For Xiao, the parameter has been set to 1 in order to eliminate this parameter from the calibration. This method can explain the difference between values obtained by this author. Globally, higher stress exponents are found for lead-free than for leaded solders.

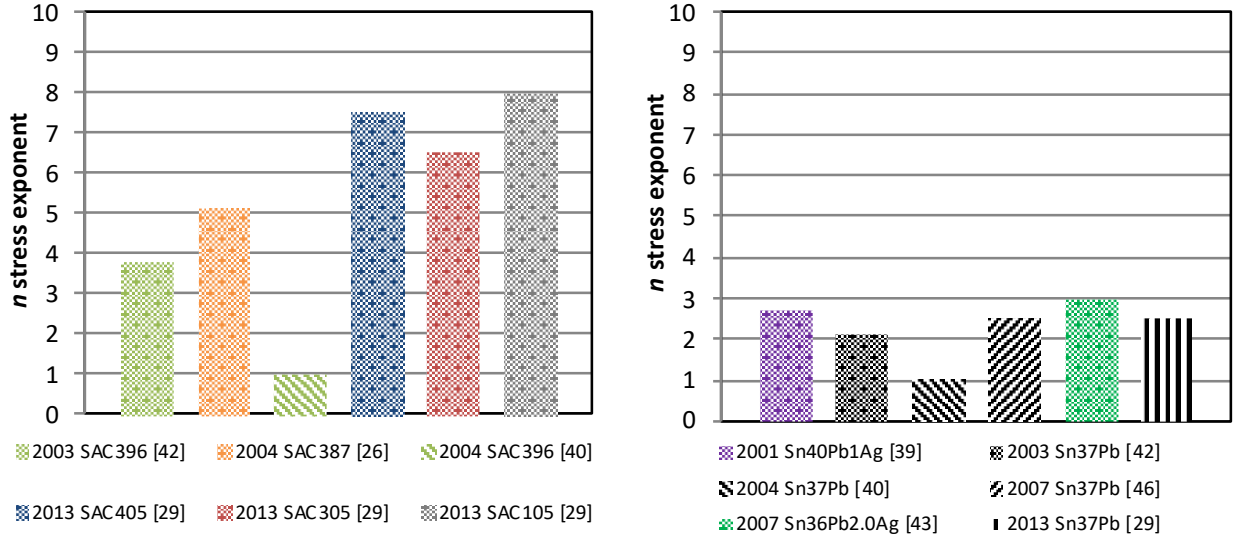


Figure 27: *n* stress exponent for sinh-formulation for lead-free (left) and leaded (right) solders

The activation energy represents the evolution of the creep strain rate with the temperature. The scatter for the leaded solders is lower than for LF solders. The high scatter for LF solders can be attributed to the different lead-free considered solders which can induce variations of this parameter.

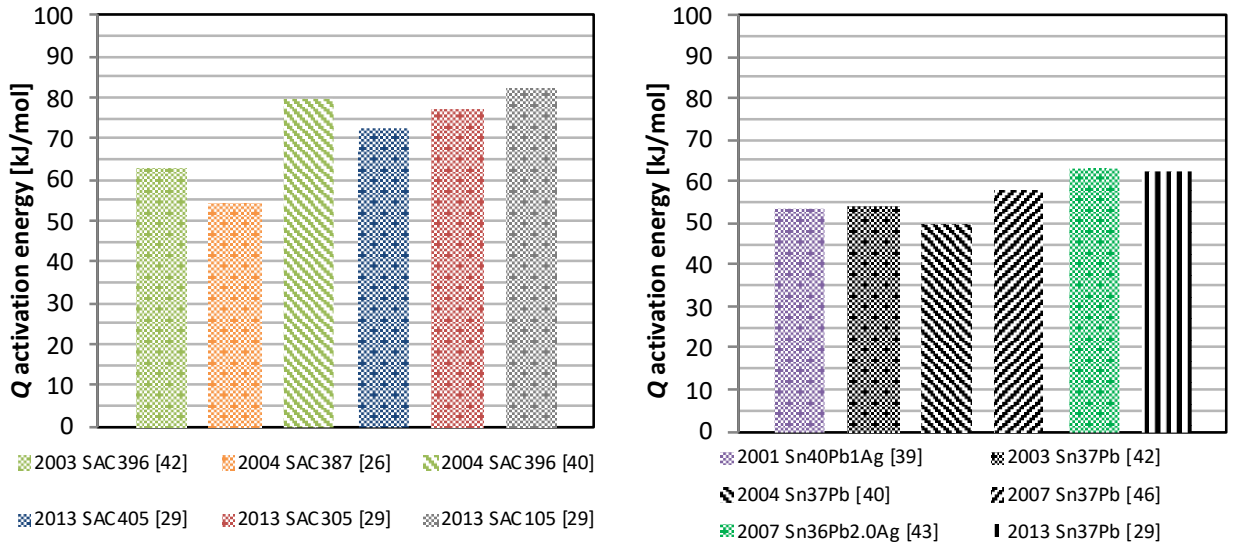


Figure 28: *Q* activation energy for sinh-formulation for lead-free (left) and leaded (right) solders

The power law formulation can also be expressed with the following Dorn's formulation. The relation describes the evolution of the shear creep strain rate  $d\gamma_c/dt$  and the applied shear stress  $\tau$  in Eq. I-6 where  $G$  is the shear modulus,  $T$  is the temperature,  $A$  is a materials constant,  $n$  is the stress exponent,  $Q$  is the activation energy,  $k$  is Boltzmann's constant and  $b$  is the Burgers vector.

$$\frac{d\gamma_c}{dt} = \frac{AGb}{kT} \left(\frac{\tau}{G}\right)^n \exp\left(-\frac{Q}{kT}\right) \quad \text{Eq. I-6}$$



Morris *et al.* [47] used a dedicated specimen in order to impose a shear loading to nine rectangular solder joints of 2.24x1.22x0.160 mm<sup>3</sup>. The steady state strain rate has been measured for different stress levels and temperature (60, 95, 130 °C) for different lead-free solders including SAC305. The Dorn’s formulation for creep has been selected and the experimental results have been used to calibrate the coefficient for the different solders. The coefficients are defined for low and high stress regimes and by introducing the previous power law break down. Another form of the Dorn’s formulation has been used by Darveaux [44] [46] [29] introducing a hyperbolic sine:

$$\frac{d\gamma_c}{dt} = C_1 \frac{G}{T} \left( \sinh \left( \alpha \frac{\tau}{G} \right) \right)^n \exp \left( -\frac{Q}{kT} \right) \quad \text{Eq. I-7}$$

where  $G$  is the shear modulus,  $T$  is the temperature in Kelvin,  $C_1$  and  $\alpha$  are materials constants,  $n$  is the stress exponent,  $Q$  is the activation energy and  $k$  is Boltzmann's constant.

As discussed in this section, the viscous properties of solder joint materials have been the main topic of numerous studies from the literature. Most studied creep regime is regime II. Some authors have examined the importance of regime I as a function of temperature and stress level [30] [44]. However, taking into account regime I requires a more complex mechanical model with additional mechanical parameters.

Steady-state creep rate of regime II is formulated as a function of temperature and stress level with the different formulations described previously. Various solders and types of samples have been studied in these regimes. The formulation most commonly used is the power law with a sinh addition in order to take into account the power law breakdown. Parameters for this law have been defined by numerous authors with a large scatter. This law will be used in order to describe the viscous behavior of solder joint from the experimental test bench presented in chapter 2 of this thesis.

### 3.d. Fatigue properties

Solder materials used for solder joint have low melting temperature. This property is required by the manufacturing process because the thermal profile must not damage other elements of the electronic board during the assembly process. Therefore, creep deformations are developed even when the solder joints are stressed at room temperature. Damage mechanisms for solder depend on the temperature and the frequency of loading as depicted in Figure 29 for leaded solder joint materials. Fatigue properties of LF solder joint materials is today less well-known. As viscous phenomena are important, creep-fatigue interaction is supposed to be taken into account even at room temperature.

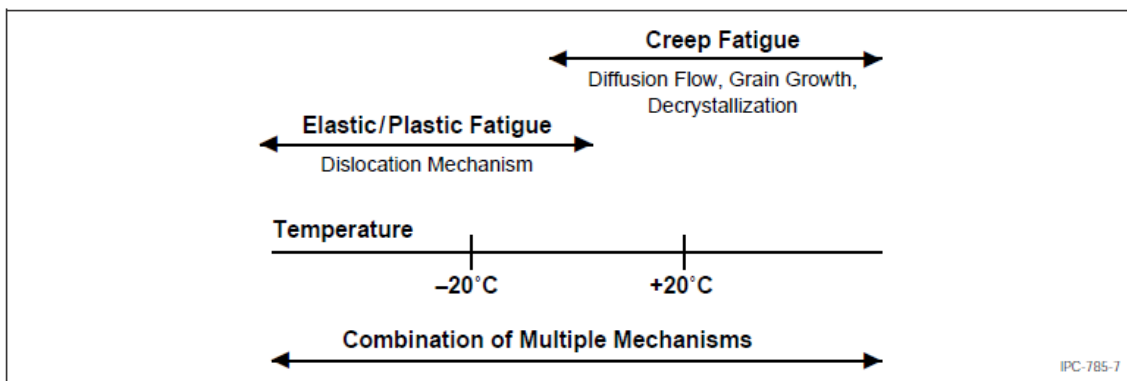




Figure 29: Thermal cycle/fatigue mechanisms for leaded alloys used for solder joint from IPC-SM-785 [1]

### 3.d.i. Fatigue laws commonly used in the industry

Operating temperatures for aerospace, defense and avionics applications can vary from -55 to 125 °C inducing creep strain development. In this context, the fatigue model for solder joints must take into account creep fatigue. First, a review of classic fatigue models is detailed in this section. Then, fatigue laws taking into account creep-fatigue interaction studied by several authors in the literature are described.

Well-known Coffin-Manson's fatigue law (CM) [48] is used in the industry for metals to describe the evolution of the number of cycles to failure with the inelastic strain  $\Delta\varepsilon_{inel}$  developed during each loading cycle. This law is expressed in Eq. I-9.  $N_f$  is the number of cycles to failure and  $C$  and  $n$  are constants of the material.

$$N_f^n \Delta\varepsilon_{inel} = C \quad \text{Eq. I-8}$$

The inelastic strain per cycle is used as damage indicator in the Coffin-Manson's fatigue law. Other damage indicators can be used. A similar expression is obtained if the inelastic strain is replaced by the density of dissipated energy per cycle  $\Delta W$  (DW), see Eq. I-9.  $\underline{\underline{\sigma}}$  and  $\underline{\underline{\varepsilon}}^p$  are the stress and inelastic strain tensors.

$$N_f^n \Delta W = C \quad \text{Eq. I-9}$$

$$\text{where } \Delta W = \int_{cycle} \underline{\underline{\sigma}} : \underline{\underline{\varepsilon}}^p dt \quad \text{Eq. I-10}$$

This criterion has successfully been applied by Charkaluk *et al.* [49] to predict failure of exhaust manifolds. Inelastic strain energy density is also suggested by Qasaimeh *et al.* to extrapolate accelerated test results to life in long term service based on the assumption of a fixed total strain energy density to failure [50]. The hydrostatic stress has been added as damage indicator to the dissipated energy in order to take into account mean stress effect and triaxiality. This approach has been successfully evaluated by Amiable *et al.* [51] for 304 stainless steel in thermo-mechanical fatigue and Tabibian *et al.* [52] for A319 alloy.

In the case of solder joints, shear fatigue tests have been performed by Lau *et al.* [53] with Plastic BGA packages assembled with 8 balls samples. The fatigue tests are performed in stress control, at 60 °C and 0.2 Hz frequency. Parameters for DW are given for the SAC405 solder balls. Identically, shear test of PBGA packages have been performed by Xu *et al.* [54] at different frequencies (from 0.1 to 5 Hz) and temperatures (25, 50, 75 and 100 °C) for different strain range (from 1 to 5%). Three solder material assemblies have been tested (Sn-37Pb, SAC105 and SAC305). Coffin-Manson's fatigue law parameters are given for the different assemblies at 25 °C and 1 Hz. Iosipescu shear specimens and rectangular bulks have been used by Mustafa *et al.* [34] [35] [36] to evaluate evolutions of CM and DW fatigue laws parameters with aging at 125°C. The solder materials considered are lead-free SAC105 and SAC305. Low cycle fatigue tests have been performed by Pang *et al.* [26] [25] [27] with cylindrical bulk samples. Different temperatures, frequencies and total strain have been

tested. An impact of frequency and temperature has been observed. CM and DW fatigue laws are used to predict the results. Parameters for these two fatigue laws for the different frequencies and temperatures are given for the lead-free SAC387 solder. A dependency of these parameters with temperature and frequency is observed.

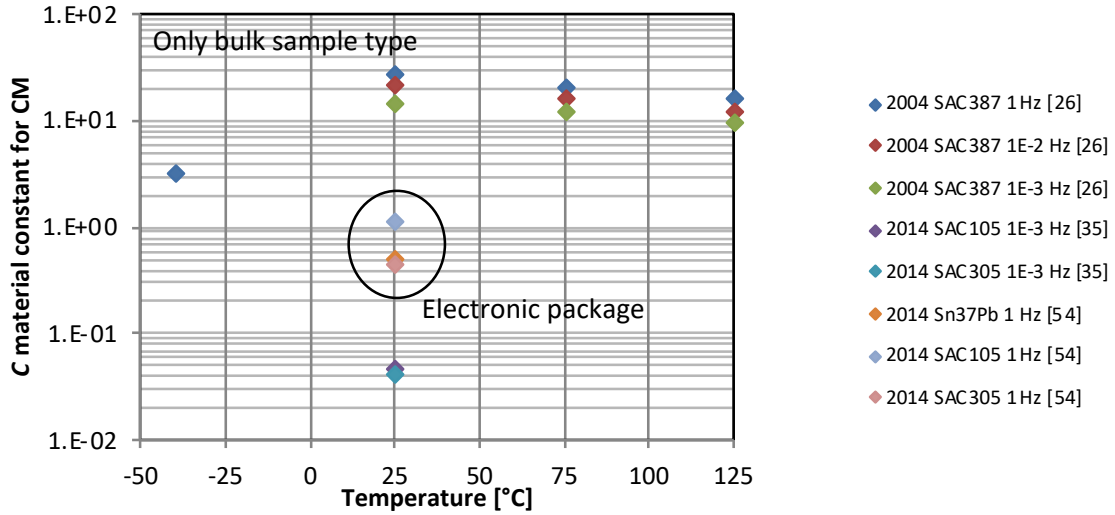


Figure 30: C material coefficient function of temperature for Coffin-Manson's fatigue law

An increase of the temperature or a decrease of the frequency seems to reduce the values of the C material constant for the CM (see Figure 30). Values of the different authors are scattered and this scatter probably comes from the frequencies, solders and methods used.

Values obtained in the literature for the n exponent are also dispersed (see Figure 31). Generally, the value found is lower than 1. The temperature seems to reduce the value of n from the results of Pang. The scattering is also present for DW parameters, as depicted in Figure 32 and Figure 33.

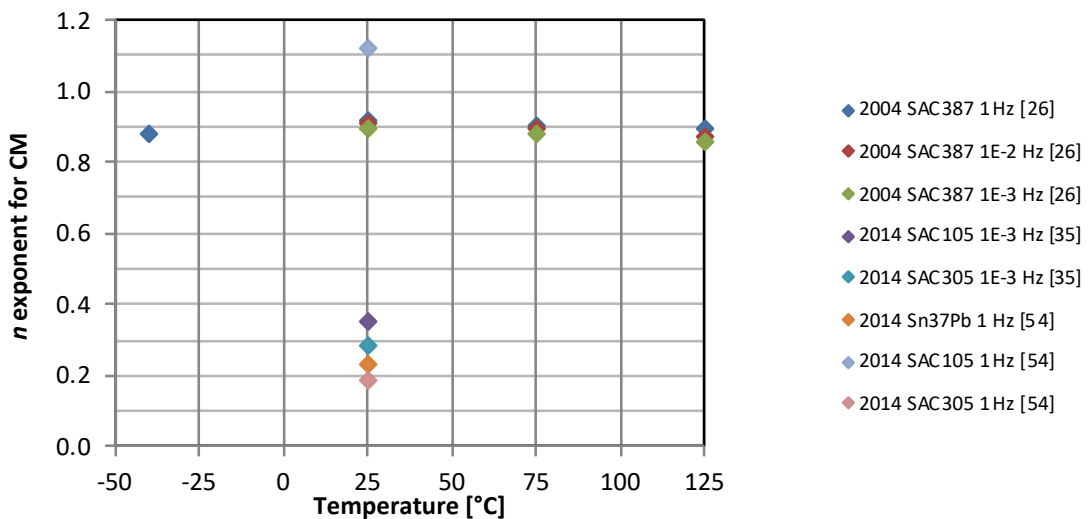


Figure 31: n exponent function of temperature for Coffin-Manson's fatigue law

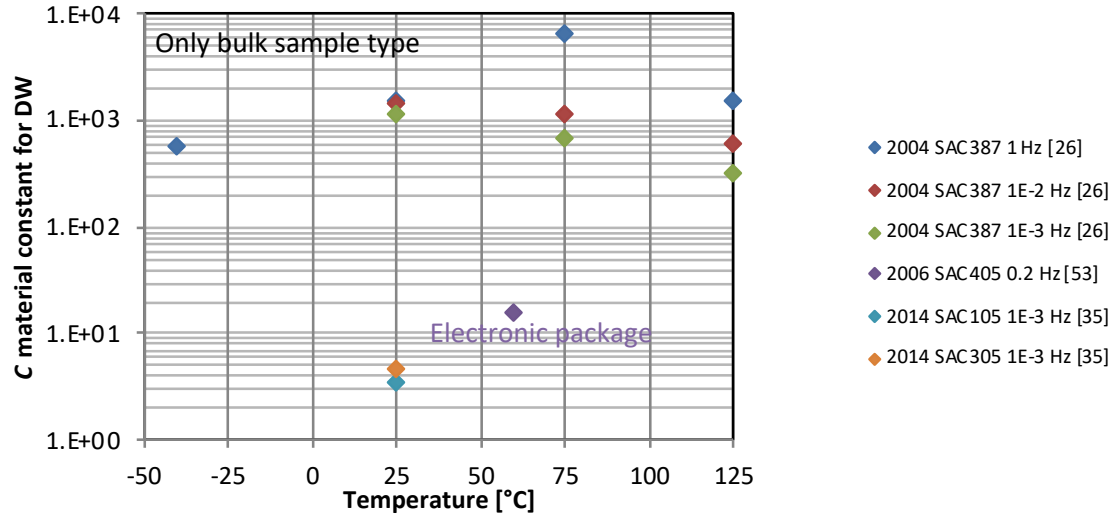


Figure 32: C material coefficient function of temperature for DW

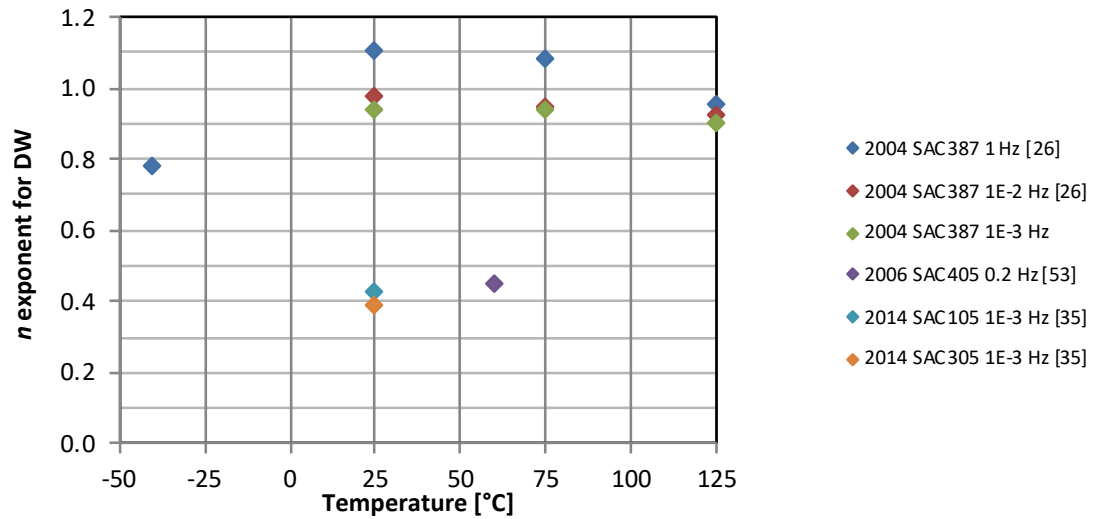


Figure 33: n exponent function of temperature for DW

### 3.d.ii. Creep fatigue laws for solder joint

As discussed, because of the creep deformation, the parameters of the CM and DW are dependent on the loading frequency. To take into account this dependency, frequency-modified fatigue laws are proposed in the literature (see Eq. I-11 and Eq. I-12). Inelastic strain (FCM) and density of energy per cycle (FDW) are used as damage indicators in these formulations in addition to the frequency:

$$(N_f \nu^{k-1})^n \Delta \varepsilon_{inel} = C \quad \text{Eq. I-11}$$

$$(N_f \nu^{k-1})^n \Delta W = C \quad \text{Eq. I-12}$$

where  $\nu$  is the frequency.  $k$ ,  $n$  and  $C$  depend on the material and are experimentally calibrated with fatigue tests. FCM fatigue law is used to describe the fatigue behavior with frequency effect by Kanchanomai *et al.* [55] for lead-free Sn-3.5Ag solder with bulk cylindrical samples with a diameter of 6 mm. The strain-stress response evolution for fatigue tests at various frequencies is described. For

the same strain range, the inelastic strain range increases with decreasing frequency, while the stress range is increased with increasing frequency. Parameters for FCM and FDW are also given by Pang *et al.* [26] at 125 °C with bulk samples. Fatigue shear tests of thin layer of SAC305 solder have been performed by Wang *et al.* [56] at different frequencies and plastic strain range with a thin layer sample of 1x1x0.1 mm<sup>3</sup>. The FDW is used to fit the results.

Table 2: FCM and FDW parameters from the literature

Author	Solder alloy	Law	Temp. [°C]	Frequency [Hz]	$C$ [MJ/m <sup>3</sup> ]	$n$	$k$
Shi <i>et al.</i> [57]	Sn-37Pb	FCM	25	10 <sup>-4</sup> -10 <sup>-3</sup>			0.41
Shi <i>et al.</i> [57]	Sn-37Pb	FCM		10 <sup>-3</sup> -1			0.9
Kanchanomai <i>et al.</i> [55]	Sn-3.5Ag	FCM	20	10 <sup>3</sup> -10 <sup>1</sup>		0.89	0.15-0.22
Pang <i>et al.</i> [26]	SAC387	FCM	125	10 <sup>-3</sup> -1	12.9	0.93	0.95
	SAC387	FDW	125	10 <sup>-3</sup> -1	1487	0.88	0.82
Wang <i>et al.</i> [56]	SAC305	FDW	25	10 <sup>0</sup> -10 <sup>2</sup>		0.41	0.51

Bulk specimens of Sn-37Pb solder material have been tested in low cycle fatigue by Shi *et al.* [57]. Fatigue tests has been carried out at different frequencies, temperatures and total strain set at different values. FCM fatigue law parameters are proposed in order to take into account the dependency of the frequency for two frequency domains.

Because of the dependency of the energy density per cycle to the temperature, one of the parameter of the fatigue law is a temperature-dependent material parameter. The dependency to the temperature has been studied by Engelmaier [10] and the evolution of the  $n$  parameter of the CM has been expressed as following for the eutectic leaded solder.

$$n = -\frac{1}{c} \quad \text{with} \quad c = -0.422 - 6 \times 10^{-4} T_{mean} + 1.72 \times 10^{-2} \ln \left( 1 + \frac{360}{t_d} \right) \quad \text{Eq. I-13}$$

In the equation,  $T_{mean}$  parameter is the mean temperature and  $t_d$  is the dwell time at high temperature.

The inelastic deformation previously introduced mingles the time-independent plastic and time-dependent creep deformations. In this context, the damage from plastic and creep is supposed equivalent. Reviews of creep fatigue models are proposed in the literature for alloys at high temperature by Wang *et al.* [56] and generally for metals submitted to high temperature during operation by Yuan *et al.* [58]. This type of review has also been performed by Wong *et al.* [59] for solder materials. The strain-range-partitioning model (SRP) proposed by Manson is one of the creep fatigue model of the reviews. In this model, the total inelastic strain of the hysteresis is categorized in four strains: plastic reversed by plastic ( $pp$ ), plastic reversed by creep ( $pc$ ), creep reversed by plastic ( $cp$ ) and creep reversed by creep ( $cc$ ) with dedicated parameters for the CM. In the equation,  $i$  and  $j$  are the different combinations of  $c$  and  $p$ .

$$N_{ij} = A_{ij} (\Delta \varepsilon_{ij})^{\frac{1}{c_{ij}}} \quad \text{Eq. I-14}$$

Number of cycles to failure is predicted by a linear law and weighting  $f_{ij}$  coefficient for each type of inelastic strain.

$$\frac{1}{N_f} = \sum \frac{f_{ij}}{N_{ij}} \quad \text{Eq. I-15}$$

$$f_{ij} = \frac{\Delta \varepsilon_{ij}}{\Delta \varepsilon_{inel}} \quad \text{Eq. I-16}$$

To reflect the effect of time, Coffin suggested a frequency-separation model (FSCM) modifying the CM relation by introducing a frequency coefficient which is depended on tension  $\nu_t$  and compression  $\nu_c$  frequencies.

$$N_f = A(\Delta \varepsilon_{inel})^{\frac{1}{c}} \nu_t^m \left(\frac{\nu_c}{\nu_t}\right)^k \quad \text{Eq. I-17}$$

Considering that the fatigue crack grows only in the tension stage, a frequency-modified-damage-function model has been set up by Ostergren to take into account the maximum tension stress  $\sigma_t$  and a frequency factor.

$$N_f = C(\sigma_t \Delta \varepsilon_{inel})^{\frac{1}{c}} \nu^m \quad \text{Eq. I-18}$$

The energy-partitioning model of Dasgupta *et al.* is applicable to strain partitioned constitutive models. The elastic, plastic and creep strains must be distinguished to evaluate the damage of each part. The linear damage accumulation (Palmer-Miner's rule) is then used in order to predict the number of cycles to failure.

$$\frac{1}{N_f} = \frac{1}{N_{fe}} + \frac{1}{N_{fp}} + \frac{1}{N_{fc}} = \left(\frac{U_e}{U_0}\right)^{-\frac{1}{b'}} + \left(\frac{W_p}{W_{p0}}\right)^{-\frac{1}{c'}} + \left(\frac{W_c}{W_{c0}}\right)^{-\frac{1}{d'}} \quad \text{Eq. I-19}$$

In the energy-partitioning model,  $U_e$ ,  $W_p$  and  $W_c$  are respectively the elastic energy density range in a cycle, the plastic energy density dissipated per cycle and the creep energy dissipated per cycle.  $U_0$ ,  $W_{p0}$  and  $W_{c0}$  are material parameters which must be calibrated with experimental tests. Parameters for the ENP are proposed by Zhang *et al.* [42] with cyclic shear loading of a thin layer of Sn37Pb solder. Two types of test are performed in order to evaluate the parameters for plastic and viscous damages. First, fatigue tests are performed at high temperature (125°C) and low strain rate in order to avoid plastic deformation. The creep parameters are defined based on these tests. Then, fatigue tests are performed at room temperature (25°C) and high strain rate. In this case, the ratio of the creep work to the plastic work increases from a negligible value to the order of one as the total inelastic strain increases.

Creep damage can also be expressed by the Robinson's law. The damage is supposed to be the ratio of the time at a stress level  $t_j$  and the time to creep fracture at this level of stress  $T_{Rj}(\sigma)$ .

$$d_c = \frac{1}{N_{fc}} = \sum \frac{t_j}{T_{Rj}(\sigma)} \quad \text{Eq. I-20}$$

The time to creep fracture can be evaluated with the Monkman-Grant equation with  $\dot{\epsilon}_s^m$  the creep strain rate and  $C$  a material dependent parameter.

$$\dot{\epsilon}_s^m T_R = C \quad \text{Eq. I-21}$$

Cumulating the plastic damage using CM and this creep damage for one stress level will give the following damage equation with  $\Delta t$  the dwell time. Shear-lap solder joint has been used by Zhu *et al.* [60] to evaluate the parameters of such a creep-fatigue law.

$$N_f = \frac{1}{d_p + d_c} = \frac{1}{\left( A(\Delta \epsilon_p)^{\frac{1}{c}} + \frac{\Delta t \dot{\epsilon}_s^m}{C} \right)} \quad \text{Eq. I-22}$$

Fatigue crack growth of lead-free solder alloys has been studied by Mutoh *et al.* [61]. Experimental results highlight the importance of creep-fatigue interaction on fatigue crack growth properties. Time-dependent creep behavior becomes especially dominant at high stresses and low frequencies.

## 4. Conclusions of the literature review and perspectives

Elastic and plastic properties found in the literature have been described and compared for different solder joint materials. Apparent Young's modulus, yield stress and ultimate tensile stress have been estimated experimentally based on tensile or shear tests performed with bulk samples or representative solder joint specimens. Evolutions of these mechanical parameters as a function of strain rate and temperature have been studied. Dependence with these parameters is mainly due to the viscosity of the materials as apparent mechanical parameters are measured without implementing a creep model. Moreover, a large scatter is observed in the literature for SAC305 alloy based on different works.

Due to the low melting temperature of solder joint alloys, large creep strains are developed even at room temperature. Viscous properties of solder materials have been studied by numerous authors based on bulk samples, representative solder joint specimens or assembled electronic packages. Creep strain rate in the secondary steady-state creep regime is generally expressed as a function of applied stress and temperature with a sinh formulation to include a power law breakdown. Large scatter exists between the authors for the parameters of this law, which can also come from the sample types and alloys, the calibration methods and the stress and temperature ranges selected.

A large panel of fatigue criteria exists in the literature covering damage indicators using cyclic stress, inelastic strain, creep strain, dissipated energy, etc. A power law formulation is generally used to convert the damage indicator to the number of cycles to failure. Extraction of these mechanical parameters is questioning when these values varies during the test. Fatigue laws used in the industry are generally simplified criteria such as the Coffin-Manson law, based on inelastic deformation, or other laws based on the dissipated energy per cycle. The drawback of the laws is that the cyclic creep and plastic strains are mingled and formulated as a unique inelastic strain. The underlying assumption is that damage contributions of creep and plasticity phenomena are equivalent. This simplified vision has to be improved as already discussed by Wong *et al.* [59]. More precisely, frequency, translated as strain rate and the temperature influences have to be taken into account as concluded from the

experiments of Shi *et al.* [57] and Pang *et al.* [26] in low cycle fatigue with bulk samples of eutectic SnPb or lead free solders. These parameters are important because they change the creep deformation per cycle. Frequency modified fatigue models are proposed in the literature but the representativeness of bulk or thin layer of solder samples with real solder joints can further be discussed.

The shape and the microstructure of solder joints is defined during the assembly process. The shape of solder joints results from the electronic package dimension and weight and the quantity of solder paste deposited. Solder joint microstructure is complex with a dendritic structure and intermetallic surfaces with the copper pads of the electronic package and the printed circuit board. In addition, the number of grains per solder joint is very reduced (until one grain for solder joint of small pitch package). In this context, the use of bulk samples to evaluate mechanical properties of solder joint can be discussed. Complexity of solder joint includes a complex microstructure and shapes, and residual stress after assembly. All of the complexities presented previously are challenging results representativeness with bulk samples. Isothermal fatigue properties of bulk and solder joint samples have been compared by Andersson *et al.* [62]. Similar trends have been obtained for the three tested solder alloys (lead-free SAC405 and Sn3.5Ag and eutectic SnPb alloys). In this work, solder joints show lower fatigue slopes compared to bulk materials, resulting in lower fatigue life at higher stress level and the opposite when subjected to higher strains. One of the reasons of this phenomenon given by the author is the crack propagation mode, which is different for the different tested stress levels for the solder joints. Even if measurements with bulk samples is easier, one should be careful when using data from bulk sample and directly apply them to solder joint as the representativeness of the material tested and the failure mode with real solder joints can be discussed.

In a previous study [63], the wear out reliability of BGA packages with tin-lead solder-joint was evaluated by torsion test. Effect of several loading parameters (angle of torsion, temperature and dwell time) has been studied. The study revealed that the number of cycles to failure in torsion was reduced up to a factor of 10 when dwell time was increased from 1 to 300 seconds and/or temperature was increased from 25 to 125°C. Results can be justified by the strong dependency of creep strain on dwell time and temperature, which increases the damage in the solder alloy. Influence of dwell time has also been studied in accelerated temperature cycling by Coyle *et al.* [64]. Limitation of these tests is the knowledge of mechanical stress state of solder joints during the cyclic loading. In fact, stress and strain are not monitored and hypothesis must be made to evaluate the stress state with simulation.

## 5. Objectives

A lack of clear experimental data separating plastic and creep deformation during fatigue tests has been underlined. Representativeness of experimental tests based on bulk samples can be discussed because of the complex microstructure of solder joints. Representativeness of experimental tests based on thin layer of solder can also be discussed because of the residual stress after assembly and the homogeneity of the stress in the layer during the test. In this context, it is relevant to perform fatigue test with assembled packages. Even if impact of dwell time and temperature have been measured on electronic packages, the knowledge of real measured cyclic mechanical response is often unknown.

Loadings of solder joints in the product life include shear loads of the solder joints because of thermal expansion mismatch in thermal cycling or PCB bending in vibration. In this context, the most convenient loading of assembled package is a shear loading. The deformation must be concentrated in the solder joint. The use of rigid package is therefore important.

## Chapter I. Context and Objectives

Creep deformation is function of different factors including stress level and temperature. In this context, the fatigue test plan must include at least these parameters. In order to evaluate the impact of creep and plastic deformation on the number of cycles to failure, the loading must include or not dwell times at high stress levels. In this case, the impact of the dwell time will be analyzed by the number of cycles to failure.

Lifetime prediction for derisking and simulation requires the characterization of solder joint fatigue. Classic fatigue laws are not sufficient for solder joint materials because of the ductility of the material and in particular for harsh environment and long dwell time. Thus, an innovative experimental setup has been developed in order to perform cyclic fatigue tests of solder joints of an electronic package. A low strain rate of loading is further used to measure the mechanical response of the electronic package during the test and to estimate fatigue properties.



## Chapter II. Experimental Setup

*General context of the study and thesis objectives have been described in the previous chapter. Mission profiles of electronic products include temperature variations. These temperature variations impose cyclic shear stress in solder joints inducing a cumulative damage. Knowledge of fatigue laws for solder joints of electronic package are thus required to guarantee reliability, define acceleration factors and predict failure with simulation.*

*The literature review highlights the lack of experimental data to calibrate a creep-fatigue interaction law. The difficulty with solder joint alloys is to perform fatigue tests with representative samples. Experimental results obtained with bulk samples must be carefully considered because of the specific microstructures of solder joints after assembly.*

*This chapter presents the innovative experimental developed shear test bench. This shear test bench performs cyclic shear tests with assembled electronic packages. Measurements of force and displacement are very accurate because of the small dimensions of electronic packages. The low displacement rate allows a high loading control. Considered electronic packages are assembled with a standard manufacturing process in order to ensure the representativeness of solder joints. The fatigue loading can include or not a dwell time at extreme force values in order to evaluate the impact of creep strain on fatigue failure. Solder joint temperature is controlled in order to perform fatigue tests at higher temperature.*

*Post-processing methods for the data are presented. Validations steps, mechanical values extraction and output analysis are developed in this chapter. Preliminary monotonic and step-stress tests are also described for illustration.*

## 1. Innovative shear test bench

The experimental shear test bench comprises: (i) the micro shear tester, (ii) the data acquisition module, (iii) the CCD camera (Charge Coupled Device) and (iv) two computers (one for command and the other for data acquisition). The test bench is depicted in Figure 34. The command computer uses the data acquisition module to control the micro shear equipment and to record measures of local displacement and force. The command displacement of the micro shear test equipment controls the shear displacement of the sample. Digital Image Correlation (DIC) evaluates the local displacement between the two jaws based on images taken by the CCD camera.

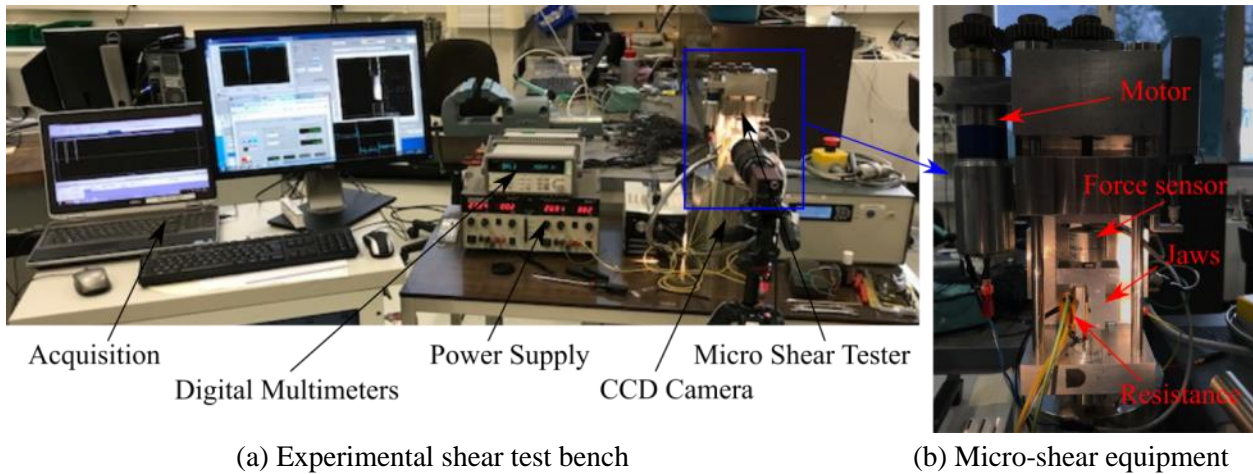


Figure 34: General test bench description

### 1.a. Shear test bench description

The shear test bench has been described in [65]. Figure 35 shows the shear loading mounting.

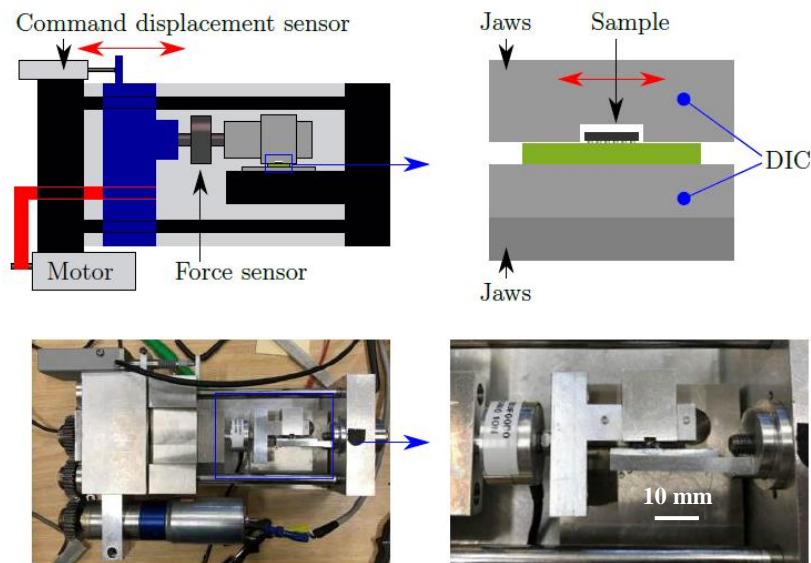


Figure 35: Micro shear tester developed to perform shear test of assembled package

The motor rotation controls the command displacement in the system. This displacement is transmitted to the sample by the jaw (mobile part in blue in the Figure 35). The force sensor measures the applied force to the package. The force sensor is a bi-directional sensor with a force amplitude capability of 100 N in positive and negative values.

The jaw of the package side is manufactured with a square notch containing the package. Sides of the notch are parallels to the package side to ensure the shear loading. The jaw is manufactured with a mobile part in the vertical direction. This mobile part is removed during the positioning of the sample and is then inserted when the square notch is aligned with the package before running the test. The alignment of the notch and the package is performed by the user who can control the package location relatively to the notch with the CCD camera images in real time.

### 1.b. Samples of the shear test bench

Two parts make up the sample: (i) the assembled electronic package sample on the PCB and (ii) the substrate (see Figure 36). The package sample is secured to the secondary jaw by fixing screws of 1.2 mm diameter (M1.2). These screws are aligned with the loading direction to perfectly secure the PCB in horizontal direction during the shear loading of the package. The screw penetration in the jaw is larger than 1mm to secure the sample at all times during the test. The PCB is manufactured with two non-plated through holes for the screws. The screws dome heads are buried in the PCB with the second drilling diameter. In fact, the movement of the jaw that is in contact with the electronic package must be free in the vertical and horizontal directions. The substrate jaw, and thus the assembled package, is finally secured to the jaw of the shear test equipment with screws of 2.5 mm diameter (M2.5).

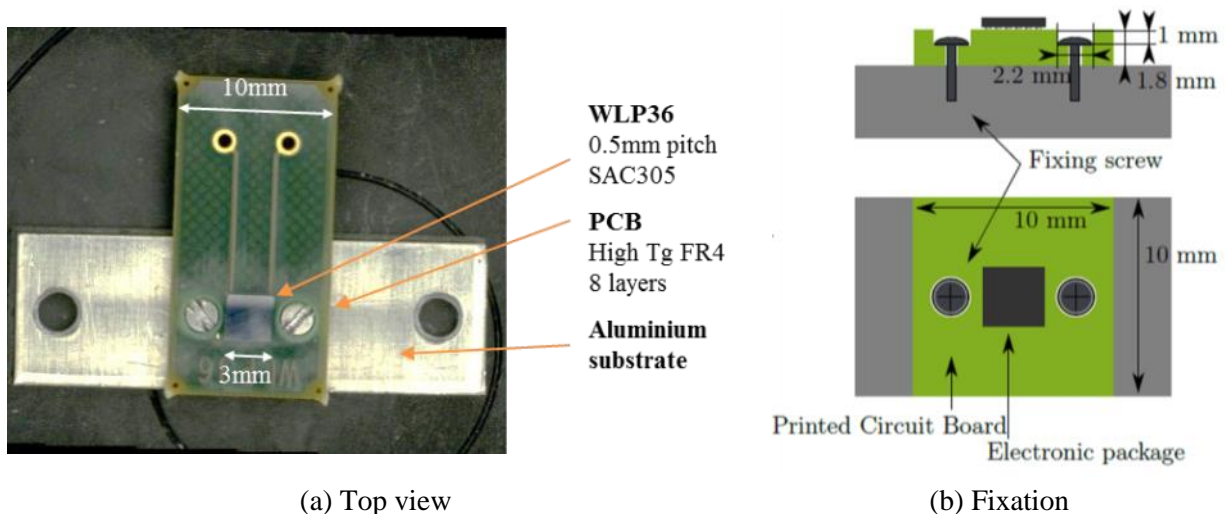


Figure 36: Sample description: (a) top view and (b) fixation of the sample to the jaw with screws

The electronic package of the sample is a Wafer Level Package (WLP). A cross section of the package is depicted in Figure 37. Details about sample preparation for the cross section are given in following chapter 3. The distance between two solder balls is 0.5 mm. This distance is called pitch in electronics. The WLP has a matrix of 36 solder balls which connects the silicon die to the PCB.

The sample and the jaw are designed to guarantee that the strain are focused on the solder joints matrix during the shear loading. The fixing screws prevents the displacement of the PCB and the substrate in aluminum ensures the planarity during the loading. The rigidity of the package in silicon

guarantees the distribution of the loading in all of the solder balls. After the test, the sample can be removed from the aluminum substrate unscrewing the fixing screws without damaging the solder balls to verify the failure mechanism after all the tests.

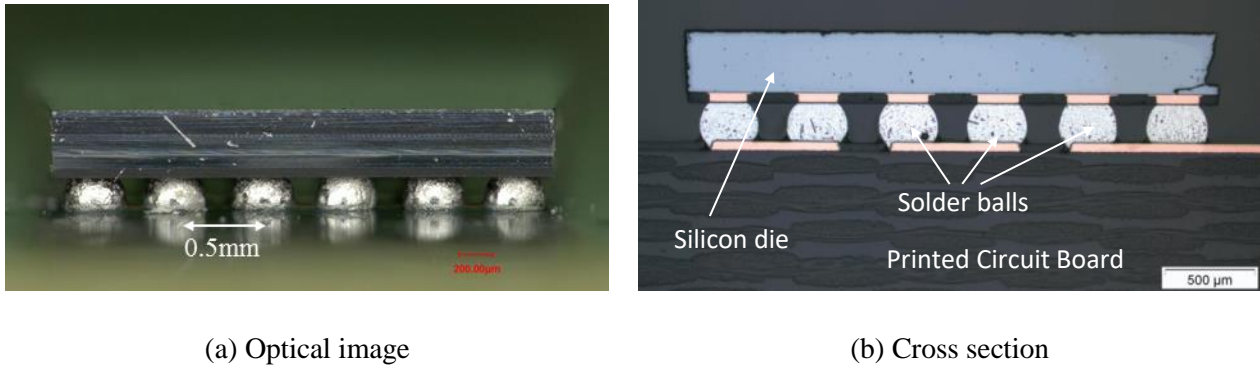


Figure 37: Wafer Level Package of the sample assembled on the Printed Circuit Board: (a) optical image of the package and (b) cross section showing the matrix of solder balls

### 1.c. Schematic representation of the shear test bench

A schematic representation of the shear test bench is depicted in Figure 38. The sample is the assembled electronic package described in the previous section. This sample is connected in series with the force sensor and is fixed to the jaw of the micro shear tester. The force sensor measures the force  $F$  applied to the sample. The displacement sensor delivers the command displacement  $u_c$  and the digital image correlation delivers the local displacement  $u_l$ .

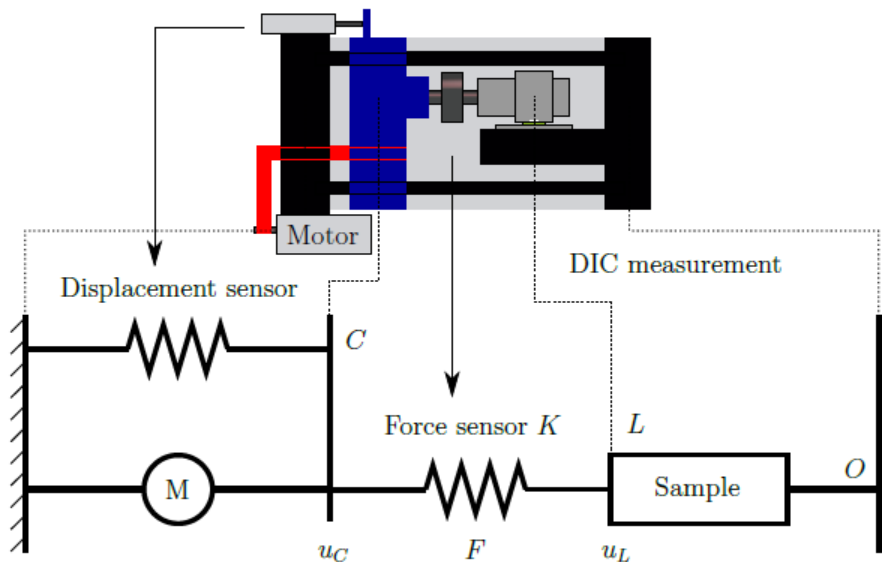


Figure 38: Schematic representation of the shear test bench for monotonic tests

One of the relation of this model is the relation between the command ( $u_c$ ) and the local ( $u_l$ ) displacements. This relation is function of the measured force  $F$  and the stiffness of the force sensor  $K$ . Force sensor deformation induces a difference between command and local displacements and:

$$K(u_c - u_l) = F \quad \text{Eq. II-1}$$

The assembled electronic package and the jaw are always in contact for the schematic representation in Figure 38. This model is valid in the case of monotonic tests after the jaw starts being in contact with the package. However, this model is no longer valid for cyclic loadings because a gap exists between the package and the jaw. This gap introduces a new element in the schematic representation of the shear test bench as depicted in Figure 39. The gap includes an additional displacement between the displacement  $u_l$  and the real displacement of the sample. Evaluation of the real displacement from  $u_l$  and  $F$  is detailed in the following section dedicated to post-processing methods.

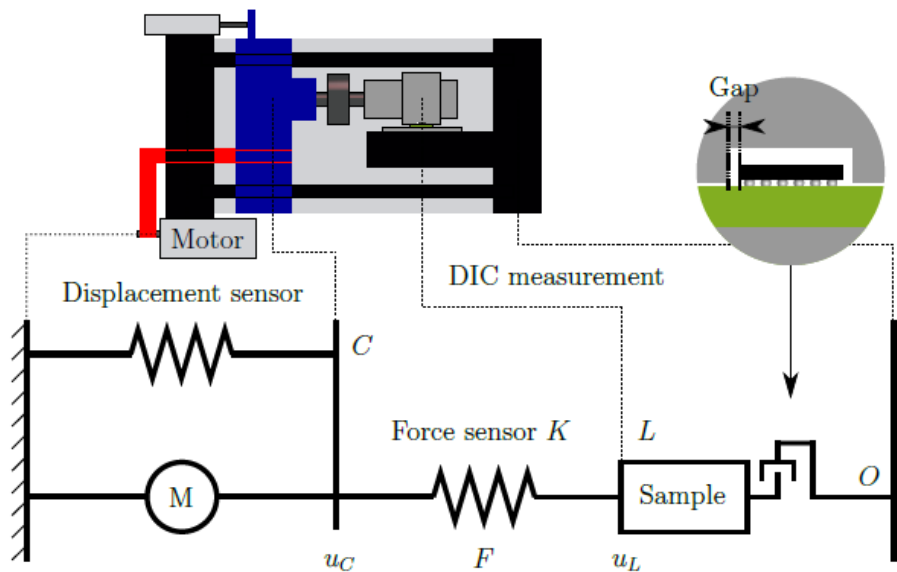


Figure 39: Schematic representation of the shear test bench with the gap during fatigue tests

### 1.d. Experimental results post-processing

This section reports post-processing methods used to evaluate the hysteresis response of the electronic package from the measurements of local displacement and force. Digital Image Correlation, hysteresis construction and mechanical parameters extraction are detailed.

#### 1.d.i. Local displacement measurement with Digital Image Correlation

The local displacement between the two jaws is measured with Digital Image Correlation. Images used for the tracking are black and white images of 2452x2054 pixels captured by the CCD camera. Images are post-processed to measure pixel displacements with a dedicated software developed in the laboratory. Two patterns of 400x400 pixels placed in the two different jaws are tracked. The relative displacement of these two patterns is evaluated by the software.

The relative displacement of the two patterns is measured in pixels. This displacement needs to be converted in micrometers. The coefficient of conversion pixel to micrometer is  $C_{p \rightarrow m}$  and has a unity of micrometer per pixel. This coefficient depends on the distance between the CDD camera and the micro shear tester. The coefficient increases when the distance increases because the dimension in



micrometer of one pixel also increases. The coefficient is constant during one experimental test but can vary between two experiments because the camera is manually positioned. The coefficient is evaluated for each experimental test with two methods. Measurements must be analyzed with a particular attention if the two methods give different results.

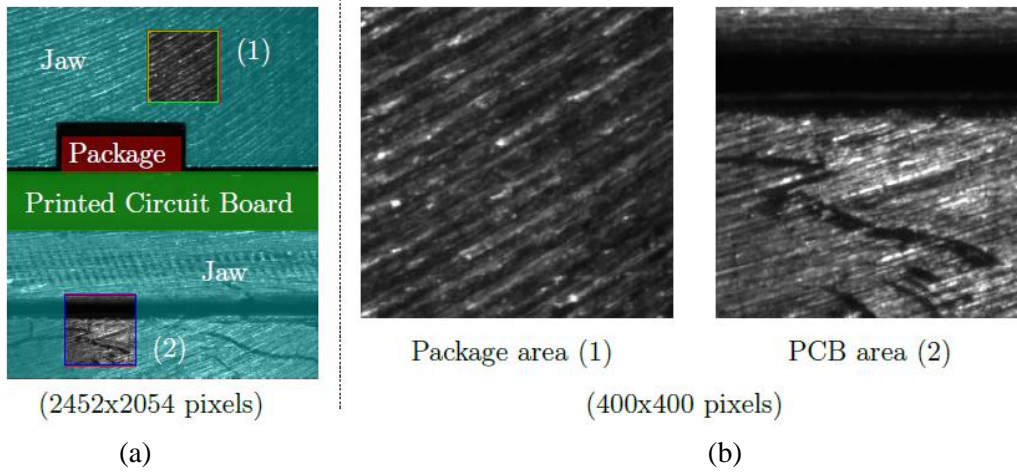


Figure 40: Images used for Digital Image Correlation: (a) image from the CCD camera and (b) patterns tracked in the jaws of the package and PCB sides

The first method is a static method based on the measurement of an initial image. At the beginning of the test, an image of the setup (see Figure 41) is used to measure the dimension of the notch in pixel. This dimension is known and has been previously measured with an optical image in micrometer. The ratio of these two measurements in pixel and micrometer gives the coefficient of conversion pixel to micrometer  $C_{p \rightarrow m}$  for the test.

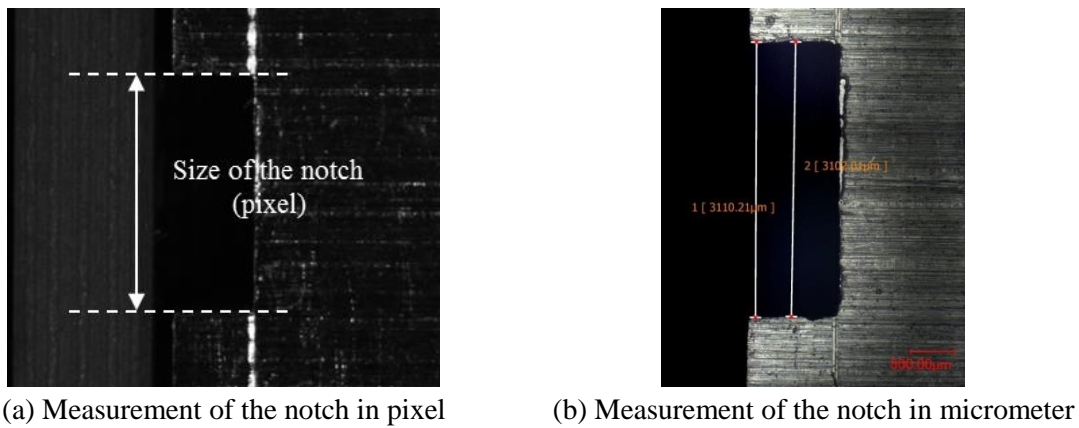


Figure 41: Images used for the first static method of measurement of the pixel to micrometer coefficient  $C_{p \rightarrow m}$  using (a) pixel and (b) micrometer dimensions of the notch

The second method is performed during the post-processing of the results. As discussed previously, the difference between the command displacement and the local displacement of the sample is due to the deformation of the force sensor. If no force is measured ( $F = 0$  N), the command  $u_c$  and the local  $u_l$  displacements are equal as described by the force sensor relation in Eq. II-1. The coefficient of conversion pixel to micrometer  $C_{p \rightarrow m}$  can be measured with the values of command  $u_c$

and local  $u_l$  displacements when no force is measured because the command displacement is in micrometer and the local displacement in pixel. The absence of force means that the package and the jaw are not in contact as depicted in Figure 42. This moment appears two times per cycle due to the presence of the gap. The coefficient of linear regression between values of command displacements in micrometer and related local displacements in pixel gives the coefficient pixel to micrometer  $C_{p \rightarrow m}$ .

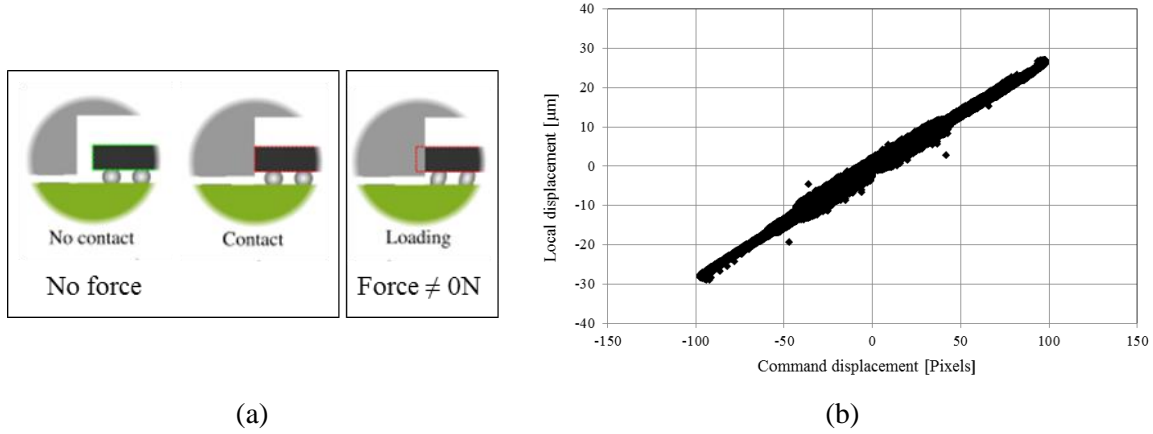


Figure 42: Second method of measurement of the coefficient  $C_{p \rightarrow m}$  during post-processing: (a) schematic representation without contact and (b) related command and local displacements

The first method is performed for all the experimental tests (monotonic and cyclic). The second method is only performed for the cyclic tests. The first method is limited because only based on one image. The second method is more precise because it corresponds to an average value for all cycles. In this context, for cyclic test, if the coefficient for the first and the second methods are close ( $< 10\%$  of difference), the coefficient  $C_{p \rightarrow m}$  evaluated by the second method is selected to analyze the results. Otherwise, the results of the test have been analyzed in more details. The first method is used: (i) to measure the coefficient pixel to micrometer for monotonic test and (ii) as control of the coefficient calculated with the second method for cyclic test.

#### 1.d.ii. Post-processing method

Raw data are the force magnitude, the time, the local displacement and the electrical resistance. The shear test bench and the acquisition software collect these data during the experimental test. The general post-processing algorithm in Python language developed during the thesis is represented in Figure 43.

The gap introduces two periods without loading for each cycle. Points measured during these periods are first dissociated from the other. Lists of command and corresponding local displacements are created. The correlation coefficient pixel to micrometer is evaluated based on these lists by linear regression as detailed in the second method of the previous section. Other local displacement measured during loading and unloading periods are converted after from pixel to micrometer with this coefficient.

The gap distance needs to be removed from the local displacement in order to obtain the sample displacement. The specific post-processing method is illustrated in Figure 44. The contact between the package and the jaw is evaluated positively if the force is higher than a force limit (1.5 N). For each loop, the “real” point of contact is different than the first point detected due to the force limit tolerance required. In order to evaluate the “real” point of contact, a linear regression of the following points with force values lower than 15 N and the corresponding displacement is performed to

## Chapter II. Experimental Setup

characterize the sample stiffness. These force value of 15 N has been defined with the results of the monotonic tests. In fact, these results show that the solder joints matrix is in the elastic domain under 15 N which justifies the use of a linear regression. Connection of measured points after unloading and at the beginning of loading for the following cycle finally allows to obtain the hysteresis response of the sample without the gap (see Figure 45). Mechanical parameters extraction step is detailed in the following section.

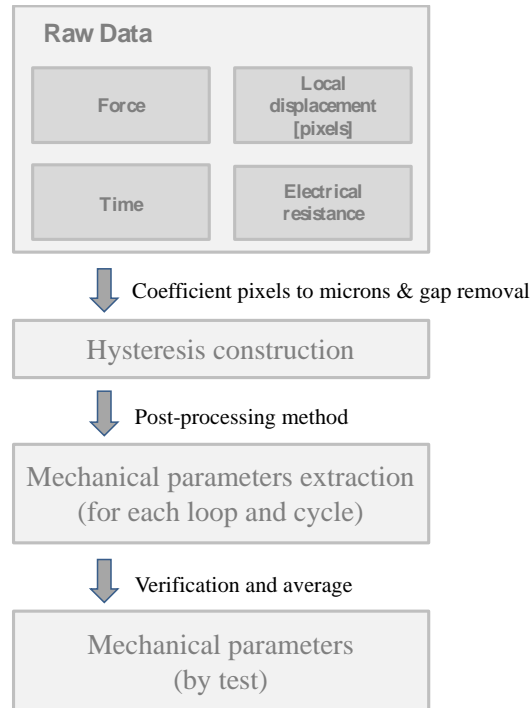


Figure 43 - Post-process program architecture

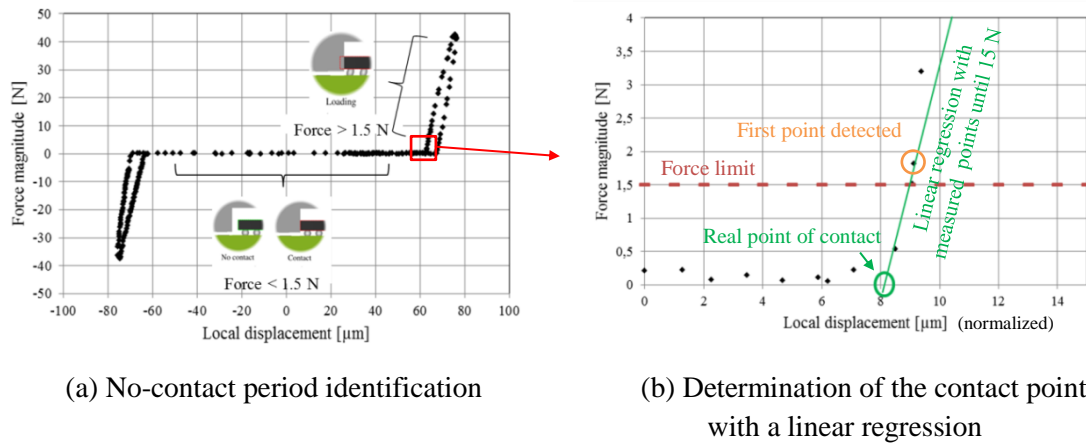


Figure 44 - Removal of the data generated by the gap



## Chapter II. Experimental Setup

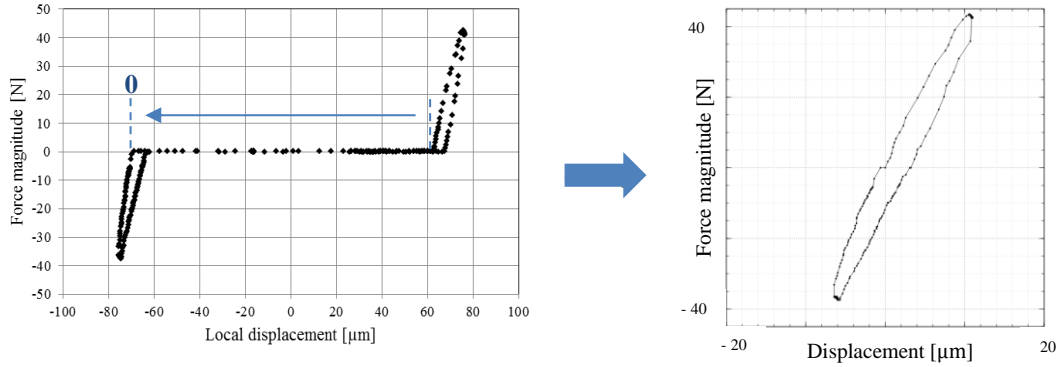
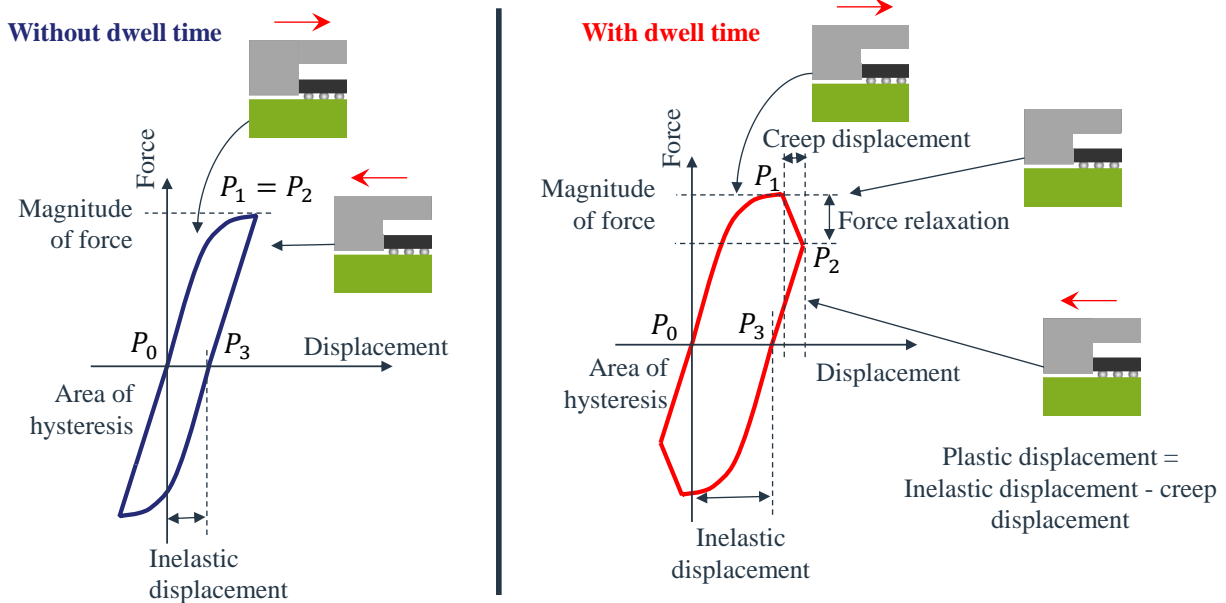


Figure 45 - Characteristic hysteresis construction

### 1.d.iii. Mechanical parameters extraction

Mechanical parameters are extracted from the hysteresis response. Damage indicators, such as force magnitude, inelastic and plastic displacements and dissipated energy are extracted from the hysteresis response of each cycle. This step is schematically illustrated in Figure 46. These parameters are extracted for fatigue test with loadings that include or not dwell time which is a period with a constant command displacement at extreme force level included to the cyclic loading. Two additional parameters are extracted for fatigue tests including dwell times: the creep displacement and the force relaxation. All of these parameters are extracted for each loading cycle and are then averaged from the beginning of the test until half of the number of cycles to failure. Evolution of these mechanical parameters during the fatigue test are discussed in chapter 3 and the average method is also described.



Characteristic points:

- $P_0$ , contact and begin of the loop
- $P_1$ , begin of dwell time
- $P_2$ , end of dwell time
- $P_3$ , end of the loop.

Values:

- $F$  measured shear force [N]
- $u_l$  measured displacement [ $\mu\text{m}$ ]
- $d_i = u_l(P_3)$  inelastic displacement [ $\mu\text{m}$ ]
- $d_v = u_l(P_2) - u_l(P_1)$  creep displacement [ $\mu\text{m}$ ]
- $d_p = d_i - d_v$  plastic displacement [ $\mu\text{m}$ ]
- $F_a = F(P_3)$  force amplitude [N]

$$F_v = F(P_2) - F(P_1) \text{ force relaxation [N]}$$
$$A \text{ area of the hysteresis [N} \cdot \mu\text{m]}$$

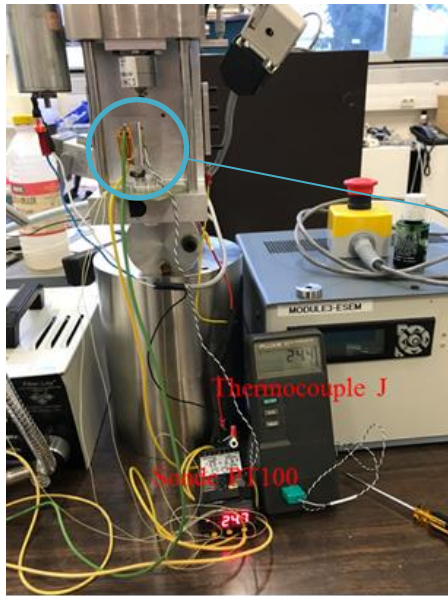
*Figure 46 - Analysis of the hysteresis response (schematic representations) and mechanical parameters extracted for loading with or without dwell time*

Force magnitude per cycle is defined by the average of the force magnitudes obtained during the positive and the negative loops of the cycle. For tests without dwell time, we consider that no creep displacement is developed during loading and unloading. The creep strain during these phases will be calculated with a mechanical model in the chapter 5. The inelastic displacement is measured with the difference of displacement at the beginning of the loop and at the end (when the force magnitude is equal to zero). As for the force magnitude, the inelastic displacement recorded is an average of the two values obtained during positive and negative loadings. The inelastic displacement corresponds to the plastic displacement in the case of a loading without dwell time. This displacement is due to irreversible inelastic strain developed during the loading.

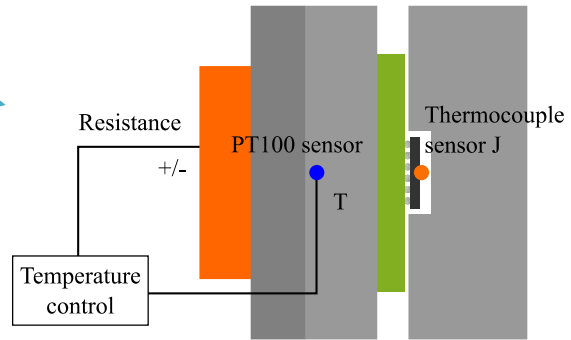
In case of loading with dwell time creep is taken into account as an additional damage mechanism. It corresponds to an irreversible deformation of the material subjected to a constant loading above its yield stress. The creep is measured by the force relaxation and the displacement variation (creep displacement) during the dwell time period. Average values of this parameters are recorded from the positive and negative loops. Finally, the plastic displacement measured during loading and unloading periods is computed subtracting the viscous displacement to the inelastic displacement. The area of the hysteresis, expressed in  $\text{N} \cdot \mu\text{m}$ , is also calculated. This value is proportional to the dissipated energy released throughout the test. Sample stiffness is evaluated with a linear regression between 1.5 N and 15 N.

### 1.e. Test in temperature

The test bench allows to vary the temperature of the sample during monotonic or fatigue tests. Figure 47 shows the experimental procedure used to calibrate the temperature variation. The objective temperature is measured by the PT100 sensor which is located in the jaw. A resistance is fixed on the jaw and behind the sample to increase the temperature. The amperage submitted to the resistance is controlled by the temperature control module in order to maintain the desired temperature.



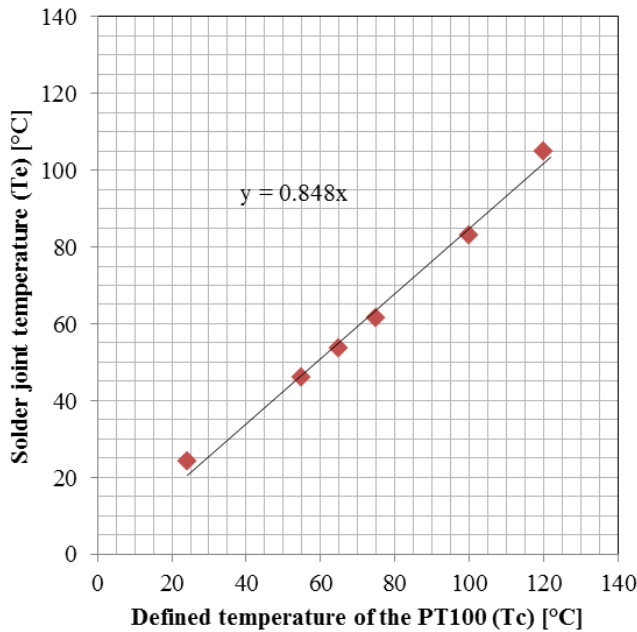
(a) General view



(b) Schematic

Figure 47: Test bench equipped with PT100 and J sensors for the experimental procedure used to calibrate the temperature variation

The measured value of temperature in the jaw (PT100 sensor) is different from the solder joints temperature because of the temperature gradient from the PT100 sensor to the package. Preliminary tests have been performed in order to evaluate this gradient of temperature. The sample is equipped with a thermocouple sensor J fixed on top of the WLP. The gradient is characterized for different temperatures from room temperature to 120 °C degrees. Obtained results are reported in Figure 48. The gradient of temperature is linear in the considered temperature range. A linear regression is used to calculate the coefficient of conversion from jaw temperature to package (and solder joints) temperature.



The temperature calibration curve is used in order to predict the temperature of the solder joints as a function of the defined temperature of the PT100 fixed on the jaw.

Figure 48: Temperature calibration curve: recorded temperatures in the jaw and corresponding measurements on top of the package

## 2. Accuracies of force and displacement measurements

The shear test bench shall be adequate for the measurement of the hysteresis response of the electronic package. Accuracies on force and displacement measurements are evaluated in this section. Statistical methods used in this section for the analysis of the experimental measurements are detailed in [66]. Uncertainty of measurement corresponds to the square root of average square deviation. If a variable  $X$  takes a finite number of values  $x_1, \dots, x_n$  and  $m$  is the average of these measurements, the uncertainty of measurement  $s_m$  is evaluated as formulated in Eq. II-3.

$$m = \frac{1}{n} \sum_{i=1}^n x_i \quad \text{Eq. II-2}$$

$$s_m^2 = \sum_{i=1}^n \frac{1}{n} (x_i - m)^2 \quad \text{Eq. II-3}$$

Relative uncertainty is a measure of the uncertainty of measurement considering the size of the measurement. For  $n$  measurements, the relative uncertainty  $\delta$  is evaluated as formulated in Eq. II-4.

$$\delta = \sqrt{\frac{1}{2(n-1)}} \quad \text{Eq. II-4}$$

The uncertainty accuracy is the number of significant digits that needs to be used in the final result. From the uncertainty of measurement, one number must be used if the relative uncertainty is close to 30 %/ Otherwise, two numbers can be used if the relative uncertainty is close to 10 %.

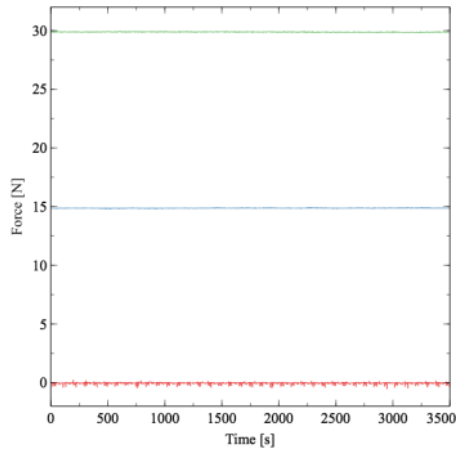
Uncertainty of measurement, relative uncertainty and uncertainty accuracy values measured for the force sensor and the local displacement by Digital Image Correlation are given in the following sections. The last section is related to experimental tests in temperature.

### 2.a. Accuracy of the force sensor

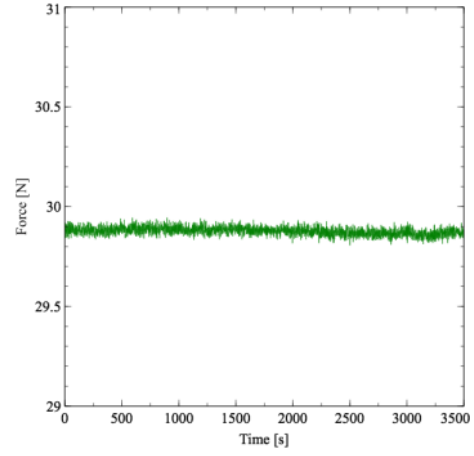
The accuracy of the force sensor is measured for different loading levels. These levels are selected to cover force amplitude values expected during experimental tests. Uncertainty accuracy are evaluated at three force levels  $F_1$ ,  $F_2$  and  $F_3$  close to 0, 15, and 30 N. Measurements are recorded during approximately 1 hour (3500 s) for these different force levels. The sampling rate is 5 measurements per second and is the same as during experimental tests.  $n = 17500$  measurements are considered for each level. Relative uncertainty is lower than 1 % so two numbers of significant digits can be used based on the uncertainty of measurement.

Evolution in time for the three force levels are plotted in Figure 49. Corresponding histogram repartitions are plotted in Figure 50.

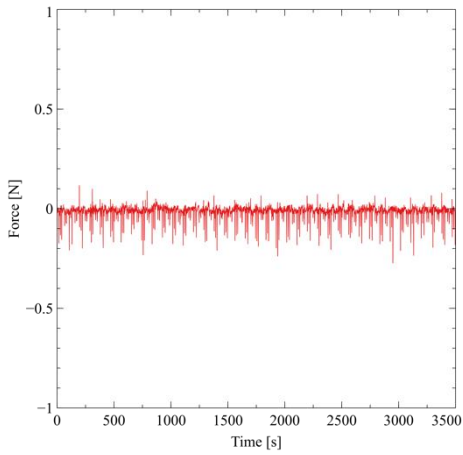
## Chapter II. Experimental Setup



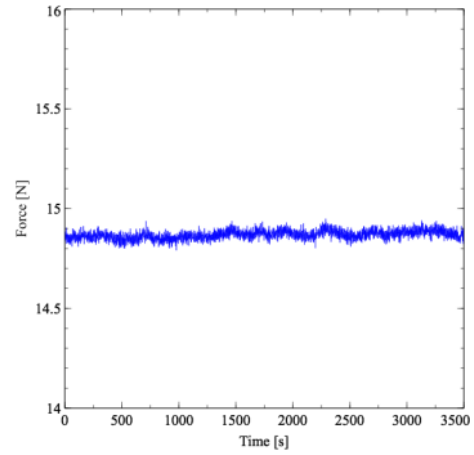
(a)



(b)

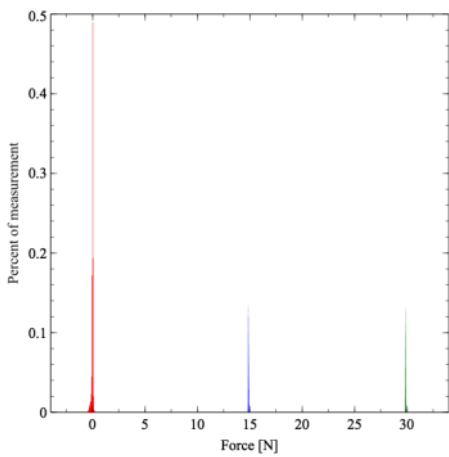


(c)

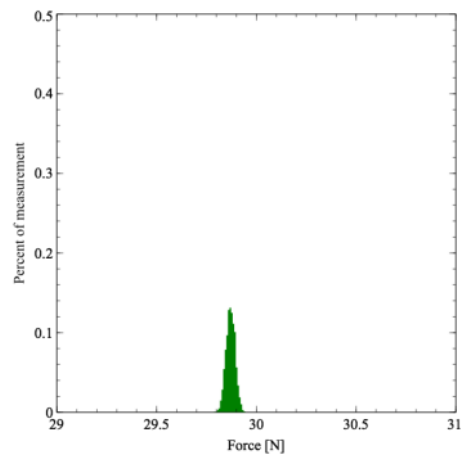


(d)

Figure 49: Evolution in time of force sensor measurements for accuracy evaluation for (a) all force levels and zoom at (b)  $F_1$ , (c)  $F_2$  and (d)  $F_3$



(a)



(b)

## Chapter II. Experimental Setup

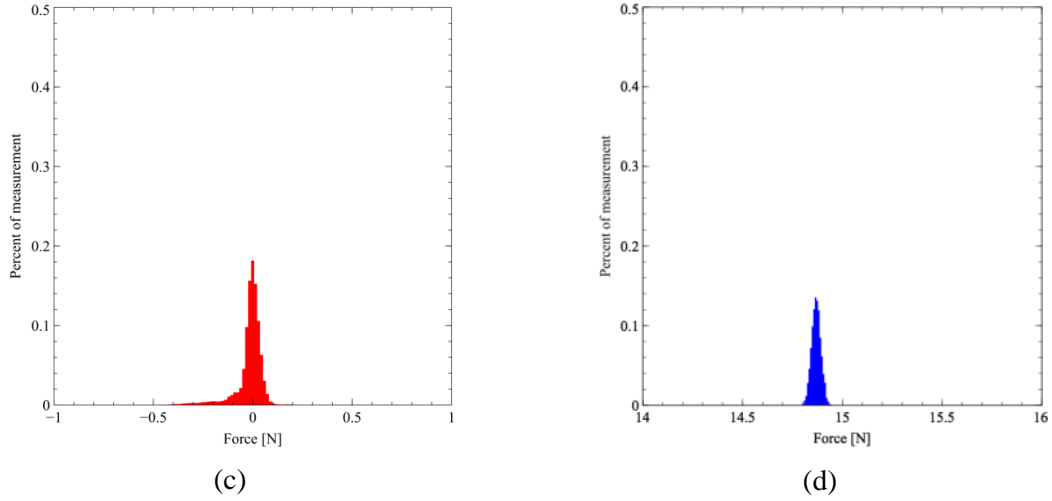


Figure 50: Histogram repartitions of force sensor measurements for accuracy evaluation (a) for all force levels and zoom at (b)  $F_1$ , (c)  $F_2$  and (d)  $F_3$

Average, relative uncertainty, uncertainty of measurement and accuracy values obtained for the three force levels are reported in Table 3. Results show that the accuracy is increased when the force sensor is loaded. This result was expected regarding time evolution obtained for  $F_1$ . This characteristic of the sensor is interesting but nevertheless the results show that the accuracy of force is at least 0.1 N.

Minimum and maximum values obtained for the  $F_1$  force level are interesting. A force limit (1.5 N) has been introduced in the previous section to analyze the hysteresis response of the sample. The results show that this tolerance is sufficiently high to cover the force sensor deviations. Average force values of  $F_1$  and  $F_2$  are also interesting. Displacements of 16 and 31  $\mu\text{m}$  have been used to reach these force values which gives an average sensor stiffness of 1.0 N/ $\mu\text{m}$ .

Table 3: Accuracies evaluated for the three force levels considered

Force level	Average $m$ [N]	Min [N]	Max [N]	$\delta$	$s_m$ [N]	Accuracy [N]
$F_1$	-0.0171	-0.2755	0.1321	< 1 %	0.0725	0.1
$F_2$	14.8812	14.8145	14.9413	< 1 %	0.0213	0.01
$F_3$	29.8709	29.7861	29.9447	< 1 %	0.0228	0.01

### 2.b. Accuracy of the local displacement

The local displacement is measured by Digital Image Correlation and the displacement accuracy is evaluated in this section. Local displacement is recorded in pixel with a 5 measurement per second sampling rate during 30 min.  $n = 9000$  measurements are considered which gives a relative uncertainty lower than 1 %. The method used for monotonic tests is used to evaluate the correlation coefficient and to convert displacement measurements from pixel to micrometer. Evolution in time and histogram repartition of local displacement are plotted in Figure 51.

## Chapter II. Experimental Setup

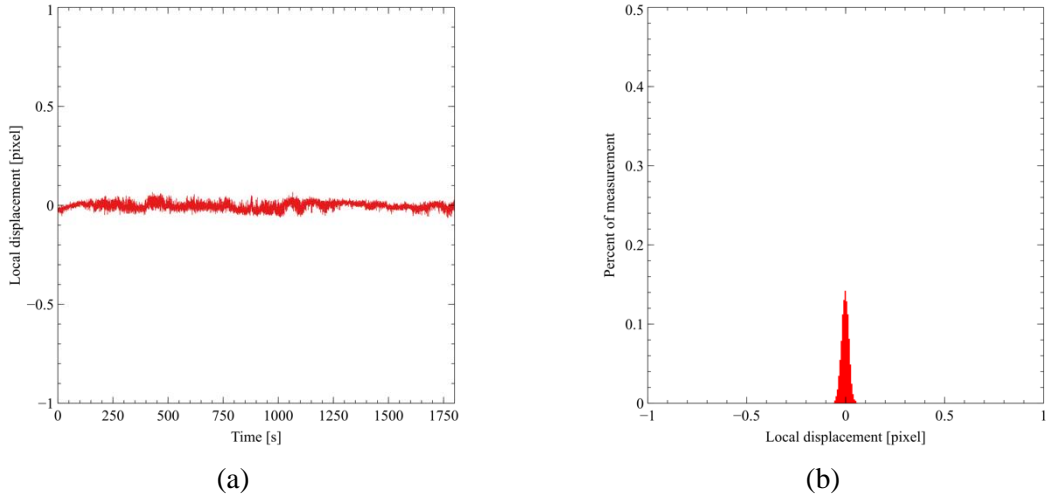


Figure 51: Accuracy of the local displacement measured by Digital Image Correlation: (a) evolution in time and (b) histogram repartition

Average, relative uncertainty, uncertainty of measurement and accuracy values obtained for the three force levels are reported in Table 4. Results show that the accuracy of local displacement measurement is  $0.1 \mu\text{m}$ .

Table 4: Accuracy evaluated for the local displacement measured by Digital Image Correlation

Displ.	Average $m$ [ $\mu\text{m}$ ]	Min [ $\mu\text{m}$ ]	Max [ $\mu\text{m}$ ]	$\delta$	$s_m$ [ $\mu\text{m}$ ]	Accuracy [ $\mu\text{m}$ ]
Origin	-0.0111	-0.2568	0.2672	< 1 %	0.0737	0.1

### 2.c. Accuracy of tests in temperature

Accuracies measured in the previous section for force and displacement are still available for test in temperature. The area submitted to a temperature increase gradient during the test in temperature is localized close to the sample. Neither the coefficient pixel/micron (measured without loading) nor the force sensor (located far from the resistance source) are affected by the temperature increase. Thus, the force sensor accuracy does not change. The local displacement is measured by digital image correlation. Displacement accuracy is not modified during test in temperature because the image captured is not modified. Accuracies of force sensor ( $0.1 \text{ N}$ ) and local displacement ( $0.1 \mu\text{m}$ ) are identical during test in temperature.

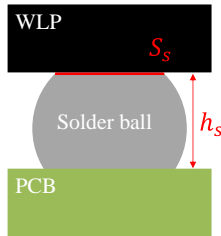
### 3. Monotonic tests

#### 3.a. Results of the mechanical characterization

Preliminary monotonic tests are performed in order to evaluate the mechanical response of the WLP sample submitted to a shear loading. The loading rate of the command displacement  $u_c$  is  $0.5 \mu\text{m/s}$ . The sensor relation (Eq. II-1) previously introduced is derived in time in Eq. II-5.

$$K \left( \frac{du_c}{dt} - \frac{du_l}{dt} \right) = \frac{dF}{dt} \quad \text{Eq. II-5}$$

In the elastic domain, the solder joint material response can be modeled with  $\tau_s = G_s \gamma_s$ , with  $\tau_s$  the shear stress,  $G_s$  the shear modulus, and  $\gamma_s$  the shear strain in the solder joint. Considering an homogeneous stress state, the shear strain and stress in the solder joints matrix can be expressed as formulated in Eq. II-6 and Eq. II-7.



$$\text{Stress } \tau = \frac{F}{n_s \cdot S_s} \quad \text{Eq. II-6}$$

$$\text{Strain } \gamma = \frac{u_l}{h_s} \quad \text{Eq. II-7}$$

Figure 52: Shear stress and strain conversion from solder joint dimensions and force and displacement measured during fatigue test

$S_s$  is the solder joints surface and  $h_s$  the solder joint height. The sensor relation finally gives the equation of shear strain rate as a function of the command displacement velocity in the elastic domain.

$$\frac{d\gamma_s}{dt} = \frac{1}{h_s} \left( \frac{du_l}{dt} \right) = \frac{1}{h_s} \frac{du_c}{dt} \left( 1 + \frac{G_s S_s}{h_s K} \right)^{-1} \quad \text{Eq. II-8}$$

Solder joint height  $h_s$  ( $180 \mu\text{m}$ ) is measured with a cross section of the sample. Solder joints surface is evaluated with the pad diameter ( $250 \mu\text{m}$ ) and is approximatively  $1.77 \text{ mm}^2$ . All details about the evaluation of the height and the surface of solder joints are given in chapter 3.

Schematic representation

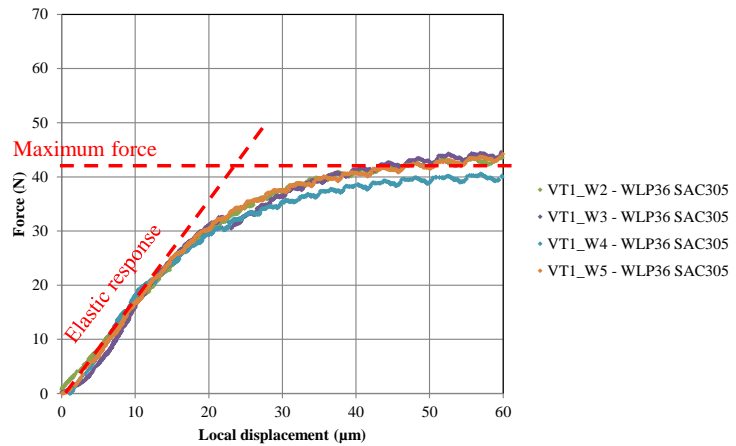
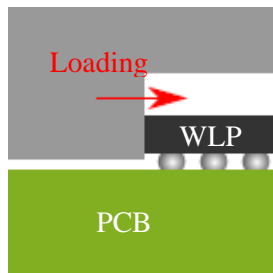




Figure 53: Mechanical response obtained with monotonic tests using four WLP samples assembled in SAC305

Approximate values of the sensor stiffness  $K$  and the sample stiffness  $G_s S_s / h_s$  are respectively 1.0 and 1.7 N/ $\mu\text{m}$ . For a command displacement rate equal to 0.5  $\mu\text{m/s}$ , the shear strain rate in the solder joint matrix is approximately  $1 \cdot 10^{-3}$  1/s.

Measured values for the stiffness of the sample in the elastic domain and the maximum force are summarized in Table 5. The shear stress has been calculated with the homogeneous formulation previously introduced. As depicted in Figure 53, the yield stress is approximately reached after 20 N (11 MPa) for the different samples. This approximative value is graphically estimated.

Table 5: Monotonic test results

Sample	Sample stiffness	Maximum force	Shear stress
VT1_W2_WLP36 SAC305	1.7 N/ $\mu\text{m}$	43 N	24 MPa
VT1_W3_WLP36 SAC305	1.7 N/ $\mu\text{m}$	44 N	25 MPa
VT1_W4_WLP36 SAC305	1.7 N/ $\mu\text{m}$	40 N	23 MPa
VT1_W5_WLP36 SAC305	1.7 N/ $\mu\text{m}$	42 N	24 MPa

### 3.b. Comparison of the monotonic test results with the literature

Shear stress values are compared with the values obtained by Darveaux [45] with the shear loading of solder joints matrix of balls in SAC305. For the strain rate calculated in the previous section ( $1 \cdot 10^{-3}$  1/s), the maximum shear stress measured is between 35 and 40 MPa. This difference probably comes from the homogeneous stress state assumption which differs for the two different test benches. The solder joint height for Darveaux is 210  $\mu\text{m}$  compared to 180  $\mu\text{m}$  in our case and the pad diameter 280 compared to 250  $\mu\text{m}$  in our case. The number of solder joints for Darveaux (196) is also higher than in our case (36) which can have an influence on the stress homogeneity.

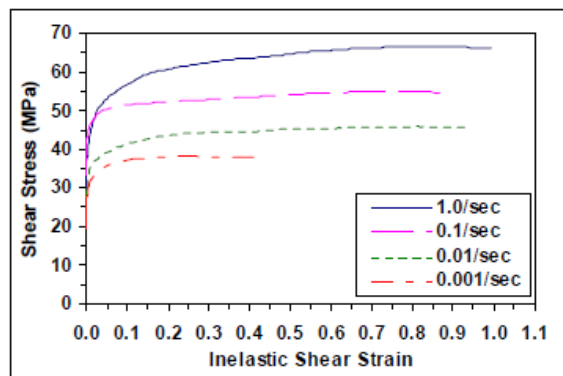
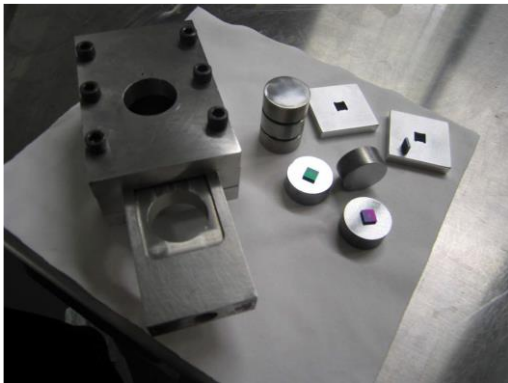


Figure 54: Monotonic shear test results of Darveaux for different strain rate [45]

### 3.c. Residual stress for test in temperature

Methodology for test in temperature has been introduced previously. Results from fatigue test at 50 °C will be detailed in following chapter 4. Temperature increase induces stress in the solder joints matrix of electronic packages due to the thermal expansion “difference” between the package and the

PCB as described in chapter 1. Residual stress can thus be developed during tests in temperature. The residual stress in the solder joints matrix of the WLP is evaluated in this section for an increase of  $\Delta T = 25$  °C from room temperature.

The considered package is mostly composed of silicon with a coefficient of thermal expansion  $CTE_{pack}$  of 2.5 ppm/K. PCB coefficient of thermal expansion  $CTE_{PCB}$  is estimated based on the datasheet of the used laminate material (13 ppm/K). The largest distance from the center to the corner of the package is  $d = \sqrt{2} * l = 2.1$  mm (with  $l$  being the half-length of the package). The maximum relative displacement  $\Delta d$  can be evaluated as formulated in Eq. II-9.

$$\Delta d = (CTE_{PCB} - CTE_{pack}) * d * \Delta T \quad Eq. II-9$$

Numerical estimation gives an approximate relative displacement of 0.55  $\mu\text{m}$ . The sample stiffness has been measured in the previous section for a shear loading (1.7 N/ $\mu\text{m}$ ). The corresponding force required to move the package is thus  $\Delta F = 0.55 * 1.7 = 0.9$  N. This force level is negligible compared to the force magnitude of fatigue tests (>25 N) described in the following chapters and is equivalent to an homogenous shear stress of 0.5 MPa.

## 4. Step-Stress Results

### 4.a. Step-stress test

A stair case loading test is performed in order to define the parameters of the fatigue test plan. This test is called step-stress. The step-stress consists of successive steps of 50 cycles with an increasing command displacement amplitudes. The cyclic displacements are set to include or not dwell times at low and high amplitude levels. The objective is to evaluate with these two types of loading the impact of dwell times on measured values of stress and plastic/creep deformations. The dwell time consist in 10 s with a constant command displacement (see Figure 55). The tests are performed with two command displacement rates. The high rate (20  $\mu\text{m/s}$ ) is used to accelerate the test in the non-loading step of the sample during the gap period (see Figure 55). The lower rate (5  $\mu\text{m/s}$ ) is used during the loading of the sample.

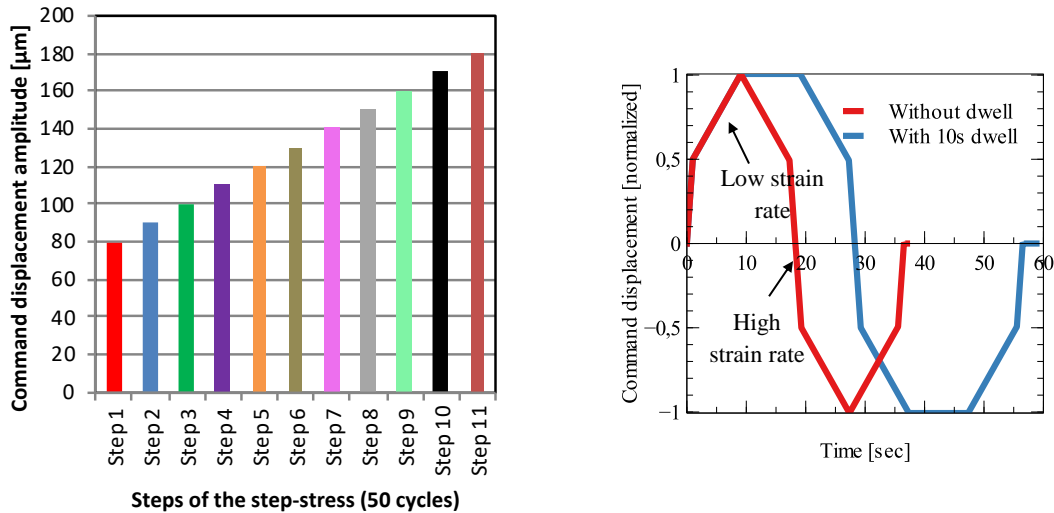


Figure 55: Command displacement loadings with and without dwell time

The failure of the sample is estimated with the monitoring of the electrical resistance of the package daisy-chain. A digital voltmeter is used with a sampling rate of 1/s. The failure criterion is described in IPC [1] and more details about this electrical failure criterion are given in following chapter 3. Tested samples are reported in Table 6.

Table 6: Step-stress configurations

Package	Alloy	Dwell time	Reference
WLP36 0.5mm	SAC305	0 s	S1
WLP36 0.5mm	SAC305	0 s	S2
WLP36 0.5mm	SAC305	10 s	S3
WLP36 0.5mm	SAC305	10 s	S4

#### 4.b. Step-Stress Results

Hysteresis curves coming from without and with dwell time (10 s) configurations are plotted in Figure 56.

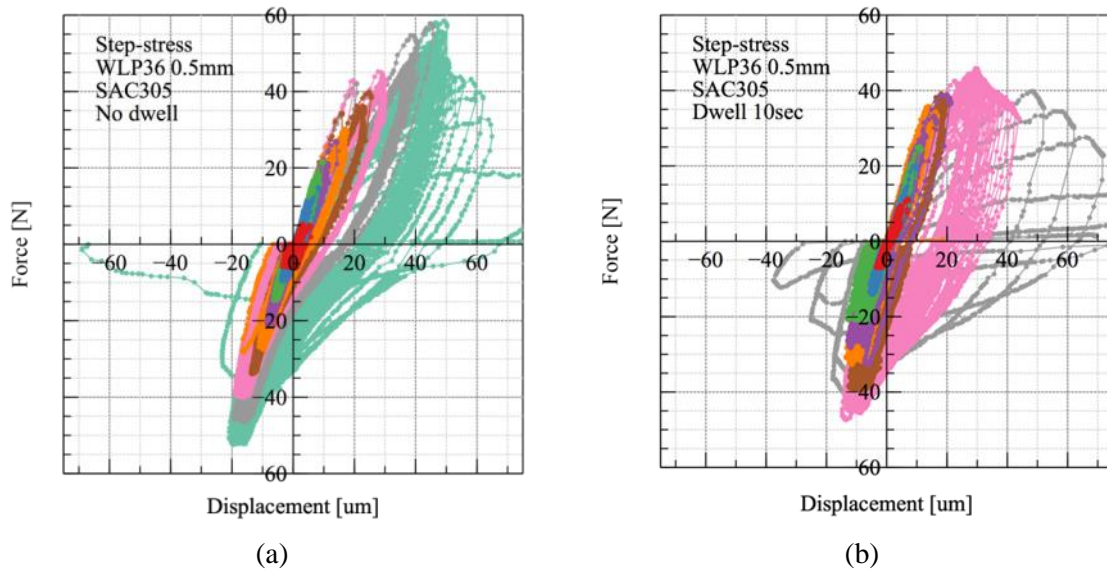


Figure 56: Hysteresis curves obtained during step-stress test (colors representing steps):  
 (a) without dwell time and (b) with 10 s dwell time

The post-processing method is used for the analysis of step-stress results. Mechanical parameters described in the previous sections are extracted for each loading cycle. These parameters are the force magnitude, the inelastic and plastic displacement, the force relaxation, the creep displacement and the hysteresis area.

Results of the post-processing method are reported in Figure 57. Each step is illustrated with a color. The force magnitude increases for each successive step due to the increase of command displacement. The force magnitude is constant during each the step. The force magnitude decreases after each cycle for the last step due to cracks in the solder joints matrix (fracture of the sample). Electrical and mechanical failure occur at the same step.

Plastic displacement increases also for each successive step: more and more inelastic strain are developed. As for the force magnitude, the plastic displacement is constant during each step excepted for the last one due to the sample stiffness decrease during the fracture.

Creep displacement, force relaxation and hysteresis area follow the same evolution. Creep measurements are more scattered than plastic ones. This larger scatter of creep displacements can explain by the lower values obtained for plastic displacements (from 0 to 30  $\mu\text{m}$ ) compared to creep ones (from 0 to 2  $\mu\text{m}$ ).

The sample tested with 10 s dwell time breaks before the sample loaded without dwell time. The number of cycles to failure is 448 without dwell time and 341 with dwell time. The fracture occurs at step number 9 without dwell time and 7 with dwell time which suggests a more important damage per cycle for the loading with dwell time.

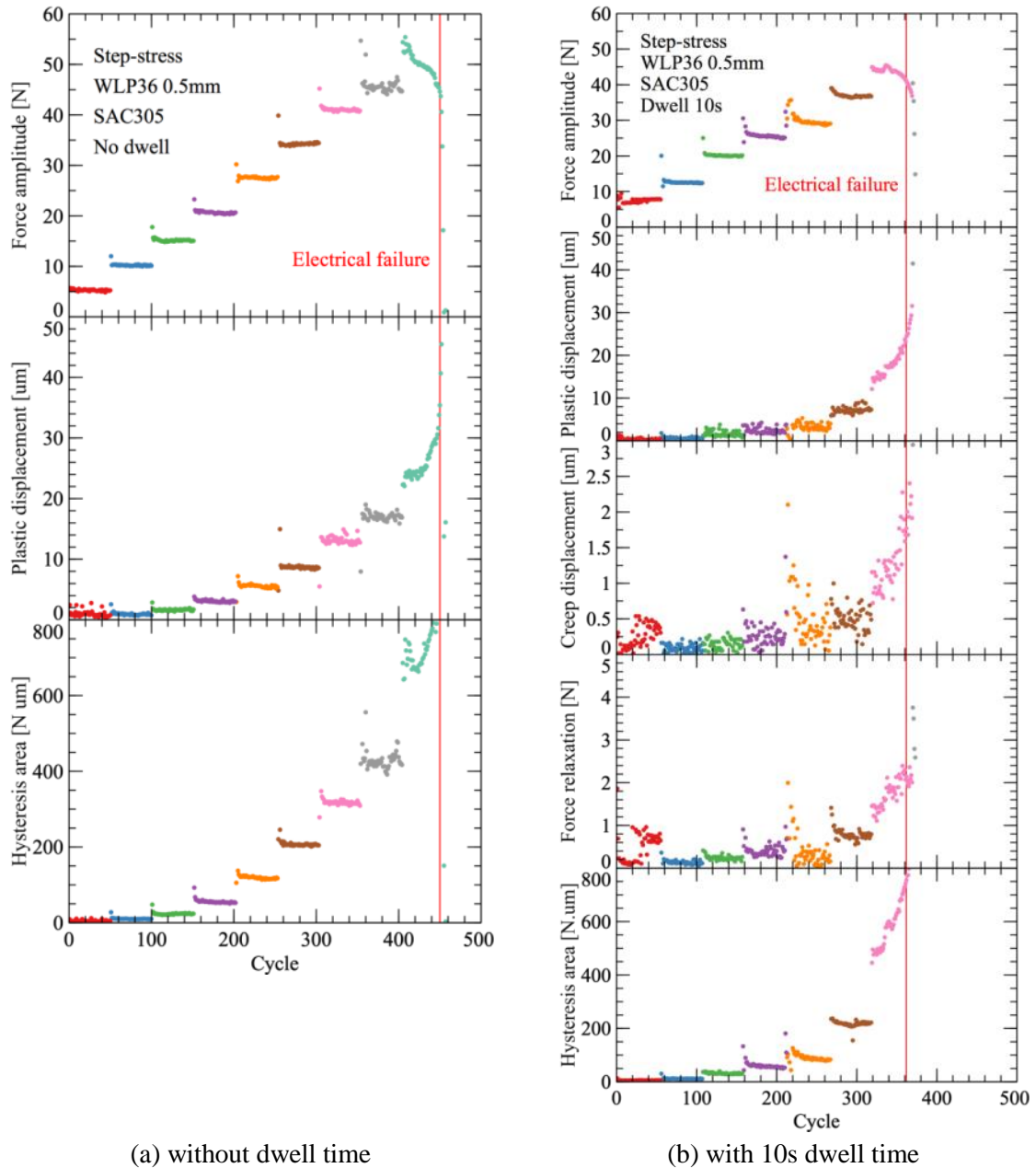


Figure 57: Evolution of the measured mechanical parameter for step-stress tests (colors representing steps): (a) without dwell time and (b) with 10 s dwell time

#### 4.c. Analysis of step-stress results

Measured mechanical parameters are converted in local stress and strain in the balls matrix. Displacement and force values are converted in strain and stress in the solder joints considering an homogeneous stress state as for monotonic tests. Displacement values are divided by the height of solder balls (Eq. II-7) in order to obtain the shear strain. Stress measurements are obtained with the ratio between the force values and the surface of the solder joints matrix (see Eq. II-6). The dissipated energy  $E_d$  is calculated with the area of the hysteresis previously computed with the post-processing method and the solder balls matrix volume  $V_s$  as formulated in Eq. II-10.

$$E_d = \int_{Cycle} \tau_s \cdot \gamma_s dt = \int_{Cycle} \frac{F}{S_s} \cdot \frac{u_l}{h_s} dt = \frac{A}{S_s \cdot h_s} = \frac{A}{V_s} \quad Eq. II-10$$

The results of the different step-stress are summarized in Figure 58. Evolutions of mean values of mechanical parameters obtained for each step are plotted as a function stress level.

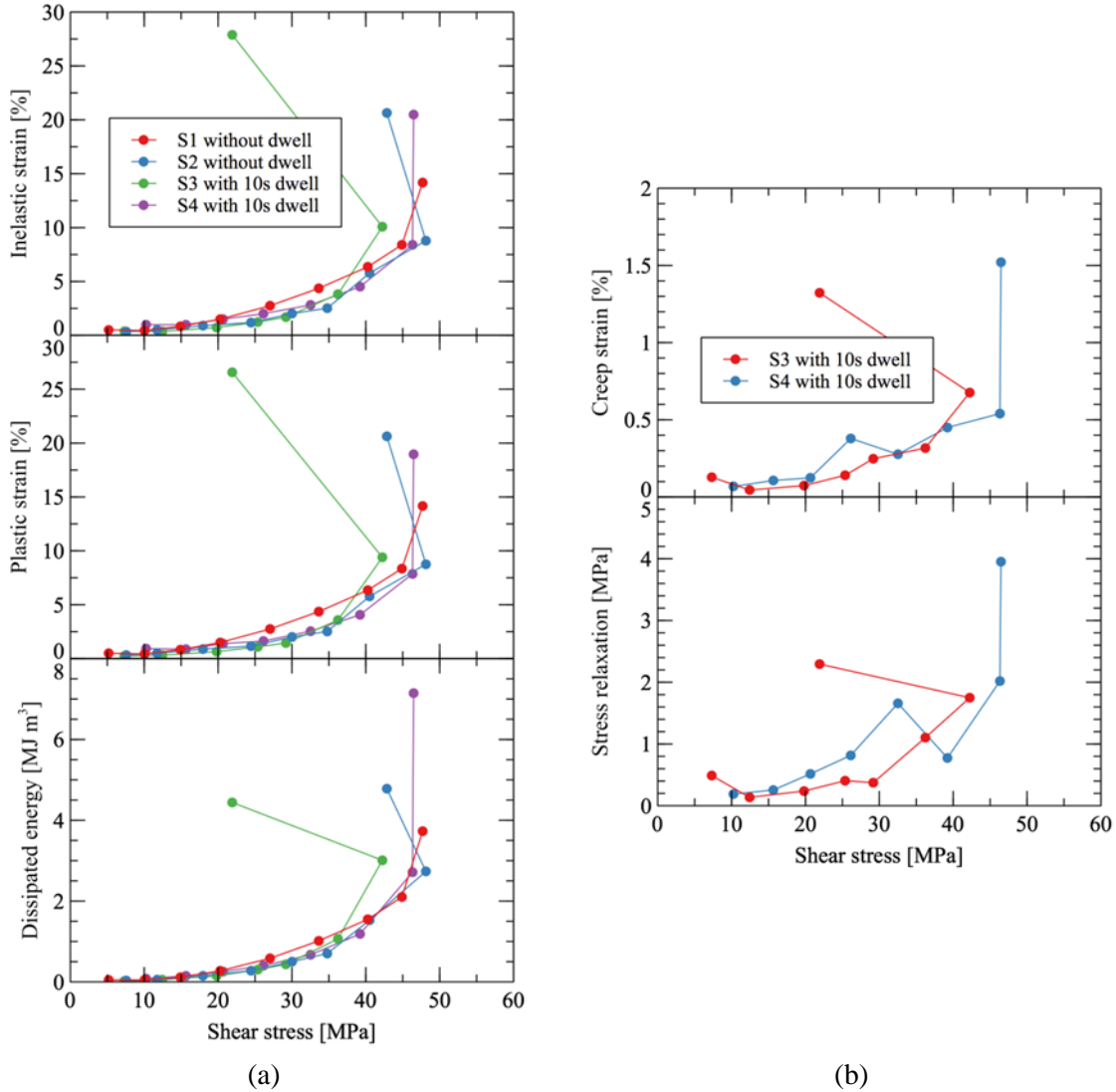


Figure 58: Evolution of the measured mechanical parameters as a function of stress level: (a) inelastic and plastic strains and dissipated energy and (b) creep strain and stress relaxation

The results show that all parameters are increasing with the stress level. The inelastic strain associates the plastic strain developed during the loading phase and the creep strain developed during the dwell time. Evolutions of inelastic and plastic strains are similar without and with dwell time. The creep strain is significantly lower than the plastic strain which explains this similarity. Addition of creep strain to the total inelastic strain is not significant. This negligible effect of the dwell time is also noticeable. Negligible inelastic strain are developed per cycle before 10 MPa. This yield stress value is close to the value measured during monotonic tests.

Last points of each sample are the points measured for the steps which have conducted to the fracture. These points must be excluded from the analysis because: (i) an evolution of these

parameters have been observed in the previous section and an average value is not relevant and (ii) because cracks reduce the surface of solder joints which invalidate stress calculation.

## 5. Conclusions

The innovative shear test bench developed has been described in this chapter. The shear test bench and the sample are detailed. Schematic representations of the shear test bench with and without the gap are proposed to illustrate the sensor stiffness equation. This equation gives the relation between the command and the local displacements. Post-processing methods to evaluate the hysteresis response of the sample for the recorded force and local displacement are detailed. Details of the calculation of the coefficient of conversion pixel to micrometer of the local displacement are given. Accuracies of force (0.1 N) and local displacement (0.1  $\mu\text{m}$ ) have been estimated.

Preliminary monotonic shear tests have been performed to measure the mechanical response of the WLP sample. Sample stiffness and force limit have been measured based on four samples with a low monotonic shear loading. Force and local displacement have been converted into stress and strain in the solder joint considering an homogeneous stress state. The sensor stiffness equation has been used to convert the command displacement rate into the solder joint strain rate. It is estimated that the strain rate is  $1 \cdot 10^{-3}$  1/s.

Step-stress tests have been performed in order to validate the feasibility of cyclic loading. The mechanical response of the WLP sample has been evaluated for an increasing force levels. The results show that the shear test allows to measure values of displacement and force. Different values, including inelastic, plastic, and viscous displacement, force amplitude, force relaxation and area of hysteresis have been estimated. The test bench can perform cyclic loads including or not dwell times at extremes force magnitudes.

Estimated values of creep strains are significantly lower than plastic ones. Inelastic strain evolutions as a function of stress are similar without and with dwell time. The number of cycles to failure is reduced with dwell time which suggests an additional damage per cycle.

Damages from each step are cumulated during step-stress. It is difficult to evaluate this cumulative damage. Perspectives of this chapter are the results of the fatigue tests plan which will be described in the chapter 4. Fatigue tests will be performed with constant force level in order to evaluate constant damage indicators.

## Chapter III. Failure Definition

*This chapter describes methods used for the analysis of fatigue tests. These methods are defined based on fatigue tests results obtained with the electrical resistance monitoring, the post-processing analysis to extract mechanical parameters per cycle and cross-sections observations. Mechanism of failure, damage variables and criteria are discussed.*

*Electrical resistance of solder balls matrix is monitored during fatigue tests with the daisy-chain of the package. An increase of the electrical resistance indicates cracks development in the solder joints. Two failure criteria are compared based on the monitoring of (i) the force magnitude and (ii) the electrical resistance. Monitoring of the electrical resistance only captures the failure of the first solder joint of the matrix during fatigue tests.*

*The considered failure mechanism is the mechanical fracture of the first solder joint that results from an accumulative damage from cyclic shear loads. The failure criterion is based on the electrical resistance monitoring of the package daisy-chain. An increase of the electrical resistance indicates that at least one solder joint is completely fractured. The failure mechanism is verified with cross-sections of fractured samples after fatigue tests without and with 10 s dwell time. Initial inspections are also performed to analyze the sample structure and to measure the height of solder joints.*

*Post-processing analysis gives mechanical parameters per cycle for each fatigue test as the plastic displacement and the force magnitude. Average value of these cyclic values is required to define a fatigue law. Thus, the evolution during the test of these mechanical parameters is analyzed. Stabilized parameters are obtained for cycles before half of the electrical failure. This limit is therefore used to define the average method. Average values of mechanical parameters are calculated with the cycles before half of electrical failure.*

*Solder joint height and surface are estimated in order to convert measured local displacements into strains and force into stress in the solder joints. These values will be used in the following chapter 4 for the analysis of the mechanical response of the sample.*



# 1. Mechanical and electrical failures

Based on recorded parameters, the failure criterion indicates the cycle of the sample fracture that is defined by the occurrence of a failure mechanism. In our case, the sample fracture occurs at the complete fracture of the first solder joint of the matrix. Failure criterion usually uses the evolutions of mechanical parameters per cycle in the case of fatigue tests based on bulk samples. Due to the specific used sample of our test bench, the monitoring of the electrical resistance of the package daisy-chain is required to capture the fracture of the first solder joint. The specificities of our sample and the failure criterion are described in this section.

## 1.a. Mechanical failure

Examples of cylindrical and rectangular specimens used for fatigue tests are depicted in Figure 59 [67]. Failure criteria are usually based on the appearance, the presence or the aggravation of a recorded phenomenon. The selection of the criterion must take into account the behavior of the material during the test and the evolution of mechanical parameters such as the maximum stress per cycle. For example if the strain per cycle is controlled, the failure can be defined by the percent of maximum stress decrease due to the accumulated damage in the sample. Maximum stress per cycle decrease results from macro-cracks propagation in the sample which reduces the loaded surface.

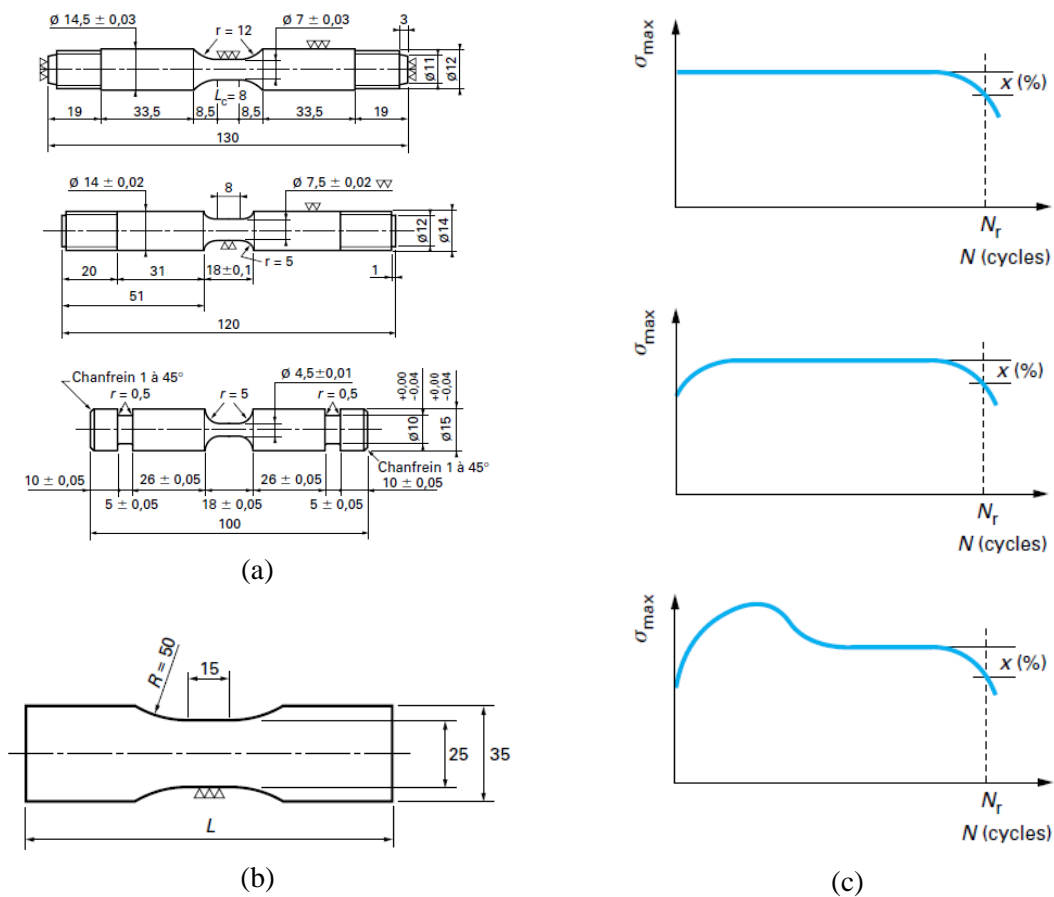


Figure 59: (a) Cylindrical and (b) rectangular specimens for low cycle fatigue tests and (c) definition of failure criteria based on the evolution of the maximum stress per cycle [67]

As no theoretical values of decrease/increase from the initial value of the recorded mechanical parameters exist, the value is fixed by the author. For example, evolutions of maximum stress per cycle during fatigue tests and definition of failure criteria are schematically represented in Figure 59. In this particular case, 25 percent reduction of the maximum stress is suggested for strain controlled fatigue tests [67].

In the electronic industry, mechanical monotonic tests such as pull test, ball shear, die shear or shear test of passive packages are used to control the assembly process [68]. The manufacturing quality is evaluated with the force to failure. Failure mechanism is verified after test through visual inspection. Mechanical failure criteria have also been used in the case of cyclic fatigue shear tests of assembled packages. These criteria are based on the variation of one of the monitored mechanical parameters. Force magnitude decreases of: 25 % [69] or 50 % [69] [70] from the initial value have been used. Displacement increase has also been used (by a factor of 2 in [53]) when the fatigue test is controlled in force.

### 1.b. Electrical failure

Solder joint failure of an electronic package is defined by the loss of electrical continuity. Electrical resistance monitoring of the package daisy-chain is a method commonly used in the electronic industry to detect solder joints failure. Electronic packages used are dummy packages which means that the package is not functional and substrate is manufactured to connect in series the solder joints matrix of the package. The daisy-chain of the samples used in our shear test bench is depicted in Figure 60. Package daisy-chain have been revealed with an X-Ray inspection.

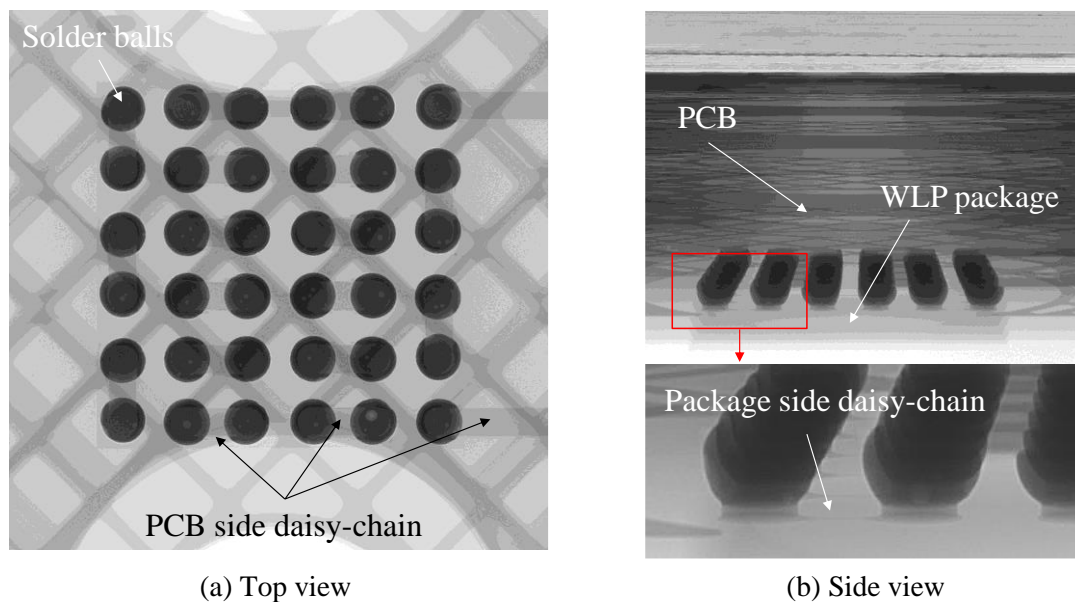


Figure 60: Package daisy-chain of the sample used in our shear test bench revealed with X-Ray inspections: (a) top view and (b) side view

Two possible methods of electrical resistance monitoring are described in IPC Standard [1]. The first method uses a high sampling rate monitoring (thousands of samplings per second) and the second one a slow sampling rate (one per second). The first method considers the failure when 10 events higher than 1000 ohms longer than one  $\mu$ second (transitional events) are recorded. The second method

considers the failure after 5 measurements of the daisy-chain resistance higher than 20 percent from the initial value.

Correlation between electrical resistance monitoring and fracture of solder joints has been studied with torsion tests [63]. The friction of the two surfaces of the fractured solder joint induces perturbations of the electrical resistance monitoring as contact forces applied by non-fractured solder joints maintain the contact between the two fractured surfaces. The fracture of the solder joints has been verified with cross section observations after transitional events in torsion. Before these events, fluctuations of the resistance around 10 ohms have been observed with the slow sampling method. However in practice, these fluctuations are difficult to identify because the nominal value of the resistance is in the same order of magnitude.

Electrical resistance monitoring is commonly used in the electronic industry as failure criterion for Accelerated Thermal Cycling tests. Continuous electrical resistance monitoring of the package daisy-chain has also been used in the case of fatigue shear tests of assembled package [54]. This method has been used to detect solder joints failure due to the absence of force magnitude monitoring in this study for strain controlled fatigue tests.

### 1.c. Specific configuration in this work

The test bench developed in this work combines both daisy-chain resistance and mechanical response recordings. Electrical resistance of the daisy-chain is monitored with a sampling rate of 1 measurement per second using a digital voltmeter in addition to the cyclic force and local displacement (see Figure 61).

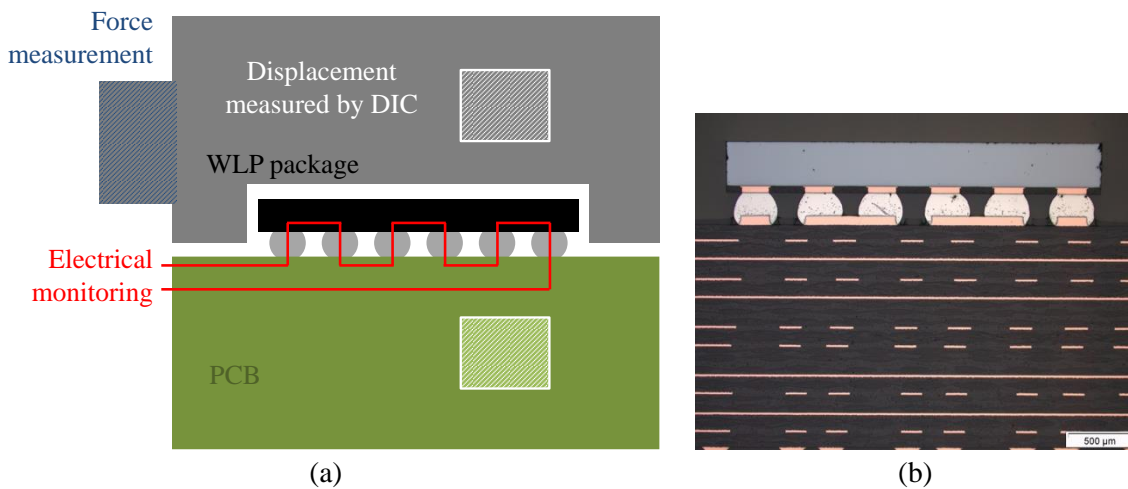


Figure 61: Electrical resistance and force and local displacement recordings: (a) schematic representation and (b) assembled WLP cross-section

Mechanical and electrical criteria based on respectively mechanical and electrical resistance recordings are compared for fatigue tests performed with our shear test bench. The mechanical criterion is based on the force magnitude. Number of cycles to mechanical failure ( $N_{f,mech}$ ) is reached when the force magnitude is divided by two. Number of cycles at electrical failure ( $N_{f,elec}$ ) is evaluated with IPC criterion. The failure is reached after 5 measurements of the resistance higher than 20 percent from the initial value. Intermediate cycles are also introduced for discussion: number of cycles at half of the electrical ( $N_{f,elec/2}$ ) and mechanical ( $N_{f,mech/2}$ ) failures.

## 2. Criterion and mechanism of failure

The shear test bench uses coupled measurement of mechanical and electrical parameters. The results coming from different fatigue tests are discussed in this part in order to validate the failure definition. Results and method have been published in [71]. Evolution of force and electrical monitoring are first analyzed during a fatigue test at 30 N. Different phases are observed. Cross-sections are then performed for two samples to analyze the failure mechanism.

### 2.a. Force and electrical resistance monitoring

Figure 62 presents the results of a fatigue test at 30 N. Evolutions of force magnitude and electrical resistance monitoring are compared. Electrical and mechanical criteria are indicated. Two different phases are identified. The stabilized first phase (1) is followed by a disruption phase in the electrical resistance monitoring (2). The electrical fluctuations before the mechanical failure can be explained by the sliding of the two surfaces of the failed solder joints as for torsion tests [63]. Non-fractured solder joints of the matrix hold the contact between these surfaces maintaining partially the electrical contact in the failed solder joint. This hypothesis is verified by the force magnitude: no real change is detected on the force magnitude at electrical failure which indicates that the solder joints matrix contains non-failed elements.

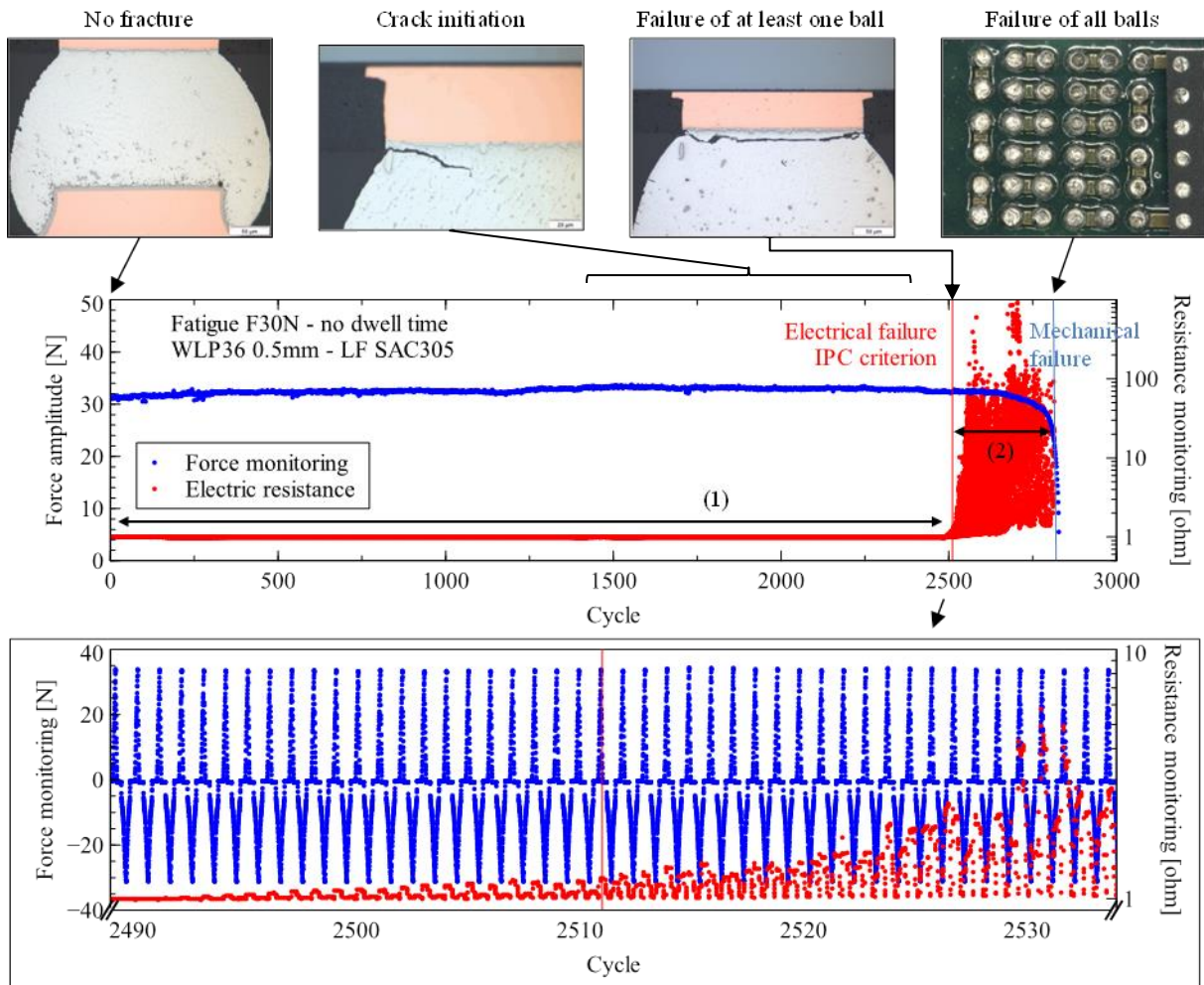
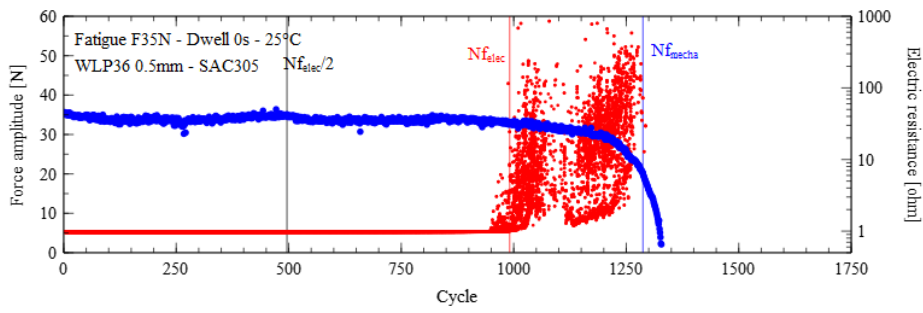
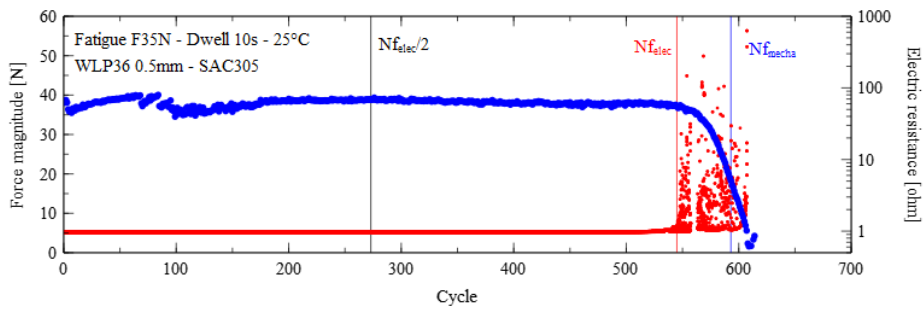


Figure 62: Evolution of force and electrical resistance for a fatigue test at 30 N

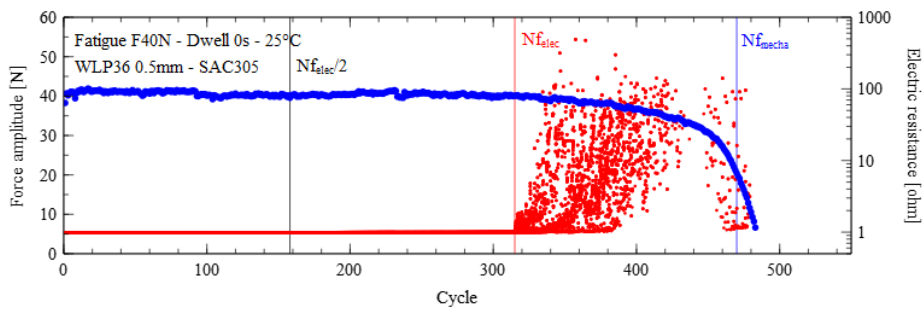
Solder materials are highly viscous even at room temperature due to the low melting temperature required for the assembly. The viscosity of the material induces low propagation rate of macro cracks [13] [72]. During fatigue tests with bulk samples, several cycles are performed with low variation of the mechanical parameters before the total fracture of the sample. In this work, the difficulty to identify the failure is even larger because the different solder joints of the package can fail at different times, inducing a partial failure of the matrix. This partial failure is not detected by mechanical parameters variations as demonstrated by the presence of the second phase (2). In fact, the failure of one of the 36 balls of the matrix will reduce only the stress by a factor of 1/36, which is lower than 3 percent. Therefore, electrical before mechanical failure has been observed for all fatigue tests (examples are depicted in Figure 63).



(a) Fatigue test at 35 N without dwell time



(b) Fatigue test at 35 N with 10 s dwell time



(c) Fatigue test at 40 N without dwell time

Figure 63: Evolution of force and electrical resistance for different fatigue tests

Influence of force magnitude and number of cycles to electrical failure on the force magnitude change at electrical failure is analyzed. Experimental results are plotted in Figure 64. One can observe that: (i) increase of force magnitude at electrical failure decreases the force magnitude change at  $N_{f,elec}$  and (ii) large force magnitude variations are only measured for low numbers of cycles to electrical failure. In fact, high values of force magnitude change at electrical failure are obtained only for fatigue tests with low number of cycles to failure and low force magnitude at electrical failure. Change of force magnitude at electrical failure is representative of the surface of solder joints still unfractured when the first solder joint is completely fractured. Weakness of one solder joint of the matrix is more critical for fatigue tests with high number of cycles to failure as indicated by the low force magnitude change at electrical failure.



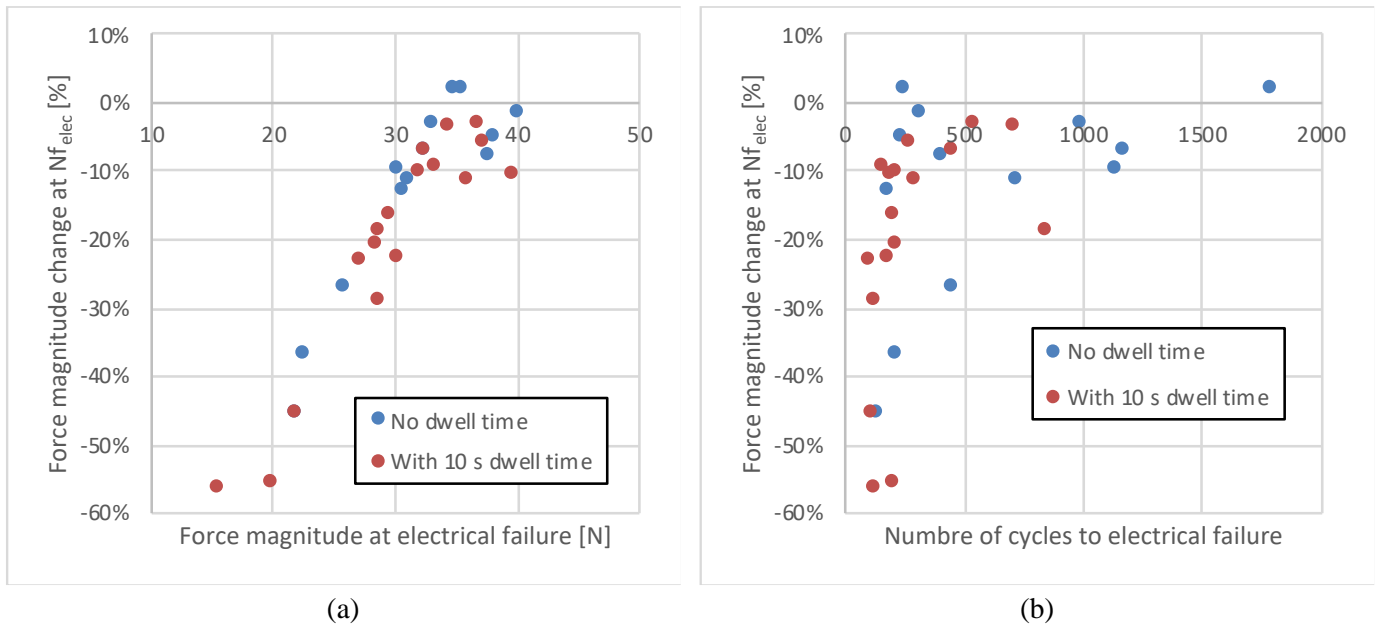


Figure 64: Force magnitude change at electrical failure as a function of (a) force magnitude at electrical failure and (b) number of cycles to electrical failure

Experimental results indicate that the force magnitude change at electrical failure is not identical for all fatigue tests. It is not possible to define the failure criterion based on the evolution of the force magnitude. Therefore, the monitoring of the electrical resistance is necessary to capture the failure of the first solder balls of the matrix.

## 2.b. Initial inspection

Samples used for fatigue tests have been inspected with optical images. SAC305 structure of solder joints is observed after assembly with a cross-section of the package. One of the first row of the solder joints matrix from package side is selected for the inspection. Images obtained with an optical microscope are depicted in Figure 65. The 6 solder joints of the row are visible. Copper pads of the PCB side are also exposed. Solder joints are fixed to the silicon die with copper pads in the package side.

The sample is prepared by a polishing with different sand paper grades and a chemical treatment. The sample preparation steps are detailed in Table 7. The sample preparation and optical images have been performed by the LATPI Laboratory (Thales Research & Technology France in Palaiseau).

Table 7: Steps used for the preparation of the sample before optical imaging.

Step	Name	Description
1	Draft	Sand paper (SiC grains) + water. Grain size: 500, 1200, 2000 and 4000
2	½ finish	Felt + abrasive paste 3 µm (solution with diamond grains) + lubricant (alcohol)
3	Finish	Felt + abrasive paste ¼ µm (solution with diamond grains) + lubricant (alcohol)
4	Super-finish	Silice colloidal solution (OPS) slightly acidic to remove chemically last scratches and superficial hardening and to reveal the structure

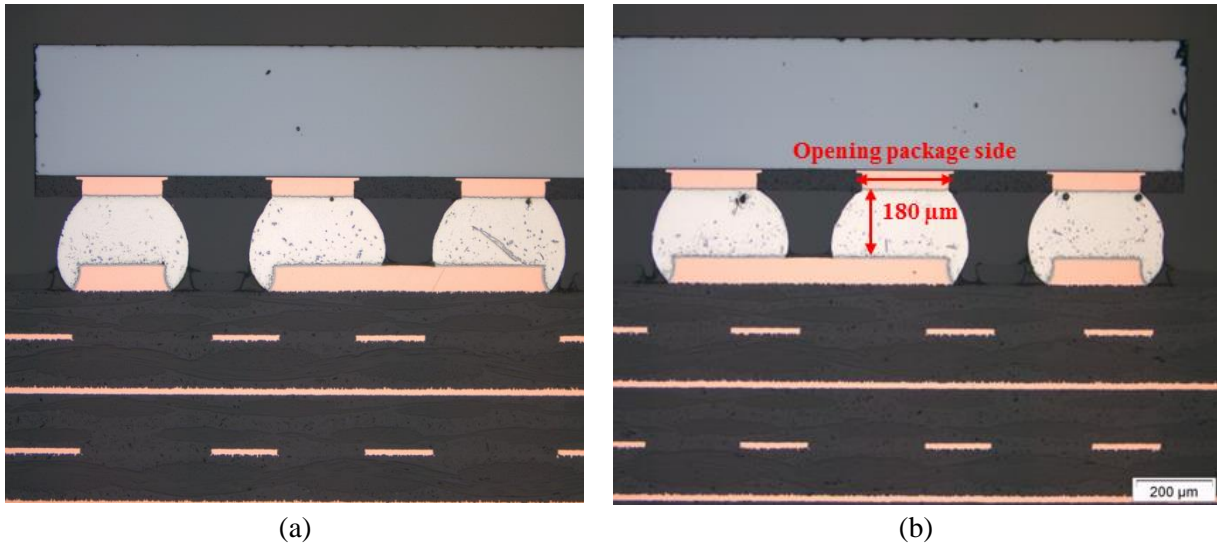


Figure 65: Cross section of the SAC305 sample observed before testing: (a) balls 1,2,3 and (b) balls 4, 5 and 6

Solder joint height is measured with these optical images from the cross-section (180  $\mu\text{m}$ ). The measure is based on the solder joints heights of the 6 balls of the cross-section (see Table 8). The solder joint height cannot be predicted accurately without cross section because it depends on several parameters including the package weight, the quantity of solder paste used, the copper pad height, etc. Accuracy of measurement (2.5  $\mu\text{m}$ ) is higher than scatter of measured heights. 2 % accuracy must be considered for the measure of solder joint height.

Solder joint diameter cannot be measured with the cross section because the measured opening package side depends on the cross section location. The cross section has probably not being performed exactly in the center of the solder joints. The most precise measurement of solder joints diameter is given by the datasheet of the package. The opening in the package side given in the datasheet is 250  $\mu\text{m}$ . 10 % accuracy from manufacturing defect can be considered. The total surface of solder joints is estimated considering 36 circular surfaces. 20 % accuracy must be considered for the measure of surface of solder joints (1.77  $\text{mm}^2$ ).

Table 8: Measurement of solder joints height

Solder joint height [ $\mu\text{m}$ ]					
1	2	3	4	5	6
179.3	178.8	181.1	181.8	180.8	178.8

Accuracy of measurement = 2.5  $\mu\text{m}$   
 Mean = 180.1  $\mu\text{m}$   
 Standard deviation = 1.3  $\mu\text{m}$

### 2.c. Failure mechanism during fatigue tests

Fatigue tests are performed until the electrical failure and stopped before the mechanical failure in order to evaluate the failure mechanism. These tests are performed at room temperature and at 35 N of force magnitude. One test is performed without dwell time and the other with a 10 s dwell time. Evolution of force magnitude per cycle and electrical resistance monitoring for the test without dwell time are plotted in Figure 66.



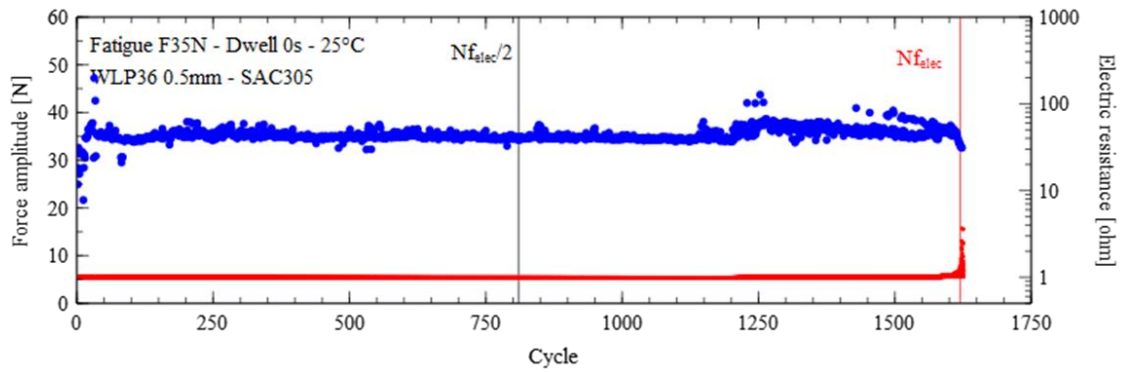


Figure 66: Evolution of force magnitude and electrical resistance monitoring for the fatigue test at 35 N without dwell time

A temperature mapping with high speed transient is performed after the fatigue test. The equipment used is an infrared camera. The daisy-chain is submitted to a current of 10 mA and a bias of 100 mV (resulting in 1 mW of dissipated power). This intensity is significantly low to ensure the non-damage of the solder joints during the measurement. The fracture reduces the conductivity of the failed solder ball. The resistance of this solder ball is increased inducing a local increase in the temperature. Cycles of alternative periods of ON and OFF current are performed in order to obtain cyclic temperature variations in the failed solder joints. Temperature variations are captured by the camera subtracting the temperature during ON and OFF periods. 100 cycles are averaged to obtain the final image (see Figure 67). Red color indicates the hottest temperatures. Figure 67 (b) shows the superposition of the initial image and the warmest temperature from the temperature mapping.

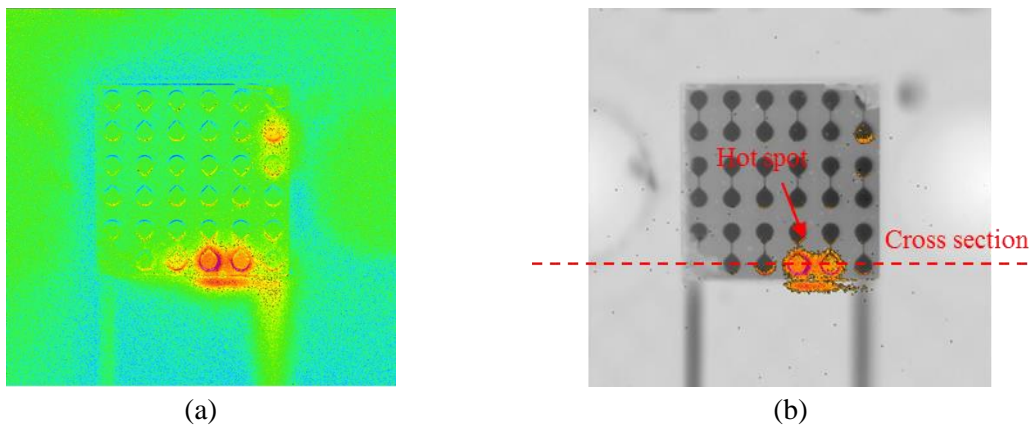


Figure 67: Temperature mapping with high speed transient obtained for the sample submitted to a fatigue test at 35 N without dwell time: (a) temperature mapping and (b) superposition of temperature mapping with initial image (red color indicates the warmest temperature)

A cross-section is performed in the most dissipating area (see Figure 68). The fractured solder joints of the cross-section confirm the failure mechanism even if the mechanical criterion is not reached: at least one of the solder joints of the matrix is completely fractured at the electrical failure.

The fracture of the WLP corner is responsible for the difficulty to see the solder balls at two corners in Figure 67 (b). Two package pads (in black) are not perfectly visible. This fracture is confirmed with the cross section and is visible in Figure 68. The temperature mapping shows that the fracture is located in the corner of the package only. Fatigue test results have not been significantly affected by

the fracture because it is localized only in the corners without significant effect in the global response. Fractures of solder joints are all located in the upper part of the solder joints. Solder joints are weaker in this area because (i) of the stress concentration due to the geometry of the assembly and (ii) the solder joint diameter is larger in PCB side than in the package.

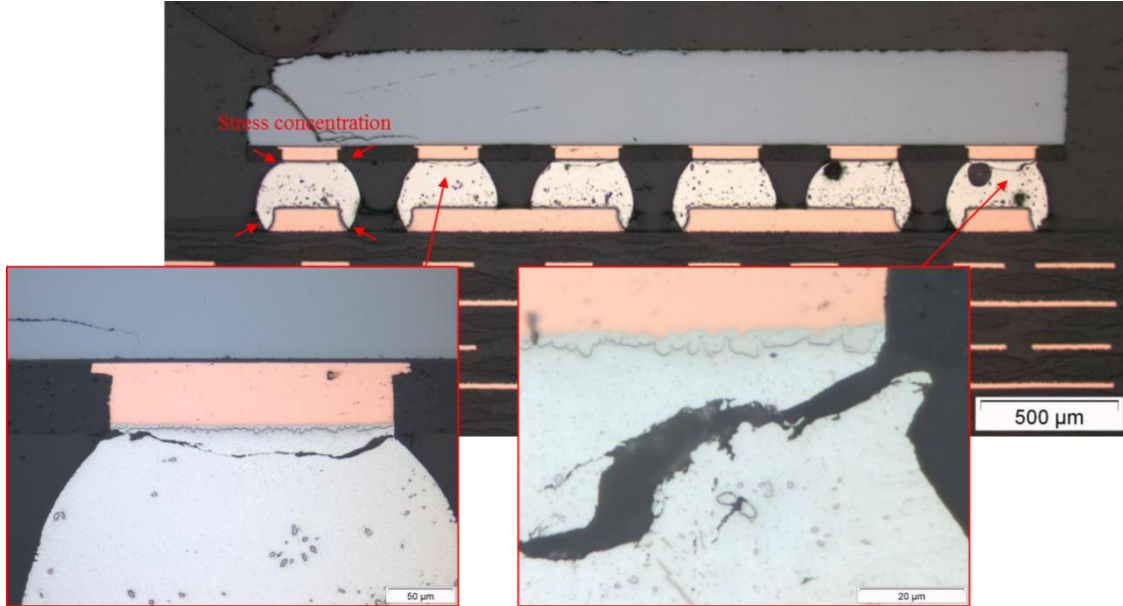


Figure 68: Optical images obtained with the cross-section of sample submitted to the fatigue test at 35 N without dwell time after electrical failure and before mechanical failure

The same analysis is performed with a fatigue with 10 s of dwell time. Evolution of force magnitude and electrical resistance monitoring are plotted in Figure 69. Electrical failure is reached before significant change in the force magnitude. The test is stopped before mechanical failure.

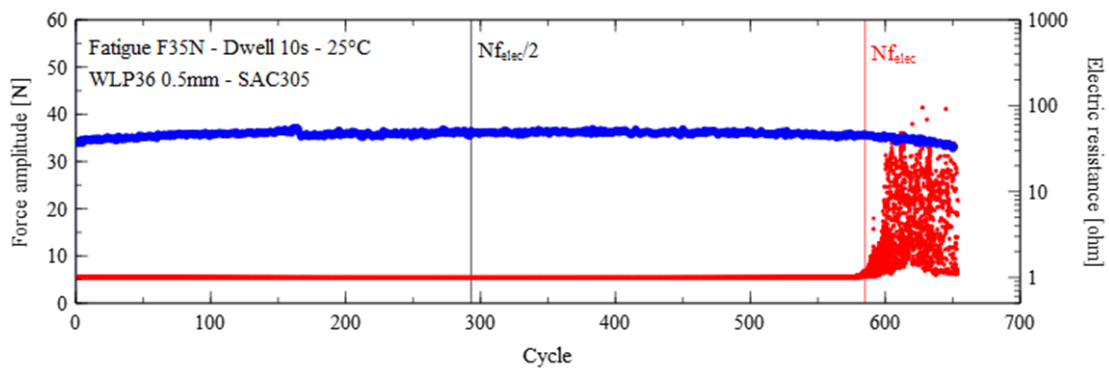
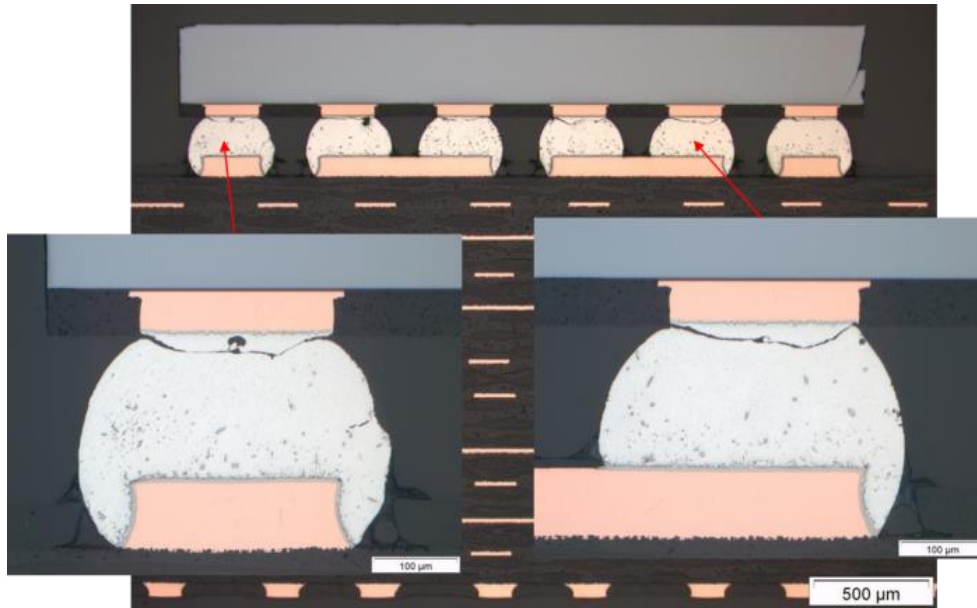


Figure 69: Evolution of force magnitude and electrical resistance monitoring for the fatigue test at 35 N with 10 s of dwell time

The same temperature mapping is performed for this sample in order to detect the location of fractured solder joints. As for the other sample, a cross section is performed in the direction of the shear loading and with the most dissipating solder joints. Optical images from this cross-section are depicted in Figure 70. Same conclusions are done with this sample: (i) several completely fractured solder joints are observed and (ii) fractures are located in the upper part of solder joints.



*Figure 70: Optical images obtained with the cross-section of sample submitted to the fatigue test at 35 N with 10 s dwell time after electrical failure and before mechanical failure*

Optical images from samples cross-sections submitted to loading without and with dwell time show that the matrix of solder joints contains several fractured solder joints after electrical failure. Several solder joints are completely fractured after electrical failure and before mechanical failure. Cracks are located inside the solder balls in the upper part of the solder joints. Importance of electrical resistance monitoring to detect solder joints failure is demonstrated because once again the mechanical response is not affected, even if cross-section images show that more than one solder joints are completely fractured. Electrical resistance monitoring contributes to the early identification of fractured solder joints.

#### 2.d. Homogeneity of the loading

Homogeneity of the shear force applied to the package must be verified. The total force applied to the package is measured by the force sensor and controlled by the shear test bench but the induced force applied to each individual solder ball of the matrix cannot be measured. The shear test bench and the loading of the package must be sufficiently precise to applied the same load to each solder ball of the matrix.

Crack initiations inside solder joints have been observed during one step-stress test with optical images of two cross-sections. The considered step-stress test is composed of four loading steps. 200 cycles have been performed for each step. Consecutive steps are performed with an increasing command displacement magnitude (see chapter 2 for additional information on step-stress tests). The last step has been stopped after 100 cycles (before electrical and mechanical failures).

Cross-sections have been performed in the peripheral and middle axis of the sample as shown in Figure 71. Solder balls of these two axis are observed in order to verify the failure mechanism at different locations of the matrix. Crack initiations located at the corners of the solder joints of all solder balls of both axis are observed. This homogeneous distribution of crack initiations indicates that the shear force loading is correctly distributed on the different solder balls of the package. Crack initiation is the result of the cumulative damage from cyclic loadings. Although the shape of solder balls concentrates stress in the upper corners which shows that the stress is not homogeneously

distributed inside each joint, the distribution homogeneity of the force applied to the package by the test bench is verified.

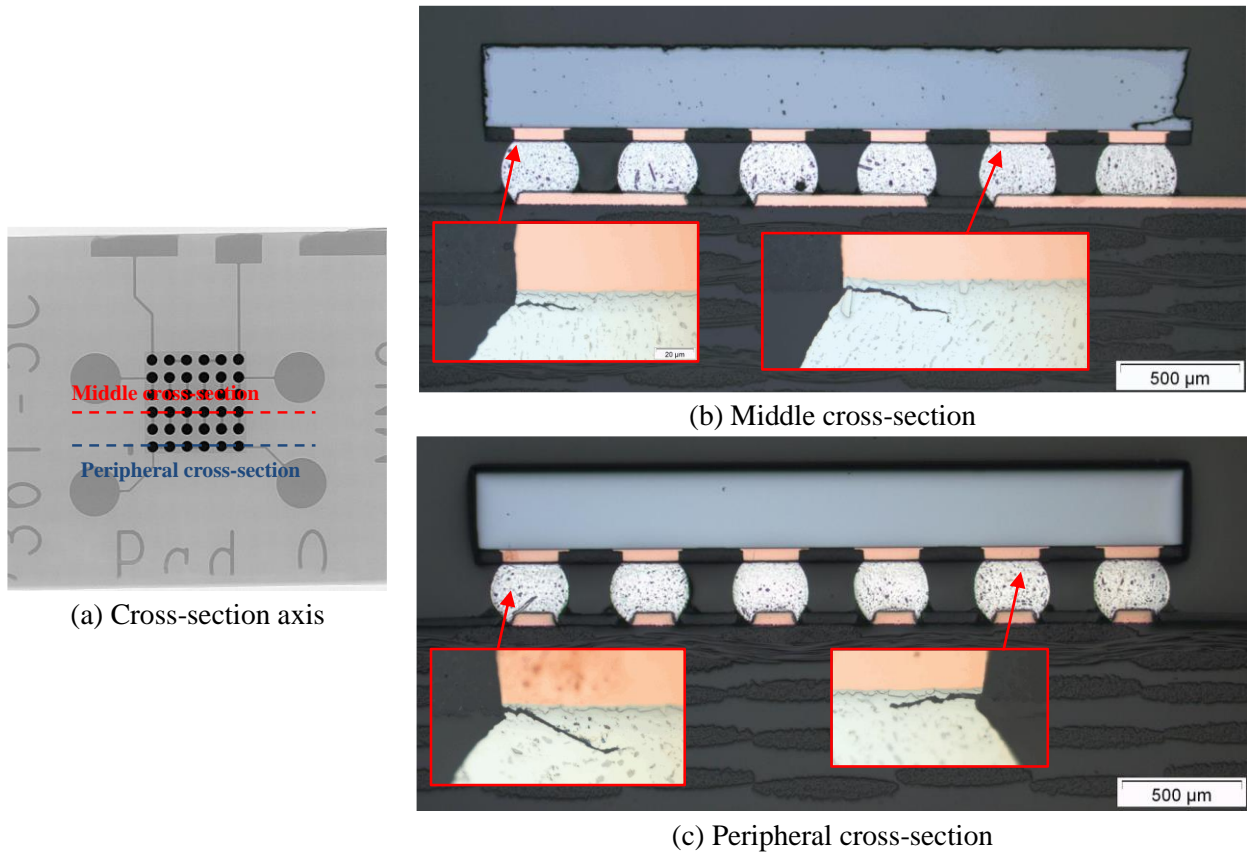


Figure 71: (a) Cross-sections performed after cyclic fatigue test before total solder ball fracture: crack initiations are visible on each solder ball of (b) middle and (c) peripheral axis

### 3. Mechanical parameters extraction

Contribution of the electrical resistance monitoring to the early identification of fractured solder joints has been demonstrated in the previous part. Completely fractured solder joints have been observed after electrical failure. Force applied and local displacement recordings are post-processed in order to obtain the cyclic mechanical response during fatigue test. Mechanical parameters are extracted from the mechanical response for each cycle (parameters signification is reminded in the first section of this part). Average values of these parameters for each fatigue test are required in order to compare the results of the different fatigue tests. Evolutions of plastic and creep mechanical parameters are described in this part. The method used to extract average values of parameters in the period of stabilized response is detailed.

#### 3.a. Methodology

The hysteresis response of the sample is obtained with the post-processing method detailed in chapter 2 from measurements of force and local displacement. Mechanical parameters extracted from the hysteresis response are reminded in Figure 72. Force magnitude, inelastic and plastic displacements and hysteresis area values for each cycle are recorded for all fatigue tests. Creep displacement and force relaxation are extracted during maintain phases for fatigue test that include dwell times.

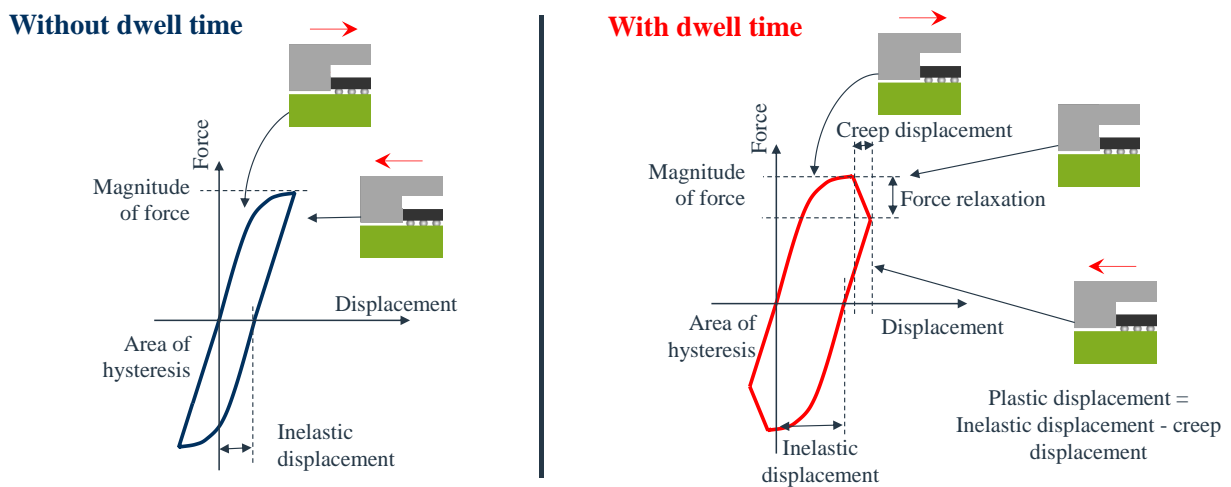


Figure 72: Mechanical parameters extracted from the hysteresis response of the sample for each cycle of fatigue tests that include or not dwell time

#### 3.b. Mechanical parameters for fatigue tests without dwell time

Recordings of force and local displacement of a fatigue tests at 35 N of force magnitude without dwell time at room temperature are post-processed in order to obtain the cyclic hysteresis response of the sample during the test. Mechanical parameters previously introduced are extracted for each cycle. Figure 73 shows the evolutions of these parameters during this fatigue test and the corresponding hysteresis responses for specific cycles ( $1^{\text{st}}$  cycle,  $N_{f,elec}/2$ ,  $N_{f,mech}$  and  $N_{f,elec}$ ). Results show that extracted parameters are not constant during the test. Average values of these parameters from recorded values during all the test will be not significantly representative the stabilized response.



Fatigue shear tests with typical BGA lead free balls have been performed by Qadaimeh *et al.* [73]. Similar evolutions of stiffness and hysteresis area have been obtained. The stiffness shows an initial increase, reflecting strain hardening, and is followed a steady-state period with a constant value during the cyclic saturation stage. Strain hardening, usually occurring because of dislocation and movement and generation, is the process of making solder harder. The stiffness drops when cracks start growing due to the reduction of the loaded sample surface induced by the fracture. It is thus consistent to observe a stiffness drop (see Figure 73 (b)) after electrical failure because at least one solder joint is completely fractured as described in the previous part.

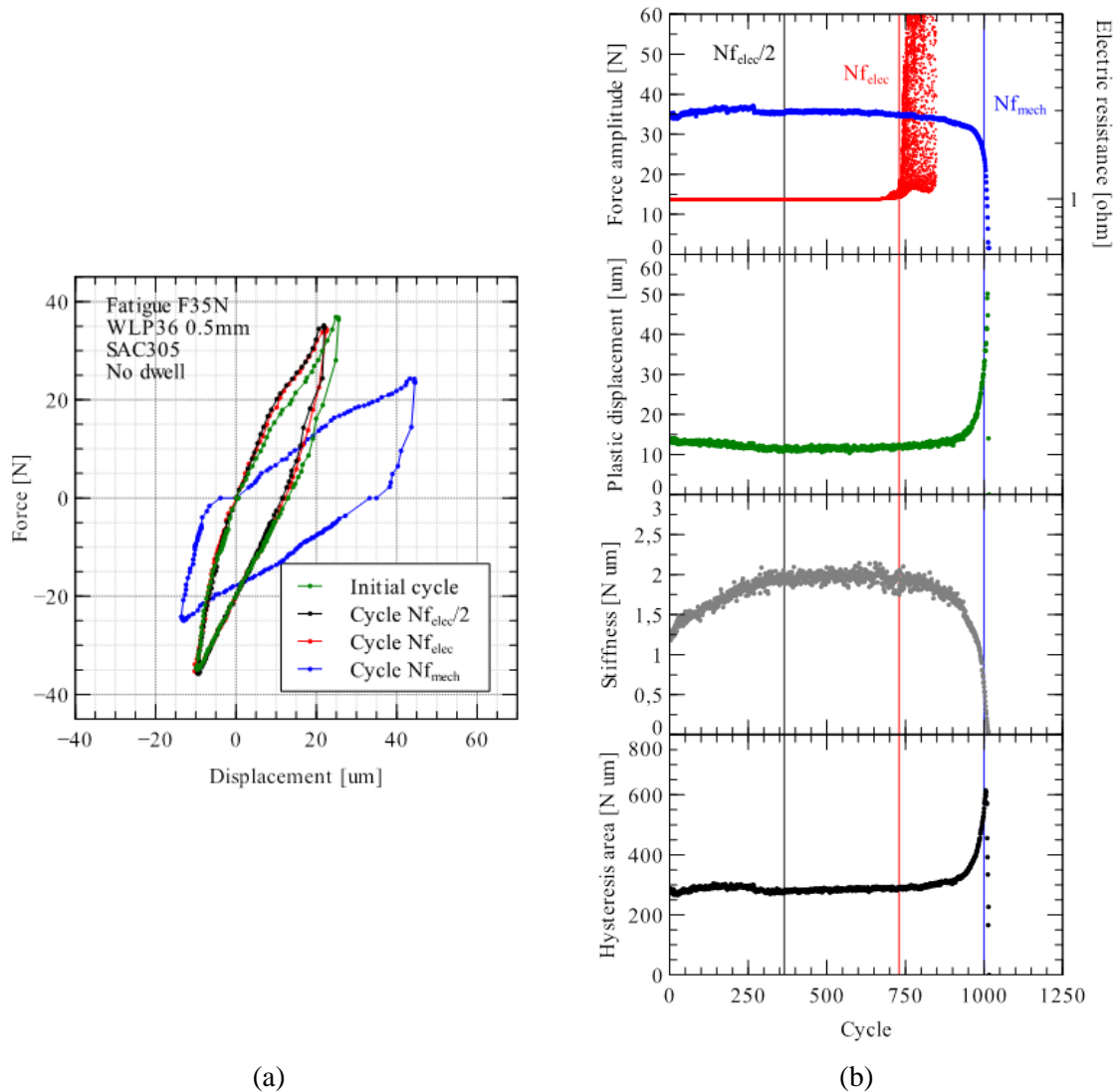


Figure 73: Results of a fatigue test without dwell time: (a) hysteresis area and (b) evolutions of mechanical parameters

Three periods in the evolution of the force magnitude are noticeable. These periods are compared with those expected for bulk samples represented schematically in Figure 74. Force magnitude increases slightly from the beginning of the fatigue test until the stabilization point (transient phase). This cyclic hardening corresponds to an increase of the resistance to deformation, then a plastic displacement decrease. Stabilization of force magnitude is reached after a saturation of work hardening with a tangent point where initiation of cracks due to the cumulative damage reduces fastly the force magnitude until the complete failure. In the case of our sample, the tangent point is reached

before the quick decline of the force magnitude because at least one solder joint is completely fractured as indicated by the electrical resistance monitoring (see Figure 73).

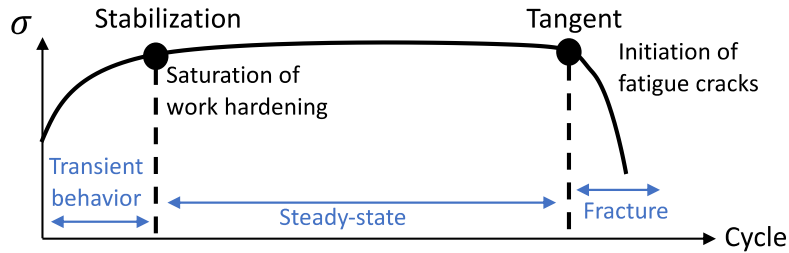


Figure 74: Evolution of stress magnitude with hardening for metals by cyclic stressing

Two data sets of recorded cyclic mechanical parameters are compared. The 1<sup>st</sup> data set contains the mechanical parameters cyclic values obtained from the 1<sup>st</sup> cycle and until mechanical failure. The 2<sup>nd</sup> data set contains mechanical parameters obtained from the 1<sup>st</sup> cycle and until the electrical failure. Standard deviation (STD) and mean values of the different mechanical parameters are calculated for the two data sets. Table 9 summarizes obtained results. Stabilities of mechanical parameters from the two data sets are compared with the change (in percent) which indicates variations of average values and standard deviations from the 1<sup>st</sup> data set (until mechanical failure) to the 2<sup>nd</sup> one (until electrical failure).

Table 9: Measurements of mechanical parameters

		Force magni. [N]	Plastic displ. [um]	Hysteresis area [N um]	Stiffness [N/um]
Until mechanical failure (1)+(2)	Mean	34.6	13.2	299.6	1.8
	STD *	2.9	5.6	46.6	0.3
Until electrical failure (1)	Mean	35.4	11.9	287.0	1.8
	STD *	0.7	0.6	7.7	0.2
Change **	Mean	2.3 %	-9.8 %	-4.2 %	4.2 %
	STD *	-77 %	-89 %	-83 %	-40 %

\* Standard deviation

\*\* The change between averages until mechanical and electrical failures: 2.3 % change of force magnitude mean signifies 2.3 % of change between means obtained until mechanical (34.6 N) and electrical (35.4 N) failures

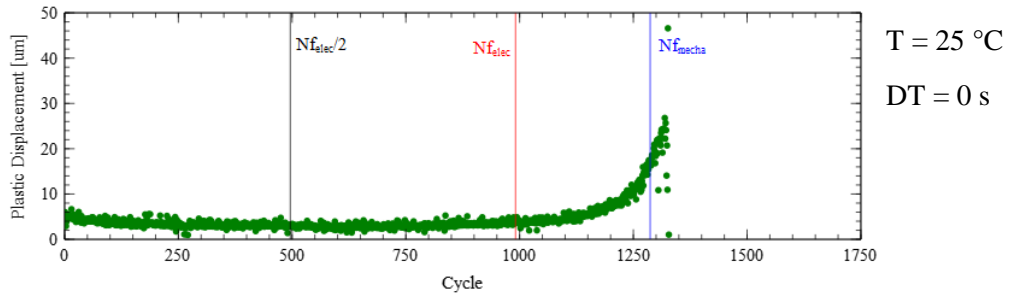
Change values of the standard deviation (in Table 9) indicate that populations of the 1<sup>st</sup> data set (until mechanical failure) are more distributed than those of the 2<sup>nd</sup> data set (until electrical failure). The large variations of the mechanical parameters after tangent point during cracks propagation are responsible of this scatter. Electrical failure indicates that the tangent point is already reached because of the presence of completely fractured solder balls.

Cyclic evolutions of plastic displacement of several fatigue tests are plotted in Figure 75. The plastic displacement slowly decreases during the first cycles for fatigue test at room temperature and slowly increases for fatigue test at 50 °C. This softening can be explained by the viscosity of the solder material which is higher at 50 °C. Slight variations of the plastic displacement are observed from  $N_{f,elec}/2$  to electrical failure for all fatigue tests. After electrical failure, the plastic displacement increases quickly until mechanical failure for all configurations.

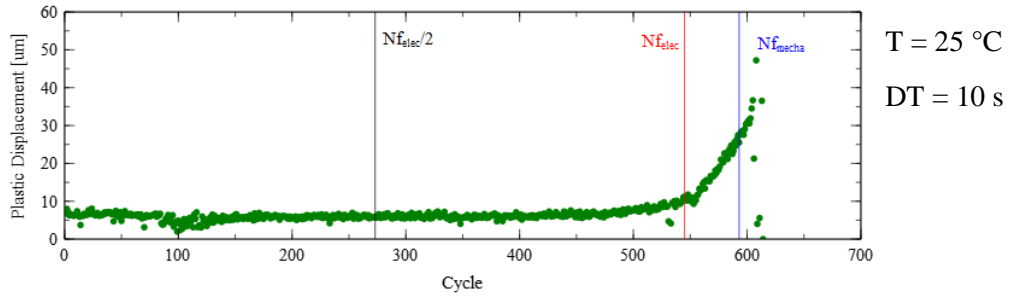
### Chapter III. Failure Definition

The symmetry of the response of the sample is verified with a comparison of plastic displacement values obtained during positive and negative loops. Cyclic values of plastic displacement are plotted in Figure 76 for a fatigue test at 35 N without dwell time. Results show that measured values during positive and negative loops are similar which validate the use of an average cyclic value. The symmetry has been verified before each analysis for all fatigue tests.

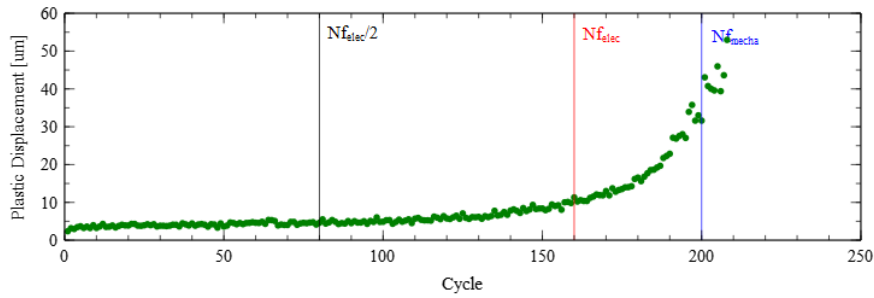
Average values of mechanical parameters must be extracted from cyclic measurement in order to compare results obtained for the different fatigue tests. The evolutions of mechanical parameters extracted from a fatigue test without dwell time have been described. An average value of measured data during the steady-state period is ideal but complicated to use in our work because the stabilization point cannot be precisely identified due to the slight variations during the transient behavior phase. The tangent point is reached at electrical failure because at least on solder joint is completely fractured which justifies that the tangent point is not reached at half of the electrical failure. Thus, average values of mechanical parameters will be calculated with a data set which contains cyclic values from the beginning of the test (1<sup>st</sup> cycle) until the cycle at half of electrical failure.



(a) Fatigue test at 35 N without dwell time at 25 °C



(b) Fatigue test at 35 N with 10 s dwell time at 25 °C



(c) Fatigue test at 35 N without dwell time at 50 °C



Figure 75: Evolution of plastic displacement during fatigue tests at 35 N: (a) without dwell time at 25 °C, (b) with 10 s dwell time at 25 °C and (c) without dwell time at 50 °C

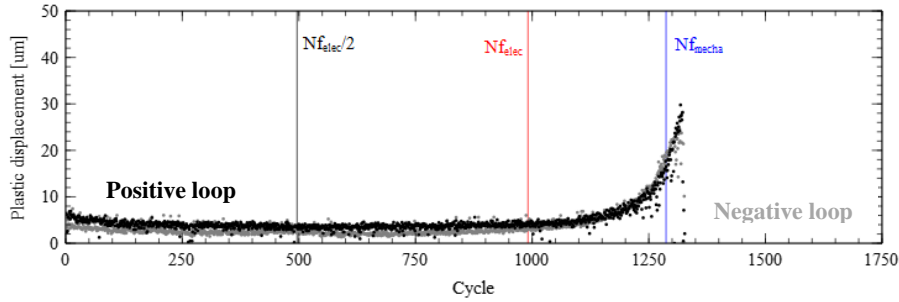
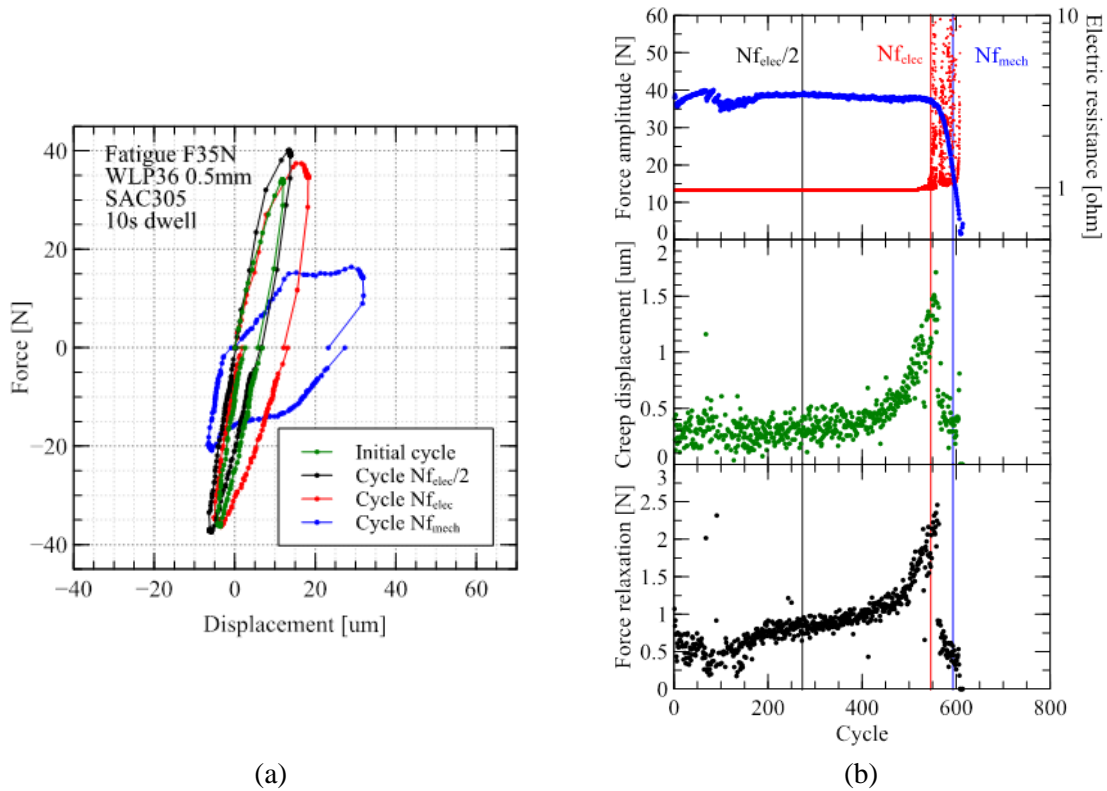


Figure 76: Positive and negative part of the plastic displacement for a fatigue test at 35 N without dwell time at room temperature

### 3.c. Mechanical parameters for fatigue tests with dwell time

Additional mechanical parameters are extracted from the hysteresis response of the sample for fatigue tests with dwell time. Cyclic creep displacement and force relaxation are measured at extreme force values during dwell time. Evolutions of these parameters for a fatigue test at 35 N with 10 seconds of dwell time are plotted in Figure 77. Hysteresis responses measured at specific cycles are also represented.

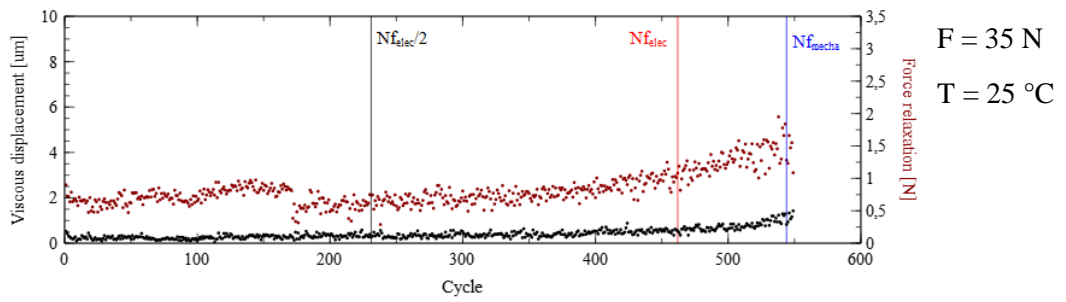


*Figure 77: Results of a fatigue test with 10 s dwell time: (a) hysteresis area and (b) evolutions of creep mechanical parameters*

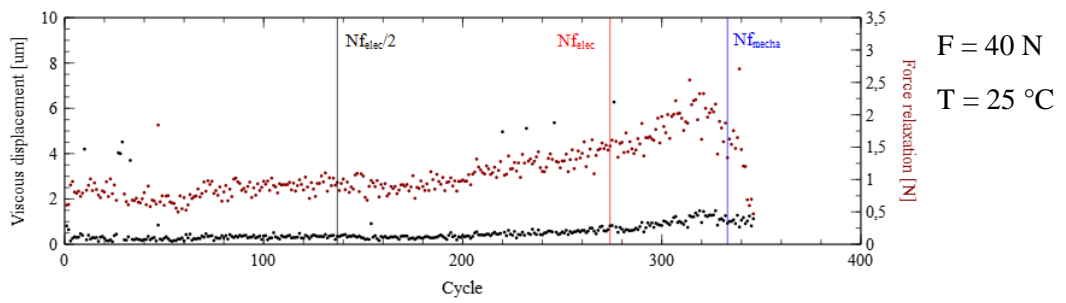
Creep displacement and force relaxation are representative of creep strain developed during dwell time. Evolutions of creep displacement and force relaxation are similar. These parameters are constant at the beginning of the test and until half of the electrical failure ( $N_{f,elec/2}$ ) before increasing first with a slow then high rate. The force magnitude is still constant during this phase. The creep behavior is modified during dwell time by the cumulative damage without significant changes of the response measured during loading and unloading. An increase of the creep displacement per cycle measured during dwell time could be considered as an indicator of highly damaged solder joints. Electrical and mechanical number of cycles to failure are similar which means that the different solder joints of the matrix have failed in a reduced number of cycles (defined as phase (2) in Figure 62).

Several evolutions of creep mechanical parameters are plotted in Figure 78 for different configurations of tests: (i) at 35 N and room temperature, (ii) at 40 N and room temperature and (iii) at 35 N and 50 °C which shows similar evolutions. The evolutions of viscous displacement and force relaxation are correlated. Both creep displacement and force relaxation are stable until  $N_{f,elec/2}$ . After, these parameters increase until  $N_{f,elec}$ . The increase rate increases with the number of cycle. After electrical failure and before mechanical failure, both force relaxation and creep displacement per cycle evolution changes and these parameters start to decrease until the complete fracture of the sample and the end of the test.

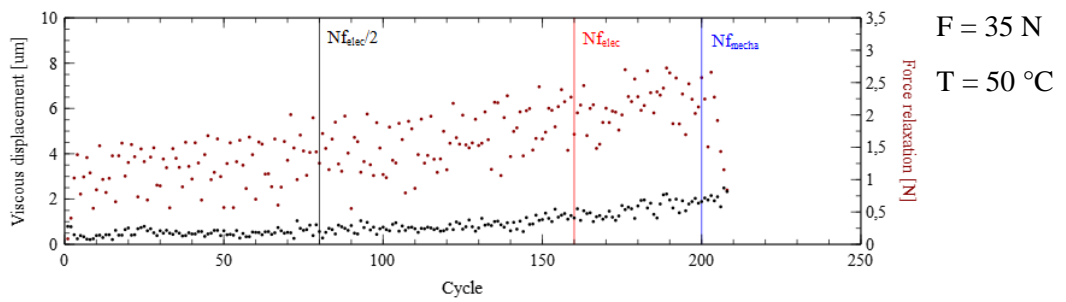
Plastic displacement, stiffness, and hysteresis are per cycle have also been extracted during post-processing for fatigue tests with dwell time. Plastic displacement is calculated by subtracting the creep displacement to the total inelastic displacement measured at the end of the loop. As for the fatigue test without dwell time, evolutions of these mechanical parameters are stable until half of the number of cycles at electrical failure. Average values of creep mechanical parameters (creep displacement and force relaxation) will be calculated with the same methodology than other mechanical parameters. A data set which contains cyclic values from the beginning of the test (1st cycle) until the cycle at half of electrical failure will be used to calculate average values for each fatigue tests with dwell time.



(a) Fatigue test at 35 N and room temperature



Fatigue test at 40 N and room temperature



(c) Fatigue test at 35 N and 50 °C

Figure 78: Evolution of creep mechanical parameters during fatigue tests: (a) at 35 N and 25 °C, (b) at 40 N and 25 °C and (c) at 35 N and 50 °C

## 4. Conclusions

The developed shear test bench developed performs cyclic shear fatigue tests of assembled electronic packages. Fatigue tests number of cycles to failure must be defined with a failure criterion which indicates when the sample is fractured. The sample used by our shear test bench is specific compared to traditional fatigue tests based on bulk sample. The solder joints matrix of the electronic package can be compared with a matrix of 36 individual bulks loaded simultaneously. The premature fracture of one of the solder joints of the matrix cannot be identified by global measurements of force and local displacement at the scale of the package because of the remaining solder joints. Failure criteria based on the variation of the global mechanical response are not sufficient.

Monitoring of electrical resistance is commonly used in the electronic industry in order to identify the failure of solder joints during accelerated thermal cycling tests. Dummy packages with daisy-chain are used in order to monitor the electrical resistance of the solder joints matrix. The fracture of bulk samples for fatigue test performed in strain controlled is generally identified with a force magnitude decrease because cracks reduce the sample surface. Failure criteria based on the electrical resistance monitoring (electrical failure) and on the force magnitude evolution (mechanical failure) have been compared for different fatigue tests.

Initial inspections have been performed in order to analyze the structure of solder joints after sample manufacturing. Solder joints structure has been observed with optical images after cross-section. Solder joint height has been measured based on the measured heights of six solder balls. Samples submitted to fatigue tests that include or not dwell time have been used to verify the failure mechanism. Optical images from cross-sections show completely fractured solder joints after electrical failure and before mechanical failure. Distribution homogeneity of the force applied to the package by the test bench on the solder joints matrix has been verified with an observation of the distribution of crack initiations in both peripheral and middle axis of the sample.

Comparison of electrical and mechanical criteria indicates that the electrical resistance monitoring contributes to the early identification of the first fractured solder ball of the matrix. Completely fractured solder balls have been observed with cross-section without significant variation of force magnitude during two fatigue tests (with and without dwell time). The solder joint matrix behaves like a matrix of bulk samples loaded simultaneously. Structure variabilities between the different solder balls of the matrix induce a partial failure state which can only be caught by the electrical resistance monitoring.

Average values of mechanical parameters are required in order to compare the results of the different fatigue tests. The electrical failure criterion is used to evaluate these average values. Evolutions of all mechanical parameters as a function of loading cycles are stable until half of the number of cycles to electrical failure. In this context, average values of mechanical parameters will be calculated with a data set which contains cyclic values from the beginning of the test (1st cycle) to half of electrical failure.

Solder joint structure, failure criterion and failure mechanism have been analyzed with samples of the fatigue tests plan. This plan contains fatigue tests performed at different force magnitudes and temperatures. Average mechanical parameters have been calculated with the methodology described in this chapter for the fatigue tests of the test plan. Chapter 4 describes configurations of the fatigue tests plan and the analysis of the averaged mechanical parameters obtained for each fatigue test.

## Chapter IV. Fatigue Results

*This chapter describes the results of the fatigue test plan which has been performed with the shear test bench. Shear cyclic fatigue tests at different force magnitude, performed with or without dwell time, at room temperature or 50 °C make-up the test plan. Samples assembled with two assembly processes are studied: classic lead-free SAC305 process and specific leaded backward SnPb+ process. Preliminary test controls have been used in order to validate fatigue tests.*

*Fatigue test results are analyzed using Weibull statistical model. Impact of force magnitude, dwell time and temperature on the number of cycles to failure is estimated based on fatigue test results. Both SAC305 and backward SnPb+ assembly processes are studied. Addition of 10 s dwell time and temperature increase from room temperature to 50 °C reduce number of cycles to failure until a factor of 9 for SAC305.*

*Mechanical parameters are extracted for each fatigue test. These parameters are used in order to measure the cyclic mechanical response of the sample. The evolution of the mechanical response with dwell time and temperature is discussed. Inelastic displacement and hysteresis area increase when the force magnitude increases. These parameters are studied as indicators of damage in order to propose fatigue laws. However, predictions are not relevant for configurations that include dwell time and for fatigue tests at 50 °C.*

*Therefore, creep displacement during dwell time have been measured. These measurement are used in the chapter 5 in order to define a mechanical model of the sample.*

## 1. Fatigue tests

This part describes configurations of the fatigue tests based on preliminary monotonic and step-stress tests detailed in chapter 2. Configurations parameters have been selected in order to obtain numbers of cycles to failure close to those obtained with accelerated thermal cycling (from 500 to 2,000), expecting that failure mechanism will be similar.

Configurations of the test plan are reported in Table 10. SAC305 and backward SnPb+ assembly processes are tested. Three parameters define each configuration: the force magnitude, the temperature and the dwell time. Fatigue tests are performed at room temperature (25 °C) and at 50 °C with the method described in chapter 2. The cyclic loading without and with dwell time is also described in this chapter.

Nominal value of 10 s of dwell time is chosen in order to have a loading frequency which allows to obtain fatigue test durations lower than 24 h. This limit of test duration must be respected in order to obtain measurements of force and local displacement with a high sampling rate (5 recordings per second) without exceeding a reasonable data volume for each test. Dwell time duration is also studied with a 100 s configuration.

Table 10 - Configurations of the fatigue test plan

Assembly process	Temperature	Force	Dwell time	Frequency	Samples
	[°C]	[N]	[s]	[Hz]	[#]
SAC305	25	30	0	0.025	1
			100	0.004	1
		35	0	0.025	7
			10	0.016	6
		40	0	0.025	3
			10	0.016	3
	45	0	0.025	2	
		10	0.016	2	
	50	35	0	0.025	3
			10	0.016	3
Backward SnPb+	25	35	0	0.025	4
			10	0.016	4
		40	0	0.025	3
			10	0.016	3
	50	35	0	0.025	2
			10	0.016	2

In order to obtain results which are statistically representative (from samples manufacturing, measurement accuracies, etc.), several samples are tested for each configuration. Numbers of samples per configuration are also reported in Table 10.

## 2. Test controls

Fatigue tests are verified and validated with several criteria before results analysis. These criteria have been defined in order to detect anomalies that may occur during the test and to control the validity of results. Test controls are performed to ensure that nothing has disturbed the experimental test and impacted data from measurements. This part describes the validation methodology used to define whether the test results are validated and can be used for further analysis or whether the test should not be considered.

### 2.a. Validation of experimental results based on selection criteria

Disturbances are classified into two categories as reported in Table 11. They are detected (i) during the test or (ii) after post-processing. Exploitation of measured parameters (cycles to failure and force and local displacement measurements) depends on the disturbance. Examples are given for each disturbance in the following sections with an illustrative example.

*Table 11 - Tests validation disturbance classification and data exploitation*

Type	Disturbance	Data exploitation		
		Cycles to failure	Force	Local displacement
During the test	Manipulation	No	No	No
	Displacement tracking	Yes	Yes	No
	Force sensor	Yes	No	No
Detected after post-processing	Gap distance	No	No	No
	Sample stiffness	Yes	Yes	No

### 2.b. Disturbance detected during the test

#### *2.b.i. Manipulation*

Incorrect manipulations may occur as tests are manually controlled via the dedicated software. For example, the sample can undergo an uncontrolled force magnitude if the selected command displacement or the force limit are not restricted enough. This incorrect manipulation may occur at the beginning of the test or during the test when the command displacement must be adjusted to maintain a constant force magnitude. Test results cannot be used if an incorrect manipulation occurs as the sample is submitted to an additional uncontrolled deformation and damage. An example of this type of disturbance is plotted in Figure 79. The sample has been submitted to a force magnitude higher than the nominal value during two cycles which led to premature failure.

#### *2.b.ii. Displacement tracking and force sensor disturbance*

Local displacement is measured with Digital Image Correlation. Relative movement of two patterns on both sides of the sample are tracked. If the patterns are incorrectly defined or the light decreases abruptly (lamp breakdown) the tracking by the software of the jaws movements is no longer possible causing incorrect recording of the local displacements (see an example in Figure 80). It is obvious that local displacement measurements are not available in this case. However, the force

magnitude is still available for this type of disturbance as the loading is controlled by the command and not by the local displacement.

Local displacement measurements are also not available in the case of force sensor disturbance. Force measurements are used by the post-processing method to remove the gap distance and prepare hysteresis curves which renders local displacement measurements unusable.

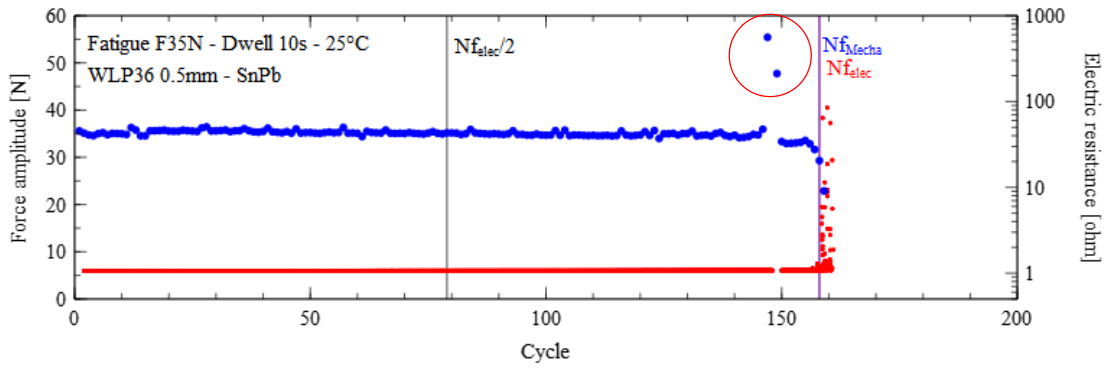


Figure 79 - Incorrect manipulation during a fatigue test that induces premature failure

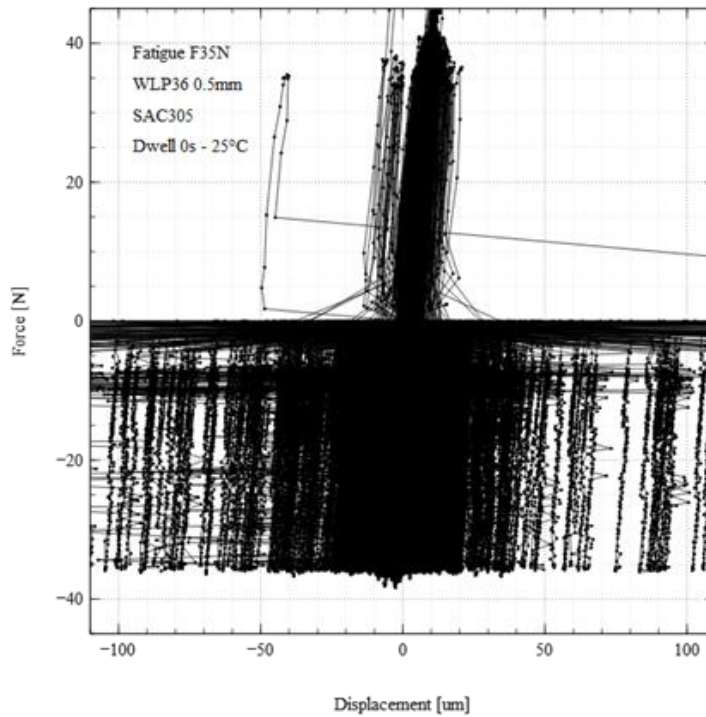


Figure 80 – Hysteresis curves obtained with troubles due to lamp breakdown

## 2.c. Disturbance detected after post-processing

### 2.c.i. Gap distance

The gap is the distance between the package and the jaw. The gap distance is removed during post-processing to obtain the hysteresis curve. Gap distance as a function of cycle of one fatigue test is plotted in Figure 81. A constant gap distance value over the test indicates a correct assembly as in



this case, the sample remains aligned with the jaw during all the test. Otherwise it highlights an assembly problem as the misalignment of the package and the jaw.

The expected gap distance in the case of perfect alignment between the package and the shear test setup is known. In fact, the opening of the equipment has been measured in optical image (3110  $\mu\text{m}$ ) and the package sizes are defined in the datasheet (3000  $\mu\text{m}$ ). The expected gap value is 110  $\mu\text{m}$  and a different value means that the sample is not parallel to the jaw. Neither the force magnitude nor the number of cycles to failure can be used in the case of a misalignment because the package loading is complex (with package torsion) and cannot be compared with pure shear loadings.

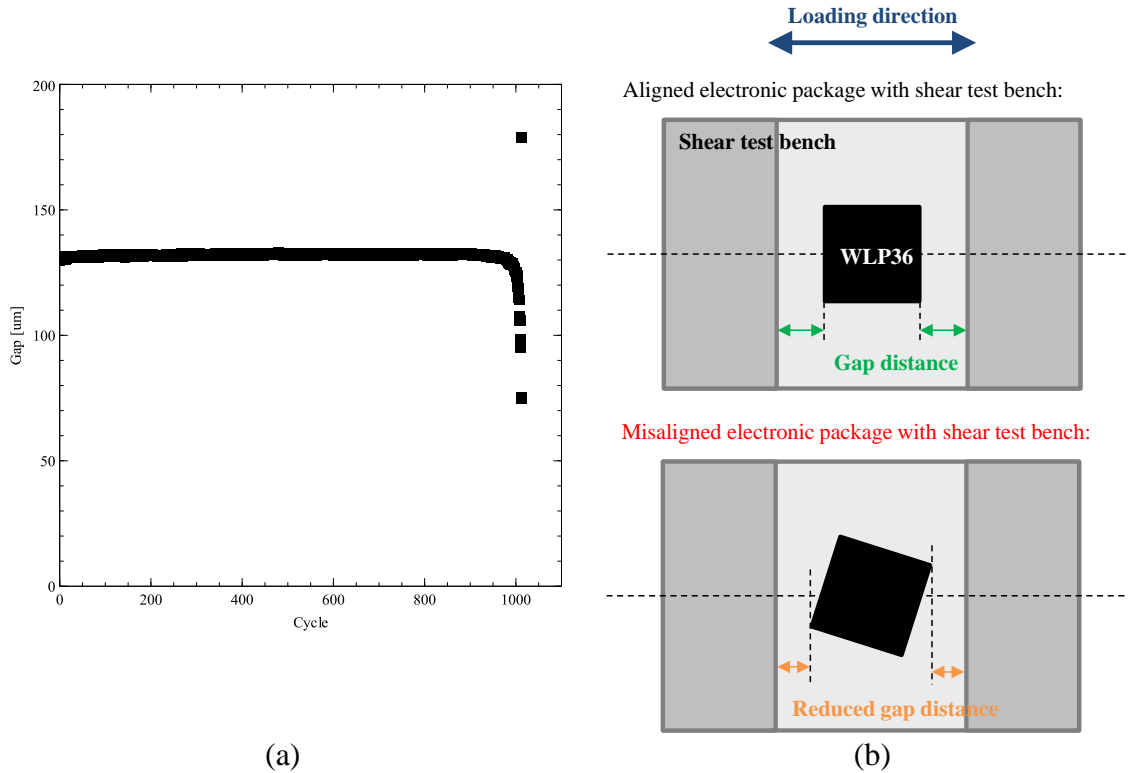


Figure 81 - Gap evolution post-processing analysis: (a) normal evolution of gap distance during fatigue test and (b) schematic representation of gap distance change with misalignment

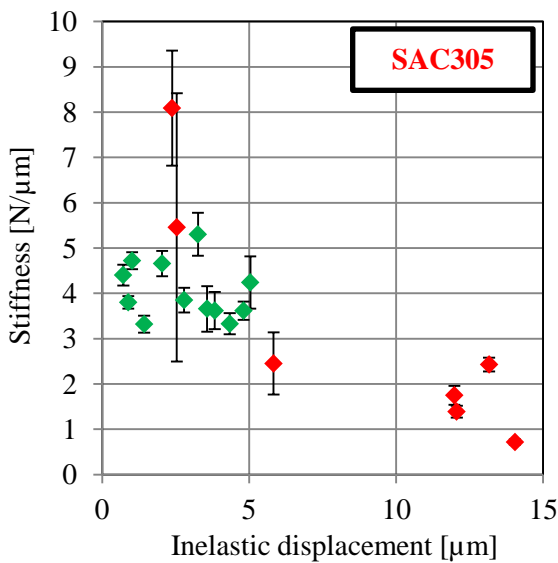
### 2.c.ii. Sample stiffness

The sample stiffness is one of the mechanical parameters extracted from the hysteresis curves. This parameter is used after test to verify that the sample has been properly mounted. It is important to be sure that the measured local displacement corresponds to the shear displacement of the solder joints and does not come from internal movement in the setup. A minor inattentiveness during the setting up of the test bench or the sample induces a weakness that distorts the measured local displacement and the loading. For instance if the sample is not perfectly secured on the jaw, the measured local displacement does not corresponds to the displacement of the solder joints due to the internal movements. A test is invalidated when the stiffness is lower than the nominal expected value.

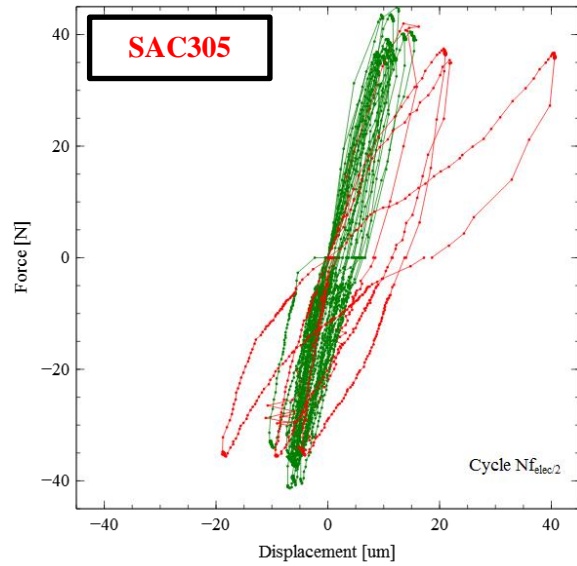
Two graphs are used to verify the stiffness value: (i) the evolution of the stiffness as a function of the plastic displacement and (ii) the hysteresis curves obtained at half of the fatigue test. Graphs obtained for SAC305 and backward SnPb+ are plotted in Figure 82. Unexpected points are depicted in red. The stiffness is not supposed to vary from a sample to the other as the stiffness is measured in

the elastic phase. Relevant stiffness values (in green) are between 3 and 5.5 N/ $\mu\text{m}$ . Points excluded from this area, in red, are considered outliers (five in case of SAC305 alloy and 8 for the backward alloy).

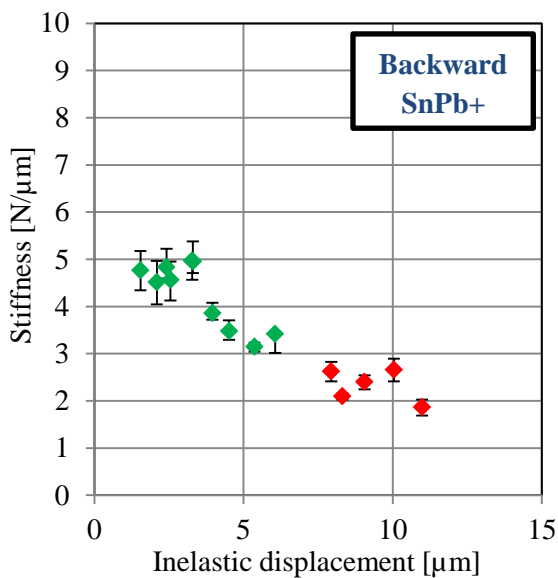
Observation of hysteresis curves confirms the selection previously made. It is noticeable that red curves are clearly different from green ones: initial slopes of red hysteresis curves are lower than those of green ones which induces a stiffness decrease. The point with a high standard deviation of the stiffness (in SAC305) is excluded from the results because it means that the sample response is not stable. The point with a high stiffness ( $> 8 \text{ N}/\mu\text{m}$ ) has also been excluded because frictions have been observed between the sample PCB and the jaw which explains this high value of stiffness.



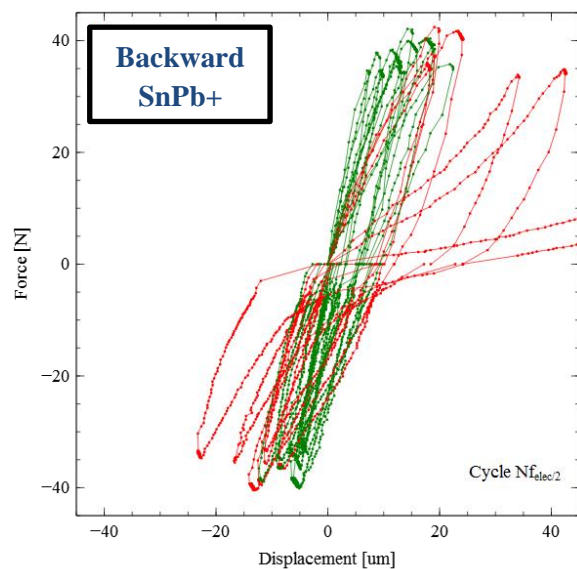
(a) Stiffness values for SAC305



(b) Hysteresis curves for SAC305



(c) Stiffness values for backward SnPb+



(d) Hysteresis curves for backward SnPb+

Figure 82 - Verification of sample stiffness with (a, c) stiffness values as a function of measured cyclic inelastic displacement and (b, d) corresponding hysteresis curves

Fatigue tests are stress controlled and there is no disturbance in the force measurements for fatigue tests without validate stiffness values. Thus, the obtained numbers of cycles to failure can still be used for these tests.

## 2.d. Test control synthesis

Tests results are validated with the criteria defined previously in this part. The regular running of the tests is verified several times during the test. Incorrect manipulations and force and displacement recordings are referenced. Gap distance removal, hysteresis curves and stiffness criteria are applied after post-processing in order to validate the tests. Table 12 summarizes performed and validated results. As previously disclosed, number of cycles to failure and force magnitude values can be valid for fatigue tests without a validated stiffness criterion.

Table 12 – Summary of performed and validated tests after application of validation criteria

Alloys	Temp.	Force	Dwell time	Frequency	Tested samples	Validated samples		
	[°C]	[N]	[s]	[Hz]		Nf / force	Displacement	
SAC305	25	30	0	0.025	1	1	0	
			100	0.004	1	1	0	
		35	0	0.025	7	6	3	
			10	0.016	6	6	3	
		40	0	0.025	3	3	3	
			10	0.016	3	3	3	
	45	0	0.025	2	2	1		
		10	0.016	2	2	2		
	50	35	0	0.025	3	3	3	
			10	0.016	3	3	3	
	Backward SnPb+	25	35	0	0.025	4	4	1
				10	0.016	4	4	2
40			0	0.025	3	3	1	
			10	0.016	3	3	2	
50		35	0	0.025	2	2	2	
			10	0.016	2	2	2	

## 3. Results and discussions

Fatigue tests of the test plan have been verified with the validation criteria developed in the previous section. Numbers of cycles to failure of validated results are analyzed for the different test configurations with a Weibull distribution. Impact of configuration parameters on the number of cycles to failure is studied. This analysis is followed by an analysis of the mechanical parameters extracted from the tests. Results obtained for the different configurations are analyzed in order to characterize the mechanical response of the sample.

### 3.a. Weibull distribution

## Chapter IV. Fatigue Results

Weibull distribution is used to analyze numbers of cycles to failure with a continuous probability distribution. The probability density function of a Weibull random variable (for  $x \geq 0$ ) is:

$$f(x) = \left(\frac{\beta}{\theta}\right) \left(\frac{x}{\theta}\right)^{\beta-1} e^{-\left(\frac{x}{\theta}\right)^\beta} \quad \text{Eq. IV-1}$$

where  $\theta > 0$  is the scale parameter and  $\beta > 0$  is the shape parameter

The scatter of the results is represented by the shape parameter, also known as the Weibull slope. The shape parameter is low when the results are scattered. The scale parameters gives the number of cycles after which more than half of the samples are failed (precisely more than  $1 - e^{-1} \sim 63\%$ ). Number of cycles to failure for both assembly processes are studied for the different test configurations with the Weibull distribution. Shape and scale parameters are evaluated by Minitab software based on the results for each configuration.

### 3.a.i. SAC305 results

Influences of force magnitude, dwell time, temperature and combination of dwell time and temperature for SAC305 assembly process are depicted in Figure 83. Results show that increase of force magnitude, dwell time and temperature have an impact on the number of cycles to failure. Results have been analyzed and published in [74]. Increase of force magnitude from 35 to 40 N naturally reduces the number of cycles to failure because the force magnitude can be related to the applied stress. Addition of 10 s of dwell time and increase in temperature also reduce the number of cycles to failure. Results show that increase of both temperature and dwell time drastically reduces the number of cycles to failure.

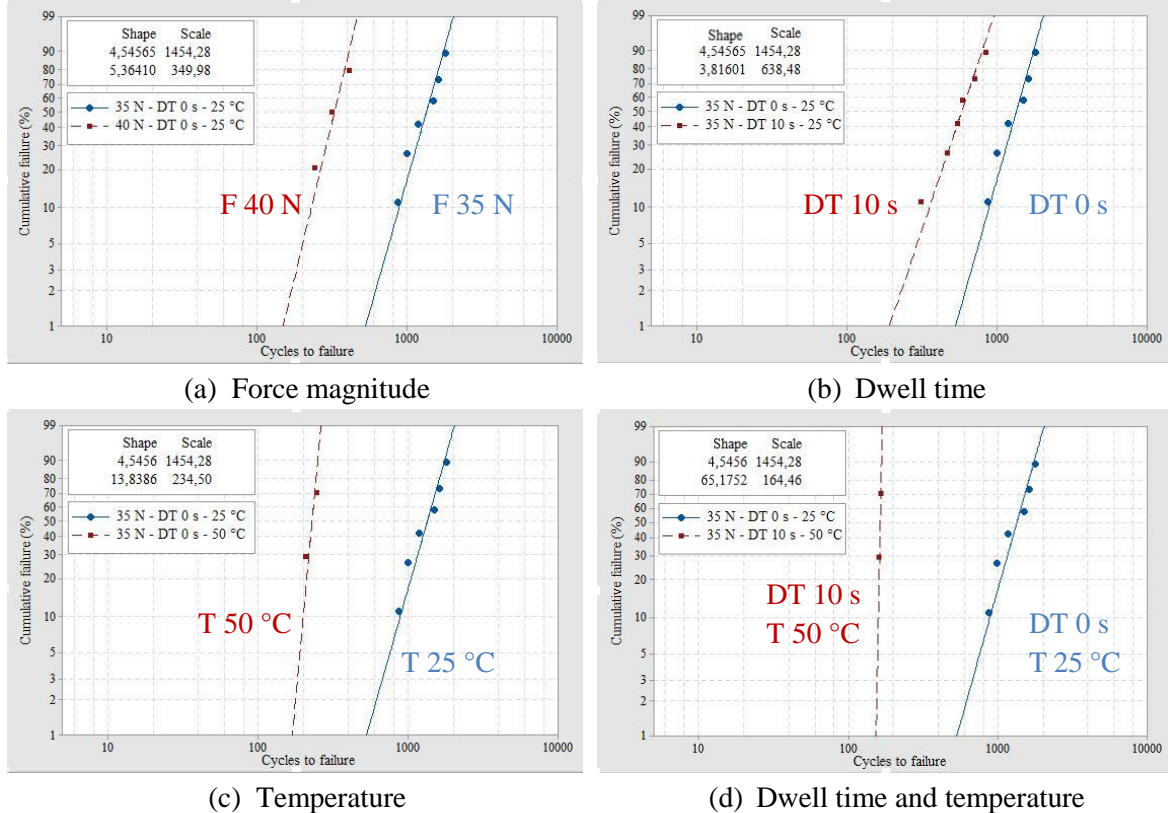


Figure 83 – Parameters influence on cycles to failure for SAC305 assembly process: impact of (a) force, (b) dwell time, (c) temperature and (d) combination of dwell time and temperature

The influence of the different test parameters is quantified with the Weibull distribution. The scale parameter is used in order to compare the different configurations even if numbers of samples per configuration are different. The number of cycles to failure of each configuration is the scale parameter of the Weibull distribution. Following tables summarize the results obtained. Table 13 shows the influence of the force magnitude. Increase of force amplitude from 35 to 40 N reduces the number of cycles to failure with a factor of 4. More damage per cycle is generated at 40 N. Influence of dwell time is reported in Table 14. The number of cycles to failure is reduced by 2 when 10 s dwell time are added for a loading at 35 N and room temperature. Table 15 synthetizes the impact of temperature increase without and with 10 s dwell time configurations. Results show that temperature increase from 25 to 50 °C reduces the number of cycles to failure with a factor of 6 without dwell time and 4 with dwell time. Results also indicates that combination of temperature increase and addition of dwell time reduces the number of cycles to failure with a factor of 9 (from 1454 to 164 cycles).

Table 13 - Impact on cycles to failure of increase of force magnitude for SAC305

Dwell Time	Temperature	Force		Factor between 35 N and 40 N
[s]	[°C]	35 N	40 N	
0	25	1454 cycles	350 cycles	4.1

Table 14 - Impact on cycles to failure of addition of 10 s dwell time for SAC305

Force	Temperature	Dwell time		Factor between 0 and 10 sec
[N]	[°C]	0 sec	10 secs	
35	25	1454 cycles	638 cycles	2.3

Table 15 - Impact on cycles to failure of increase in temperature for SAC305

Force	Dwell Time	Temperature		Factor between 25 and 50 °C
[N]	[°C]	25 °C	50 °C	
35	0	1454 cycles	253 cycles	6.2
35	10	638 cycles	164 cycles	3.9

Inelastic plastic strain developed per cycle increases with the increase of force magnitude, which reduces the number of cycles to failure. Creep strain are developed during the dwell time inducing an additional damage per cycle. This creep damage per cycle can explain the reduction of the number of cycle to failure with an addition of 10 s dwell time. Temperature has also an impact on the creep damage per cycle as the material is more viscous at 50 °C than at room temperature. Combination of

## Chapter IV. Fatigue Results

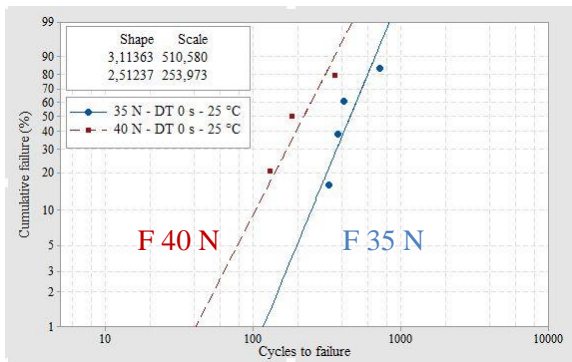
addition of 10 s dwell time and increase of temperature results in an important increase of the creep damage per cycle which can explain the change of the shape parameter. At 50 °C, the shape parameter is much higher (>14) than for other configurations (<6) which may be explained by the change of the predominant mechanism of damage from plastic inelastic strain per cycle at room temperature to creep inelastic strain per cycle at 50 °C.

Mechanical parameters representative of inelastic plastic and creep strains per cycle are extracted from the hysteresis response of the sample. The analysis of these parameters is described in the following part and will be used in the chapter 5 to validate the statements formulated in the previous paragraph. Fatigue tests with backward SnPb+ assembly process are described prior to this analysis and compared with SAC305 in the following sections.

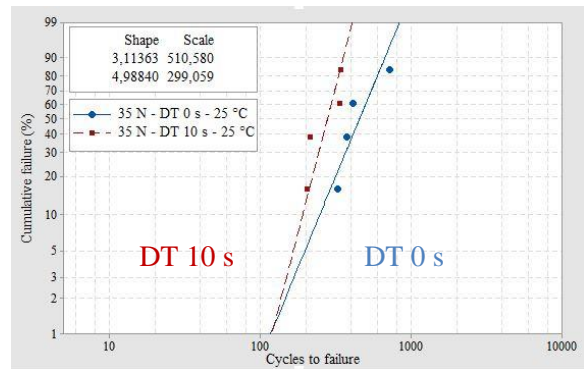
### 3.a.ii. Backward SnPb+ results

Fatigue test results for backward SnPb+ assembly are described in detail in this section. Influences of force magnitude, temperature and dwell time are studied with the Weibull distribution. Figure 84 presents the results obtained for backward SnPb+ assembly process.

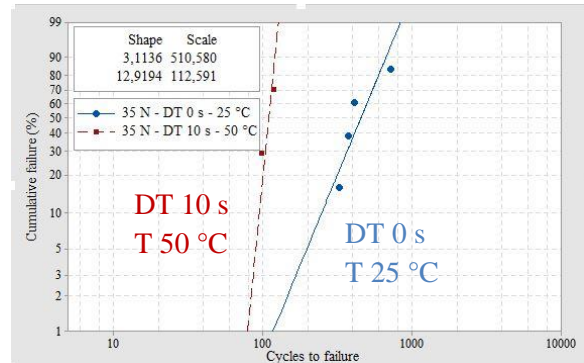
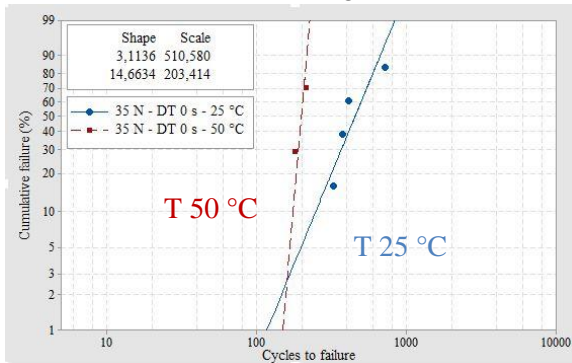
As previously, the scale parameter of the Weibull distribution is used in order to compare the different configurations. Scale parameters are extracted and used in the tables below to define parameters impacts on the number of cycles to failure. Same trends are observed for the backward SnPb+ assembly process. Numbers of cycles to failure are reduced with an increase of force magnitude and/or in temperature and also by the addition of 10 s dwell time. Reduction factors for the different parameters are defined in the tables below. At room temperature, increase of 5 N reduces the cycles to failure with a factor 2 while it is divided by 1.7 with the addition of 10 s dwell time. Increase of both temperature and dwell time reduces cycles to failure with a factor of 4.



(a) Force magnitude



(b) Dwell time





(a) Temperature

(b) Dwell time and temperature

Figure 84 - Parameters influence on cycles to failure for backward SnPb+ assembly: impact of (a) force, (b) dwell time, (c) temperature and (d) combination of dwell time and temperature

Table 16 Impact on cycles to failure of increase of force magnitude for Backward SnPb+

Dwell Time	Temperature	Force		Factor between 35 N and 40 N
[s]	[°C]	35 N	40 N	
0	25	511 cycles	254 cycles	2

Table 17 - Impact on cycles to failure of addition of 10 s dwell time for Backward SnPb+

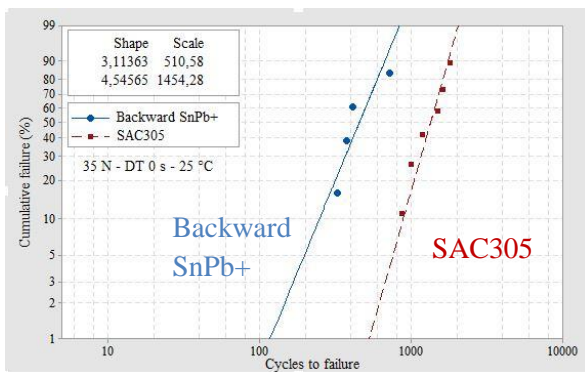
Force	Temperature	Dwell time		Factor between 0 and 10 sec
[N]	[°C]	0 sec	10 secs	
35	25	511 cycles	299 cycles	1.7

Table 18 - Impact on cycles to failure of increase in temperature for Backward SnPb+

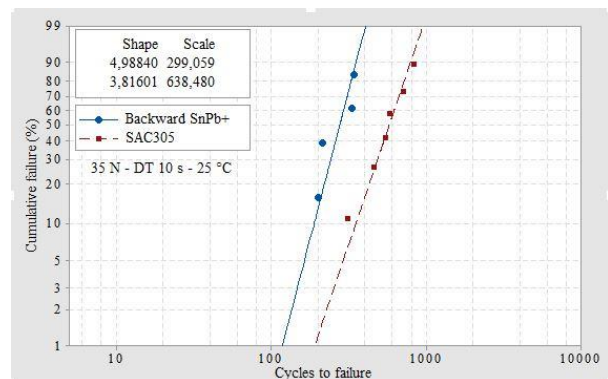
Force	Dwell Time	Temperature		Factor between 25 and 50 °C
[N]	[°C]	25 °C	50 °C	
35	0	503 cycles	203 cycles	2.5
35	10	299 cycles	112 cycles	2.6

3.a.iii. Comparisons of SAC305 and backward SnPb+ assembly processes

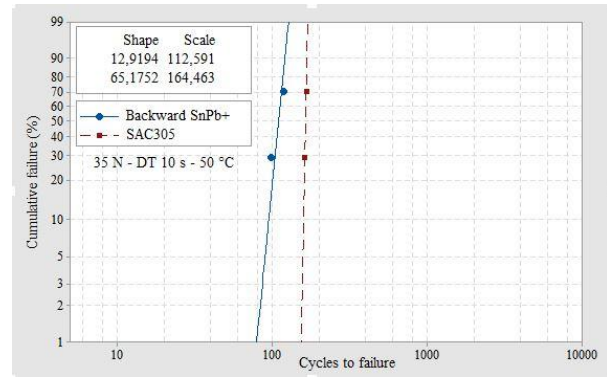
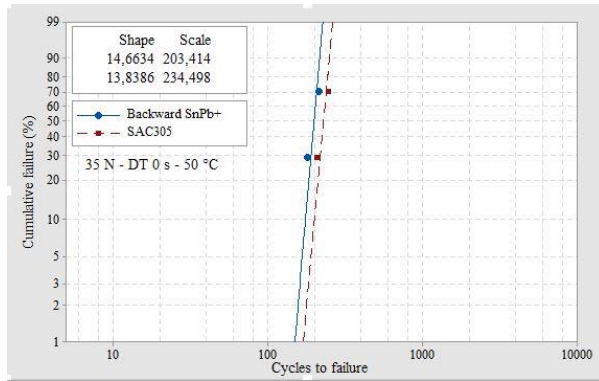
Numbers of cycles to failure for the different configuration are compared for the two assembly processes. The result of the comparison is represented on graphs of Figure 85.



(a) At 35 N without dwell time at 25 °C



(b) At 35 N with 10 s dwell at 25 °C



(c) At 35 N without dwell at 50 °C

(d) At 35 N with dwell at 50 °C

Figure 85 - Comparison of SAC305 and backward SnPb+ assembly processes for the different configurations: (a) at 35 N, (b) with dwell time, (c) at 50 °C and (d) with dwell at 50 °C

From a same loading condition, the numbers of cycles to failure are higher for SAC305 assembly process than for backward SnPb+ assembly process irrespective of the configuration. However, it cannot be concluded that SAC305 assembly process is better from a reliability point of view than backward SnPb+ assembly process. In service, stress levels in the solder joint are lower than those applied during the shear tests. Number of cycles to failure are then expected to be higher than those obtained during accelerated tests (<3000 cycles to failure). The prediction of numbers of cycles to failure in this case requires the knowledge of the acceleration factor and nothing suggests that the same acceleration factor can be applied for SAC305 and backward SnPb+ assembly processes.

Impacts of force magnitude at room temperature without dwell time and temperature without dwell time are lower for backward SnPb+ assembly process than for SAC305 assembly process. Impacts of dwell time at 25 and 50 °C are similar for the two assembly processes. The sensitivity to creep damage of the lead-free assembly process is highlighted by the lower factor of reduction with the combination of increase in temperature and addition of dwell time for backward SnPb+ (4) than for SAC305 (9). Without dwell time, the difference of numbers of cycles to failure for the leaded and the lead-free assembly processes is more pronounced at 25 °C than at 50 °C.

Impact of dwell time has been studied in accelerated thermal cycling in the literature for different BGA packages and lead-free alloys [64]. Reduction of the number of cycles to failure up to 40 percent is observed with the addition of 60 minutes of dwell time. The wear-out reliability of BGA packages have also been studied in torsion with different electronic packages [63]. Results show that torsion angle, temperature and dwell time parameters have an impact on the number of cycles to failure. Same trends are observed with the present shear test bench. The torsion angle in torsion can be compared with the force magnitude in this study as it changes the global cyclic stress in the solder joints matrix.

As detailed in the previous paragraphs, the impact of dwell time on the number of cycles to failure has been observed with our test bench but also with various experimental setups from the literature. Creep strains are developed during this maintain phase which increases the damage per cycle. Our shear test bench measures the hysteresis response of the package during the cyclic loadings which is interesting to quantify inelastic plastic and creep cyclic strains. Mechanical parameters per cycle extracted from the hysteresis response are discussed in the following part for the different test configurations. These parameters are used to draw the mechanical response of the sample.



### 3.b. Mechanical response

Mechanical parameters extracted from the hysteresis curves are used to characterize the mechanical response of the sample. As described in previous chapter 3, these parameters include the inelastic displacement, the plastic displacement and the hysteresis area. In the case of configuration with dwell time, the creep displacement and the force relaxation are also measured during the dwell time. Mechanical parameters are extracted for each cycle. As justified in chapter 3, values reported in this section are average values over the cycles until half of the electrical failure. Values are studied for each of four tests configuration: 0 sec of dwell time at room temperature (25 °C) and 50 °C and dwell time of 10 secs at room temperature and 50 °C. Mechanical parameters are plotted as a function of the force magnitude in order to evaluate the mechanical response of the package. Only samples with SAC305 assembly process are analyzed in order to avoid the impact of the assembly on the results.

#### 3.b.i. Inelastic and plastic displacements

The influence of the force magnitude on the inelastic displacement is analyzed. The evolution of inelastic displacement as a function of force magnitude is plotted in Figure 86 for the different test configurations. Different colors are used to represent the different temperatures (blue for room temperature and red for 50 °C). The major noticeable trend is the increase of the inelastic displacement with the increase of force magnitude. This trend was expected because more inelastic strains are developed at high force than low force magnitude. The temperature increase seems to increase the inelastic displacement for the same level of force magnitude. This increase is more noticeable for the configuration with 10 s dwell time. The inelastic displacement contains the creep displacement developed during the dwell time which can explain this increased temperature effect. The alloy is more viscous at 50 °C which increases creep displacement. Evolution of creep displacement with temperature will be discussed in the following section.

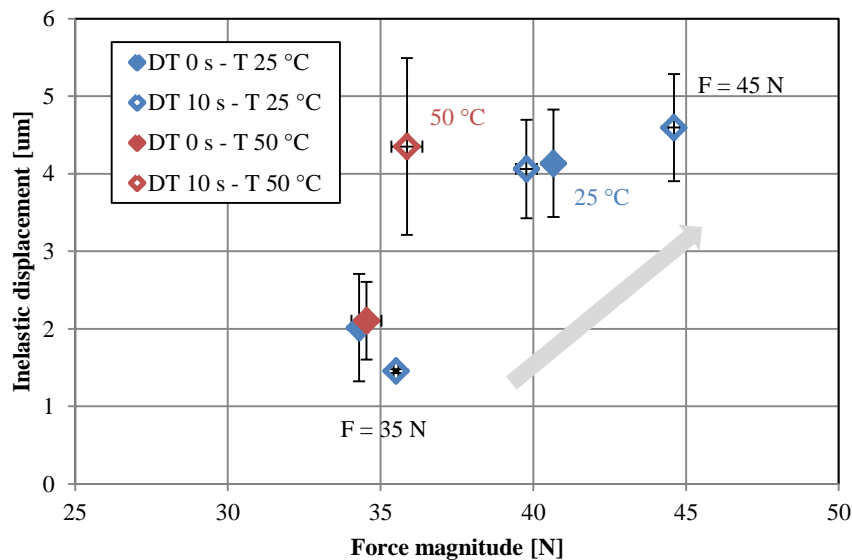


Figure 86- Inelastic displacement evolution as a function of force magnitude for SAC305 assembly process with noticeable impact of force level and temperature

The inelastic displacement is composed of the plastic displacement developed during loading phase and the creep displacement developed during dwell time. In the case of dwell time, the creep displacement is subtracted from the inelastic displacement to obtain the plastic displacement. Figure 87 shows the evolution of the measured plastic displacement for the different configurations as a function of the force magnitude. The same trend is noticeable for the plastic displacement than for the inelastic displacement: an increase in force magnitude increases the measured plastic displacement. It is also noticeable that temperature increase increases also the plastic displacement for the same level of force magnitude. The influence of the temperature is not restricted to the variation of creep displacement. The temperature has also an impact on the plastic displacement which can be explained by the viscous behavior of the alloy during loading. This behavior will be discussed in the following chapter 5 because separation of plastic and creep strains in the plastic displacement requires a mechanical model.

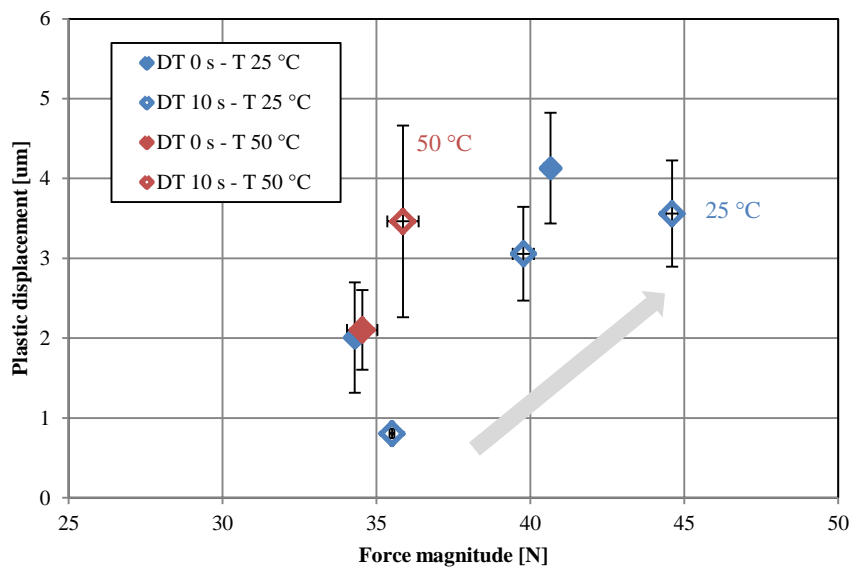
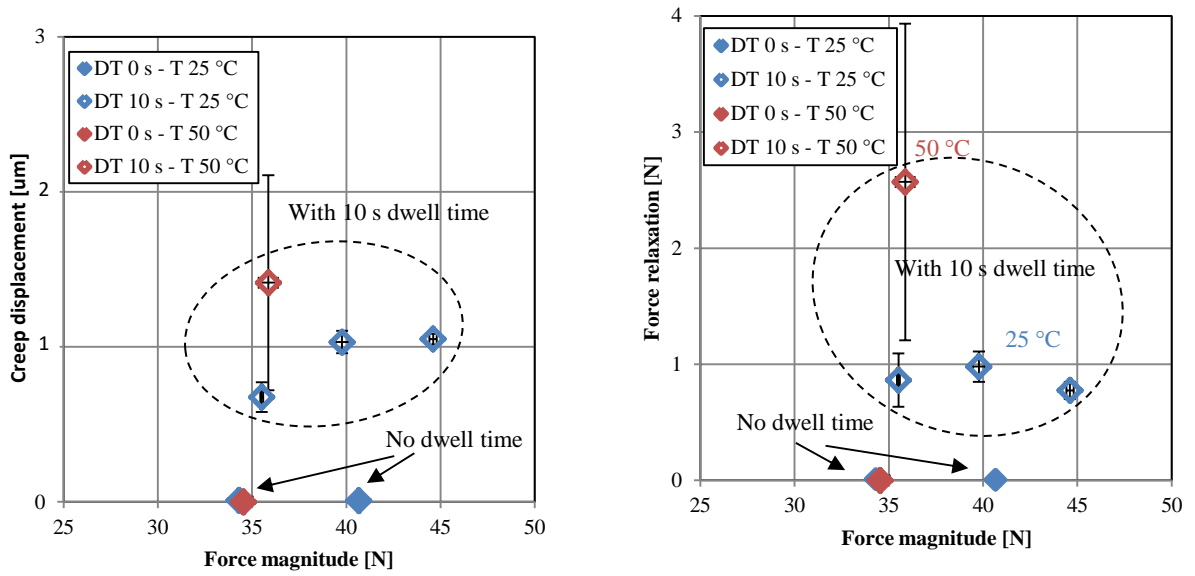


Figure 87 - Evolution of the plastic displacement as a function of the force magnitude for SAC305 assembly process with noticeable impact of force level

### 3.b.ii. Viscous mechanical parameters

Two mechanical parameters are measured during the dwell time: the creep displacement and the force relaxation. The design of the shear test bench induces this combined creep and relaxation state in the solder joints matrix during dwell time with a constant value of displacement control. Figure 88 presents creep displacement and force relaxation values obtained for the different configurations. Creep displacement and force relaxation are not measured in the case of configurations without dwell time because these parameters are only measured during dwell time. Impact of force magnitude is not particularly significant. The creep displacement increase for an increasing in force magnitude is lower for creep than inelastic displacement. This result may be due to the lower measured value of creep displacement (around 1 micrometer) as compare to those of inelastic displacement (from 1 to 5 micrometers).



(a) Creep displacement

(b) Force relaxation

Figure 88 - Evolution of the viscous mechanical parameters as a function of force magnitude for SAC305 assembly process with noticeable impact of temperature

### 3.b.iii. Hysteresis area

Evolution of hysteresis area as a function of force magnitude follows the same observed trend of the inelastic and plastic displacements (see Figure 89). Hysteresis area can be correlated to dissipated energy. More inelastic strains are developed at higher force inducing higher dissipated energy.

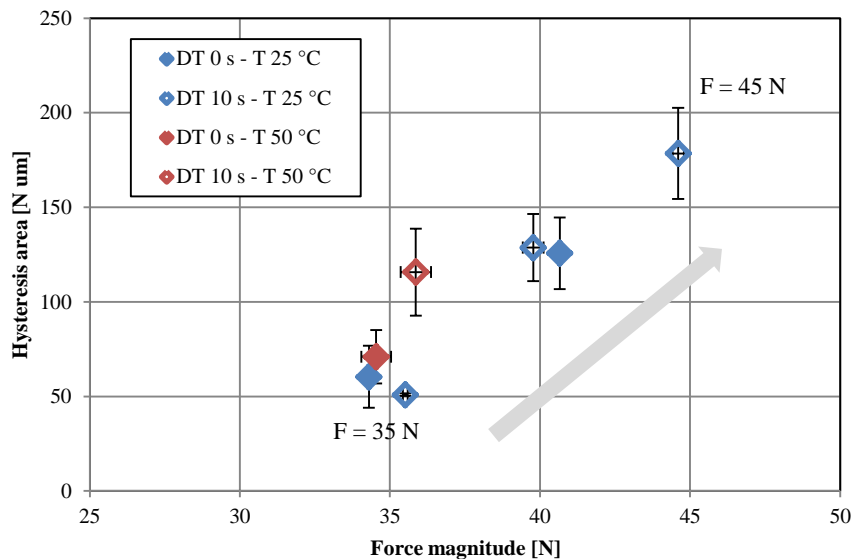


Figure 89 - Evolution of the hysteresis area as a function of the force magnitude for the different configurations performed with SAC305 assembly process samples

Impact of temperature and dwell time on the hysteresis area is not clearly observable. Evolutions of hysteresis area as a function of force magnitude are similar without and with 10 s dwell time at 25 °C. The hysteresis area increases from 50 to 175 N · μm when the force magnitude is increased from 35 to 45 N. Higher hysteresis area are obtained at 50 °C than at room temperature but this observation is hardly noticeable due to the scatter in the results.

*3.b.iv. Mechanical response conclusions*

Evolutions of mechanical parameters as a function of force magnitude have been described for the different test configurations. Impacts of temperature and dwell time have been described. Large dispersions are observed between the different samples. Observed trends with our sample are similar to those expected with standard bulk samples. Inelastic, plastic and creep displacements are increased when force magnitude is increased as the alloy is more viscous at 50 °C than at room temperature. Analysis and comparison with the obtained mechanical responses of electronic packages assembled in backward SnPb+ is a perspective.

**3.c. Damage indicators**

Mechanical parameters are now used in order to find relevant damage indicators for SAC305 alloy. These parameters are used in classical fatigue laws as damage measurements per cycle. For example, Coffin-Manson’s fatigue law uses the inelastic strain per cycle as a damage indicator. The damage per cycle is correlated with the developed inelastic strain per cycle. Force magnitude, inelastic displacement and hysteresis area are studied as damage indicator.

*3.c.i. Force magnitude impact on number of cycles to failure*

Evolution of force magnitude as a function of number of cycles to electrical failure is depicted for both assembly processes in Figure 90. Trend lines are obtained for each configuration considering a power law. Results are more scattered for SAC305 than for backward SnPb+ assembly processes.

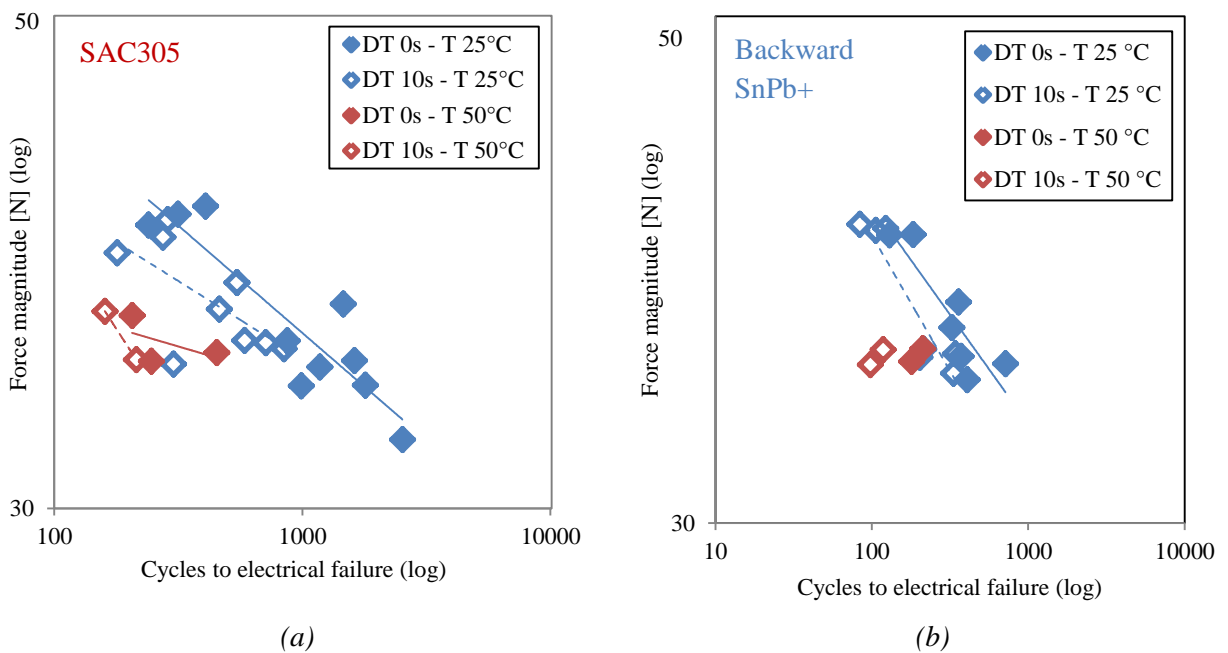


Figure 90 - Evolution of force magnitude as a function of number of cycles to electrical failure for both (a) SAC305 and (b) backward SnPb+ assembly processes

Results show that the force magnitude is a relevant damage indicator focusing on each configuration separately. The number of cycles to failure can be predicted with the force magnitude in a given configuration (without dwell time at 25 °C for example) using the trend line of this configuration. The force magnitude is however not a relevant damage indicator when all configurations are mingled. The different configurations cannot be represented precisely with one trend line. It means that the force magnitude cannot be used as unique damage indicator because other parameters have an influence on the number of cycles to failure. This result was expected because the force magnitude can be related to the applied stress.

3.c.ii. Inelastic displacement impact on number of cycles to failure

The inelastic displacement can be correlated to the inelastic strain per cycle developed in the solder joint matrix. The displacement can be converted into strain considering an homogeneous stress state as described in the previous chapter 2 (Eq. II-6 and II-7). The inelastic strain per cycle is used as damage indicator in the Coffin-Manson's fatigue law. Our results are plotted in Figure 91 for the different configurations.

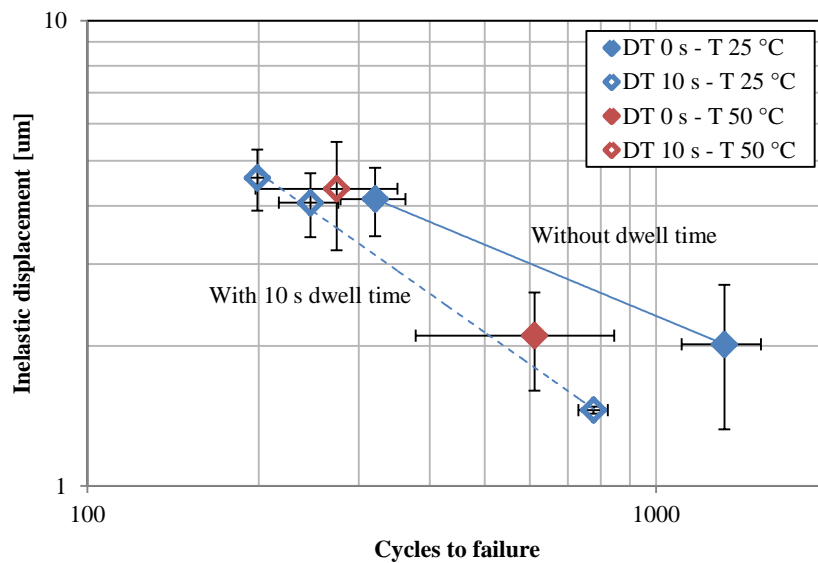


Figure 91 - Evolution of the inelastic displacement as a function of the number of cycles to electrical failure for SAC305 assembly process

Trend lines are obtained for the different configurations. The trend line obtained for the configuration without dwell time at room temperature (continuous blue line) is not aligned with the trend line obtained with 10 s dwell time (dotted blue line). Results show that the inelastic displacement cannot be used as a unique damage indicator. As for the force magnitude, the number of cycles to failure cannot be predicted with the inelastic displacement for all configurations which means that other parameters must be considered. The Coffin-Manson's fatigue law is not relevant with our results.

3.c.iii. Hysteresis area impact on number of cycles to failure

As described in the literature review in chapter 1, the density of dissipated energy per cycle is commonly used as damage indicator. The hysteresis area can be related to the density of dissipated energy which is interesting to assess the relevance of this damage indicator.

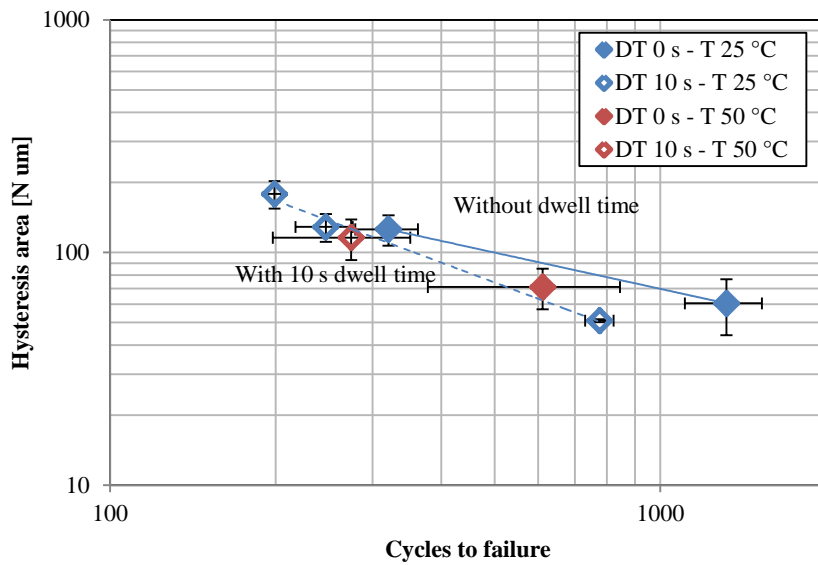


Figure 92 - Evolution of the hysteresis area as a function of the number of cycles to electrical failure for SAC305 assembly process

The evolutions of the hysteresis area as a function of the number of cycles to failure for the different configurations are plotted in Figure 92. Results show that different trend lines are obtained for the different configurations meaning that, as for force magnitude and inelastic displacement, the hysteresis area cannot be used as unique damage indicator. Dwell time and temperature parameters have an additional impact that is not discernable with the hysteresis area alone. The use of the density of dissipated energy per cycle as unique damage indicator is not relevant based on our results.

### 3.d. Discussions

The analysis of the mechanical response showed that effect of force, dwell time and temperature are similar than those expected for bulk specimens. Measured mechanical parameters have been studied as damage indicators based on their evolutions as a function of the number of cycles to failure. Inelastic displacement and dissipated energy cannot be used as damage indicators to predict the number of cycles to failure for all configurations. Different trend lines are obtained for the different configurations which means that the coefficients of the fatigue law would depend on the considered configuration. It is not sufficient because the fatigue law must be appropriate regardless of the configuration.

The number of cycles to failure is strongly reduced with the addition of 10 s dwell time at room temperature. This effect is also noticeable at 50 °C. Numbers of cycles to failure for SAC305 assembly process obtained without and with 10 s dwell time are compared in Figure 93. Values indicated for each configuration are: (i) the mean value in the center of the box, (ii) the standard deviation at the box extremities and (iii) minimum and maximum values at the ends. Dwell time parameter has a strong effect on the number of cycles to failure.

The strong reduction of the number of cycles to failure with dwell time does not correlate with a strong increase of the inelastic displacement. Figure 94 shows the increase of inelastic displacement with the addition of dwell time for SAC305 assembly at room temperature. The inelastic displacement variation with the addition of dwell time is not noticeable. The inelastic displacement is composed of the plastic displacement measured during loading and the creep displacement measured during maintain phase. Measurements of plastic and creep displacements are reported in Figure 95 for SAC305 assembly process at room temperature without and with dwell time. Plastic and creep displacement are mingled in the inelastic strain. It means that damages from plastic and creep displacements are supposed equivalent when the inelastic displacement is used as unique damage indicator. Dissociation of damages coming from plastic and viscous parts of the inelastic strain has been successfully applied in the case of torsion tests [3]. This method is evaluated with our results in the chapter 5.

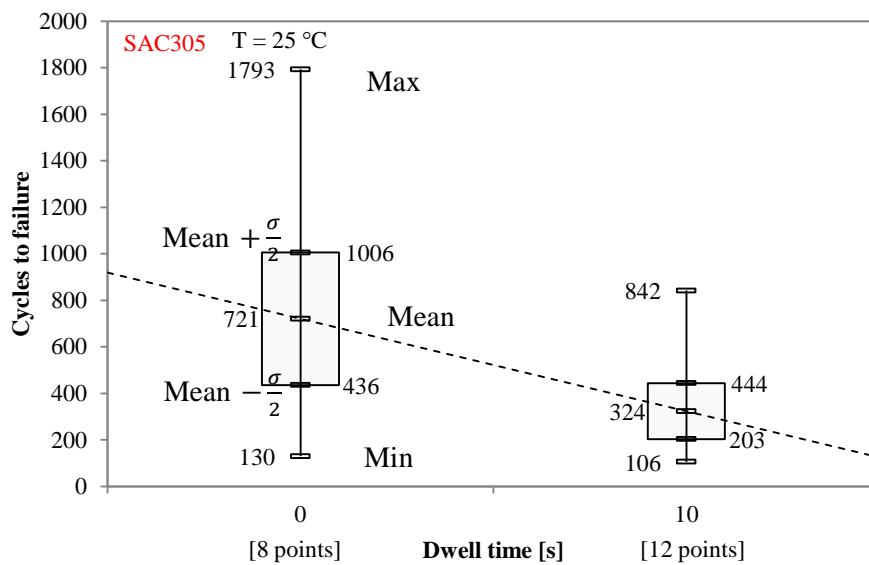


Figure 93 – Reduction of the number of cycles to failure with dwell time for SAC305 assembly process at room temperature

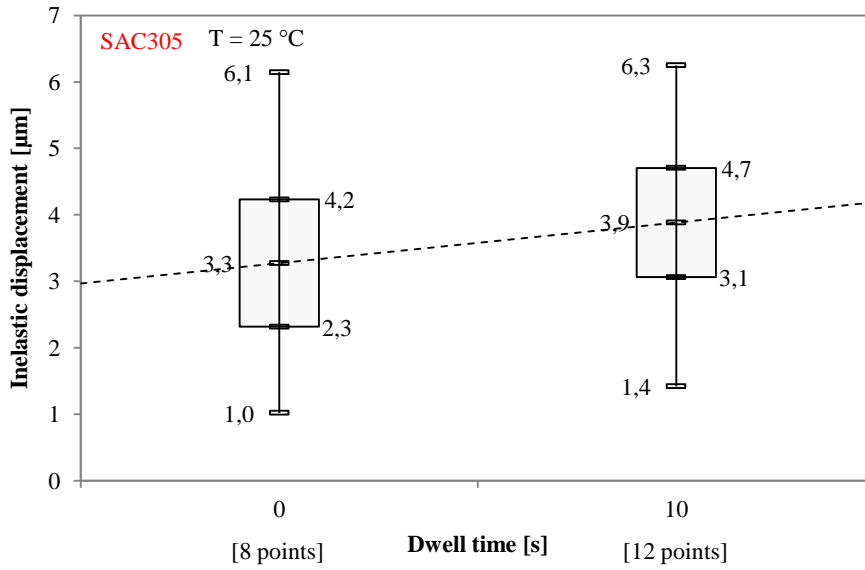


Figure 94 – Increase of inelastic displacement with dwell time for SAC305 assembly process at room temperature

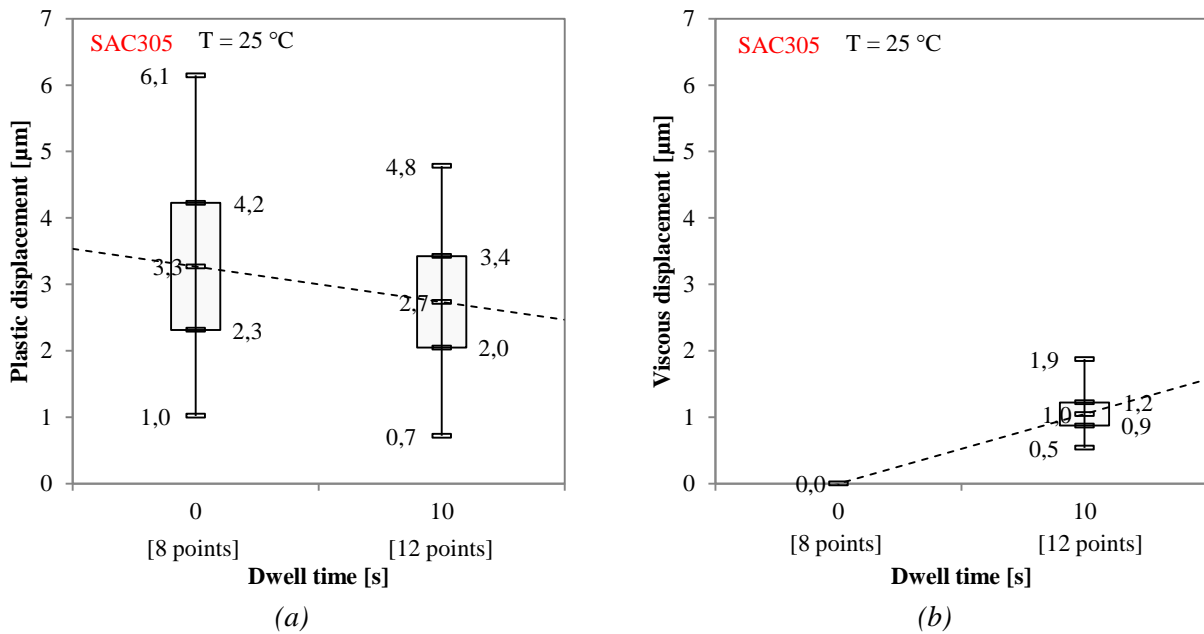


Figure 95 – Measured displacements without and with 10 s dwell time for SAC305 assembly process at room temperature: (a) plastic and (b) creep displacements



## 4. Conclusions

The fatigue test plan has been performed with samples assembled using lead-free SAC305 and leaded SnPb+ assembly processes. The test plan is composed of cyclic shear fatigue tests at different force magnitudes (from 30 to 45 N) and temperatures (25 and 50 °C). The impact of viscous damage has been studied with loadings which include 10 s of maintain phase at extremes force values (dwell time). A post-treatment analysis has been defined to validate tests and obtained results.

Numbers of cycles to failure for the different configurations have been analyzed considering a Weibull distribution. The number of cycles to failure is reduced when the force magnitude is increased. Addition of 10 s dwell time reduces the number of cycles to failure. Increase of temperature from room temperature to 50 °C reduces also the number of cycles to failure. Combination of addition of dwell time and temperature increase reduces the number of cycles to failure until a factor of 9 for SAC305 assembly process. Same trends have been observed for other package types in torsion [3].

Mechanical parameters have been extracted from the hysteresis curves with the method developed in the chapter 2. The mechanical response of samples assembled in SAC305 has been studied based on the measured mechanical parameters. Evolutions of inelastic, plastic and creep displacements with force magnitude have been analyzed for the different configurations. Inelastic and plastic displacements increase when the force magnitude is increased as obtained for classic bulk specimens. Higher inelastic and plastic displacements are obtained when the temperature is increased due to the viscosity of the alloy. As observed for the inelastic displacement, the hysteresis area increases when the force magnitude is increased. The comparison of measured mechanical parameters for backward SnPb+ assembly process with SAC305 is a perspective.

Several damage indicators have been analyzed as potential candidates to predict lifetime for solder joints. Evolutions of inelastic displacement and hysteresis area as a function of numbers of cycles to failure has been studied for the different test configurations. Results show that several trend lines are required for the different configurations which means that these damage indicators cannot be used alone in order to predict lifetime without using other parameters. Thus, commonly used Coffin-Manson's fatigue laws or other fatigue laws that use the density of dissipated energy per cycle as unique damage indicator are not relevant to predict lifetime for all configurations based on our results. The inelastic displacement is composed of the plastic displacement measured during loading phases and creep displacement measured during dwell time. Damages from plastic and creep parts of the inelastic strain are supposed equivalent when the inelastic displacement is used as unique damage indicator. Dissociation of plastic and creep damages in the fatigue law in order to take into account creep fatigue interaction is an interesting perspective that will be detailed in the chapter 5.

## Chapter V. Cyclic damage analysis

*The results of the fatigue tests have been presented in chapter 4. This chapter describes the methodology used to propose a new fatigue law for solder joint material based on these results. A viscoplastic model for SAC305 alloy is defined based on the mechanical response of the samples during creep and fatigue tests, and then used to evaluate cyclic plastic and creep strains per cycle of each fatigue test.*

*In this work, fatigue law defines a relation between the damage per cycle and the associated number of cycles to failure. For example, the inelastic strain per cycle is used as damage indicator in the Coffin-Manson's fatigue law. The frequency modified Coffin-Manson's fatigue law uses an additional parameter which is the frequency of the test. Both forms have been tested on our fatigue tests and results from the literature. While the frequency modified form takes into account frequency effect in a better way, results indicate prediction limitations for fatigue tests at high temperature.*

*As increase in temperature increases the development of creep strains per cycle, the dissociation of plastic and creep strains in the total inelastic strain is used in a new fatigue law to take into account the creep-fatigue interaction. Specific damages are defined for these two strain types. Additional results from the literature have been used to expand the reach of the law in other environments. The defined new creep-fatigue law gives interesting predictions even for fatigue tests at high temperature.*

*Dwell time impacts the number of cycles to failure because it generates cyclic creep strains during the maintain phase. The evolution of the number of cycles to failure with the dwell time duration has been studied in torsion [3] and in this work. Theoretical evolutions from the defined fatigue laws are compared with experimental results. The creep-fatigue law is sufficiently precise to reproduce the evolution of experimental numbers of cycles to failure as a function of dwell time duration.*

*The dissociation of plastic and creep damages in the fatigue laws gives relevant predictions for fatigue tests (i) at high temperature and (ii) with dwell times. Damage induces microstructural changes which are accumulated in the solder joints during each cycle of the fatigue tests. A preliminary study of the specific markers of plastic and creep damages is performed with two samples. These preliminary results open large perspectives on the study of the microstructure evolutions induced by cyclic damages for solder joint alloys.*

# 1. Fatigue of solder joints

Wear-out failure arises as a result of cumulative damage related to loads applied over an extended time. Creep-fatigue interaction requires to dissociate damages from plastic and creep strains in this cumulative damage. Importance of creep-fatigue interaction for solder joints alloys is highlighted in this part for the specific environments of aeronautic, space and defense applications.

## 1.a. Fatigue regimes

The fatigue of materials is classically divided in two regimes: the low cycle and the high cycle fatigue regimes. These two regimes are depicted in Figure 96. The limit between the two domains is defined by the presence or not of cyclic macroscopic inelastic strain in the stabilized asymptotic mechanical response.

Schematically, in the high cycle fatigue regime, the stabilized response of the sample is elastic and two domains are defined: limited and unlimited lifetimes. For stresses lower than the theoretical stress limit  $\sigma_e$ , the mechanical response is in the unlimited lifetime domain. In the low cycle fatigue, the hysteresis response can stabilize or not (ratcheting). The stress magnitude is sufficiently high to develop cyclic inelastic strains. The stabilized hysteresis response can be reached after several cycles.

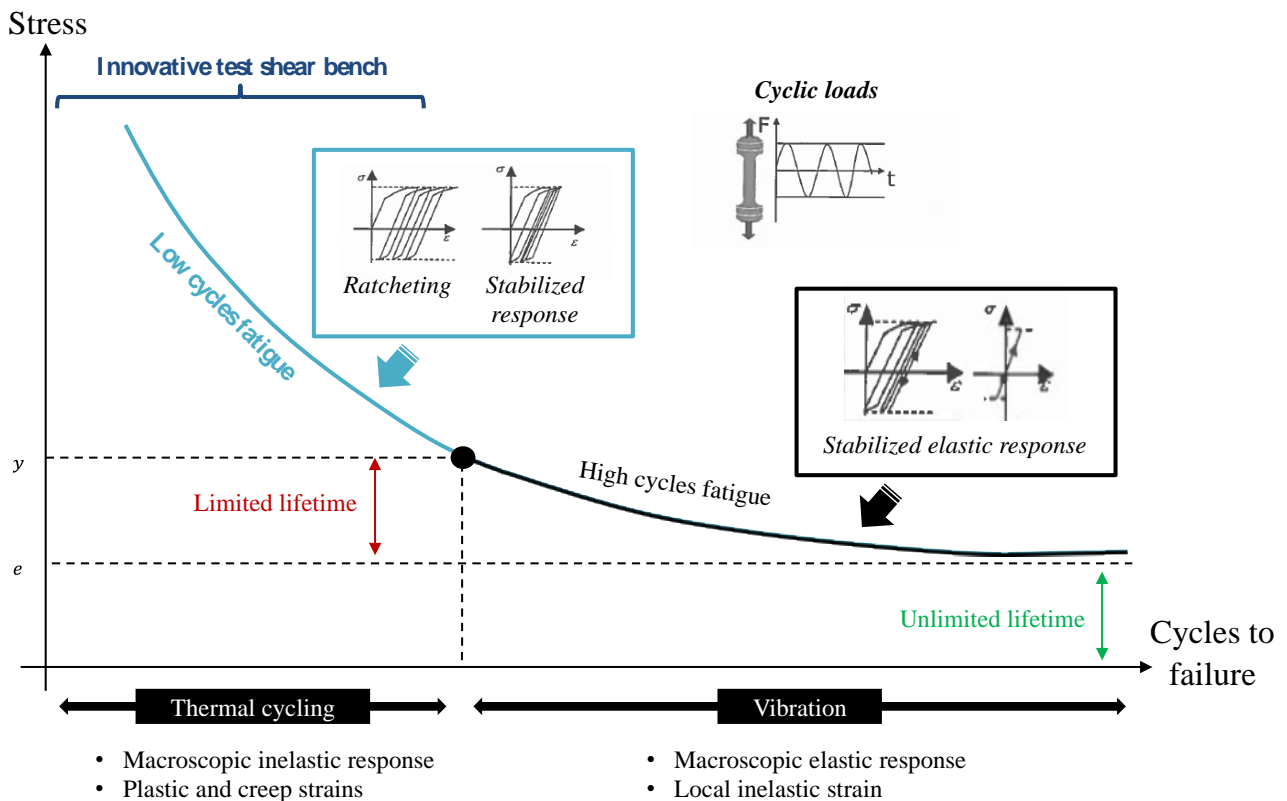


Figure 96: Schematic representation of the evolution of the applied cyclic stress as a function of cycles to failure for low cycle fatigue and high cycle fatigue regimes based on [48]

As introduced in chapter 1, two main environments are considered in the electronic industry to study reliability of solder joint. Mechanical vibrations induce high frequencies loadings in the solder joints: stresses coming from the cyclic bending of the Printed Circuit Board are transmitted to the

solder joint by the stiffness difference of the materials of the Printed Circuit Board and the electronic package. Due to the high frequencies of mechanical vibrations and the long lifetime of aeronautic, space and defense applications, the loading regime conducts to high cycle fatigue. Temperature variation is the other loading described in chapter 1. Temperature variations occur during ON / OFF operating, day / night climatic changes or during mission. Due to the low number of thermal cycles performed to qualify products with Accelerated Temperature Cycling (around 2,000), the loading regime corresponds to the low cycle fatigue.

### 1.b. Importance of creep-fatigue interaction for solder joint alloys

One of the specificities of alloys used for solder joint is their low melting temperature. This property is required by the assembly process of electronic board as temperature profile has to be higher than the melting temperature but without exceeding temperatures that would damage other parts of the electronic board. Melting temperatures of two solder alloys (lead SnPb and lead-free SAC305 solders) and that of aluminium are compared in Figure 97.

The temperature limit of “visible” viscosity can be estimated dividing the melting temperature (in Kelvin) by two. Melting temperatures of solder alloys varies between 180 and 240 °C which gives temperature limits of visible viscosity between -46 to -16 °C. All operating environments of products of aeronautic, space and defense industries have temperatures above these limits which indicates that solder joints have a significative viscous behavior. Creep strains will be generated during dwell time at constant temperature, for example during the flight after take-off in avionics.

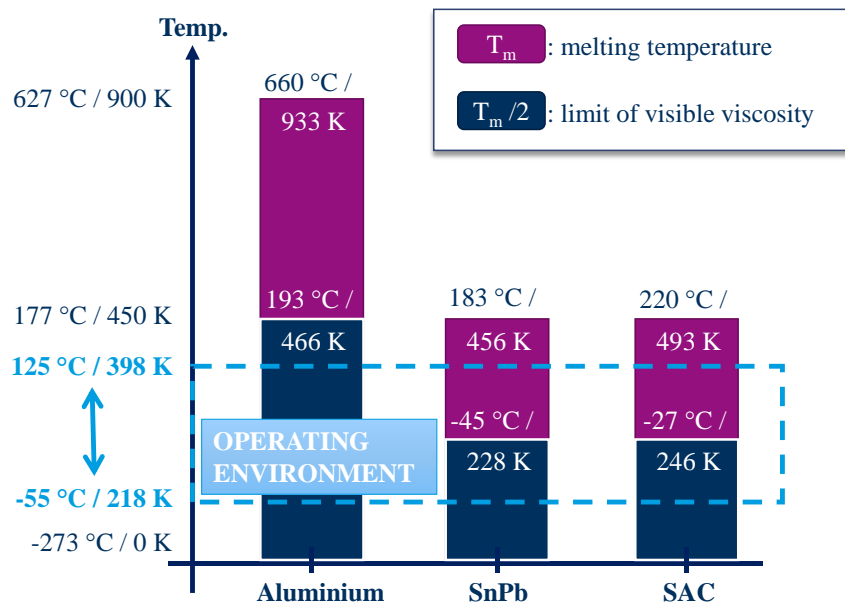


Figure 97: Melting temperature and creep domains for Aluminium, Leaded solder Sn37Pb and Lead-Free Sn3.0Ag0.5Cu solder

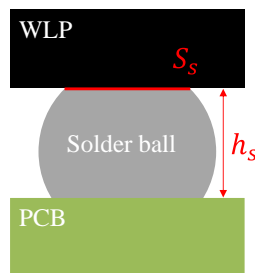
Fatigue test plan results obtained with our shear test bench indicate that dwell time and temperature parameters have an important impact on the number of cycles to failure which has to be associated to viscosity. The addition of dwell time introduces cyclic creep strains which increase the damage per cycle. Increase in temperature increases the viscous behavior of the alloy. These effects are quantified in the following part with measurements of plastic and creep strains in order to evaluate a fatigue law for solder joints which takes into account the creep-fatigue interaction.

## 2. Analysis of the results of the fatigue tests plan

Measured mechanical responses of the samples are used to define a constitutive law for the solder alloy. Force and displacement measurements are converted into intrinsic stress and strain quantities. The mechanical response of the sample is compared with experimental data from the literature. Parameters of the constitutive relation are calibrated using experimental measurements. The defined constitutive relation is used in order to distinguish creep and plastic strains from the experimental results for each fatigue test.

### 2.a. Shear stress and strain

Mechanical parameters are extracted from the hysteresis of the sample for each fatigue test. Force and displacement measurements must be converted into intrinsic stress and strain mechanical parameters in the solder joints matrix (36 balls) in order to: (i) compare the results with those of literature that use other sample types and (ii) use the results to calibrate a constitutive relation of the solder alloy which can be used in other contexts. Conversions from force to shear stress and from displacement to shear strain are made considering an homogeneous stress state. Eq. V-1 and Eq. V-2 give estimated values of homogeneous shear stress  $\tau$  and strain  $\gamma$  as a function of measured force  $F$  and displacement  $u_l$  with  $S_s$  the equivalent surface of solder joints,  $n_s$  the number of solder joints of the matrix and  $h_s$  the solder joint height.



$$\text{Stress } \tau = \frac{F}{n_s \cdot S_s} \quad \text{Eq. V-1}$$

$$\text{Strain } \gamma = \frac{u_l}{h_s} \quad \text{Eq. V-2}$$

*Figure 98: Shear stress and strain conversion from solder joint dimensions and force and displacement measured during fatigue test*

Accuracies of stress and strain are evaluated from accuracies of experimental measurements. Accuracies of force (0.1 N) and displacement (0.1  $\mu\text{m}$ ) have been measured in chapter 2 and 2 % accuracy must be considered for the measure of solder joint height (180  $\mu\text{m}$ ) and 20 % for the solder joint surface (1.77  $\text{mm}^2$ ).

Stress accuracy for stresses higher than 5 MPa is 20 % as detailed in Table 19. The accuracy is measured at three force levels (1, 10 and 30 N). The stress accuracy is evaluated with cumulative measurements accuracies of force and surface of solder joints.

*Table 19: Accuracies of stress from accuracies of force and surface of solder joints*

Stress accuracy	Surface of solder joints	Stress
Force level = $1 \pm 0.05$ N	$1.77 \text{ mm}^2 \pm 20 \%$	$0.6 \text{ MPa} \pm 25 \%$
Force level = $10 \pm 0.05$ N		$5.6 \text{ MPa} \pm 20 \%$
Force level = $30 \pm 0.05$ N		$11.3 \text{ MPa} \pm 20 \%$

Similarly to the stress accuracy, strain accuracy is measured at three displacement levels (1, 5 and 10  $\mu\text{m}$ ). The strain accuracy is evaluated with cumulative measurements accuracies of displacement and height of solder joints. Strain accuracy for strains higher than 5 mm/m is lower than 10 % as reported in Table 20.

Table 20: Accuracies of strain from accuracies of displacement and height of solder joints

Strain accuracy	Height of solder joints	Strain
Displ. level = $1 \pm 0.05$ $\mu\text{m}$	$180 \mu\text{m} \pm 2 \%$	$5.6 \text{ mm/m} \pm 7 \%$
Displ. level = $5 \pm 0.05$ $\mu\text{m}$		$27.8 \text{ mm/m} \pm 3 \%$
Displ. level = $10 \pm 0.05$ $\mu\text{m}$		$55.6 \text{ mm/m} \pm 3 \%$

## 2.b. Inelastic strains

Shear stress and inelastic strain are estimated using measurements of force magnitude and inelastic displacement and the assumption of the homogeneous stress state. Evolutions of shear stress as a function of inelastic strain are plotted in Figure 99 for monotonic and cyclic step-stress and fatigue tests. For monotonic tests, the inelastic strain  $\gamma_{ine}$  is obtained by subtracting the elastic strain  $\gamma_e$  from the total strain  $\gamma$  evaluated with the local displacement (Eq. V-3).

$$\gamma_{ine} = \gamma - \gamma_e \quad \text{Eq. V-3}$$

The increase of force magnitude for step-stress tests gives the mechanical response of the sample at different stress levels. Each step gives one measurement. Fatigue tests are performed for a given force level. Only one point is measurement by test for shear stress in the range 20 to 25 MPa. Results of fatigue tests are consistent with those from step-stress tests. Fatigue tests measurements are aligned with the mechanical responses of step-stress tests. Without and with dwell time configurations are mingled for both fatigue and step-stress results.

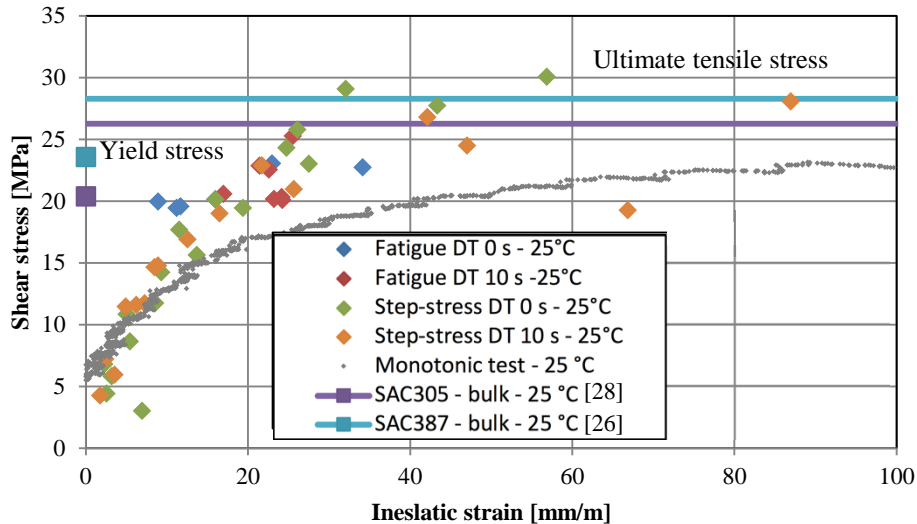


Figure 99: Mechanical responses measured from results of step-stress and fatigue tests

A difference between cyclic step-stress and fatigue tests and the monotonic test is noticeable. Cyclic tests are performed with a higher strain rate than monotonic tests which explains this difference. In fact, creep strains are developed during the loading of the sample due to the viscosity of the alloy. Thus, the amount of creep strain for a given shear stress level is higher for monotonic tests than for cyclic ones because the loading rate is lower.

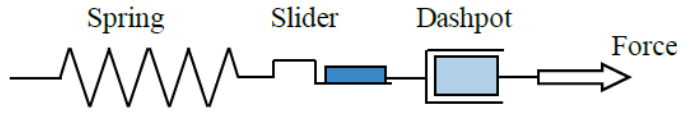
The mechanical response is compared with ultimate tensile stresses and yield stresses measured in [26] and [28] with bulk samples for the same temperature and at similar strain rates. Tensile measurements are converted into shear measurements using the von-Mises equivalent stress (see Eq. I-2 in chapter 1). Step-stress results are consistent with ultimate stresses from the literature. The shear stress measured during step-stress test reaches ultimate stresses from the literature when the inelastic strain increases.

Measured yield stresses with the present shear test bench are different than from bulk samples used in the literature measured with bulk samples. In the shear test bench, the sample is composed of a matrix of solder joints. The yield stress obtained with our experimental test bench (around 5 MPa) is lower than those from the literature that use bulk samples: cyclic inelastic strains are measured with our test bench for shear stresses higher than 5 MPa while yield stresses higher than 20 MPa have been measured in the literature. The stress concentration in the corners of solder joints is important in our case which induces local plasticity even for low stress levels. The surface of our samples (around 2 mm<sup>2</sup>) is significantly lower than those of bulk samples from the literature (around 10 mm<sup>2</sup>), increasing local plasticity effect, and opening interesting works on the stress homogeneity hypothesis.

Damages coming from plastic and creep strains are dissociated in order to take into account creep-fatigue interaction. A viscoplastic constitutive model (calibrated on the measured mechanical responses of the sample) is thus required to separate plastic and creep strains as following. The mechanical response measured during dwell times and the results of preliminary creep tests are used to define first the parameters of the creep part of the constitutive model. Parameters of the plastic part are then defined based on the results of fatigue and monotonic tests. To achieve this, the plastic strain is obtained subtracting the computed creep strain from the measured inelastic strain.

2.b.i. Viscoplastic model

The viscoplastic constitutive model is described in Figure 100. Plastic and creep parts of the inelastic strains are separated. The total strain is composed by the elastic  $\gamma_e$ , plastic  $\gamma_p$  and creep  $\gamma_c$  shear strains, as formulated in Eq. V-5. The stress is equal in the three elements representing the elastic part (spring), the plastic part (slider) and the creep part (dashpot). Eq. V-4 gives the relation defined by the spring between the elastic part of the total strain and the applied shear stress  $\tau$ . The spring stiffness is the shear modulus of the solder joint  $G$ .



$$\tau = G \cdot \gamma_e \quad \text{Eq. V-4}$$

$$\gamma = \gamma_e + \gamma_p + \gamma_c \quad \text{Eq. V-5}$$

Figure 100: Maxwell representation to describe the material; the spring gives the elastic strain, the slider the plastic strain, and the dashpot the creep strain. The force is equal for all three elements, whereas the strains are additive [75]

The creep strain is computed by integrating the creep strain rate  $\dot{\gamma}_c$  with time (see Eq. V-6). Creep strain rate is modeled using the sinh power law breakdown formulation (Eq. V-7) which is commonly used in the literature for solder joint alloys as described in chapter 1.

$$\gamma_c = \int \dot{\gamma}_c dt \quad \text{Eq. V-6}$$

$$\dot{\gamma}_c = A \left( \sinh \left( \frac{\tau}{\tau_N} \right) \right)^n \exp \left( -\frac{Q}{kT} \right) \quad \text{Eq. V-7}$$

The plastic strain  $\gamma_p$  follows the yield stress  $\tau_y$  evolution which is described in the following equation Eq. V-8. Yield stress and strain rate are linked with a linear relation on a log-log scale at intermediate and low strain rates [75] [76].  $\tau_{y,ref}(\dot{\gamma}_p)$  denotes the yield stress at a reference strain rate,  $C_1$  and  $C_2$  are fitting coefficients,  $\dot{\gamma}$  is the total strain rate,  $Q$  is the activation energy,  $k$  is the Boltzmann constant and  $T$  is the absolute temperature.

$$\tau_y = \tau_{y,ref}(\dot{\gamma}_p) \left( C_1 + C_2 \left( \ln(\dot{\gamma}) + \frac{Q}{kT} \right) \right) \quad \text{Eq. V-8}$$

2.b.ii. Model calibration

The mechanical response of the sample is used in order to calibrate the parameters of the viscoplastic constitutive model described by Eq. V-5, 7 and 8 as following. The double-tanh equation (Eq. V-9) is first used in order to smooth experimental noise. This step is required to extract the different mechanical parameters [75].  $C^i$ ,  $C^{ii}$ ,  $C^{iii}$  and  $C^{iv}$  are fitting coefficients based on experimental results.



$$\tau = C^i \tanh(C^{ii} \gamma) + C^{iii} \tanh(C^{iv} \gamma) \quad \text{Eq. V-9}$$

Experimental results obtained during fatigue and step-stress tests at 5 mm/s loading rate and monotonic tests performed at 0.5 mm/s. Table 21 summarizes coefficients obtained for the two loading rates. Double-tanh trend curves for both loading rates are plotted versus experimental results in Figure 101.

Table 21: Coefficients of the double-tanh trend curves for both loading rates

Tests	$C^i$ [MPa]	$C^{ii}$	$C^{iii}$ [MPa]	$C^{iv}$
Fatigue and step-stress ( $1e-2 \text{ s}^{-1}$ )	33	7	2	5
Monotonic tests ( $1e-3 \text{ s}^{-1}$ )	20	18	5	5

### 2.b.iii. Viscous part of the viscoplastic constitutive model

The total inelastic strain is decomposed into the plastic and the creep strains. Both plastic and creep parts are modeled with the viscoplastic constitutive model. The creep strain is time-dependent and only creep strains are developed during dwell time. These results are used to calibrate the parameters of the formulation of the creep strain rate (Eq. V-7) with additional preliminary creep tests.

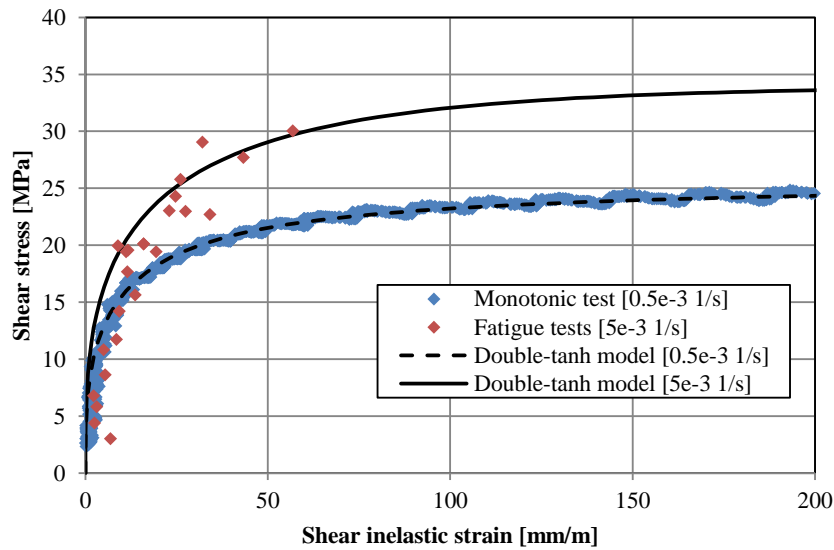


Figure 101: Double-tanh trend curves defined with experimental results from monotonic, fatigue and step-stress tests with samples assembled in SAC305

Only creep strains are developed during dwell time as previously indicated. Figure 102 shows the measurements of creep strains and stress relaxations for the different shear stress levels at the beginning of each dwell time. The results show that an increase in the shear stress induces an increase of the creep strain developed during dwell time and this evolution is not linear. For low shear stress regime, the creep strain is not significant regarding the total inelastic strain. Above a certain shear stress limit (from 10 to 15 MPa with our results), important creep strains are developed. Results are compared with theoretical evolutions from the literature determined by experimental tests using lead-free solder materials with bulk [26] [77] and BGA [29] samples. The formulation of the creep strain

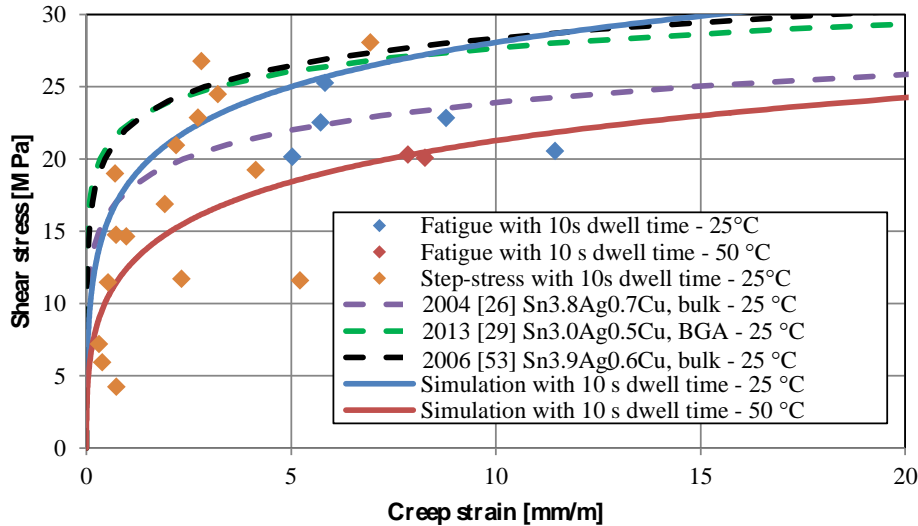
rate used by these authors is the power law breakdown. Our results are relevant with those from the literature and the creep strain rate relatively fits well with the power law breakdown.

Experimental results show that an increase in temperature increases the creep strain. This behavior is also expressed in the power law breakdown (Eq. V-7) with the exponential term, also called Arrhenius law, initially used to describe the rate evolution of chemical reaction with temperature.

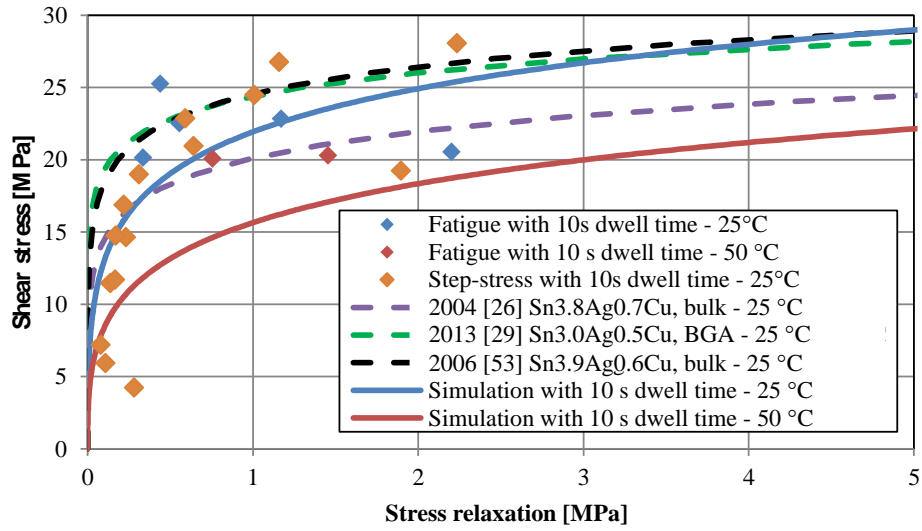
Additional preliminary creep tests have been performed and are used to define the parameters of the creep strain rate formulation. Figure 103 presents the results of these preliminary tests using our sample. Creep tests at three different force levels (10, 20 and 30 N) have been performed with three samples. Evolutions of creep displacement and force relaxation are recorded and converted into intrinsic creep strain and stress relaxation using the homogeneous stress state hypothesis. Parameters of the creep strain rate formulation are defined based on these preliminary results and are compared with the literature in Table 22. Our measured parameters are included in the large scatter of the parameters found in the literature.

Table 22: Creep strain rate formulation parameters

	$A$ [1/s]	$\sigma_N$ [MPa]	$n$	$Q$ [KJ/mol]
Lau, <i>et al.</i> 2003 [77]	325	15	3.3	53
Pang, <i>et al.</i> 2004 [26]	32000	27	5.1	54
Darveaux, <i>et al.</i> [29]	4.62E+07	29	6.5	77.2
Measured parameters	6500	24	3	50

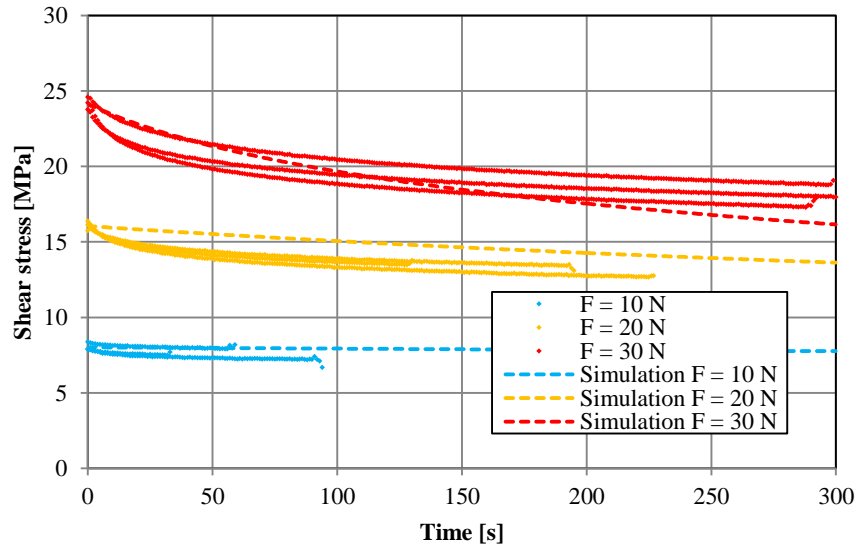


(a) Creep strain developed during dwell time as a function of applied shear stress

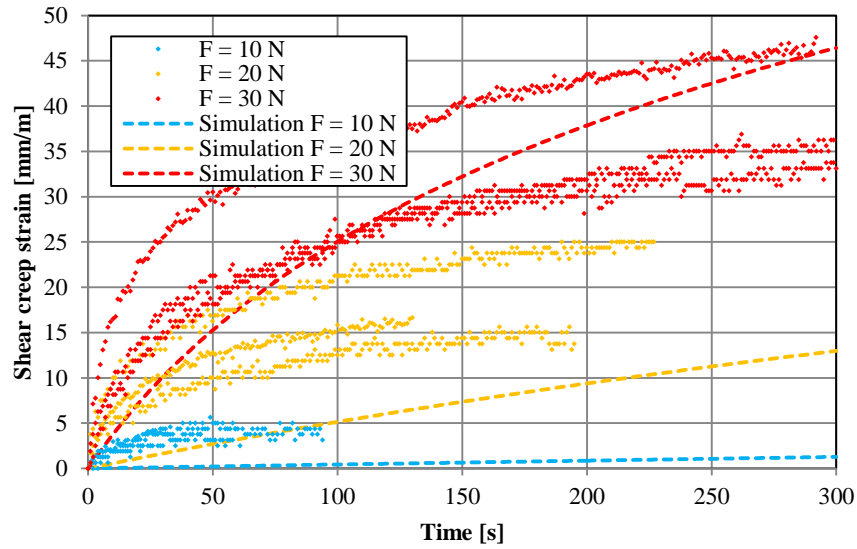


(b) Stress relaxation during dwell time as a function of applied shear stress

Figure 102: Comparison of the mechanical response during dwell time of fatigue and step-stress tests with theoretical formulations of the literature and the proposed creep simulation model



(a) Evolution of shear stress relaxation during maintain phase as a function of time



(b) Evolution of creep strain developed during maintain phase as a function of time

Figure 103: Results of preliminary creep and relaxation tests performed with our samples at different force levels (10, 20 and 30 N) and comparison with the proposed creep simulation model: evolutions of (a) stress relaxation and (b) creep strain

### 2.b.iv. Plastic part of the viscoplastic constitutive model

The plastic part of the inelastic strain is described by the evolution of the yield stress as a function of the plastic strain (see Eq. V-7). Coefficient  $C_1$  and  $C_2$  of Eq. V-8 have been determined for the SAC305 alloy in [75] and are used in our viscoplastic constitutive model (see Table 23).

Table 23: Parameters of the yield stress evolution as a function of plastic strain for SAC305 alloy from [75]

$C_1$	$C_2$
-0.090	0.039

The creep strain rate formulation, determined in the previous section, is used to separate the plastic strain rate from the total inelastic strain rate. The creep strain computed with the creep strain rate formulation is subtracted from the measured inelastic strain to obtain the plastic strain. The evolution of the plastic strain rate obtained with this method as a function of the total strain is depicted in Figure 104 for both loading rates (monotonic and fatigue tests). The results show that the plastic strain rate first increases when the total inelastic strain increases due to the exclusive development of plastic strain in the total inelastic strain at low stress regime. Then, the ratio of plastic to total strain rate decreases because the part of the creep strain rate in the total inelastic strain rate becomes important at higher stress levels.

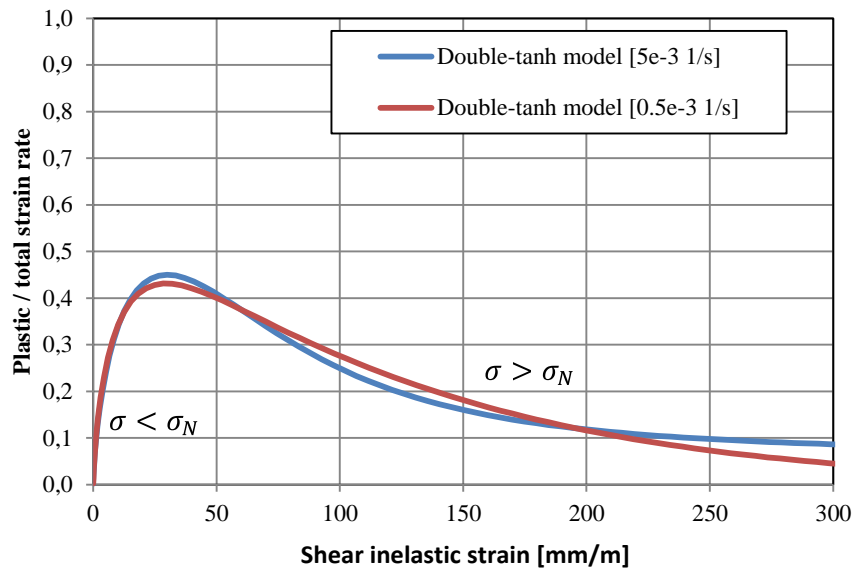


Figure 104: Plastic to total strain rate ratio as a function of the total inelastic strain for the two different loading velocities of fatigue and monotonic tests

The evolutions of the reference shear yield stress as function of the plastic strain is depicted in Figure 105 for monotonic and fatigue tests. The results show that the reference shear yield stress represents the plastic strain evolution and is time-independent. The two curves are now superposed for fatigue tests performed at  $5 \cdot 10^{-3}$  1/s and monotonic tests performed at  $5 \cdot 10^{-3}$  1/s. The plastic strain follows the yield stress evolution which is obtained with the reference yield stress evolution and the strain rate coefficient as formulated in Eq. V-7.

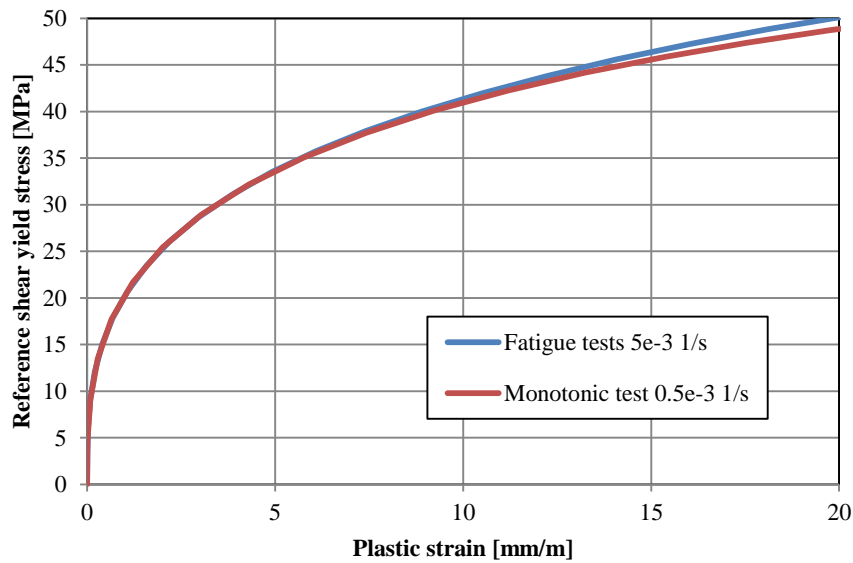


Figure 105: Reference shear yield stress as a function of the plastic strain for the two experimental different velocities of loading from fatigue and monotonic tests

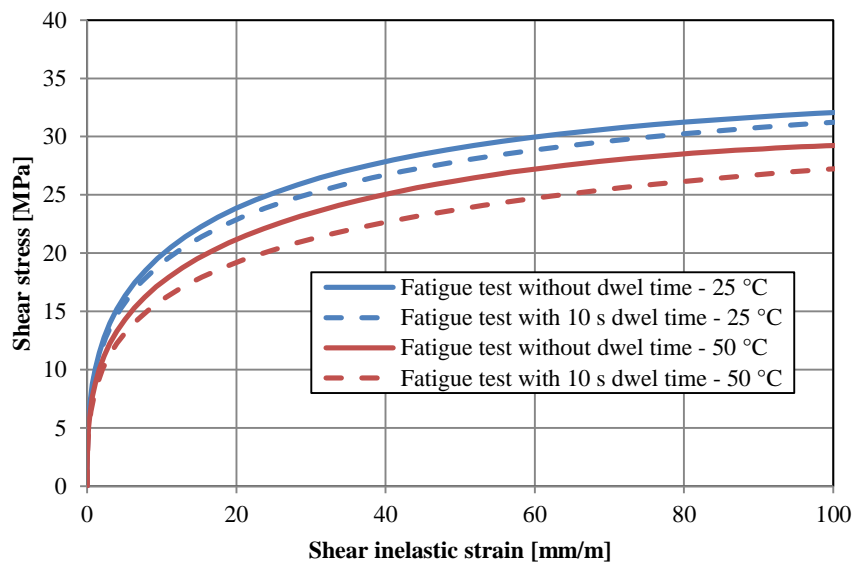


Figure 106: Theoretical mechanical response of the sample at 25 and 50 °C including or not 10 s of dwell time

### 2.c. Simulation of the sample mechanical response

The viscoplastic constitutive model can be used to compute the mechanical response of the sample for other un-tested configurations. Figure 106 presents the theoretical mechanical response of the sample for different temperatures (25 and 50 °C) and dwell times (0 and 10 s of dwell time). The computed cyclic inelastic strain is evaluated for all stress levels of the different configurations. The sensitivity to the creep strain rate causes these variations of the mechanical response.

This viscoplastic constitutive model is also interesting because the creep and plastic parts of the total inelastic strains are dissociated. This decoupling is required to apply the creep-fatigue law proposed in the following part.

### 3. Creep-fatigue-interaction law for solder joint

Experimental results of the test plan are used in this part to compare different fatigue laws for solder joint alloys. Based on measured mechanical parameters, different damage indicators are tested. The viscoplastic constitutive model is used to dissociate the plastic and creep parts of the total inelastic strain.

#### 3.a. Damage indicators synthesis

The evolution of the shear stress as a function of the cycle to electrical failure is depicted in Figure 107 for the different tested configurations. Trend curves indicate that the number of cycles to failure is reduced when the stress is increased for each configuration. They also show that the stress is not the only parameter that influences the reduction of the cycles to failure. Considering the same level of shear stress, the addition of 10 s of dwell time reduces the number of cycles to failure. The increase in temperature also reduces the number of cycles to failure. Therefore, the shear stress cannot be used as unique parameter to predict the number of cycles to failure.

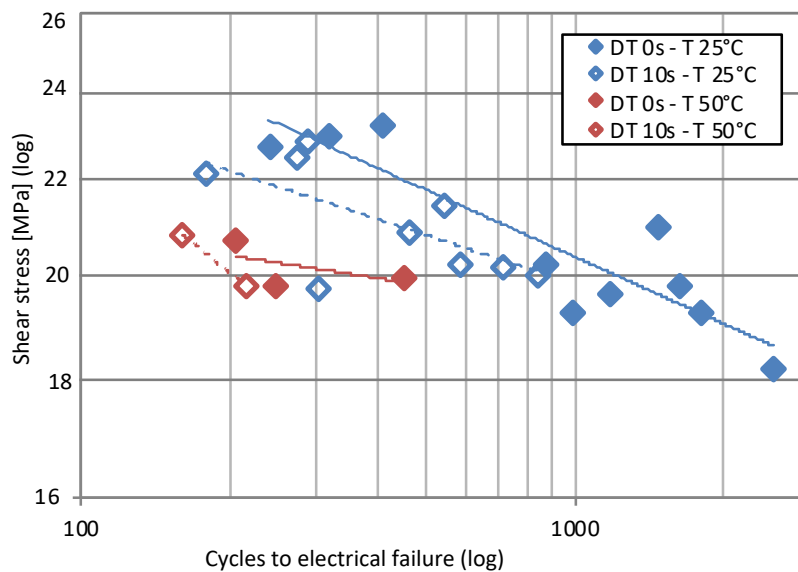


Figure 107: Influence of stress on the Sn3.0Ag0.5Cu alloy fatigue results

The literature review detailed in chapter 1 presents several fatigue laws commonly used in the industry and for solder joint alloys. The fatigue laws are composed of a damage law expressed with one or several mechanical parameters that are often linked to the number of cycles to failure with a power law. Time-independent mechanical parameters are not sufficient to predict the number of cycles to failure for solder joint due to the viscosity of the material. The mechanical quantities generally used in such damage laws are the inelastic, plastic or creep strains and the dissipated energy.

The addition of a frequency factor in the damage law is promising because the loading frequency is a test parameter which is known. Time-dependent effects as viscosity are easily incorporated in the

damage law with the frequency factor. Another possibility is to dissociate from the total inelastic strain the plastic and creep parts. Different damage contributions are affected for these two types of inelastic strain in the fatigue law. The impact of time-dependent phenomena is added with the creep strain quantity. This method takes into account the creep-fatigue interaction. Both fatigue laws have been tested with our experimental fatigue tests and with additional results from the literature.

### 3.b. Damage law for solder joint material

#### 3.b.i. Coffin-Manson's fatigue law

Commonly used Coffin-Manson's fatigue law has been introduced in chapter 1. The formulation is reminded below (Eq. V-10). The damage indicator is the inelastic strain per cycle  $\Delta\varepsilon_{inel}$ . This damage is correlated with the number of cycles to failure  $N_f$  using a power law.

$$N_f^n \Delta\varepsilon_{inel} = C \quad \text{Eq. V-10}$$

$C$  and  $n$  are constants that are material dependent and they must be determined with experimental fatigue tests. The inelastic strain per cycle  $\Delta\varepsilon_{inel}$  must be analyzed as a damage indicator. The evolution of the inelastic strain per cycle as a function of the number of cycles to failure for different fatigue tests performed with different test benches is plotted in Figure 108. The results of our fatigue test plan are completed with fatigue results from torsion tests and classic fatigue tests with bulk samples (see explanations in following paragraph). As depicted in the figure, our experimental results are constrained in a small fatigue domain from 100 to 3000 cycles but the results coming from the literature expand the validity domain of the damage law. In a log-log scale, the curve slope is the  $n$  material constant of the Coffin-Manson's fatigue law.

Table 24: Coffin-Manson's fatigue law parameters defined with our fatigue tests and additional fatigue results from the literature [3] [57] [26]

$C$	$n$
2	0.8



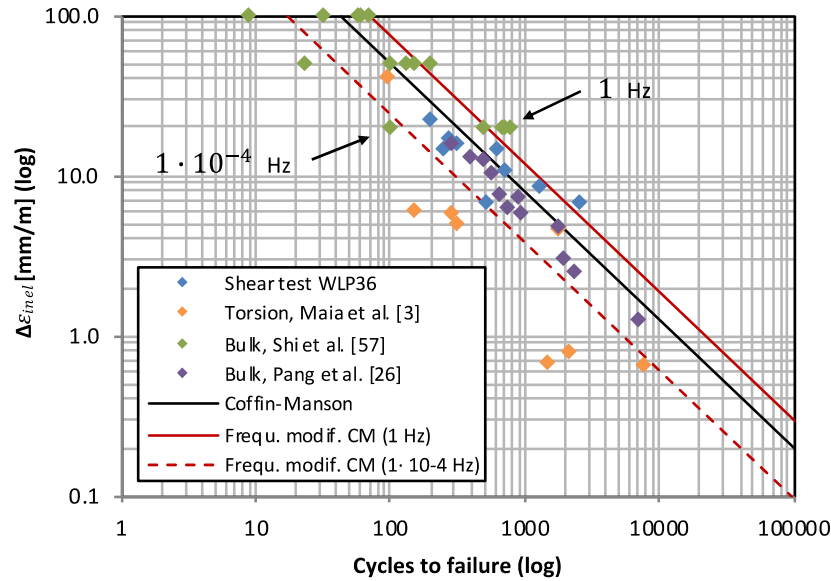


Figure 108: Coffin-Manson's fatigue laws, and frequency modified formulation, calibrated with fatigue results of our shear test bench, torsion tests and fatigue tests with bulks samples at different stress levels, dwell times and temperature

Result shows that the fatigue results obtained with our shear test bench and the different benches coming from the literature are consistent and they can be used to define material coefficients of the Coffin-Manson's fatigue law. Our results are compared with results obtained with bulk samples [57] [26]. The inelastic strain is measured directly from the measured hysteresis response of the bulk sample during the test for these setups.

Our results are also compared with fatigue tests using a torsion test bench [3]. For this specific bench, the inelastic strain is not directly measured during the test and must be estimated with simulation. Strain gages have been used to measure the Printed Circuit Board deformation during the cyclic torsion of the electronic board. The shear displacement of the solder joints is then estimated based on this deformation. The inelastic strains per cycle is finally simulated for the loading case (dwell time, temperature and shear displacement magnitude) and the solder joint geometry with the viscoplastic constitutive mechanical model defined in the previous part and considering the solder joint dimensions, the strain rate, the loading profile, the temperature and an homogeneous stress state.

Obtained results are interesting because the inelastic strain per cycle seems to be a relevant damage indicator for various sample types and test configurations. However, the analysis reveals also that the prediction accuracy with the inelastic strain as unique damage indicator is not sufficient when the frequency range of the loading is large. The loading frequency impacts the developed viscous strain per cycle and modifies the damage per cycle and the induced number of cycles to failure.

### 3.b.ii. Frequency modified Coffin-Manson's fatigue law

The addition of a frequency factor is promising because the test frequency is generally known and this factor can take into account viscous phenomena. Frequency modified formulation of the Coffin-Manson's fatigue law are proposed in the literature [26] [55] [56] [57]. These formulations use three material parameters which are calibrated with the results. These three parameters are: the material constant  $D$ , the law exponent  $m$ , and the frequency exponent  $k$  (see Eq. V-11).  $D$  and  $m$  coefficients

are already present in the Coffin-Manson's classic formulation. The frequency coefficient is used to add the impact of the frequency  $\nu$  on the damage per cycle.

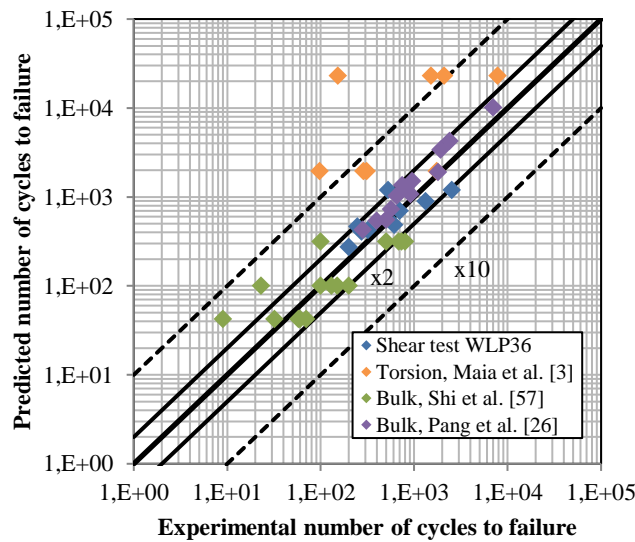
$$(N_f \nu^{k-1})^m \Delta \varepsilon_{inel} = D \tag{Eq. V-11}$$

The frequency modified Coffin-Manson's fatigue law is plotted in Figure 108 for two tests frequencies ( $1 \cdot 10^{-4}$  and 1 Hz). Prediction results obtained with Coffin-Manson's fatigue law and frequency modified form are compared in Figure 109. The parameters of the frequency modified Coffin-Manson fatigue model after calibration are summarized on Table 25.

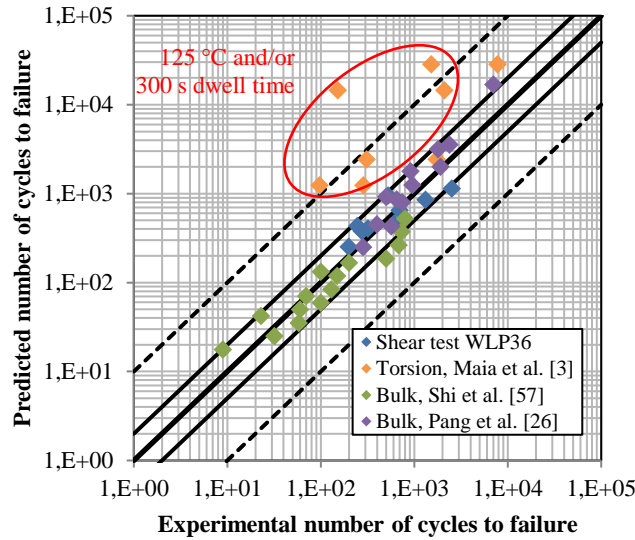
Table 25: Frequency modified fatigue law parameters

$D$	$m$	$k$
3	0.8	0.85

Experimental fatigue tests results performed with bulk samples at different frequencies clearly show the interest of the frequency modified form of the Coffin-Manson's fatigue law. The accuracy of the prediction is also increased for torsion fatigue tests as the dwell time modifies the frequency. However, the prediction of the model remains poor in the case of fatigue tests performed at high temperature ( $125\text{ }^\circ\text{C}$ ) and / or with long dwell time (300 s). Therefore, the dissociation of plastic and creep strains in the damage formulation seems promising because the developed creep strain per cycle is precisely higher for these specific configurations (high temperature or long dwell time). The creep-fatigue model is introduced in the following section.



(a) Classic Coffin-Manson's fatigue law



(b) Frequency modified form of the Coffin-Manson's fatigue law

Figure 109: Comparison of the prediction accuracies between (a) the classic Coffin-Manson's fatigue law and (b) the frequency modified form using experimental results from our shear test bench and additional results from the literature

### 3.b.iii. Creep-fatigue model

The previously introduced frequency modified form of the Coffin-Manson's fatigue law increases the prediction accuracy because the frequency factor modifies the damage per cycle using the loading frequency. Another option is to dissociate the damages coming from plastic and creep parts of the inelastic strain per cycle. They are merely added in the Coffin-Manson's fatigue law but implicitly considering a simple summation. However, nothing indicates that these damages are equivalent.

The viscoplastic constitutive model developed in the previous section is used to dissociate plastic and viscous parts of the inelastic strains. The different loading cases are simulated considering the stress magnitude and the parameters (temperature and dwell time) of the test. Figure 110 presents the results obtained for the different configurations of the test plan. The evolution of the plastic and creep strains as a function of the number of cycles to failure are plotted.

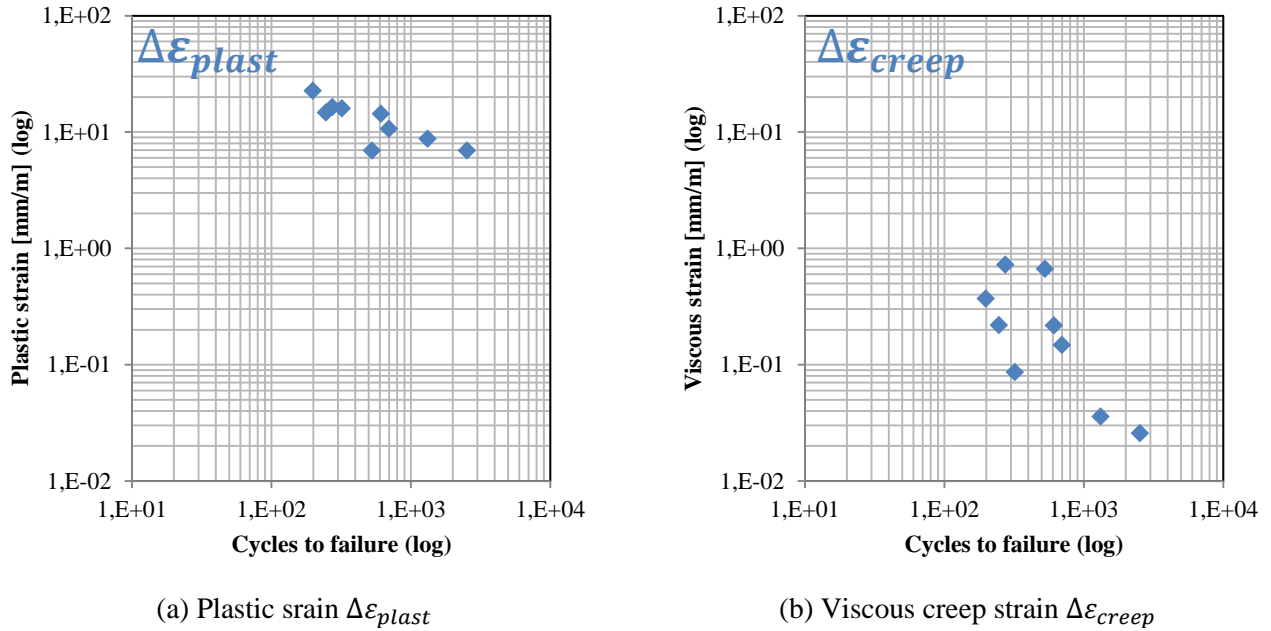


Figure 110: Comparison of the evolutions of (a) plastic and (b) creep strains as a function of number of cycles to failure for the different fatigue test configurations performed with our shear test bench

Results show that viscous strains are significantly lower than plastic one as developed plastic strains per cycle are 10 to 100 times higher than creep one. Due to this ratio, the calibration of a fatigue law that mingles these two strain types cannot take into account of creep damage because the creep part of the total inelastic strain is in fact neglected. The concept of the proposed creep-fatigue model is to weight the damage from viscous creep strain per cycle in the formulation as described in the equation below.

$$N_f^q (\Delta\varepsilon_{plast} + K\Delta\varepsilon_{creep}) = A \quad \text{Eq. V-12}$$

Material constants  $A$  and  $q$  have already been presented in Coffin-Manson's fatigue law. They are completed with an additional  $K$  viscous strain weighting coefficient. Table 26 indicates parameters of the creep-fatigue law obtained with the results of our shear test bench and torsion tests.

Table 26: Creep fatigue law parameters

$A$	$q$	$K$
10	0.9	10

Plastic and creep strains are weighted in the damage indicator of the creep-fatigue law. The creep strain per cycle is multiplied by the weighting coefficient  $K$  before being added to the plastic strain per cycle. The computed weighted inelastic strain is then used as damage indicator and is linked to the number of cycles to failure with a power law. The evolutions of the weighted inelastic strain as a function of the number of cycles to failure are plotted in Figure 111 for our fatigue results and torsion tests. The evolutions show that the weighted inelastic strain is an interesting damage indicator even for high temperature and long dwell time configurations of torsion tests. The weighted inelastic strain per cycle indicator can be used to predict cycles to failure for the different temperatures and dwell

times. This law takes into account creep-fatigue interaction in a large range of temperatures (from room temperature to 125 °C) and dwell times (from 0 to 300 s).

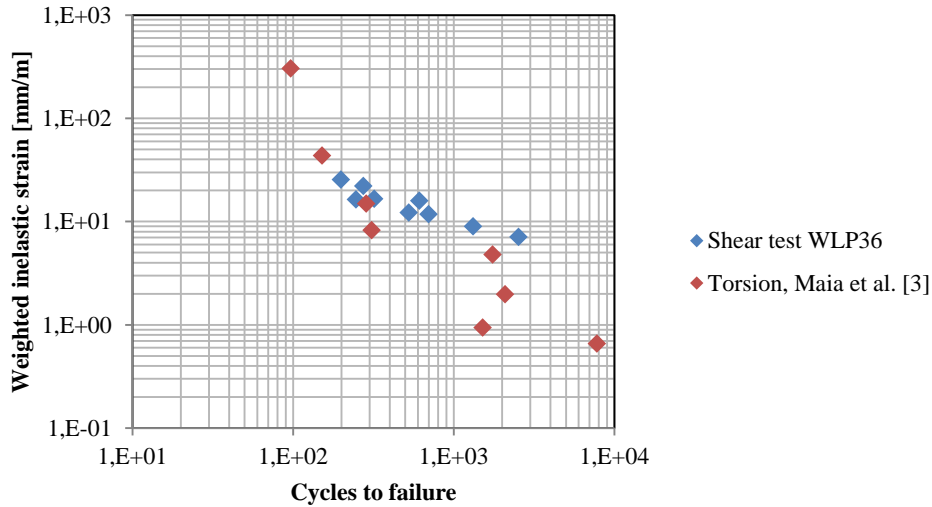


Figure 111: Weighted inelastic plastic and creep strains as a function of number of cycles to failure for fatigue tests performed with our shear test bench and in torsion at different temperatures (from room temperature to 125 °C) and dwell times (from 0 to 300 s)

Experimental and predicted numbers of cycles to failure using the creep-fatigue law are compared in Figure 112. Fatigue tests performed with our shear test bench and in torsion are used. Relevant predictions are obtained for the different test configurations, even in the case of configurations with high temperature and long dwell time. For these configurations, the viscous part of the inelastic strain provides a significant contribution to the damage per cycle. The weighting coefficient of the viscous strain allows to better take into account the contribution of the creep strain to the damage per cycle in the fatigue law.

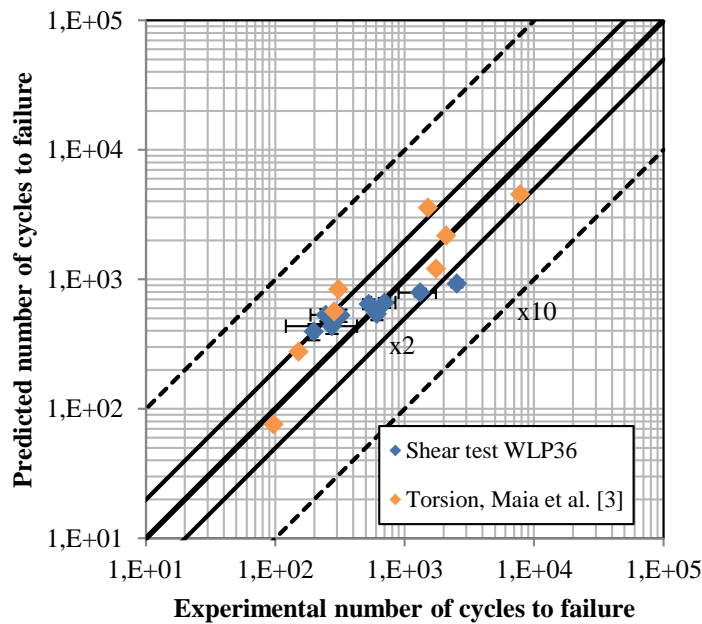


Figure 112: Correlation between predicted and experimental numbers of cycles to failure using the viscoplastic constitutive model and the creep-fatigue law with results of fatigue tests performed with our shear test bench and in torsion

### 3.c. Duration of dwell time

The addition of dwell time reduces the number of cycles to failure. The duration of the maintain phase is a parameter which is defined before running the test. For our tests plan, the duration (10 s) has been selected sufficiently high to observe an impact of dwell time without exceeding a reasonable test duration. Nevertheless, one fatigue test has been performed with a higher duration of dwell time (100 s) in order to study the impact of this duration on the number of cycles to failure.

The reduction factor ( $N_f$  reduction factor) is the quotient obtained by dividing the number of cycles to failure of a configuration without dwell time  $N_f(0)$  by the number of cycles to failure of same configuration but with a duration  $\delta T$  of dwell time  $N_f(\delta T)$ , as formulated in Eq. V-13.

$$N_f \text{ reduction factor} = \frac{N_f(0)}{N_f(\delta T)} \quad \text{Eq. V-13}$$

This reduction factor has been evaluated with the results of our shear test bench with fatigue tests performed without and with 10 s dwell time and with the unique fatigue test performed with 100 s dwell time. Additional results from torsion fatigue tests with dwell time duration from 1 to more than 300 s [3] have been added in order to complete the analysis. The evolutions of the reduction factor  $N_f$  reduction factor as a function of the duration of dwell time  $\delta T$  are plotted in Figure 113 for the two experimental test benches.

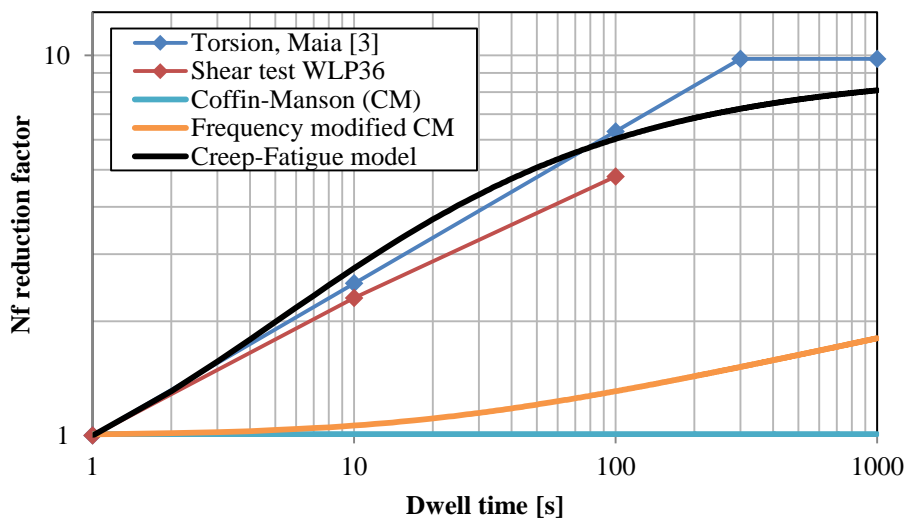


Figure 113 – Experimentally measured and theoretical evolutions of the reduction factor as a function of dwell time duration from shear and torsion fatigue tests and predicted results with the Coffin-Manson's fatigue law, the frequency modified form and the creep-fatigue law

The creep strains developed during the dwell time leads to an additional damage per cycle. The creep strain rate during the maintain phase of the dwell time is not constant because the solder joint structure tends to an asymptotic state during this phase. This phenomenon is illustrated by the evolution of the stress relaxation as a function of time obtained during creep tests (Figure 103). The creep strain rate decreases during the maintain phase. Thus, there is a time limit for the impact of the dwell time duration. After a period of time, the addition of extra time in the maintain phase doesn't

affect the quantity of developed creep strain. The quantity of viscous damage per cycle and the induced number of cycles to failure are no longer affected by dwell time duration. This effect has been observed with torsion tests using dwell time durations from 1 to more than 300 s. After 300 s of dwell time, the addition of dwell time duration doesn't affect the number of cycles to failure.

Experimental results are compared with theoretical evolutions of the reduction factor as a function of dwell time duration computed with the viscoplastic constitutive model and for the different fatigue laws defined in the previous sections (Coffin-Manson's fatigue law, frequency modified form and creep-fatigue law). The viscoplastic constitutive model is used to compute the mechanical response of the sample for different dwell time durations. The number of cycles to failure is then predicted for the considered fatigue law based on these computed mechanical responses. Numerical results are compared with experimental result in Figure 113. The Coffin-Manson's fatigue law is not relevant because the effect of dwell time is not taken into account. The frequency modified form of the law gives an evolution of the reduction factor as a function of dwell time duration because the increase of the dwell time duration reduces the test frequency. However, this evolution is not relevant compared with experimental measurements in particular for low duration. The asymptotic behavior is not modeled with this fatigue law because the increase of dwell time duration always decreases the test frequency even after the experimentally measured stabilization (at 300 s).

Only the creep-fatigue model captures the asymptotic behavior of the reduction factor. The damage is evaluated based on the computed plastic and viscous strains per cycle with the viscoplastic constitutive model. The evolution of the viscous strain per cycle as a function of dwell time duration is modeled with the constitutive model. The stabilization of the creep strain per cycle is due to the relaxation of the stress during the dwell time. This relaxation reduces the creep strain rate during the maintain phase until an asymptotic state. Additional dwell time duration will not affect the number of cycles to failure because the structure is already completely relaxed at the end of the dwell time period.

Damages induced by creep and plastic parts of the inelastic strain are dissociated in the creep-fatigue law. This separation better takes into account the experimentally measured evolution of the reduction factor of the number of cycles to failure as a function of dwell time duration. This law better takes into account creep-fatigue interaction even for high temperature and long dwell time configurations. Microstructure evolutions, as grain recrystallization, are induced by the cyclic stress. Separation of creep and plastic damages in the creep-fatigue law show interesting results. The analysis of specific microstructure evolutions induced by plastic and creep damages is thus interesting. Preliminary results on this topic are developed in annex 2. These results open interesting investigations in future works in order to evaluate specific indicators of plastic and viscous damages.

## 4. Conclusions

Chapter 4 describes the results obtained with the performed test plan. Mechanical values have been extracted of each fatigue test and are used to compute plastic and creep strains per cycle. Results have been used in this chapter in order to calibrate a viscoplastic constitutive model for solder joint. The hypothesis of homogeneous stress has been used in order to convert the measured mechanical parameters into stress and strain intrinsic values. Preliminary creep test results and measured mechanical parameters during dwell time of fatigue tests have been used in order to define the parameters of the creep strain rate law. This law has then been used to subtract the creep part of the inelastic strain per cycle in order to compute the plastic part. The evolutions of the reference shear yield stress as function of the plastic strain has been measured with this method. The viscoplastic constitutive model allows to compute the plastic and creep parts of the inelastic strain for each fatigue test in order to use different fatigue laws.

Our results show the limitation of classic Coffin-Manson's fatigue law in particular for configurations including dwell times. Experimental results from the literature have been used to complete our tests plan. Results include fatigue tests performed with bulk samples but also assembled electronic packages during torsion tests. The frequency modified form of Coffin-Manson's fatigue law increases the prediction accuracy for fatigue tests performed at different frequencies. The time-dependent damage from creep strain is better taken into account for this law with the frequency factor. However, limitations of this law exist in particular for configurations including long dwell times and at high temperatures.

A creep-fatigue law has finally been proposed. This model dissociates damages coming from plastic and viscous strains. The used constitutive model must dissociate plastic and creep parts of the inelastic strain per cycle. This fatigue law increases the prediction accuracy in the case of high temperature and long dwell time configurations. The evolution of the number of cycles to failure as a function of dwell time duration is consistent with the results from fatigue tests for this law.

Microstructure evolutions induced by the cyclic damage have been investigated using Energy Dispersive X-ray spectroscopy and Electron BackScatter Diffraction. Annex 2 describes briefly obtained results. Microstructural changes induced by the damage are observed, opening interesting perspective for further works.



## General conclusion

A fatigue law, taking into account the solder joint alloys' creep-fatigue interaction, is required for studying the reliability of electronic boards in the specific context of critical aeronautic, aerospace and defense industries. It can thus be said that no consensus exists in the literature regarding constitutive mechanical models and fatigue laws for reliability analysis concerning solder joints. Even in the case of the same alloy and the same constitutive law, large scatterings are observed in the mechanical parameters coming from different studies of the literature. A scale effect is observed between the different experimental methods and sample types of the literature.

The study has identified the lack of precise and clear measurements of the mechanical response of the assembled package, in particularly during cyclic fatigue tests to define a fatigue law that takes creep-fatigue interaction into account. The complexity of the microstructure in the final application complicates the analysis of mechanical properties of solder joint alloys. The relevance of experimental results obtained with bulk samples can be discussed. Chapter two has thus developed and discussed an innovative experimental test bench. It has been proven that fatigue shear test of assembled packages can be performed with high measurement accuracy of force and displacement, which are in turn used to evaluate mechanical stress and strain in the solder joint matrix during the fatigue test.

Monotonic and step-stress fatigue tests were performed during this study to validate test methodology. Moreover, a post-processing algorithm was used to extract the sample's hysteresis response from the measurements taken during the cyclic tests. A specific method is required to detect the failure due to the used particular sample. Chapter three thus defined electrical and mechanical failures. Monitoring the electrical resistance of the package's daisy-chain was thus essential for capturing the first solder joint's failure. No significant force magnitude changes were observed at the electrical failure due to the specific structure of the sample, which would be un-validate with classic fatigue criteria based on the evolutions of measured mechanical parameters in our case.

The electrical failure criterion was used in order to evaluate the number of cycles to failure in the analysis of the fatigue test plan's results. Analyzing the evolution of the mechanical values during the fatigue test showed that, before the electrical failure, they are indeed stable only until half-cycles. Subsequently, average values of the mechanical parameters until half of the electrical failure were used in the analysis of the results and the creep-fatigue law's calibration.

During the study, a fatigue test plan was performed with two assembly processes: leaded backward SnPb+ and lead-free SAC305. Moreover, force magnitude, dwell time and temperature impact on the number of cycles to failure were analyzed. The results reveal that all these parameters have an influence on the number of cycles to failure. The solder joint's viscous behavior is responsible for a huge reduction in the number of cycles of failure, in particular when faced with high temperature and dwell time configuration for both alloys. Classic Coffin-Manson's fatigue law is therefore unable to predict the number of cycles of failure with all parameters tested. It is therefore imperative to consider creep fatigue interaction in the law.

Within this study, a viscoplastic constitutive mechanical model for SAC305 alloy was defined through it being based on mechanical measurements from monotonic, creep and fatigue tests. Furthermore, the viscoplastic model dissociates plastic and creep strains. For each configuration, the model is then used to calculate the stress and developed inelastic strains. Based on our fatigue tests and additional results from the literature, two fatigue laws were defined in order to take into account time-dependent viscous damages originating from viscous strains. The modified frequency form of

the Coffin-Manson's fatigue law was evaluated and thus demonstrated an improvement regarding prediction accuracy. However, limitations were identified, in particular those regarding the impact of dwell time at high temperature.

A creep-fatigue model was then proposed to dissociate damages deriving from plastic and viscous strains. We found that the prediction accuracy of the model increased at high temperatures, as well as for long dwell times. Two solder joints were observed after fatigue tests, without or with dwell time, and through using Energy Dispersive X-ray spectroscopy and Electron BackScatter Diffraction. Microstructural evolutions are observed, which can be related to the creep mechanism. Further investigations into this topic are required in order to evaluate the specific markers of plastic and viscous damages.

Further works could also focus on how to improve the used hypothesis of the homogeneous stress to convert force and displacement measurement in stress and strain. In fact, the stress concentrates in the solder joint corners, which in turn, induces a complex mutliaxial loading. The analysis of solder joint stress state during the fatigue with Finite Element Analysis is a reasonable prospect.

The statistical reproducibility of fatigue tests is left to be discussed for some configurations. In future research, additional fatigue tests could provide fruitful findings to complete tendencies already observed within this study. Further test configurations with a longer dwell time for example or higher test temperature could also provide more results.

Fatigue laws, developed in this study, were indeed calibrated with experimental results performed at constant temperature values (from 25 to 125 °C), and this also included different test configurations (bulk sample, shear test and torsion). The developed creep-fatigue law demonstrates interesting prediction results within a large strain rate and temperature ranges. However, supplementary investigations are required to confirm the applicability of the law in other contexts, including temperature variations in Accelerated Thermal Cycling tests.

## Bibliography

- [1] IPC, "IPC-SM-785 Guidelines for Accelerated Reliability Testing of Surface Mount Solder Attachments," 1992.
- [2] W. Maia Filho, A. Lecavelier des Etangs-Levallois, S. Zanella and B. Candaele, "Importance of Creep Fatigue Interaction in Reliability of Solder Joint," *6th European Workshop on Reliability*, 2018.
- [3] W. Maia Filho, "Méthodologie d'essais accélérés de torsion et de détection de défaillance appliquée aux assemblages électroniques à billes," *Thèse de l'Université Bordeaux I*, Chapters 1, 2, 4 and 6, 2008.
- [4] W. Maia Filho, M. Brizoux, H. Frémont and Y. Danto, "Mission Profile Analysis for Accelerated Test Definition," *ELFNET Project Report*, 2007.
- [5] J. Galloway, L. Li, R. Dunne and H. Tsubakiet, "Analysis of Acceleration Factors Used to Predict BGA Solder Joint Field Life," *SMTA International Conference Proceeding*, 2001.
- [6] M. Pecht and J. Gu, "Physics-of-failure-based prognostics for electronic products," *Transactions of the Institute of Measurement and Control*, vol. 31, no. Sage, pp. 309-322, 2009.
- [7] R. Darveaux and K. Banerji, "Fatigue analysis of Flip chip assemblies using thermal stress simulations and a Coffin-Manson relation," *Proceedings of Electronic Components and Technology Conference*, pp. 797-805, 1991.
- [8] A. Grivon, D. Baudet, M. Brizoux, A. Lecavelier de Etangs-Levallois and W. Maia Filho, "Solder Joint Fatigue Characterization of DDR3 SDRAMs and Other Advanced BGA Packaging Memory Types," *SMTA Int.*, 2015.
- [9] R. R. Tummala, "Packaging: Past, Present and Future," *6th International Conference on Electronic Packaging Technology*, pp. 3-7, 2005.
- [10] W. Engelmaier, "The Use Environments of Electronic Assemblies and Their Impact on Surface Mount Solder Attachment Reliability," *IEEE Transactions on Components, Hybrids, and Manufacturing Technology*, vol. 13, no. 4, pp. 903-908, 1990.
- [11] T. E. Wong, B. A. Reed, H. M. Cohen and D. W. Chu, "Development of BGA Solder Joint Vibration Fatigue Life Prediction Model," *Proceeding of Electronic Components and Technology Conference*, 1999.
- [12] G. Massiot and C. Munier, "A Review of Creep Fatigue Failure Models in Solder Material - Simplified use of a Continuous Damage Mechanical Approach," *Proceeding of EuroSimE Conference*, 2004.
- [13] R. Darveaux, "Effect of Simulation Methodology on Solder Joint Crack Growth Correlation," *Journal of Electronic Packaging* 124(3), 2002.

- [14] P. Lall, M. Islam, N. Suhling and R. Darveaux, "Model for BGA and CSP Reliability in Automotive Underhood Applications," *IEEE Transactions on Component and Packaging Technologies*, vol. 27, no. 3, 2004.
- [15] L. Brownlee, "Lattice Constant of Grey Tin," *Nature*, vol. 166, p. 482, 1950.
- [16] R. Clark, G. B. Craig and B. Chalmers, "Mechanical twinning in white tin," *Acta Crystallographica*, vol. 3, p. 479, 1950.
- [17] W. Plumbridge, "Tin pest issues in lead-free electronic solders," *Lead-Free Electronic Solders, Springer US*, pp. 307-318, 2007.
- [18] M. Mueller, S. Wiese, M. Roellig and K. Wolter, "Effect of Composition and Cooling Rate on the Microstructure of SnAgCu-Solder Joints," *Proceeding of Electronic Components and Technology Conference*, pp. 1579-1588, 2007.
- [19] K. Kim, S. Huh and K. Sukanuma, "Effects of cooling speed on microstructure and tensile properties of Sn–Ag–Cu alloys," *Materials Science and Engineering*, vol. 333, pp. 106-114, 2002.
- [20] B. Dompierre, "Endommagement des matériaux sans plomb en environnement sévère," *Thèse de l'Ecole Centrale de Lille, Chapters 1, 2 and 3*, 2011.
- [21] I. Artaki and et al., "Research trends in lead-free soldering in the US: NCMS Lead-Free Solder Project," *Proceedings First International Symposium on Environmentally Conscious Design and Inverse Manufacturing*, pp. 602 -605, 1999.
- [22] D. Henderson and et al., "The microstructure of Sn in near-eutectic Sn Ag Cu alloy solder joints and its role," *Journal of Materials Research*, vol. 19, pp. 1608-1612, 2004.
- [23] L. Lehman and e. al., "Growth of Sn and intermetallic compounds in Sn-Ag-Cu solder," *Journal of Electronic*, vol. 12, pp. 1429-1439, 2004.
- [24] P. Vianco and J. Rejent, "Compression Deformation Response of 95.5Sn-3.9Ag-0.6Cu Solder," *UCLA Lead-Free Workshop*, 2002.
- [25] J. H. L. Pang, P. T. H. Low and B. Xiong, "Lead-Free 95.5Sn-3.8Ag-0.7Cu Solder Joint Reliability Analysis For Micro-BGA Assembly," *Proceeding of Inter Society Conference on Thermal Phenomena*, 2004.
- [26] J. H. L. Pang, B. Xiong and T. H. Low, "Creep and Fatigue Characterization of Lead Free 95.5Sn-3.8Ag-0.7Cu Solder," *Proceeding of Electronic Components and Technology Conference*, 2004.
- [27] J. H. Pang, B. S. Xiong, C. C. Neo, X. R. Bang and T. Low, "Bulk Solder and Solder Joint Properties for Lead Free 95.5Sn-3.8Ag-0.7Cu Solder Alloy," *Proceeding of Electronic Components and Technology Conference*, 2003.
- [28] F. Che, W. H. Zhu, E. S. W. Poh, X. W. Zhang and X. R. Zhang, "The study of mechanical properties of Sn–Ag–Cu lead-free solders with different Ag contents and Ni doping under different strain rates and temperatures," *Journal of Alloys and Compounds*, vol. 507, p. 215–224, 2010.

- [29] R. Darveaux and C. Reichman, "Solder alloy creep constants for use in thermal stress analysis," *Journal of Surface Mount Technology*, 2013.
- [30] K. Mysore, G. Subbarayan, V. Gupta and R. Zhang, "Constitutive and Aging Behavior of Sn3.0Ag0.5Cu Solder Alloy," *IEEE Transactions on Electronics Packaging Manufacturing*, 2009.
- [31] S. Pin, H. Frémont and A. Gracia, "Lead free solder joints characterisation using Single Lap Shear tests," *Proceeding of EuroSimE Conference*, 2017.
- [32] D. Bhate, D. Chan, G. Subbarayan, T. C. Chiu, V. Gupta and D. R. Edwards, "Constitutive Behavior of Sn3.8Ag0.7Cu and Sn1.0Ag0.5Cu Alloys at Creep and Low Strain Rate Regimes," *IEEE Transactions on Components and Packaging Technologies*, vol. 31, no. 3, 2008.
- [33] H. Ma, J. C. Suhling, Y. Zhang, P. Lall and M. J. Bozack, "The Influence of Elevated Temperature Aging on Reliability of Lead Free Solder Joints," *Proceeding of Electronic Components and Technology Conference*, 2007.
- [34] M. Mustafa, Z. Cai, J. C. Roberts, J. C. Suhling and P. Lall, "Evolution of the Tension/Compression and Shear Cyclic Stress-Strain Behavior of Lead-Free Solder Subjected to Isothermal Aging," *Proceeding of 13th IEEE ITherm Conference*, 2012.
- [35] M. Mustafa, J. C. Roberts, J. C. Suhling and P. Lall, "The Effects of Aging on the Fatigue Life of Lead Free Solders," *Proceeding of Electronic Components and Technology Conference*, 2014.
- [36] M. Mustafa, J. C. Suhling and P. Lall, "Experimental determination of fatigue behavior of lead free solder joints in microelectronic packaging subjected to isothermal aging," *Microelectronics Reliability*, p. 136–147, 2015.
- [37] P. Lall, S. Shantaram, J. Suhling and D. Locker, "Effect of Aging on the High Strain Rate Mechanical Properties of SAC105 and SAC305 Leadfree Alloys," *Proceeding of Electronic Components and Technology Conference*, 2013.
- [38] P. Lall, D. Zhang, V. Yadav, J. Suhling and D. Locker, "Effect of Temperature on the High Strain Rate Properties of SAC Leadfree Alloys at Temperatures up to 200°C," *Proceeding of Electronic Components and Technology Conference*, 2016.
- [39] S. Wiese, A. Schubert, H. Walter, R. Dudek, F. Feustel, E. Meusel and B. Michel, "Constitutive Behaviour of Lead-free Solders vs. Lead-containing Solders - Experiments on Bulk Specimens and Flip-Chip Joints," *Proceeding of Electronic Components and Technology Conference*, 2001.
- [40] Q. Xiao, L. Nguyen and W. D. Armstrong, "Aging and Creep Behavior of Sn3.9Ag0.6Cu Solder Alloy," *Proceeding of Electronic Components and Technology Conference*, 2004.
- [41] R. Darveaux and et al., "Effect of Joint Size and Pad Metallization on Solder Mechanical Properties," *Proceeding of Electronic Components and Technology Conference*, 2008.

- [42] Q. Zhang, A. Dasgupta and P. Haswell, "Viscoplastic Constitutive Properties and Energy-Partitioning Model of Lead-Free Sn<sub>3.9</sub>Ag<sub>0.6</sub>Cu Solder Alloy," *Proceeding of Electronic Components and Technology Conference*, 2003.
- [43] M. Röllig, S. Wiese, K. Meier and K.-J. Wolter, "Creep Measurements of 200 µm – 400 µm Solder Joints," *Proceeding of EuroSimE Conference*, 2007.
- [44] R. Darveaux and K. Banerji, "Constitutive Relations for Tin-Based Solder Joints," *IEEE Transactions on Components, Hybrids, and Manufacturing Technology*, vol. 15, no. 6, 1992.
- [45] R. Darveaux, "Shear Deformation of Lead Free Solder Joints," *Proceeding of Electronic Components and Technology Conference*, 2005.
- [46] R. Darveaux and C. Reichman, "Mechanical Properties of Lead-Free Solders," *Proceeding of Electronic Components and Technology Conference*, 2007.
- [47] J. Morris, H. Song and F. Hua, "Creep Properties of Sn-rich Solder Joints," *Proceeding of Electronic Components and Technology Conference*, 2003.
- [48] H. Maitournam, "Introduction à la fatigue des structures," *Ecole Polytechnique MEC562*, 2016.
- [49] E. Charkaluk, A. Bignonnet, A. Constantinescu and K. Dang Van, "Fatigue design of structures under thermomechanical loadings," *Fatigue and Fracture of Engineering Materials and Structures*, vol. 25, no. 12, pp. 1199-1206, 2002.
- [50] A. Qasaimeh, S. Hamasha, Y. Jaradat and P. Borgesen, "Damage Evolution in Lead Free Solder Joints in Isothermal Fatigue," *Journal of Electronic Packaging*, vol. 137, 2015.
- [51] S. Amiable, S. Chapuliot, A. Constantinescu and A. Fissolo, "A comparison of lifetime prediction methods for a thermal fatigue experiment," *International Journal of Fatigue*, vol. 28, pp. 692-706, 2006.
- [52] S. Tabibiana, E. Charkaluk, A. Constantinescu, F. Szymtka and A. Oudina, "TMF-LCF life assessment of a Lost Foam Casting A319 aluminum alloy," *International Journal of Fatigue*, vol. 53, pp. 75-81, 2013.
- [53] J. Lau, S. W. R. Lee, F. Song, D. Lau and D. Shangguan, "Isothermal Fatigue Tests of Plastic Ball Grid Array (PBGA) SnAgCu Lead-Free Solder Joints At 60°C," *Proceeding of Electronic Components and Technology Conference*, 2006.
- [54] H. Xu, T.-K. Lee and C.-U. Kim, "Fatigue Properties of Lead-free Solder Joints in Electronic Packaging Assembly Investigated by Isothermal Cyclic Shear Fatigue," *Proceeding of Electronic Components and Technology Conference*, 2014.
- [55] C. Kanchanomai, Y. Miyashita, Y. Mutoh and S. L. Mannan, "Influence of frequency on low cycle fatigue behavior of Pb-free solder 96.5Sn-3.5Ag," *Materials Science and Engineering*, vol. A 354, pp. 90-98, 2003.
- [56] C. Wang, Y. Zhu, X. Li and R. Gao, "Low Cycle Fatigue Behavior of SnAgCu Solder Joints," *Rare Metal Materials and Engineering*, vol. 45, no. 4, pp. 829-835, 2016.

- [57] X. Shi, H. Pang, W. Zhou and Z. Wang, "A Modified Energy-Based Low Cycle Fatigue Model for Eutectic Solder Alloy," *Scripta Materialia*, vol. 41, no. 3, p. 289–296, 1999.
- [58] R. Yuan, H. Li, H.-Z. Huang, Y. Liu and S. Zhu, "An Efficient Fatigue-Creep Interaction Life Prediction Model Based on Frequency Separation and Strain Energy Damage Theory," *Proceeding of Reliability and Maintainability Symposium (RAMS)*, 2013.
- [59] E. H. Wong, W. D. van Driel, A. Dasgupta and M. Pecht, "Creep fatigue models of solder joints: A critical review," *Microelectronics Reliability*, vol. 59, pp. 1-12, 2016.
- [60] Y. Zhu, X. Li, C. Wang and R. Gao, "A new creep–fatigue life model of lead-free solder joint," *Microelectronics Reliability*, vol. 55, pp. 1097-1100, 2015.
- [61] Y. Mutoh, J. Zhao, Y. Miyashita and C. Kanchanomai, "Fatigue crack growth behaviour of lead-containing and lead-free solders," *Soldering & Surface Mount Technology*, vol. 13, no. 3, pp. 37-45, 2002.
- [62] C. Anderssona, Z. Lai, J. Liu, H. Jiang and Y. Yu, "Comparison of isothermal mechanical fatigue properties of lead-free solder joints and bulk solders," *Materials Science and Engineering*, vol. 394, pp. 20-27, 2005.
- [63] W. Maia Filho, M. Brizoux, H. Frémont and Y. Danto, "Lifetime Prediction of BGA Assemblies with Experimental Torsion Test and Finite Element Analysis," *Proceeding of EuroSimE Conference*, 2008.
- [64] R. J. Coyle, K. Sweatman and B. Arfaei, "Thermal Fatigue Evaluation of Pb-Free Solder Joints: Results, Lessons Learned, and Future Trends," *The Minerals, Metals and Materials Society*, vol. 26, no. 10, pp. 2394-2415, 2015.
- [65] S. Zanella, A. Lecavelier des Etangs-Levallois, E. Charkaluk, W. Maia Filho and A. Constanteniscu, "Innovative Experimental Setup for Creep Fatigue Interaction in Solder Joints Analysis," in *MINaPAD Proceeding*, 2018.
- [66] K. Protassov, "Analyse statistique de données expérimentales," *EDP Sciences*, 2002.
- [67] P. Rabbe, H.-P. Lieurade and A. Galtier, "Essais de fatigue - Partie II," *Technique de l'Ingénieur*, no. M4171, 2000.
- [68] MIL-STD 883K change 2, "Test method standard microcircuits," 2017.
- [69] R. Metasch, M. Roellig, M. Kuczynska, N. Schafet, U. Becker, K. Meier and I. Panchenko, "Accelerated Life Time Measurement with In-situ Force and Displacement Monitoring during Thermal Cycling on Solder Joints," *EuroSimE Proceeding*, 2017.
- [70] M. Kuczynska, N. Schafet, U. Becker, R. Metasch, M. Roellig, A. Kabakchiev and S. Weihe, "Validation of Different SAC305 Material Models Calibrated on Isothermal Tests Using In-Situ TMF Measurement of Thermally Induced Shear Load," *EuroSimE Proceeding*, 2017.
- [71] S. Zanella, A. Lecavelier des Etangs-Levallois, E. Charkaluk, W. Maia Filho and A. Constanteniscu, "Importance of Electric Resistance Monitoring in Shear Test," *Microelectronics Reliability*, Vols. 88 - 90, pp. 733 - 737, 2018.

- [72] R. Darveaux, S. Enayet, C. Reichman, C. J. Berry and N. Zafar, "Crack Initiation and Growth in WLCSP Solder Joints," *Proceedings of Electronic Components and Technology Conference*, 2011.
- [73] A. Qasaimeh, S. Hamasha, Y. Jaradat and P. Borgesen, "Damage Evolution in Lead Free Solder Joints in Isothermal Fatigue," *Journal of Electronic Packaging*, vol. 137, 2015.
- [74] S. Zanella, A. Lecavelier des Etangs-Levallois, E. Charkaluk, W. Maia Filho and A. Constanteniscu, "Importance of Creep Fatigue Interaction in Solder Joint Reliability Analysis," in *Proceeding of Electronic System-Integration Technology Conference*, 2018.
- [75] M. Van Soestbergen and J. Zaal, "Predictive modeling of competing failure mechanisms using a dedicated constitutive relation for solder alloy," *Proceeding of Electronic System-Integration Technology Conference*, 2018.
- [76] X. Long, I. Dutta, V. Sarihan and D. Frear, "Deformation Behavior of Sn-3.8Ag-0.7Cu Solder at Intermediate Strain Rates: Effect of Microstructure and Test Conditions," *Journal of Electronic Materials*, vol. 37, pp. 189-200, 2008.
- [77] J. Lau, W. Dauksher and P. Vianco, "Acceleration Models, Constitutive Equations, and Reliability of Lead-Free Solders and Joints," *Proceedings of Electronic Components and Technology Conference*, 2003.
- [78] R. Darveaux, "Thermal Cycle Fatigue Life Prediction for Flip Chip Solder Joints," *Proceeding of Electronic Components and Technology Conference*, 2014.



## Annex 1: Résumé en français

L'analyse de la durée de vie des joints brasés est un challenge pour les industries du spatial, de l'aéronautique et de la défense qui ont besoin d'équipements très fiables pour des environnements sévères et de longues durées de vie. L'évolution des technologies de boîtier électronique, principalement conduite par les marchés civils, introduit de nouvelles architectures et de nouveaux matériaux dont la fiabilité doit être étudiée pour les exigences de ces marchés critiques. Un des éléments critiques d'une carte électronique est l'interconnexion effectuée par le joint brasé. Dans ce contexte, les connaissances des propriétés de fatigue des matériaux utilisés pour le joint brasé sont nécessaires pour développer des cartes électroniques, définir les essais accélérés de qualification ou pour réaliser des simulations de durée de vie.

Les lois de fatigue utilisées communément dans l'industrie sont généralement des critères simplifiés comme la loi de Coffin-Manson, basée sur la déformation inélastique, ou celles basées sur l'énergie dissipée. Les déformations plastique et visqueuse sont dans ces lois indissociées et appelées déformation inélastique, supposant que les contributions au dommage des déformations plastique et visqueuse sont similaires. Cependant, la pertinence de ces lois dans le cas du matériau joint brasé et les profils de mission des marchés critiques doit être étudiée. En effet, le joint brasé possède une température de fusion faible qui entraîne un comportement visqueux même à température ambiante. Celle-ci est nécessaire à l'étape d'assemblage des boîtiers. Ainsi, d'importantes déformations visqueuses sont développées notamment pour les environnements sévères et les longues phases de maintien de ces marchés critiques. Dans ce contexte, il est important de prendre en compte l'interaction fatigue-fluage dans les matériaux du joint brasé pour atteindre les exigences de ces applications.

Les limitations de la littérature sont le manque de données expérimentales précises dissociant les déformations plastique et visqueuse en essai de fatigue. La représentativité des éprouvettes massiques par rapport à l'application finale est en effet discutable au vu de la microstructure très spécifique du joint brasé. De plus, il n'existe pas de consensus réel sur les modèles matériaux à utiliser. Dans ce contexte, un banc de mesure innovant a été développé. Le banc de mesure développé permet de réaliser des essais de fatigue en cisaillement sur des boîtiers électroniques assemblés. Les boîtiers sont chargés cycliquement avec une très faible vitesse de sollicitation. Un couplage de mesure mécanique et électrique permet d'extraire les courbes d'hystérésis ainsi que de capter la défaillance du premier joint brasé du composant. Le déplacement local au niveau des joints est mesuré par corrélation d'image. Une méthode de post-traitement permet d'extraire des paramètres mécaniques représentatifs de la réponse de l'éprouvette composant.

Le temps de maintien, la température et la force appliquée ont un impact sur le nombre de cycles à défaillance. La combinaison d'une augmentation de la température avec l'ajout du temps de maintien réduit jusqu'à un facteur dix le nombre de cycles à rupture. Les courbes d'hystérésis du boîtier ont été converties en contrainte et déformations plastique et visqueuse dans le joint brasé dans le but de calibrer un modèle matériau et une loi de fatigue. Les résultats montrent que l'intérêt des lois de fatigue utilisées communément est limité. Des résultats utilisant différents dispositifs expérimentaux de la littérature ont été ajoutés pour compléter ceux trouvés. Une loi de fatigue modifiée en fréquence a été testée et montre de meilleures prédictions dans le cas d'essais réalisés à différentes fréquences car elle permet de prendre des effets liés au temps comme la viscosité. Cependant, des limites avec cette loi ont été trouvées dans le cas de sollicitation avec temps de maintien.

Une loi de fatigue prenant en compte l'interaction fatigue fluage a ensuite été proposée avec de bonnes prédictions notamment pour des températures plus élevées. Cette loi de fatigue nécessite de dissocier les déformations plastiques et visqueuse dans le calcul de dommage. Un modèle visco-plastique du matériau joint brasé a été calibré sur les résultats des essais de fatigue pour dissocier ces deux déformations. L'interaction fatigue-fluage dans cette nouvelle loi permet notamment une meilleure prise en compte du temps de maintien sur le nombre de cycles à rupture. L'évolution de la microstructure a montré que le dommage détruit la structure dendritique du joint et la remplace par des joints de tailles plus petites dans la zone proche de la fissure. La coalescence d'éléments a également été observée. Cependant, plus d'investigations sont nécessaires pour définir les marqueurs spécifiques des dommages plastique et visqueux.

## Annex 2: Microstructure evolutions with damage

### Initial observation

Grain structure is analyzed using angular disorientation between measured points in the solder joint. The grain boundary is defined with a limit angle value during the post-processing of the results. The grain structure is first analyzed using a large angular scale. The analysis is then refined in order to evaluate local disorientation of angular values from 0 to 2 degrees.

### Grain structure

Two WLP solder balls are observed after cross-section as depicted in Figure 114. The grain size is the diameter of the equivalent center which is formed considering all the calculated points of the grain. The two solder joints are composed of one large grain with twins. The twin structure of Tin is characterized by a disorientation of 60 degrees.

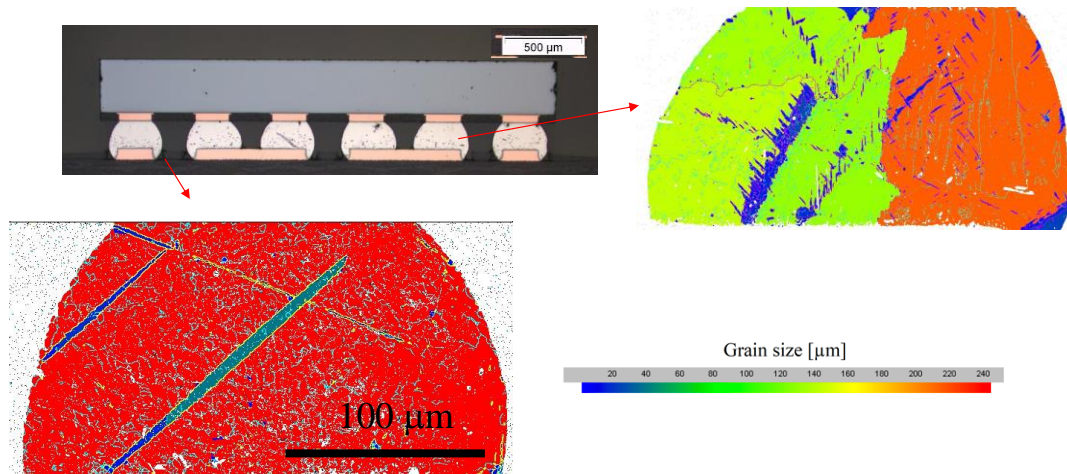


Figure 114: Initial inspection of the studied SAC305 solder ball of the WLP after assembly process with EBSD

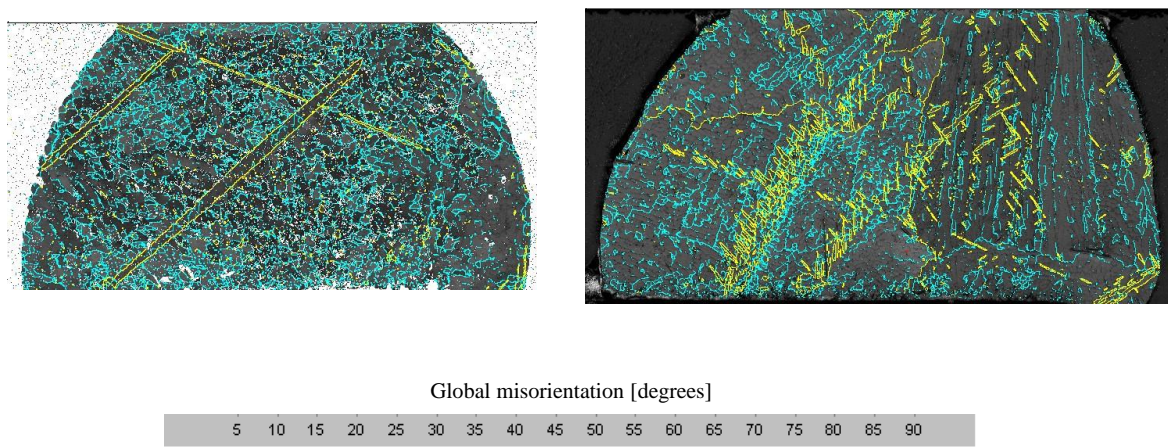


Figure 115: Analysis of the global misorientation of the studied SAC305 solder ball of the WLP after assembly process with EBSD

The global disorientation in the solder balls of the WLP specimen are depicted in Figure 115. The misorientation domains are divided between the low, represented by angles from 0 to 5 degrees, and

the large misorientation domains. The low misorientation domain is present inside solder joint grain and is composed of the noise due to the accuracy of measurement and the interdendritic structure. The large misorientation domain is composed of misorientation coming from the twin structure of solder joint around 60 degrees and macro grains.

## Local misorientation

The local misorientation in the solder balls is depicted in Figure 115. The inter-dendritic structure is characterized by local disorientation around one degree. The tin matrix of the solder is revealed with close to zero angular disorientation meaning that the crystallographic structure is unique in the matrix.

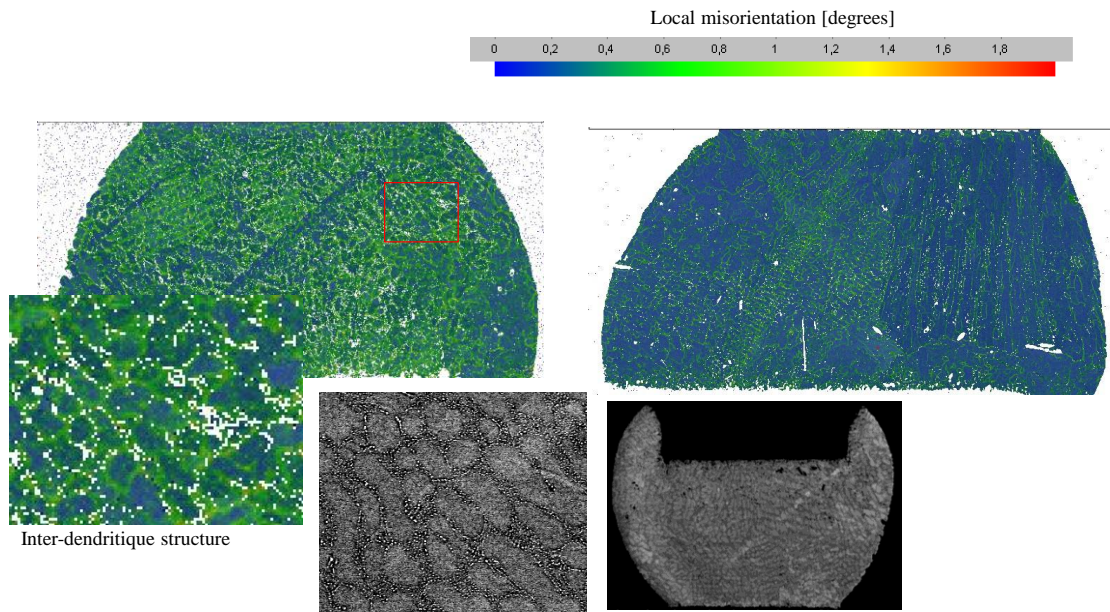


*Figure 116: Local misorientation of the studied SAC305 solder ball of the WLP after assembly process with EBSD*

## Damage microstructure evolutions

The microstructure after fatigue test is studied, comparing with the initial state, to evaluate microstructure evolutions induced by the damage. Two fatigue cyclic shear tests with the test bench, at room temperature and 35 N of force magnitude, are compared:

- one fatigue test without dwell time, in electrical failure after 1620 cycles ;
- and one fatigue test with 10 s of dwell time, in electrical failure after 585 cycles.

The fatigue test with 10 s of dwell time has more damage from viscous strain than the one without dwell time. Difference between the two microstructure evolutions will be listed in order to point out microstructure evolutions from plastic and viscous strains. However, conclusions must be carefully



considered because only one solder joint from one sample of each configuration has been observed which is not adequate statistically.

## Grain structure

The global misorientation of the fractured area of the two samples is depicted in Figure 117. The concentration around 60 degrees of the spectra which has been observed in the initial state is also present. Microstructure differences are present close to the fracture. In fact, the damage is located close to fracture or stress concentration area. This is consistent with the concentration of stress and inelastic strains close to the weakness of the solder joint inducing the fracture. In fact, despite the homogeneous stress state assumption used in the previous part, stress concentrations are present when the solder joints are loaded with a shear force in the corners.

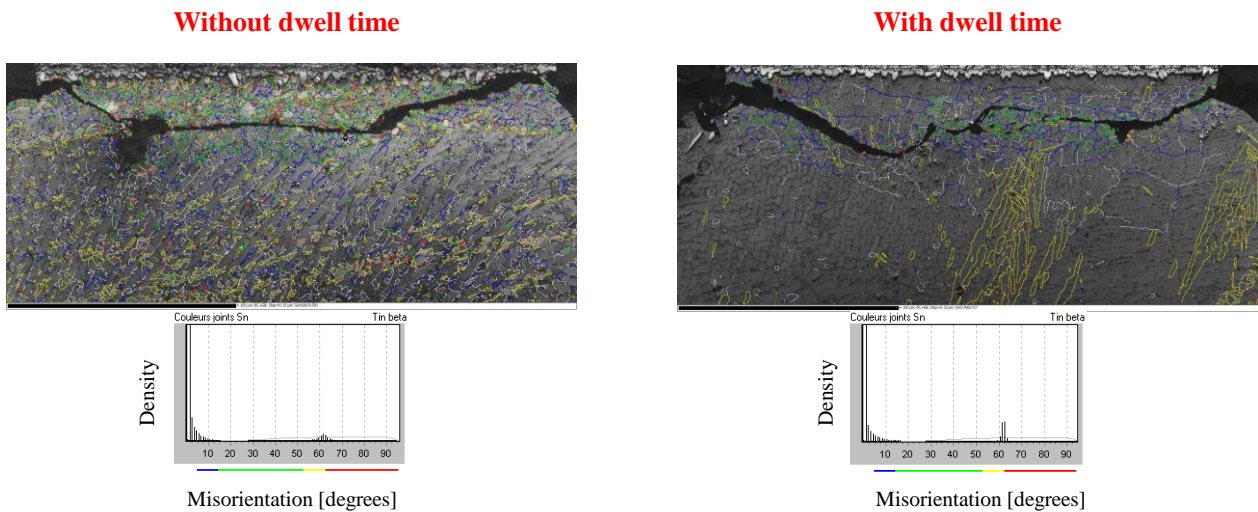


Figure 117: Grain structure with EBSD without/with dwell time of the studied SAC305 solder ball of the WLP after assembly process with EBSD

Observations of the misorientation close to the fracture reveal that the damaged area is composed of misorientations from 0 to 90 degrees with a gradient from the non-damaged area to the fracture surface for both without and with dwell time configurations. The sample with dwell time seems to have lower misorientation angle but as explained previously, all comparisons between the two configurations must be taken with precaution due to the low replicability of the study.

## Local misorientation

The local misorientation from 0 to 2 degrees is now analyzed. The result is depicted in Figure 118 for the two configurations. The results show that the local misorientation state found far from the fracture and in the initial state differs from the one in the area close to the fracture. The interdendritic microstructure has disappeared and is now composed of misorientation angles around 1 degree. This phenomenon is more diffused for the configuration with dwell time. Once again, this conclusion must be considered with precaution.

The explanation of this microstructure evolution is the destruction of the inter-dendritic structure with the energy coming from inelastic strains. The recrystallization is induced by inelastic strains which are drivers of microstructure evolutions.

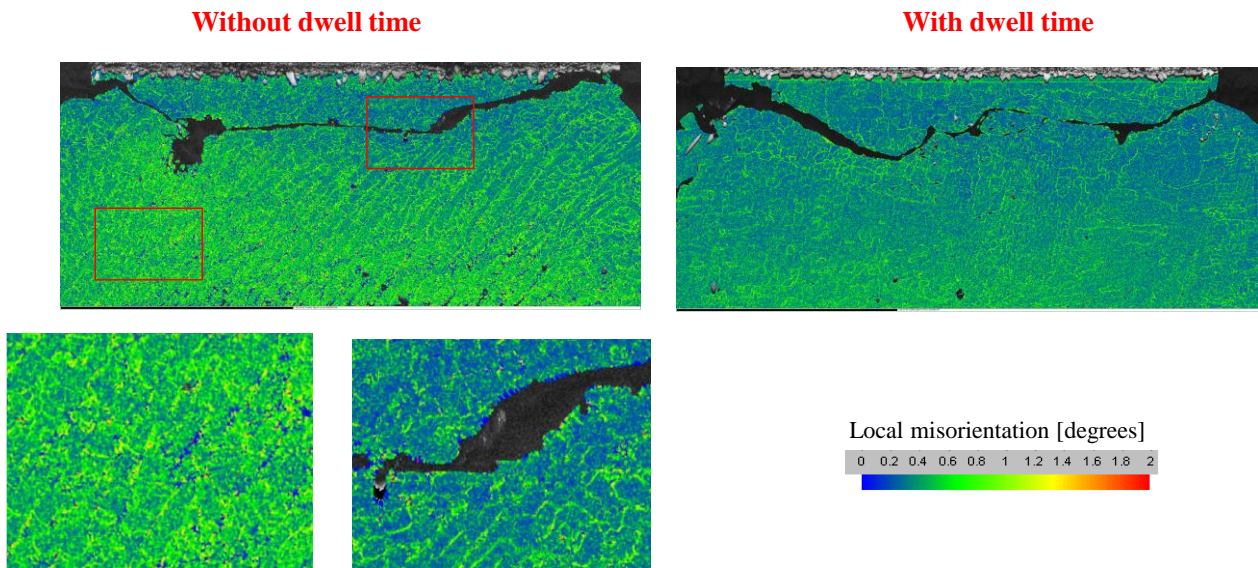


Figure 118: Local misorientation with EBSD without/with dwell time of SAC305 WLP36 solder ball

## Chemical microstructure

EDX analysis has also been performed on the two samples submitted to fatigue tests. The EDX reveals the chemical presence of predefined elements on the analyzed surface from the crystallographic diffraction. Results of the EDX analysis is depicted in Figure 119. Chemical distribution show that the solder joint surface is mostly composed of Sn crystals. The intermetallic structure between copper and solder joint material is composed of  $\text{Cu}_6\text{Sn}_5$  precipitates created during the assembly process.  $\text{Ag}_3\text{Sn}$  and  $\text{Cu}_6\text{Sn}_5$  precipitates are also present in the solder joint. The study also reveals that  $\text{Ag}_3\text{Sn}$  and  $\text{Cu}_6\text{Sn}_5$  precipitates are concentrated around the fracture for the sample submitted to the fatigue test with dwell time. Inelastic strains developed in this region have probably given the sufficient energy to form these precipitates close to the fracture. The formation of these precipitates seems to be a microstructure evolution mostly coming with viscous strains. This conclusion must be considered with precaution and required more investigation to be ensured.

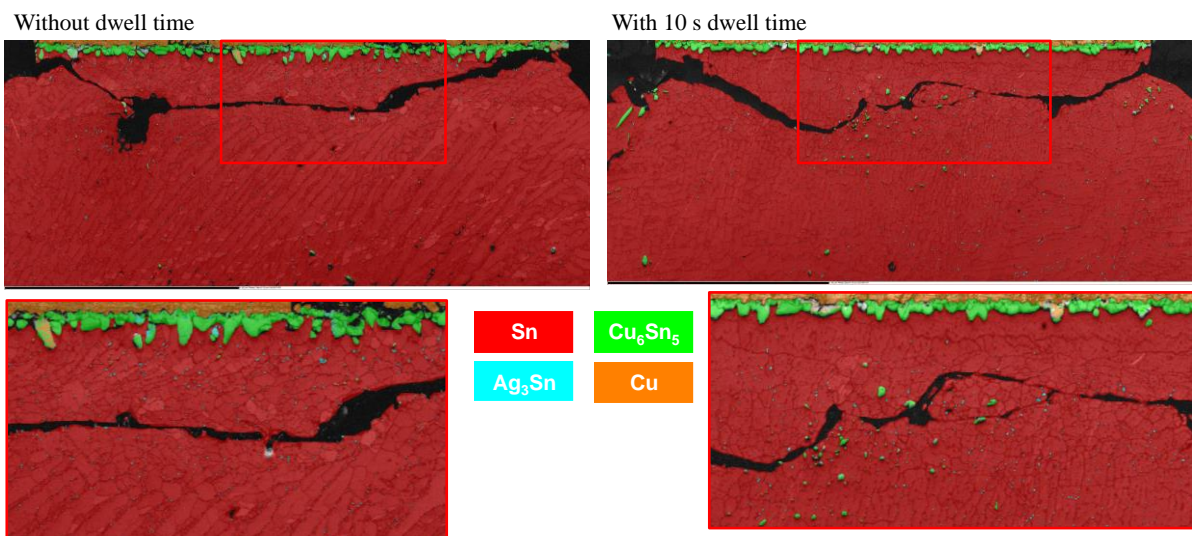
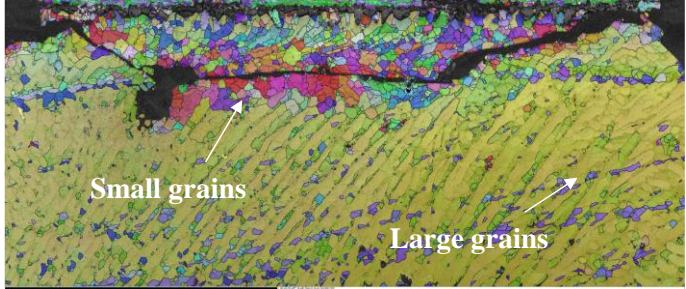
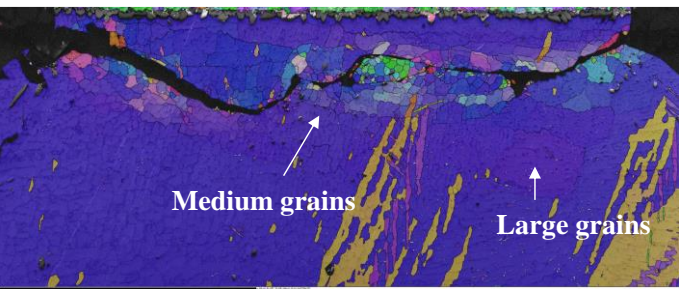


Figure 119: EDX analysis results for the two solder joints of two WLP36 samples assembled in lead-free and analyzed after fatigue at 35 N at room temperature without and with dwell time

## Plastic and creep damage

Table 27 summarized the microstructural observation made on the two samples. The microstructure evolutions observed has been also observed after thermal cycling in other studies which strengthens the close failure mechanism between accelerated thermal cycling and our shear tests.

Table 27: Microstructure evolution with damage after fatigue tests (EBSD pictures)

Without dwell time	With dwell time
Dominant « Plastic » damage	Dominant « Plastic + creep » damages
	
<p>Nf = 1620 cycles f = 0.025 Hz T = 18 hours</p>	<p>Nf = 585 cycles f = 0.017 Hz T = 9 hours 45 mins</p>
<p>Noticeable observations:</p> <ul style="list-style-type: none"> <li>• Dendritic structure disappearance</li> <li>• Small grains development</li> <li>• Granular microstructure evolution in an extent area from the fracture</li> </ul>	<p>Noticeable observations:</p> <ul style="list-style-type: none"> <li>• Dendritic structure disappearance</li> <li>• Small grains development</li> <li>• Coalescence of mostly Ag<sub>3</sub>Sn and also Cu<sub>6</sub>Sn<sub>5</sub> elements close to the fracture</li> <li>• Granular microstructure evolution in a close area from the fracture</li> </ul>



**Titre :** Interaction fatigue-fluage dans les alliages de joint brasé de boîtiers électroniques

**Mots clés :** Fatigue, joint brasé, banc expérimental innovant, interaction fatigue-fluage, durée de vie

**Résumé :** L'analyse de la durée de vie des joints brasés est un challenge pour les industries du spatial, de l'aéronautique et de la défense qui ont besoin d'équipements très fiables pour des environnements sévères et de longues durées de vie. L'évolution des technologies de boîtier électronique, principalement conduite par les marchés civils, introduit de nouvelles architectures et de nouveaux matériaux dont la fiabilité doit être étudiée pour les exigences de ces marchés critiques. Un des éléments critiques d'une carte électronique est l'interconnexion effectuée par le joint brasé. Dans ce contexte, les connaissances des propriétés de fatigue des matériaux utilisés pour le joint brasé sont nécessaires pour développer des cartes, définir les essais accélérés de qualification ou pour réaliser des simulations de durée de vie.

Un banc de mesure innovant a été développé pour étudier l'interaction fatigue-fluage dans les matériaux du joint brasé. Les résultats ont été utilisés pour calibrer une loi de fatigue avec les exigences des marchés critiques. Les perspectives sont l'analyse des évolutions de microstructure spécifiques induites par les dommages plastique et visqueux.

**Title :** Creep Fatigue Interaction in Solder Joint Alloys of Electronic Packages

**Keywords :** Fatigue, solder joint, innovative test bench, creep fatigue interaction, lifetime

**Abstract :** Solder joints reliability analysis represents a challenge for the aerospace and defense industries, which are in need of trustworthy equipment with a long lifetime in harsh environments. The evolution of electronic packages, driven by consumer civil applications, introduces new architectures and materials for which reliability needs to be qualified for the constraints of the aerospace and defense applications. One of the most critical elements of an electronic assembly is the solder joint interconnection. Knowledge of fatigue properties of solder material is required to design the assemblies, to define accelerated tests or to perform lifetime simulations.

An innovative test bench has been developed to study creep-fatigue interaction of solder joint material of assembled electronic package. Results have been used in order to calibrate a fatigue law for the requirements of critical markets. Perspectives are the analysis of the specific microstructure evolutions induced by plastic and viscous damages.

